Università degli Studi di Messina

Dipartimento di Scienze Matematiche e Informatiche, Scienze Fisiche e Scienze della Terra

Doctoral Program in Physics (Cycle XXXIII)

Defects in SiC: from hetero-epitaxial growth to ion implantation

Doctoral Dissertation of:
Cristiano Calabretta

Tutor: **Chiar.mo Prof. Lorenzo Torrisi**

Cotutor: **Dott. Francesco La Via**

Ph.D. Coordinator: **Chiar.ma Prof.ssa Vincenza Crupi**

Anno Accademico 2019/2020

Index

Chapter 1

Introduction

Progress in the field of semiconductors and epitaxial growth is driving the change in today's society towards the green revolution that exploits the use of wide bandgap semiconductors in the development of VLSI technology. SiC is a particularly versatile wide bandgap semiconductor for devices that work at high power, medium frequency, high temperature and harsh environments and has superior performance compared to the same Si devices. This is a phrase with an effect traceable in many texts of condensed matter and technology for decades and is still extremely valid and underlines why this material has been a topic of study for such a long time. SiC is a material with a large electric breakdown field, high thermal conductivity combined with high saturated drift velocity. Another key aspect is that SiC as well as Si has SiO_2 has its own native oxide. This property is strategic in the development of metal oxide semiconductor (MOS) technology. These peculiarities have made SiC challenging manufacturing captivating for the realization of working devices.

Meeting the ever increasing demand for energy efficiency in power electronics, SiC manages to fit into this area. These prospects can be achieved thanks to the reduction of devices switching and conduction losses, as well as that of devices capable of exploiting the development of power electronics resisting high temperatures. It is in this context that SiC takes a leading role among high bandgap semiconductors and recently the development of epitaxial technologies has given a strong improvement in the quality of SiC material, allowing to take the right path to fully exploit the SiC based device properties. We are slowly witnessing the progress and affirmation of a material that from its primordial state of "promising" is going to become an established reality in the field of microelectronics and sensors industry. The advantages of SiC compared to silicon are many and motivate the attention that this material has gained driven by a trend aimed at increasing the electric power conversion frequency, weight, cost and power loss of passive components.

Crystal Structure and properties

Silicon Carbide (SiC) is a compound semiconductor with a rigid stoichiometry 50% silicon (Si) 50% carbon (C). All Si and C atoms are tetravalent elements, and their outermost shells have four valence electrons. By exchanging electron pairs in sp^3-hybrid orbitals to form a SiC crystal, Si and C atoms are tetrahedrally bound. Si–C bond energy is extremely high (4.6 eV), which gives SiC a range of outstanding properties [1,2,3].

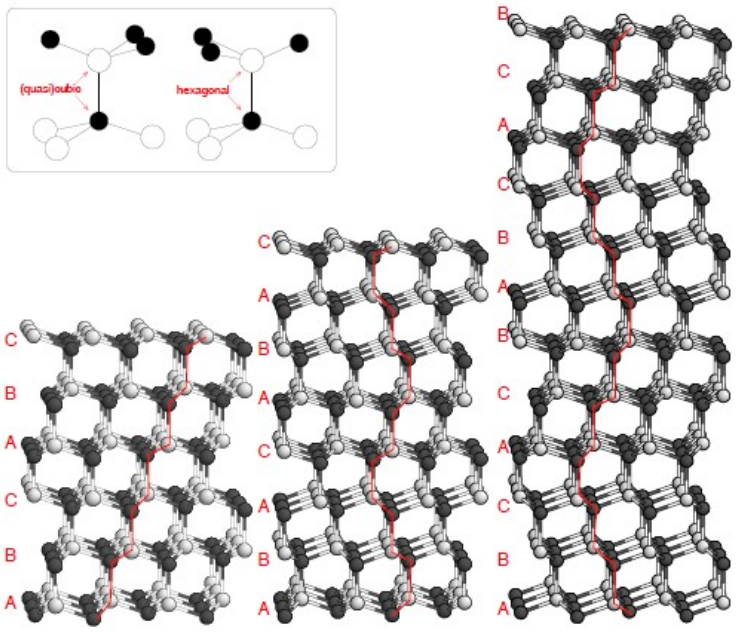

Figure 1.Schematic structures of popular SiC polytypes; from the left 3C-SiC, 4H-SiC, and 6H-SiC.

From a crystallographic viewpoint, SiC is the most well-known representation of polytypism. Polytypism is the process in which a material may follow various crystal structures that differ in one dimension (i.e., in stacking sequence) without altering the chemical composition. In a hexagonally close-packed configuration, the difference in the occupied sites along the c-axis results in various crystal structures, defined as polytypes. There are 3 alternative locations, identified as A, B, and C. Two layers cannot occupy the same site successively; either "B" or "C" sites must be occupied by the next layer on top of a "A" layer (and, similarly, "A" or "C" is allowed above "B"). From this definition the 3C-SiC is also defined as β-SiC and other polytypes are labelled as α-SiC.

As described in Figure 1, in a ball stick model, A, B, and C are the potentially populated sites within a hexagonally close-packed structure. Those site names allow 3C-SiC to be characterized by ABCABC's reiterating sequence, or simply by ABC. Similarly, ABCB (or ABAC) and ABCACB - identify 4H- and 6H-SiC, respectively. The "3C" structure is equivalent to the zincblende structure, which crystallizes most III – V semiconductors including GaAs and InP. The wurtzite form, often present in GaN and ZnS, can be referred to as "2H ". In general, crystals with strong covalent bonding crystallize under zincblende form, whereas for crystals with high ionicity wurztzite structure is more stable. The intermediate ionicity of SiC (11 % as defined by Pauling) may be a possible reason for SiC polytypism. Due to the variety of ways Si-C bilayers can be stacked, SiC has two lattice sites which vary in their immediate neighbor structures.

Lattice sites are distinguished in "hexagonal sites," and "cubic sites" depending on whether the surrounding structure is hexagonal or cubic [1].

It is useful to describe silicon carbide polytypes by the parameter "hexagonality" γ specified as the ratio of the number of atoms in hexagonal locations to the total number of atoms in the unit cell.

$$\gamma = \frac{N_H}{N_H + N_C} \tag{1}$$

A polytype hexagonality can differ between unity (2H-SiC) and zero (3C-SiC) passing through 4H with 50% hexagonality.

The main 4H-SiC properties with respect to Si (displayed in Table 1) include its three times larger bandgap, roughly ten times higher breakdown electric field strength, and three times higher thermal conductivity as compared with Si. Note that in hexagonal SiC the electron mobility along the ⟨0001⟩ direction is about 15–20% higher than that perpendicular to ⟨0001⟩, which is beneficial for the development of vertical power devices on standard SiC{0001} wafers.

	SiC	Si
Bandgap (eV)	3.26	1.12
Electron mobility for high-purity material ($cm^2 V^{-1} s^{-1}$)		
μ parallel to c-axis	1200	1350
μ perpendicular to c-axis	1020	1350
Hole mobility ($cm^2 V^{-1} s^{-1}$)	120	450
Electron saturated drift velocity (cm/s)	2.2×10^7	1.0×10^7
Hole saturated drift velocity (cm/s)	($\sim 1.3 \times 10^7$)	9×10^6
Breakdown electric field for material with a doping density of $10^{16}\,cm^{-3}$ (MV/cm)		
E_B parallel to c-axis	2.8	0.3
E_B perpendicular to c-axis	2.2	0.3
Thermal conductivity ($W\,cm^{-1} K^{-1}$)	3.3–4.9	1.3–1.5
Relative dielectric constant	9.8	11.9

Table 1. Main physical properties of 4H-SiC and Si at room temperature.[1]

One of major constraints for power devices is represented by their operating voltage which results from the critical electric field (E_{crit}) at which the breakdown avalanches takes place. Looking at Figure 2, where a field distribution in a one-sided abrupt junction for SiC and Si at the same breakdown voltage is reported, it is evident that SiC is characterized by a wide bandgap which enables great brakdown electric field meaning that the charge carriers must be accelerated at high speeds to reach the kinetic energy necessary to overcome the bandgap[4].

Following equation

$$V_B = \frac{E_C W_D}{2} \tag{2}$$

where V_B is the breakdown voltage and W_D is the drift region, breakdown voltage can be calculated. Thanks to the breakdown field strengh 10 times higher than Si, the thickness of the voltage blocking layer can be one tenth than those in Si devices.

SiC can withstand an electric field about ten times greater than Si without undergoing avalanche breakdown. Such property gave rise to the fabrication of very-high voltage, high-power devices such as, diodes, power transistors and high power microwaves devices. In addition, it allows close distancing between adjacent devices, leading to high packing density in integrated circuits.

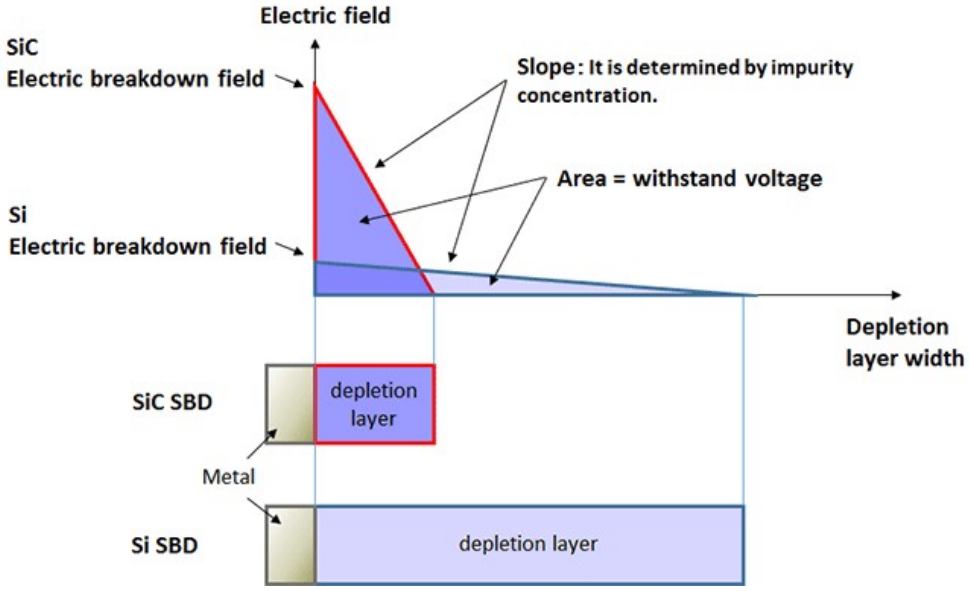

Figure 2 Electric field distribution in a one-sided abrupt junction for SiC and Si at the same breakdown voltage.

SiC high voltage devices are known to have low on state resistance, so that they can be unipolar and be fast switching. So, unlike Si, 4H-SiC 3.2 times larger bandgap energy combined with the ability to withstand high voltages and an electric field tollerance at least an order of magnitude higher than in Si, are properties that can be exploited for power devices production. The main improvements concern the possibility of using MOSFETs with a reduced drain to source R_{on}, which stands at about 300-400 times less than the corresponding Si devices with the same breakdown voltage.

4H-SiC proves to be particularly suitable in the design of power devices characterized by extraordinary efficiency. This is particularly attractive as 4H-SiC provides high power levels minimizing power loss and downsizing die size about five-fold.

Advantages of 4H-SiC over Si

4H-SiC devices show both high thermal conductivity as well as fast switching and thanks to their lower output capacity and low Ron make the SiC MOS attractive to fast switching designs such as power supplies, three-phase inverters and other kinds of electronic converters (AC to DC and DC to DC).

These improvements are achievable following 4H-SiC ability to handle high energy levels while operating at high switching frequencies that allow significant savings relating to the downsizing of the magnetic parts (transformers, chockes, inductors) implemented in all switching systems.

The extremely low 4H-SiC devices drift resistance contributes to the reduction of the on-state loss. Figure 3 plots the minimum specific on-resistance (drift-layer resistance) against the blocking voltage for Si and SiC unipolar devices. The minimum specific on-resistance (drift-layer resistance) is given by

$$R_{drift} = \frac{4V_B^2}{\eta\varepsilon\mu E_B^3} \tag{3}$$

where ε, μ, and E_B are the dielectric constant, mobility, and breakdown field strength, respectively and η is the ionization ratio for the dopants at room temperature.

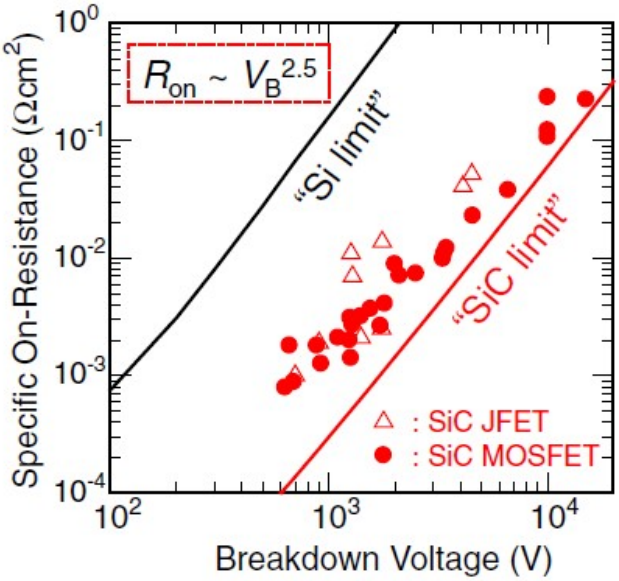

Figure 3. Minimum specific on-resistance (drift-layer resistance) for Si and 4H-SiC unipolar devices (so-called "Si limit" and "SiC limit") versus the blocking voltage.[5]

Although the drift-layer resistance (R_{drift}) is proportional to V_B^2 in Eq.(3), the actual resistance increases in proportion to $V_B^{2.3-2.5}$, as seen in Figure 3, because the breakdown field strength decreases in the lightly-doped materials employed for high-voltage devices.

A remarkable aspect regarding 4H-SiC power devicecs is represented by the contained reverse recovery. Medium and high voltage bipolar devices (PiN diodes, insulated gate bipolar transistor (IGBT), bipolar junction transistors (BJT) and thrysistor) are widespread because the high R_{on} is suitable for being remodeled by minority carrier injection [6]. Nevertheless bipolar device are affected by minority carrier storage which is the main cause of slow switching speed and large reverse recovery in turn-off operation. On the other hand, SiC unipolar device appears to be a viable solution. Indeed, in SiC SBDs and FETs R_{on} remains low and there is no minority carrier storage. Moreover, thanks to the blocking voltage region ten times smaller, the stored charge is ten times less so that SiC bipolar devices too can exhibit fast switching times. Because of its wide bandgap, the intrinsic carrier density (n_i) in SiC is extremely low, $5 \cdot 10^{-9}$ cm^{-3} at room temperature, while the corresponding value for Si is $1 \cdot 10^{10}$ cm^{-3}. An Arrhenius plot of the intrinsic carrier densities for 4H-SiC and Si is shown in Figure 4. In general, carrier generation is proportional to n_i^2 in the case of band-to-band generation and to n_i in the case of generation via a deep level [7]. This is the main reason why 4H-SiC devices exhibit a low leakage current even at elevated temperatures.

4H-SiC high thermal conductivity favors operating temperature up to 250 °C without need for cooling equipment, unlike Si. The operation can be extended to higher temperatures [8], at the price, however, of a reduction in the R_{on} which degrades with the rising temperatures.

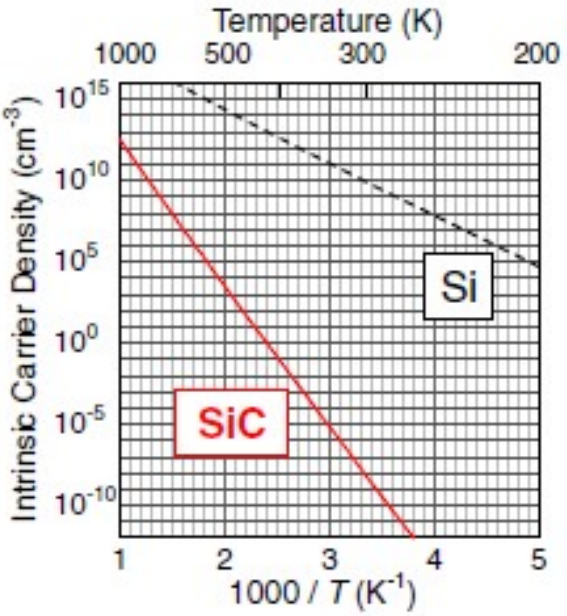

Figure 4. Arrhenius plot of the intrinsic carrier density for 4H-SiC and Si [5].

The high thermal conductivity permits to dissipate heat coming from power losses, to avoid device overheating and performance degradation. 4H-SiC devices expected excellent performances are often defined by a figure of merit; since many years several analyses on the material parameters impact have been carried out. Johnson derived a figure of merit (JFOM) [9], where v_s represents the electron saturation velocity

$$JFOM = \frac{E_B^2 v_s^2}{4\pi^2} \tag{4}$$

which establishes the power-frequency product for a low voltage transistor. Such merit figure indicates that 4H-SiC is an outstanding source for high frequency applications.

Keyes' figure of merit (KFOM) [10] provides a thermal limitation to the switching behavior of transistors used in integrated circuits

$$KFOM = k\sqrt{\frac{c \cdot v_s}{4\pi\varepsilon_s}} \tag{5}$$

where k is the thermal conductivity, c is velocity of light and ε_s is the static dielectric constant.

A figure of merit originating from Baliga (BFOM) defines parameters to minimize the conduction loss in low-frequency applications [11]

$$BFOM = \varepsilon_s \mu E_g^3 \tag{6}$$

where μ is the carrier low-field mobility.

The results of these figures of merit, normalized with respect to Si, are summarized in Table 2 and evidence how 4H-SiC power devices are able to attract increasing interest in high-temperature, high-power, and high-frequency devices

	JFOM	***KFOM***	***BFOM***
Si	**1**	**1**	**1**
3C-SiC	**324**	**4.83**	**163**
4H-SiC	**400**	**4.17**	**464**
GaAs	**1.78**	**0.32**	**14.6**
Diamond	**8,100**	**32.2**	**23,000**

Table 2. Relative figures of merit of different semiconductors [1].

SiC devices and applications

With an increasing adoption of power diodes, the manufacture of vertical SiC switching devices appeared at initial '90s. Palmour et al. validated a vertical 6H-SiC trench MOSFET and subsequently developed 4H-SiC trench MOSFET, thrysistors and BJTs. In 1997 Cooper et al succed in designing the first planar double-implanted MOSFET (DIMOSFET) adopting 760 V blocking voltage with a low on resistance, and in 1998 new SiC trench MOSFET implementation was concluded. A 660 V 1.8 $m\Omega cm^2$ SiC MOSFET with a innovative channel design was presented in 2006. To avoid interfacial MOS issues, vertical junction FETs (JFETs) were designed [12] and subsequent commercialization became soon reality in 2006. Subsequently through steady improvement of MOS channel mobility and oxide maturity, SiC power DIMOSFETs have become available on the market since 2010 [13]. The world of microelectronics is strongly focused on the development of these devices. For example, the volume and weight of a power supply or inverter system can be shrinked by a factor 2-10, depending on how many SiC electronic parts are inserted. Besides the dimension and mass reduction a sensible lowering in power dissipation has been confirmed to conversion efficiency benefit thanks to the use of SiC-based components. At present the research is interested in the creation of double trench MOSFETs with an R_{on} below the threshold of 1 $mOhm \cdot cm^2$ [14], and recently a 10 kV working DIMOSFETs has been demonstrated.

To date, 4H-SiC power switching devices still have an expensive cost and need further improvements. Figure 3 shows the difference between the theoretical R_{on} curve compared to the experimental data. Although still improvements have to be acquired in the low voltage devices field (600-1200 V), it is clear that the SBDs performances are orders of magnitude better than the same technology in Si. Figure 5 shows actual reference voltages for Si and 4H-SiC based devices. The limit between unipolar and bipolar devices is marked by the material blocking voltage. This boundary is located at 300-600 V for Si and at several kV in 4H-SiC. However, it should be stressed that on 4H-SiC there is not the same experience and knowledge gained from decades of research on Si.

Many physical properties indispensable for improving simulations are still under investigation. Defects impact on device performance is a hot topic as their behavior mechanism during growth and during device operation remain poorly understood. Although 4H-SiC brings numerous benefits in electrical and thermal characteristics, many factors are hindering large scale 4H-SiC growth and devices production, such as micropipes, screw dislocations stacking faults wich have the effect of limiting device reliability. However, these difficulties did not prevent the spread of 4H-SiC power

devices. SiC wafer production is currently involving a great deal of research for wafers realization with a larger size through chemical vapor deposition (CVD) and goals such as 4H and 3C-SiC 8 inches technology development for manufacturing vertically integrated structures are the next challenges.

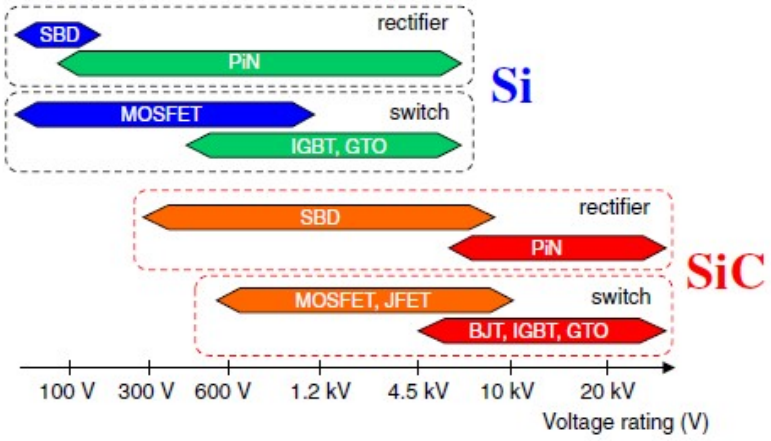

Figure 5 Actual voltages fields for 4H-SiC and Si unipolar devices [5].

An increase in the diameter of the wafer would help improve productivity and significantly reduce production costs. In the same way, the improvement of the production processes and in particular of bottleneck processes such as activation by ion implantation and the reduction of the induced defectiveness would entail an advancement for goals of greater reliability of the devices and the achievement of the SiC theoretical operating limits.

3C-SiC and 4H-SiC differences

3C-SiC is the only polytype with isotropic properties due to its cubic crystal symmetry. In addition, it is not subjected to micropipe defects formation and is the most thermodynamically stable polytype with the specific advantage that it can be grown at lower temperatures (below 1500 °C). The resticted thermal budget needed for 3C-SiC growth, restricted the production of efficient 3C-SiC bulk homoepitaxial wafers which required faster growth of subsequent homo-epitaxial layers in order to obtain device-grade 3C-SiC epilayers.

3C-SiC suffers high quality substrates lack on which carry out homoepitaxial growths, so heteroepitaxy has been implemented, but still requires substantial research investment [15,16]. Nevertheless, 3C-SiC epitaxial layers growth on a Si substrate with the largest possible area would

be an important research milestone that would allow to fully exploit polytype properties. Cubic Si is considered to be the most appealing substrate as well as crystal seed for thin epitaxial layer or thick substrate growths. Recently important results have been achieved by means of the chemical vapor deposition (CVD) technique which would allow 3C-SiC high purity epitaxial layer production. The guideline followed in 3C-SiC technological device development is based on the concrete possibility of reducing wide band-gap materials production costs growths. In recent years a considerable scientific effort has been made for 4H-SiC based tecnology manufacturing and the development of large area seeds for high purity electronic-grade epitaxy has been spent. [17]. However, considerable drawbacks remain regarding the material production cost and in power electronic device reliability, for example MOSFET.

A notable difference consists in SiC epitaxy costs reserved to Schottky diodes. If, on the one hand, an 8-inch 4H-SiC homoepitaxial layer would amount \$ 10/cm^2, on the other hand a 3C-SiC epitaxial layer grown on Si would cost about \$ 2/cm^2. Obviously, 4H-SiC homoepitaxy is nowadays a consolidated technology with high purity epitaxial layers, while 3C-SiC grown on Si still shows a crystalline quality to be improved and is still significantly stressed suffering from bowing. Although this still hinders any wafer lithographic processing, it must also be underlined that 8 inches 4H-SiC is still in the primordial phase.

Property	Si	3C-SiC	6H-SiC	4H-SiC
Bandgap (eV)	*1.12*	*2.35*	*3.08*	*3.28*
Breakdown field E_b (MV/cm @ $N_D = 5 \times 10^{15}$/cm^3)	*0.3*	*1.5*	*2.2*	*2.3*
Intrinsic carrier concentration n_i (cm^{-3} @ T = *300* K)	1×10^{10}	1.5×10^{1}	1.6×10^{6}	5×10^{9}
Electron Mobility μ_n (cm^2/(V s))	*1350*	*900*	*370*	*800*
Hole Mobility μ_n (cm^2/(V s))	*480*	*40*	*80*	*120*
Saturated electron velocity v_s ($\times 10^7$ cm/s)	*1*	*2*	*2*	*2*
Thermal conductivity κ (W/(cm K))	*1.5*	*3.2*	*4.9*	*3.7*
Dielectric constant ε	*11.7*	*9.7*	*9.6*	*9.6*

Table 3 Relevant electrical properties for Si, 3C-SiC, 6H-SiC and 4H-SiC[1].

As shown in the Table 3 which show the main SiC polytype properties, 3C-SiC finds application in the field of MOSFETs with equal interest as 4H-SiC. Among all the 3C-SiC advantages over hexagonal polytypes there are high channel and bulk mobility. Indeed, a channel mobility of up to 250 cm^2/ Vs has been recorded [18, 19,20, 21] thanks to 3C-SiC crystalline symmetry. Furthermore

it is worth noting that the density of the 3C-SiC/SiO_2 states is an order of magnitude lower than those deduced for 4H-SiC, thanks to the smaller bandgap and the consequent interface states inclusion within the bandgap [22,23,24,25.] The reduced density of states at the interface between SiC and SiO_2 is crucial for MOS applications. The interface states deeply affect 4H-SiC channel mobility and threshold voltage in the MOS based deviced. In Figure 6 a review of the best results obtained on 4H-SiC [26,27] and 3C SiC [28] in terms of channel mobility is shown. It is evident that in 3C-SiC case, channel mobility can reach a value a factor 10 higher than the standard 4H-SiC processing implemented with NO nitridation. In addition, a reduced value of the device on state resistance R_{on} is obtained through high channel mobility, expecially for low voltage breakdown devices.

This feature allows to reduce the conduction losses when a MOSFET is in forward biased and, moreover, it is possible to notice a lower leakage current in reverse bias, even in low-medium power regime, due to the limited intrinsic carriers concentration as characteristic of SiC polytypes with respect to Si. Among all the applications, those related to sensors and devices operating at Si devices prohibitive temperatures as well as harsh environments are also a viable path for 3C-SiC based technology. Recently Acreo and HOYA Corporation have made considerable progress in 3C-SiC based technology and have demonstrated how power MOSFETs operate at 610 V voltages with low resistance and good channel mobility [29].

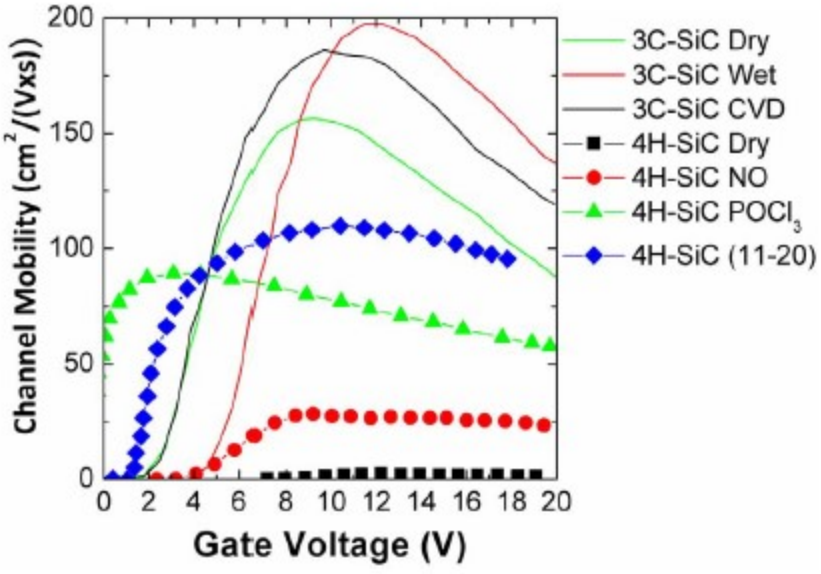

Figure 6 Comparison between the channel mobility in 3C-SiC and 4H-SiC.[29]

Defects in 3C-SiC

The development of 3C-SiC films on a Si substructure implies, fundamentally, that two separate materials are brought together leading multiple results in the subsequent epitaxy. First of all, a strain impact is generated at the Si/SiC interface following the difference in reticular parameter between SiC and Si which stands at around 19.7%. This misfit arises from the materials different lattice parameters which are 4.5489 Å and 5.4311 Å, for SiC and Si respectively [30].

At the interface, a high density of misfit dislocations is generated as partial relaxation by such intrinsic stress. The high concentration of these dislocations are mainly Lomer and lambda dislocations with average spacing of 1 nm between them. A high density of both planar and volume defects start from the interface, such as micro-twins, anti-phase boundaries and stacking faults. Such defects that are responsible for device failure are slowly reduced with increasing growth thickness. A further defect source arises from difference between the thermal expansion coefficients existing between Si and SiC ($2.77 \cdot 10^{-6}$ K^{-1} for Si and $2.57 \cdot 10^{-6}$ K^{-1} for SiC) [31]. This stress contribution is particularly manifested during the cooling phase from the growth temperature to the room temperature. During growth this mismatch grows from 8% to 20% (above 1000 ° C). During the cooling phase, the stress turns tensile and causes an upward bending of the wafer as well as the generation of cracks in the epitaxy. As previously anticipated, defects minimization starts from the reduction of defects born at interface. The reduction occurs during growth following self-annihilation processes. Microtwins and SFs coming from planes {111} in opposite directions tend to intercept and annihilate each other, consequently reducing defect density by increasing growth thickness [32, 33]. Some of these defects are generated during epitaxial growth, away from the Si/SiC interface. The final density of SFs therefore stands at a saturation value during growth, not completely disappearing. Misfit dislocations act to release a large portion of stress created at interface and stacking faults vary their concentration from 10^9 cm^{-2} in the initial nanometers, up to their decrement in density by increasing the thickness of the film. After 250 µm of growth the SFs density reaches about $2x10^3$ cm^{-1} (Figure 7). Such high density per unit of length is highly compromising for devices reliability, following their electrical activity. SFs density reduction is driven by the mutual annihilation process that occurs in the first layers of growth. As the density of SFs decreases, the annihilation process also slows down.

A large SFs reduction can be obtained at lower thickness only using a compliance substrate [29], while to further reduce the defect density, different process parameters should be tuned. By increasing the growth temperature to 1400 °C and by lowering the growth rate a considerable lowering in SFs density was observed. Such lowering is even greater if the silicon substrate is

melted and the epitaxy process is performed at temperatures higher than the Si melting temperature as shown in Figure 7.

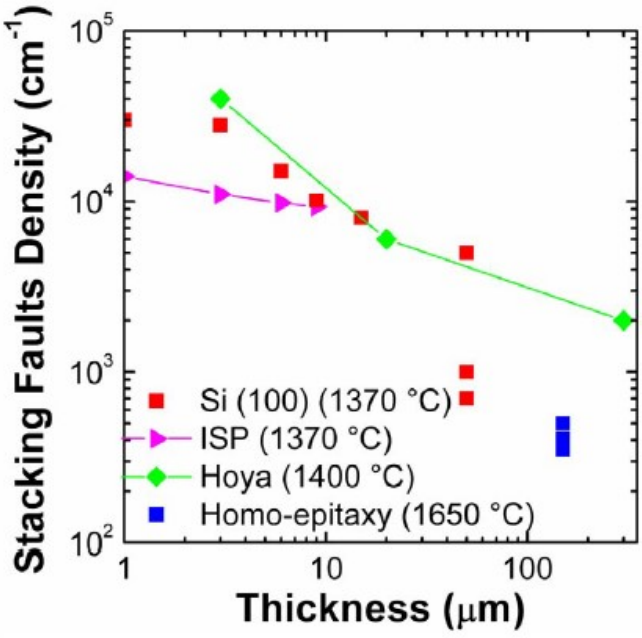

Figure 7 Stacking faults (SFs) density as a function of epitaxial grown thickness for 3C-SiC samples developed on different substrates. [29].

Defects in 4H-SiC growth

Within the epitaxial wafers used for the devices manufacture, despite the maturity reached in material growth, numerous crystalline imperfections are present in the form of point and extended defects. In the epitaxial layer most of the them are replicated from the underlying layer, but some typologies are generated during the growth of the epitaxial layer or from subsequent growth processes, such as ion implantation. Here a brief overview is exposed.

A micropipe defect is made up of a hollow core associated with a superscrew dislocation [1]. The Burger vector is characterized by a magnitude of | 3c | for 4H-SiC where c is the fundamental translation vector along the *c* axis, which correspond to 3 nm. A micropipe can be described as a pinhole that propagates along the <0001> direction through the entire SiC wafer. Devices that include a micropipe exhibit heavy degradation due to the onset of leakage current as well as a premature breakdown. The density of the micro pipes should therefore remain below 0.1 cm^{-2} [34]. Threading screw dislocation (TSD) propagates along <0001> direction and can only occasionally be found along the basal plane, with a Burger vector magnitude equal to 1c + a (as they are not pure screw dislocations). A threading edge dislocation (TED) and a basal plane dislocation (BPD) are united by the same Burger vector equal to ax (<11-20> /3). As shown in Figure 8a the BPD and the TED differ only in the slip plane. For this reason BPD to TED and TED to BPD conversions are

commonly observed in boule crystals (Figure 8b). The dominant nucleation process of BPDs is represented by thermal stress caused by temperature gradient during growth. The vast majority of TSDs propagate during homoepitaxial growths and only a small percentage changes in the form of Frank type dislocation. A TSD can also act as a nucleation site for a "carrot defect". Since the dislocation elastic energy is proportional to the dislocation length, the replication of BPD in BPD during off-axis growth is strongly hampered. This energy is strongly reduced by the growth from BPD to TED following the shortening of the dislocation with a length factor cot(θ) where θ is the off-angle. It is worth noting that perfect BPD in SiC are dissociated into two partial dislocations and one Schockley SF. The majority of SFs are caused by slipping in the basal planes (Schockley-type). SFs are nucleated during epitaxial growth even if they are absent in substrate and remain invisible to optical microscopy as for dislocations.

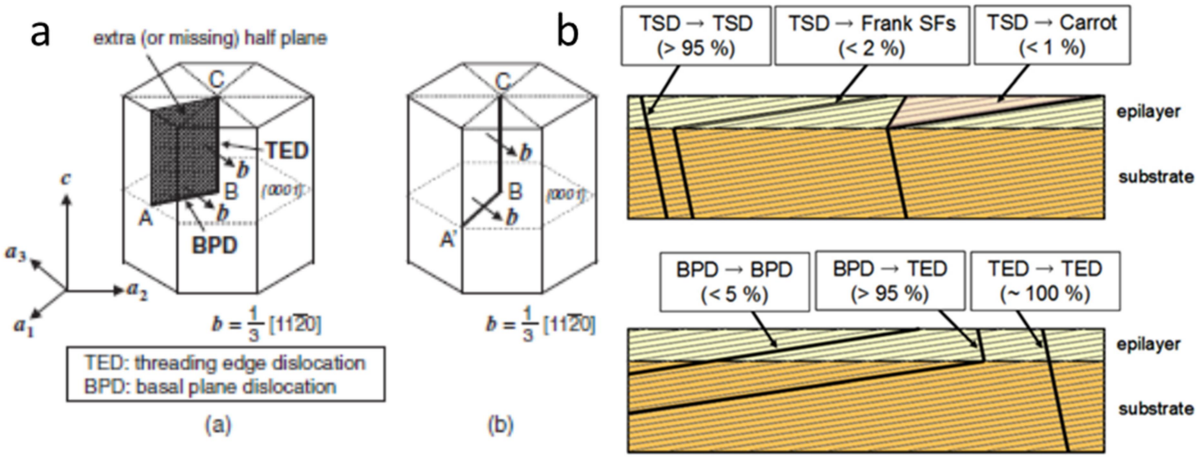

Figure 8 Schematic illustration of an extra (or missing) half plane in a SiC crystal. In this case, a dislocation with a Burgers vector of <11$\bar{2}$0>/3 exists along the edge of the extra half plane. (b) Typical configuration of threading edge and basal plane dislocations, where the basal plane dislocation lies along one of the <11$\bar{2}$0> directions. Schematic illustration of dislocation propagation in 4H-SiC epilayers grown on off-axis {0001} by chemical vapor deposition[35].

If TSDs produce a PL signal between 750-900 nm, SFs can also be detected by PL imaging with associated PL peaks at 455, 480 and 590 nm depending on whether it is an “in grown stacking fault” IGSF1, IGSF2 or IGSF3 [36].

The expansion of SFs into SiC can take place following the charge carriers injection and their recombination within SiC. As reported in Figure 9, in correspondence with a BPD or other dislocations, the expansion of the SFs takes place in the operating device, causing failure. The expansion of SSFs involves an important reduction in carrier lifetime, leakage in reverse voltage, as well as the creation of potential barriers for the transport of charge carriers resulting in an increase in the forward voltage drop of junction devices. This phenomenon, is called "bipolar degradation".

SFs expansion takes place following the lowering of the activation energy for the glide motion of the partial dislocations following the energy transfer in the electron-hole recombination.

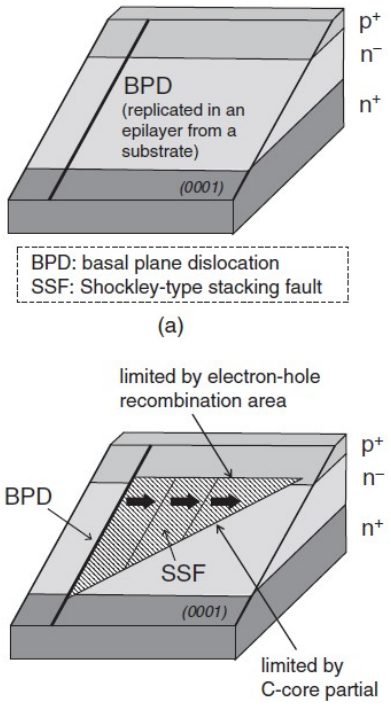

Figure 9 Schematic illustrations of single SSF expansion from a screwtype BPD in a SiC epitaxial layer replicated from a substrate; (a) before and (b) after expansion of SSF [1]

In PiN diodes a recombination has been observed occurring in the lightly-doped i-regions where a dense electron plasma hole has been generated by forward voltage. The expansion of SFs culminates at the interface between the p^+/i or i/n^+ region. Bipolar degradation can also affect 4H-SiC field effect transistors when the body diodes (p^+ body / n^- drift layer) are forward biased.

A further important type of epitaxial defectiveness is given by point defects that cause levels within the bandgap. The density of these deep levels in lightly-doped 4H-SiC (0001) epitaxial layer is between $5 \cdot 10^{12}$ cm^{-3} and $2 \cdot 10^{13}$ cm^{-3}. This value could be suitable for working unipolar devices, where the largest point defects source is, actually, represented by ion implantation process and subsequent annealing, however it is strongly hindering bipolar devices.

The defects that mostly reduce charge carriers lifetime are $Z_{1/2}$ (Ec - 0.63 eV) and $EH_{6/7}$ (Ec - 1.55 eV) [37] , commonly observed with a density of $0.3–2 \cdot 10^{13}$ cm^{-3} in CVD epitaxy. As visible in Figure 10 the defects that are located in the lower part of the bandgap are HK_2 (Ev + 0.84 eV), HK_3 (E_v + 1.24 eV), and HK_4 (E_v + 1.44 eV) [1,37] with concentrations around $(1 – 4) \cdot 10^{12}$ cm^{-3}. If the latter tend to disappear with annealing at 1450-1550 °C [38], $Z_{1/2}$ and $EH_{6/7}$ are instead stimulated in generation by annealing at high temperatures and have been found to increase rapidly through thermal annealing in Ar at temperatures above 1500°C. In addition to these levels there are impurity

centers provided by Boron acceptor levels [E_v + (0.28–0.35) eV], the boron related "D center" (E_v + 0.55 eV) and Ti impurity related shallow electron traps (E_c - 0.11 eV) with density respectively of (0.5–5) × 10^{13} cm^{-3} for B and (0.5–5) × 10^{12} cm^{-3} for Ti [39].

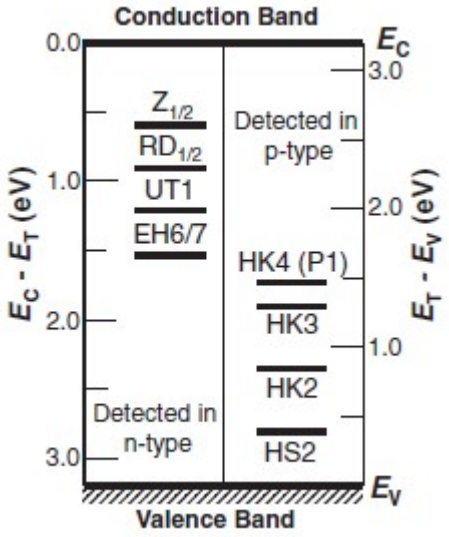

Figure 10 Energy levels of major deep levels observed in as-grown n- and p-type SiC epitaxial layers[1].

Those $Z_{1/2}$ and $EH_{6/7}$ are the most affecting device defects and according to theoretical calculation and the comparison between results from deep level transient spectroscopy DLTS and electron paramagnetic resonance EPR have been traced back to C monovacancies with different charge states,

Ion implantation defects

Ion-implantation is an indispensable technique for SiC devices planar selective-area doping. Thermal diffusion of desired dopants is not enabled as consequence of their extremely low diffusivities in SiC at temperatures lower than 2000°C [39,40,41,42]. Ion-implantation allows accurate control of doping depth profiles, since distributions depth and shape are primarily influenced by factors such as the energy with which the dopant ions impinge on the substrate and the atomic mass. Dopant ions distribution in the substrate can be precisely modeled for the specific ion energy and fluence. The realization of selectively doped regions is generally carried out through ion implantation processes followed by thermal treatments whose role is dopant activation. N-type doping is achieved by N, P or As while p-type conductivity is achieved by B, Al, Ga. At present, P and Al, which are the main donor and acceptor atoms used in microelectronic devices, have an ionization energy of 60/120 meV for the P and 198 / 210 meV for the Al, respectively in the hexagonal (h) and cubic (k) sites [39].

For a given ion energy and fluence it is possible to accurately model the distribution of the dopant ions in the substrate, which is convenient for device design. Using ion-implantation, one can obtain a variety of doping profiles including buried doped regions, sharp shallow junctions, hyper-abrupt doping profiles,etc [39].

The electrical activation of the implanted species takes place following a heat treatment which is usually carried out at temperatures above 1600 °C, suitable for sample crystalline recovery and electrical activation. A necessary condition is that lattice preserves memory of the crystalline order of the original polytype after the implantation step, so that the structure is highly strained but still crystalline. Thus, to contrast SiC tendency to crystallize in a multitude of structurally stable states (polytypes) during post implantation annealing the strategy adopted consists in carrying out the ion implantation step at high temperature (between 300 °C and 600 °C).

At higher implant concentrations, however, the activation obtained is only partial and higher activation temperatures than 1600 °C are necessary to place the dopant in substitutional position. Sheet resistance slightly increases in the case of higher N implant concentrations [39]. This seems to be due to the formation of electrically neutral Si-N and Si-C-N complexes for high N doses. For this reason, there is no benefit in using high-dose ($>5\cdot10^{19}$ cm^{-3}) N implantations. Substitutional P donor activation is 80–90% for P concentrations up to ~ 1×10^{18} cm^{-3} and then decreases with increasing P concentration owing to residual lattice damage [43]. For 3×10^{19} cm^{-3} P, the measured substitutional P activation is ~30%. Substitutional donor concentrations of mid to high 10^{19} cm^{-3} values can be obtained with P implantation because P has a high solubility limit in SiC and does not form electrically neutral complexes with Si or C. At present, B and Al represent the most used acceptors. Al has valid applications thanks to the lower ionization energy compared to B (190 meV for Al versus 285 meV for B in 4H-SiC) which leads to a lower sheet resistance. The Al implantation is still preferred on B one, if a higher activation is desired , since the solubility limit is two orders of magnitude higher and implantation profile results also thermally stable. Due to the high ionization energy not all acceptors are ionized. The incomplete ionization has a profound effect on devices performances. N and P donors tend to be completely ionized, as they have low ionization energies, therefore in most cases the concentration of ionized donors $N_D^+ = N_D$ (donors in substitutional lattice sites). At doping levels above 10^{19} cm^{-3} the mean spacing between dopant atoms is less than 5 nm, and electron wavefunctions from adjacent atoms overlap, giving rise to an impurity band that reduces the effective bandgap. This process reduces dopant ionization energies $E_{A,D}$, leading to more complete ionization than predicted by charge neutrality equations [1].

During post implantation annealing vacancies and interstitials become mobile and contribute to point defects complex formation such as vacancy clusters, interstitial clusters, antisite-vacancy pairs

and so forth. The interstitial and vacancies profile generated can be estimated through SRIM code, which, however, overestimates the damage creation and does not account on self annealing during hot ion implantation. Indeed, there are no thermal effects in SRIM, so the damage calculated is that resulting after a T=0 K ion implantation process. Ignoring thermal effects changes the quantity of final damage, but the basic damage types which are involved will still occur. As a result of the annealing process, vacancies, interstitials and antisites can combine with the implanted impurities, forming levels located in the bandgap. Moreover, point defect density is such that they often segregate in the implant region during annealing, leading to extended defects formation, such as, for example, dislocation loops and stacking faults. Since the activation annealing is carried out at high temperature, additional stress gives rise to the generation of new dislocations or causes the movement of pre-existing ones. It is worth noting that the total number of atoms in the extra planes is proportional to the implant dose, and the absolute number is almost identical to that of the number of implanted ions. This result suggests that Si and C atoms kicked out by ion bombardment become mobile and segregate in the basal planes during annealing, leading to formation of extra planes. Furthermore, high-dose implanted regions exhibit a lattice tilt with respect to the original *c*-axis [1,44].

It has been shown that at long thermal annealing periods and elevated temperatures, dislocation processes are accompanied by conservative coarsening phase in which wide loops expand at the cost of smaller loops [45].

Hence, a large number of Si-C pairs are formed during the high temperature processing conditions to which SiC undergoes, both during growth and during post implantation annealing. While the number of generated pairs is still orders of magnitude lower than the peak ion concentration, the migration energy for C interstitials has been found to be about 1 eV, which enables the C interstitials to migrate several microns during the post-implantation annealing process. It is therefore plausible that some of C atoms present in the extrinsic Si-C bilayer are formed both during epitaxial layers growth and during the high temperature annealing and contribute to stabilize the bilayer. Furthermore, it is possible that the C interstitials are supplied from the remaining ion implantation damage distribution [46].

Despite a wide portion of implantation damage is healed, as a result of thermal annealing, a large number of C interstitials will be created in the vicinity of the growing loops giving rise to growing dislocation loops.

These dislocation loops were identified within Al^+ or P^+ 4H-SiC implant doses interesting for microelectronics, such to obtain concentrations higher than 10^{18} and with post implantation annealing greater than 1600 °C [1]. Figure 11 shows a cross-sectional weak beam WB TEM (-g, 4

g), g=[0004] with $5 \cdot 10^{20}$ cm^{-3} Al implanted 4H-SiC samples, after 1950 °C /5 min annealing. A and B are polygonal loops differing in size, particularly B are Al precipitates and vacancy agglomerates, D are dislocation loops forming a network of orthogonal traces that correspond to the $\{\bar{1}2\bar{1}3\}$ and/or $\{\bar{2}4\bar{2}3\}$ planes. C defects are SFs lying on the basal plane. With the increase of dopant concentration to 10^{20} cm^{-3} and the increase of post implantation temperatures to 1850 °C, local planar extrinsic grown stacking fault is such that could cover an important implant region fraction [47].

Studies carried on through energy dispersive X ray spectroscopy (EDS) conducted on SFs lying on the (0001) basal plane show that SFs have reported no sign of implanted dopant accumulation [48]. Although further research still needs to be conducted, all studies converge on confirming the relationship between the presence of SFs and the implant concentration. Mobility of SFs in 4H-SiC subjected to current stress, such as that of an operating device, lead to defectiveness minimization necessity.

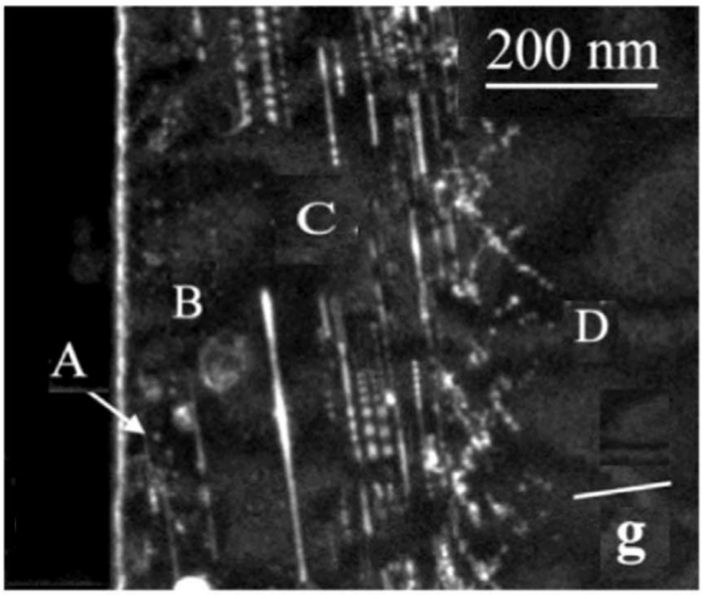

Figure 11 cross-sectional WB (-g,4 g) g = [0004] micrograph of the near surface regions of: (a) 1×10^{19} cm^{-3} and (b) 5×10^{20} cm^{-3} Al implanted 4H-SiC specimens, after 1950 °C/5 min annealing.[47].

At present, several processes have been considered to maximize the activation temperature and to reduce the implant dose. This increase in temperature involves, however, point defects enhancement and entails a conspicuous increase in intrinsic defects which are known as carrier lifetime killers and responsible for drift resistance in the device.

Abstracts of Chapters 2 and 3

Within the second chapter an extensive discussion on the research activity concerning the extended bidimensional defects within the 3C-SiC will be exposed. These defects are, in fact, one of the main causes that hinders the use of 3C-SiC heteroepitaxies grown on Si substrates. TEM investigations together with molecular dynamics simulations have been used to trace the structure of the main two-dimensional defects affecting the heteroepitaxial layers in 3C-SiC, with particular reference to Inverted Domain Boundaries (IDBs) and Stacking Faults (SFs).

In this work Domain boundaries (DBs) generated during the growth of 3C-SiC on (001) Si and their interaction with stacking faults (SFs) will be studied. Direct Scanning Transmission Electron Microscopy (STEM) images will exhibit that DBs are inverted domain boundaries otherwise called antiphase boundary (IDBs or APB). The atomic arrangement of this IDB is different from the expected boundaries described in the literature, nevertheless, it has a highly coherent nature. The IDBs propagate in a complex way through the crystal. A close relationship will be identified between the IDBs lying on the (111) plane and the SFs, which appear to be coupled. Furthermore, it will be observed that the Partial dislocations surrounding the SFs possess an unconventional lying plane, i.e. [112], [123], [134]. Molecular dynamics simulations demonstrate the stability of the directions [110] as well as [112] direction, while the directions [123] and [134] of the partial dislocations (PDs) evolve towards [112] and [110]. The unusual directions will be identified by experimental investigation as they obey to rules of minimization of the strain energy, in partial dislocations.

A structural characterization and distribution of SFs was performed by μ-Raman spectroscopy and room-temperature μ-photoluminescence. Two kinds of SFs, 4H-like and 6H-like, will be identified near the substrate interface. Each kind of SFs shows a characteristic photoluminescence emission of the 4H-SiC and 6H-SiC located at 393 and 425 nm, respectively. 4H-like and 6H-like SFs show different distribution along film thickness. The reported results were discussed in relation with the experimental data and theoretical models present in the literature.

Investigations related to the temperature influence on the homo-epitaxial growth process of 3C-SiC will be presented. Different morphological analyses indicate that the growth temperature and the growth rate play a fundamental role in the stacking faults density. In details, X-ray diffraction and micro-Raman analysis show the strict relationship between growth temperature, crystal quality, and doping incorporation in the homo-epitaxial chemical vapor deposition CVD growth process of a 3C-SiC wafer. Furthermore, photoluminescence spectra show a considerable reduction of point defects during homo-epitaxy at high temperatures.

Furthermore, properties of cubic silicon carbide (3C-SiC) grown epitaxially on a patterned silicon substrate composed by squared inverted silicon pyramids (ISP) will be shown. This compliant substrate prevents the stacking faults, usually found at the SiC/Si interface, to reach the surface. We investigated the effect of the size of the inverted pyramid on the epilayer quality. We noted that anti-phase boundaries (APBs) develop between adjacent faces of the pyramid and that the SiC/Si interfaces have the same polarity on both pyramid faces. Structure of the heterointerface will be investigated. Moreover, due to the merging of APB in the vertex of the pyramid, voids buried on the epilayer form. We will demonstrate that careful control of the growth parameters allows to modify the height of the void and the density of APBs, improving SiC epitaxy quality.

It will be discussed the use of a buffer layer between the epitaxial layer and the substrate in order to reduce the defectiveness and improve the overall quality of the SiC epi-film. In particular, we find that the morphology and the quality of the epi-film depends on the carbonization temperature and the concentration of Ge in close proximity of the $Si_{1-x}Ge_x$/SiC interface. Ge segregation at the interface influences the film quality, and in particular a [Ge]>12% in close proximity to the interface leads to the formation of poly-crystals, while close to 10% induces a mirror like morphology. Moreover, by finely tuning the Ge concentration and carbonization temperature, crystal quality higher than that observed for SiC grown on bare silicon will be achieved.

In chapter 3 we will study the crystal defectiveness subsequent to ion implantation and annealing by using various techniques including photoluminescence (PL), Raman spectroscopy and transmission electron microscopy (TEM). The aim of this work is to test the effectiveness of double step annealing to reduce the density of point defects generated during the annealing of a P implanted 4H-SiC epitaxial layer. The outcome evidences that neither the first 1 hour isochronal annealing at 1650 - 1700 - 1750 °C, nor the second one at 1500 °C for times between 4 hour and 14 hour are able to recover a satisfactory crystallinity of the sample.

Prismatic interstitial-type dislocation loops have been found as the dominant extended defect. Their average size are typically 1–20 nm in diameter and reside on the {0001} and {11-20} plane, consistent with Frank type dislocation behavior.

Conventional annealing do not allow lattice relaxation towards low energy configurations. Anisotropic-next-nearest-neighbor Ising model demonstrated that evolution towards prismatic dislocation loops is highly energetic. Indeed, Raman E_2(TO) mode displayed large in plane stress values up to 172 Mpa.

This work will also describes the development of a new method for ion implantation induced crystal damage recovery using multiple XeCl (308 nm) laser pulses with a duration of 30 ns. Experimental activity was carried on single phosphorus (P) as well as double phosphorus and aluminum (Al)

implanted 4H-SiC epitaxial layers. Samples will be characterized through μ-Raman spectroscopy, Photoluminescence (PL) and Transmission Electron Microscopy (TEM) and results were compared with those coming from P implanted thermally annealed samples at 1650–1700–1750 °C for 1 h as well as P and Al implanted samples annealed at 1650 °C for 30 min. The activity outcome shows that laser annealing allows to achieve full crystal recovery in the energy density range between 0.50 and 0.60 J/cm^2. Moreover, laser treated crystal exhibits an almost stress-free lattice with respect to thermally annealed samples that are characterized by high point and extended defects concentration. Implanted area was almost preserved, except for some surface oxidation processes due to oxygen leakage inside the testing chamber.

To work around surface erosion phenomena it will be proposed the practicability of coating systems designed to minimize the surface degradation of SiC following laser annealing process. This strategy based on a graphitic coating plays a key role along the annealing in a thermal non-equilibrium regime to obtain a high dopant activation. Thanks to its 3800 °C melting temperature and high absorption coefficient, graphite is, in fact, the best candidate to fully absorb laser radiation, allowing a heat diffusive regime along the underlying layers. Characterization will be performed by means of μ-Raman accurate analysis which allows to highlight the high crystalline quality and the absence of stress phenomena inside the crystal. A detailed portrait of the damage thresholds will be reported with particular emphasis on the thicknesses used to minimize sample erosion and, at the same time, ensure high activation of the implanted dopant. Circular Transfer Length Method (CTLM) measurements tests were carried out and will prove remarkable P activation on irradiated site. The 90 nm graphite coated sample will reveal at 0.5 J/cm^2 activation values equal to $6.59 \cdot 10^{19}$ ±1.95 e/cm^3 which correspond to approximately 66% of P implanted activation. This is slightly higher than the value coming from the thermally annealed sample extracted from literature (around 62%). The results of this experimental activity give way to laser annealing process viability for damage recovery and dopant activation inside the implanted area. Starting from the state of the art about the formation of extended defects in ion implanted 4H-SiC homo-epitaxial wafers following high temperature post-implantation annealing, the improvement of the laser annealing technique is proposed as a turning point of post-implantation thermal processes. The study provided within this work has, therefore, as its main ambition to provide an accurate characterization of defects in SiC films and their behavior as a function of growth as well as in doping processes. The objective therefore concerns the removal of the relevant drawbacks in the development and the viability of reliable and efficient electronics devices.

Chapter 2. Understanding the mechanism of defect reduction in 3C-SiC heteroepitaxial growth

In this chapter a detailed description of the main CVD heteroepitaxial growth defects within 3C-SiC will be performed. A comprehensive characterization of the evolution dynamics of the two main bi-dimensional extended defects structures as Inverted Domain Boundary and Stacking Faults will be provided, accompanied by an analysis on the generation and termination of stacking faults on inverted domain boundaries. Subsequently we will proceed to the definition of a characterization of 4H- and 6H-Like stacking faults in cross section of 3C-SiC epitaxial layer by room temperature μ-Photoluminescence and μ-Raman Analysis together with the crystal behavior under CVD doping following the variation of the growth parameters.
In order to alleviate crystal defectiveness, compliant substrate will be presented. In particular "SiGe buffer layer" as well as the growth on a patterned substrate as "inverted silicon pyramids" (ISP) will be discussed in detail as effective 3C-SiC defects reduction.

Introduction

The presence of great efforts by the scientific community has allowed the development of several broad bandgap semiconductors grown on Si whose quality is, however, limited by the presence of extensive defects. 3C-SiC is an ideal semiconductor to explore the issue of extended defects, due to its FCC structure close to that of Si and diamond where the structures of the dislocations are well known. Nevertheless, the lattice base has two different atoms (Si and C) that give it a "degree of freedom" with respect to the mono-atomic counterparts Si and diamond. As stated in chapter I, one of the most important benefits of this poly-type, is that it is stable at a temperature lower than the melting temperature of the silicon meaning that it can be grown on a silicon substrate, reducing considerably the cost of the SiC wafer production. Moreover, 3C-SiC has higher bulk and channel electron mobility (up to 1000 and 250 cm^2/Vs, respectively) [49,50] and lower trap density at the oxide-semiconductor interface (3C-SiC/SiO_2) [51] with respect to the most used SiC poly-type, the 4H-SiC. The use of 3C-SiC poly-type, instead of 4H-SiC, can boost the transition to a green

economy, indeed MOSFET devices working in the range of breakdown voltages below 800 V can be used to drive power electric vehicles, air conditioning, and LED lighting system applications [52,53,54].

Despite the highly important applications in the semiconductor field and although the 3C-SiC has been studied for more than 30 years, the problem of the hetero-epitaxy on silicon is far to be solved. The most important issues are related to the presence of 2D extended defects that are still present in the epitaxial layer in such an amount that it cannot be used for real applications. Stacking Faults (SFs) together with Inverted Domain Boundaries (IDB) are the most important 2D extended defects in 3C-SiC grown hetero-epitaxially on silicon [55]. Notwithstanding the importance of the extended 2D defects in the electrical and mechanical properties of the 3C-SiC, a few papers describe the fine structure of such defects [56].

The Inverted Domain Boundary (IDB) is the most important 2D extended defect that affects the properties of this material and it is related to the formation of crystallographic domains. They form, in 3C-SiC grown on (001) Si, due to two possible different configurations of the Si-C dimer on the surface: Si-C dimer can be arranged in two perpendicular configurations. Owing to crystal symmetries, a rotation of 90° around [001] is equivalent to flip the crystal upside down (i.e. rotation of 180° around [110]). These domains boundary are called, in literature, Inverted Domain boundary (IDB), or Anti-Phase Boundary (APB). In any case, the boundary between domains is the main responsible for the electrical failure of devices in 3C-SiC/(001)Si [62]. Current maps, in the nano-scale range obtained by conductive atomic force microscopy, showed that IDB is the main defect responsible for the short circuit under both reverse and forward bias polarization [62]. Recently high-resolution STEM images of the IDB, lying on the (110) plane, revealed that it is coherent, has no polar character, and is composed of distorted Si-C bonds forming a square and a semi-octahedral structure with undistorted bonds. Nevertheless, the structure of the IDBs on other planes than (110) is still not reported to the best of our knowledge.

Hetero-epitaxial growth of 3C-SiC on (001) Si suffers from two main issues: interfacial lattice mismatch between Si and SiC and the difference in thermal expansion coefficients. These two issues lead the formation of misfit and Lomer dislocations at the hetero-interface [57] and the presence of local strain field inside the epilayer. The presence of a domain boundary together with the presence of high residual stress (and other minor factors as doping segregation) [58,59] can drive the formation of both perfect and partials dislocations (together with SFs) in the epilayer and disconnections into the IDB [60,61]. The stacking faults (SFs) after being generated are able to propagate into the SiC epilayer approaching the surface and affecting the mechanical and electrical properties of the material. In particular, it was recently demonstrated by conductive-AFM that SFs

work as preferential current paths under forward polarization [62,63,64]. SF consists of a wrong sequence with respect to the 3C-SiC stacking order [65,66]. It is bordered by two PDs: they limit the plane where the wrong sequence exists from regions of perfect 3C sequence. The direction and stability of PDs bounding the SFs are of particular importance because the expansion or the shrinking of the SFs is driven by the energetic and the kinetics of the partial dislocations [67]. Moreover, the expansion of SF due to the gliding of PDs leads to the intersection of SFs and the formation of Lomer and forest dislocations [68].

In this work, we observe experimentally 2D defects using high-resolution Scanning TEM microscopy. The nature of IDB allows us to obtain atomic images of the fine structure of the boundary with high resolution (of a tenth of Å) and allows to correlate the SF to IDB. PDs are observed at low magnification. Moreover, the line directions of the PDs are found to be different from the expected ones due to the standard theory of dislocations. We thus investigate theoretically the stability and the structure of the partial dislocation in order to have more insight on the elimination of the fault.

Epitaxial growth and TEM Analysis

3C-SiC growth was performed in a horizontal hot-wall chemical vapor deposition (CVD) reactor (ACIS M10 supplied by LPE) using (100)-oriented Si substrates. The (001) Si substrate was a 6 inch 650 µm thick wafer. Before reaching the growth conditions, the Si substrate undergoes an 'etching' and 'carbonization' step. These steps were performed at 1100 °C by introducing H_2 and H_2 plus ethylene during the etching and carbonization steps, respectively. Following carbonization, there is a 'ramp' step where the temperature is raised to the final growth temperature. The growth starts at a low growth rate under C/Si ratio of 0.8. The CVD growth process was performed at low pressure (104 Pa) and at a temperature of 1370° C. In these experimental conditions only the 3C phase is detected [69,70]. The gases used during the growth were trichlorosilane (TCS) and ethylene (C_2H_4) as silicon and carbon precursors respectively. Hydrogen (H_2) is used as a gas carrier. The final 3C-SiC thickness was 30 µm.

To carry out N doping a two step growth process was applied with the carbonization plateau at 1160 °C followed by CVD growth step at 1400 °C. One 4 inches wafer was grown intrinsic while other three wafer were grown with constant 313, 800 and 1600 sccm nitrogen fluxes during growth. To increase crystal quality the growth was first performed at 3 µm/h for 30', followed by another 30' growth at 6 µm/h and then carrying on at 30 µm/h until a 70 µm layer was reached. Si substrate was then melted at 1700 °C inside the reactor to reach a free standing wafer [71], obtaining free-standing 4 or 6 inches wafers. A scheme of the synthesis process is shown in Figure 12. [72].

The remaining freestanding SiC layer was used as a seed layer for subsequent homo-epitaxial growth. The processes were realized in a low-pressure regime at different temperatures in the range between 1600 and 1700 °C. A growth rate of 60 μm/h for two hours was used to increase the substrate thickness and 30 μm/h for the last 1 h to further improve the quality of the material, as previously reported [73]. While the first 20 microns of the last step were highly doped, the final 10 microns were low doped for device realization. Nitrogen was used as the doping species for n^+ and n type layer formation. After the homo-epitaxial deposition, the total thickness of 3C-SiC samples was about 200 μm (observed by SEM analysis).

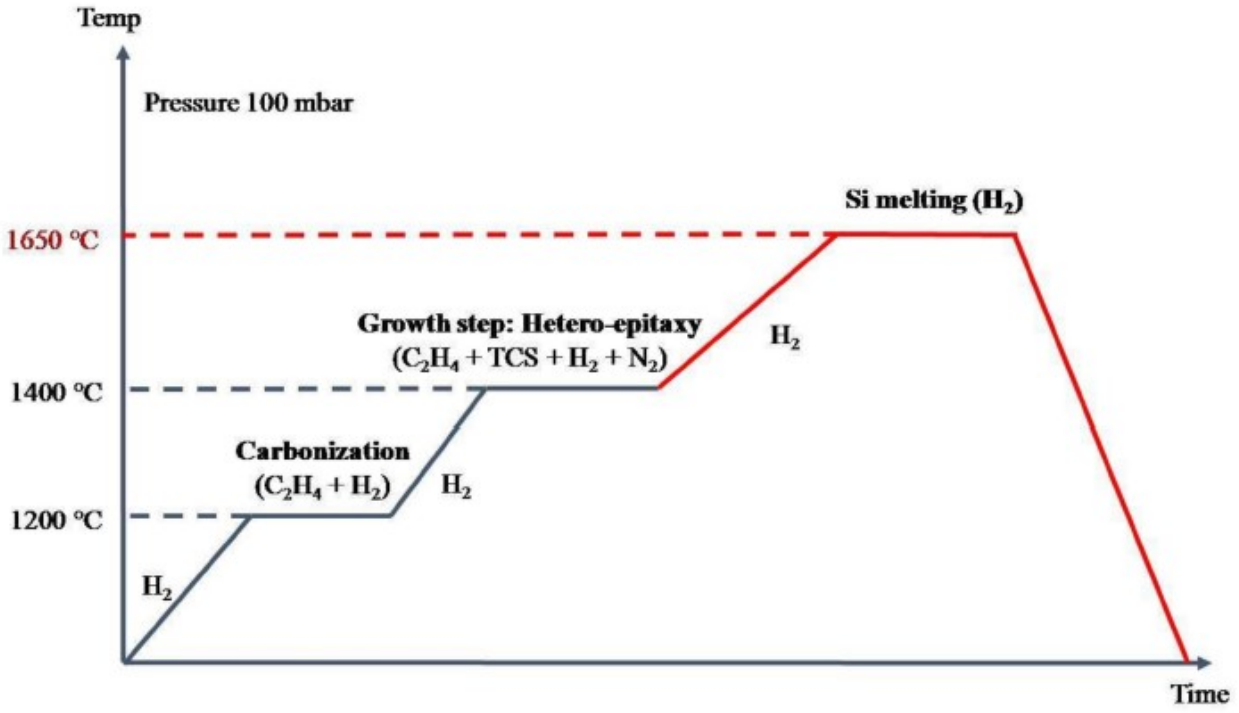

Figure 12 **Scheme of the synthesis process of free-standing 4 and 6 inch wafers of 3C-SiC [71]**

High Angle Annular Dark Field Scanning Transmission Electron Microscopy (HAADF-STEM) was carried out on a JEOL ARM200F probe Cs-corrected TEM, equipped with a cold FEG and working at 200 kV. We operated with three detectors: at low, medium and very high scattering angle. The dark field detector inner semi-angle (80 mrad) allows the signal to be roughly proportional to the atomic number Z. Under these conditions, the intensities observed in the STEM micrographs allow a direct interpretation. The microscope has a nominal resolution of 0.68 Å.

Stacking Faults

Several kinds of extended defects are placed at the Si/SiC interface. An example cross section STEM image of hetero-epitaxial 3C-SiC on Si (001) can be seen in Figure 13.

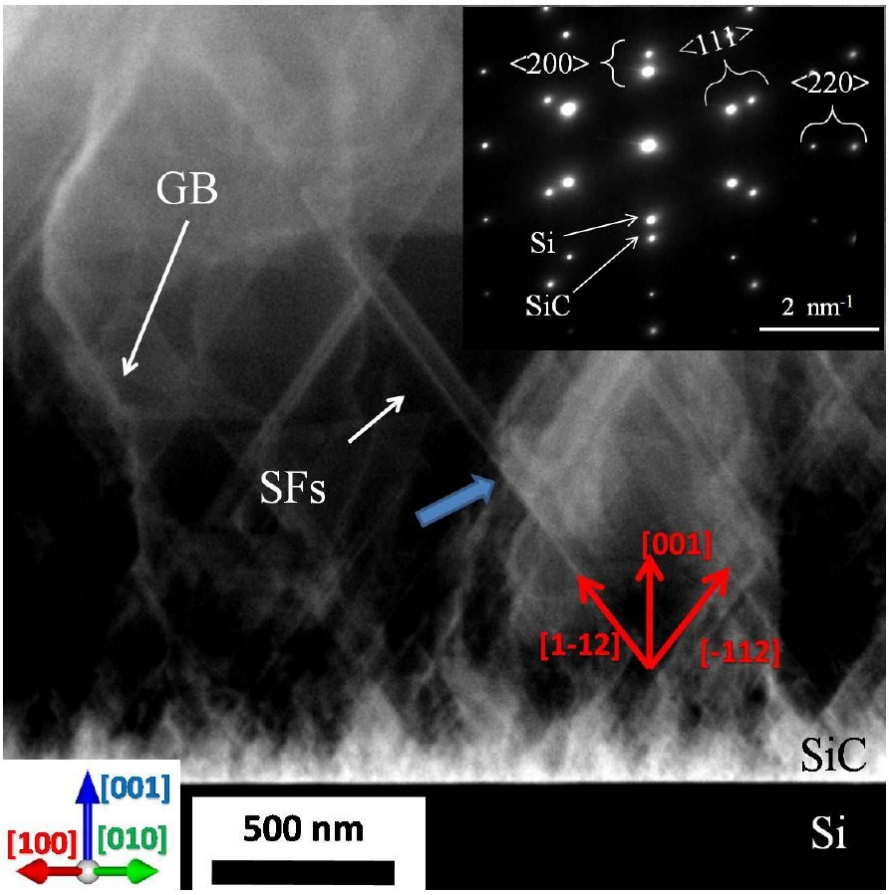

Figure 13 Example of the STEM image of the Si/SiC hetero-interface. A high density of defects formed during the growth process is apparent. The <112> directions are marked in red. The axis is drawn in the lower-left part of the figure. A domain boundary and a SF are indicated. SFs are aligned in the <112> directions (and lie in the {111} planes). The growth was performed in the [001] direction and (110) is the STEM projection plane. The insert shows a diffraction pattern obtained at the interface between Si and SiC. Main crystalline directional spots are highlighted. It is apparent the presence of spots related to both Si and SiC.

Extended defects are mainly straight lines in the <112> directions and complex curved lines roughly oriented along the [001] direction. These features individuate roughly stacking faults (SFs), and domain boundaries (DBs) respectively. These two kinds of defects are the most common extended defects in 3C-SiC on Si as early reported [74,75,76]. SFs are known to lie only in the {111} planes and are associated with thin straight lines along with the <112> directions or trapezoidal shaped structures. Indeed, since 3C-SiC is grown epitaxially on Si and the domains have the same orientation as the Si (001) substrate. DBs, differing from SFs, lies in a more complex (not planar) 3D surface and can be usually distinguished from SFs. It is worth noting that DBs can

eventually lie in the {111} planes. In Figure 13, the blue arrow indicates a region where a superimposition of a DB and a SF is observed. Nevertheless, in low magnification STEM images, it is possible to distinguish the two kinds of defects: SFs propagate only along the <112> direction while the DB changes direction.

The SFs formed during epitaxial growth are characterized by a lying plane which corresponds to the {111} plane family. As it can be seen in Low magnification TEM under [110] zone axis in Figure 14, SFs are represented by straight lines propagating towards the surface or by trapezoids. The pair of planes, i.e. (1-11) and (-111) are shown as straight lines, while planes (111) and $(1\bar{1}\bar{1})$ define a trapezoidal shape as this plane intersects the lamella. On the sides of the trapezoidal region delimited by the stacking fault the surrounding partial dislocations are highlighted in yellow, and the areas in which the stacking fault intersects the lamella are in light blue.

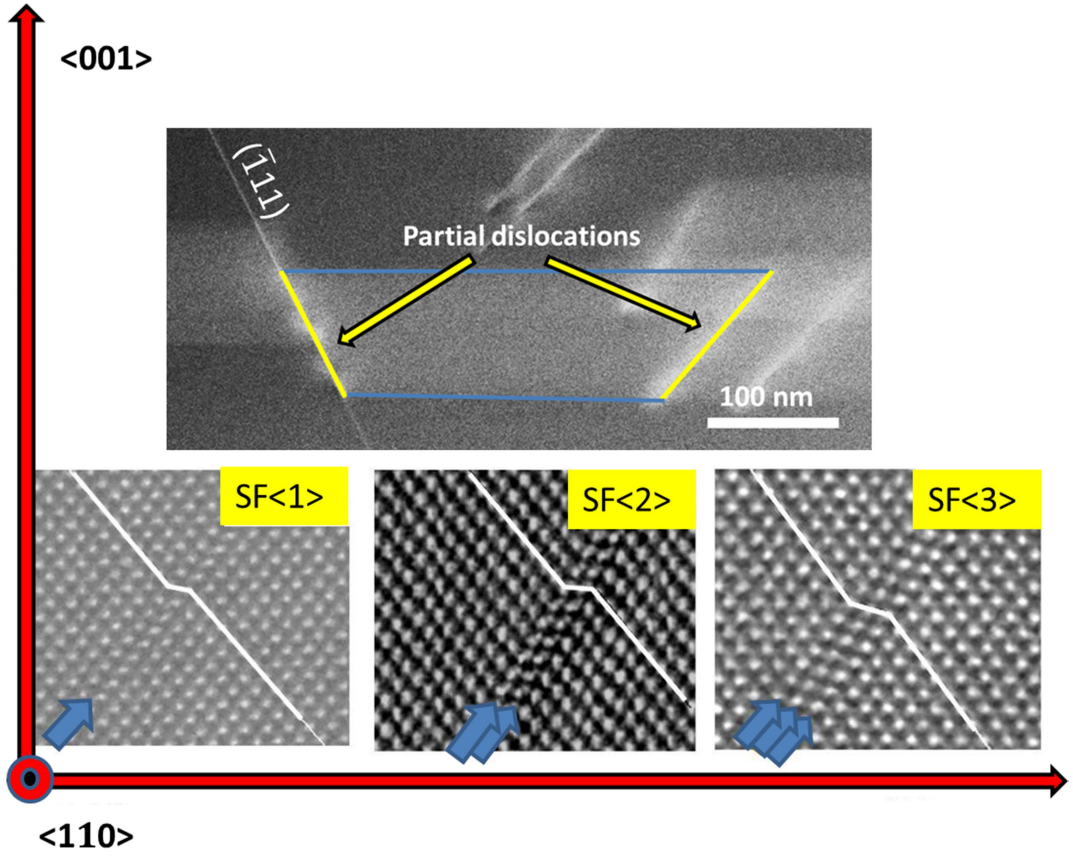

Figure 14 Low magnification TEM showing Stacking Faults shape under [110] zone axis. Red lines denote partial dislcations. In the lower part HRSTEM images of SF<1>, SF<2>, SF<3>.

Moreover, to demonstrate that SFs represent wrong sequences of the Si-C dimers, Figure 14 displays HRSTEM images that allow to define SFs atomic structure. Starting from the bottom left, the structure of a SF <1> involving a single layer is shown and is defined as “intrinsic” SF. The

center exhibits a SF <2> which consists of two slip planes and is termed extrinsic, while the bottom right displays a SF<3> involving 3 planes and named conservative SF.

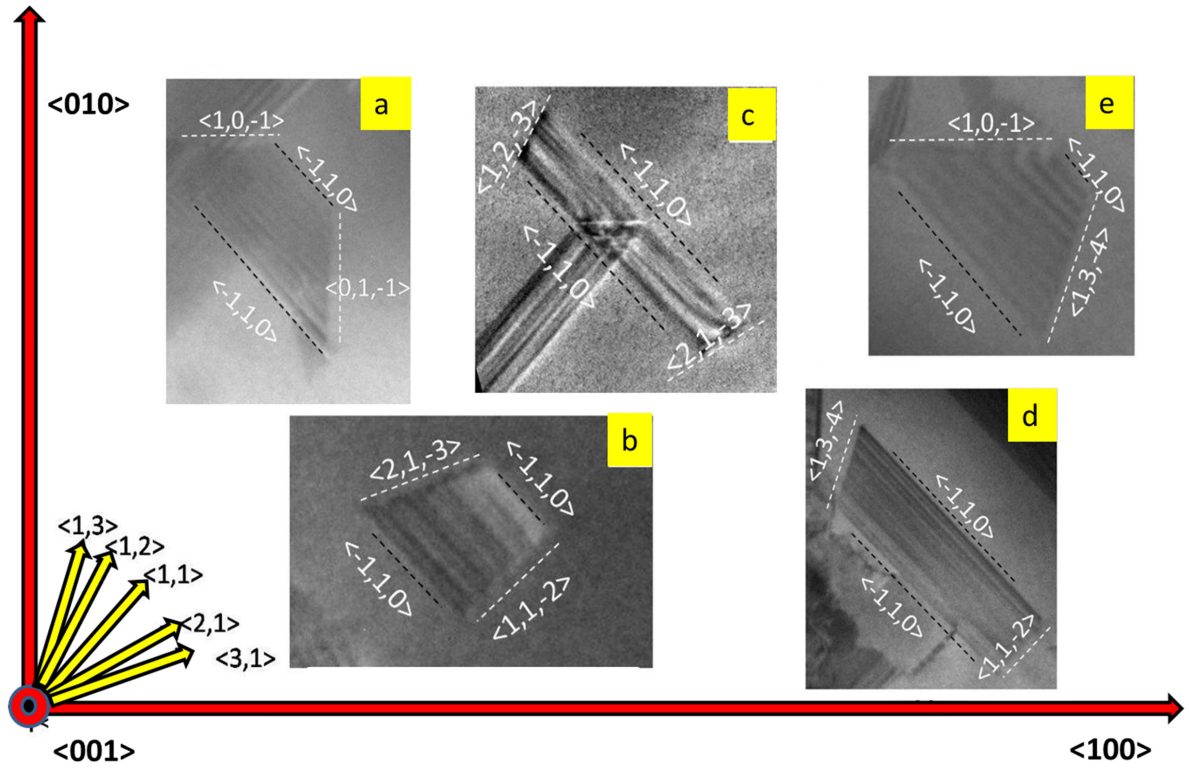

Figure 15. SFs plan views under the [001] zone axis. SFs lie always in {111} planes and manifest different partial dislocation directions. For easy direction recognition a series of arrows are reported.

To examine partial dislocations directions it is possible to consider the images of Figure 15. Assuming that all SFs lie in {111} planes (111) or $(\bar{1}\bar{1}1)$ and considering that the figure shows their projection along the plane (001) it is possible to analyze these plan views. Inside Figure 15a the regions in which the SF intersects the lamella have been outlined in black, while the partial dislocations are represented in white. Starting from the vertical partial dislocation it is easy to understand that the projected coordinate is <0,1>, so assuming that the real vector lies in the plane (111) we can deduce the 3D coordinates $<01\bar{1}>$ (or <011>). On the other hand, in the case of partial horizontal dislocation, the directions are $<10\bar{1}>$ (or <101>). Carrying out the same considerations, the line vector follows for the partial dislocations present in all the reported SFs. For an easy overview of the projections on the plane (001), the directions <1,3> <1,2>, <1,1> <2,1>, <3,1> have been outlined in Figure 15. Considering the Figure 15b the dislocations have projections <2.1> and <1.1>. The vectors in 3D space are therefore $<2,1,\bar{3}>$ (or <213>) and $<11\bar{2}>$ (or <112>).

Furthermore Figure 15c reports partial dislocations lying on [12-3] direction (and [21$\bar{3}$]), while in the case of Figure 15d they were observed lying on <1,3,$\bar{4}$> and <1,1,$\bar{2}$>. Finally from Figure 15e the extracted directions were <1.0,$\bar{1}$> and <1.3, $\bar{4}$>. From this examination it is clear that the directions available for partial dislocations are straight and specific.

The main principles followed by dislocations directions are: 1) *the dislocation assumes a direction as straight as possible* 2) *it assumes the minimum values of the Peirls potential*. It is, therefore, evident that the direction of the dislocation is established by energy minimization rules. This implies that the partial dislocations should actually run along the preferential directions within the FCC lattice i.e. <$\bar{1}$10>, <01$\bar{1}$>, <$\bar{1}$01> [77]. An important role is also by the Burger vectors, since, following the third rule governing dislocation direction, it is known that dislocations tend to have the largest possible screw component as the strain energy of an edge dislocation is notoriously larger than that of a screw. The rules reported so far provide guidelines on the direction of dislocations, however, they have to be considered as a whole, so that they simultaneously influence direction and cannot be disentangled. These rules proceed from the dislocation core energy and stress minimization and are considered as general rules that act in an ideal and isotropic environment and are not able to explain the experimental images in Figure 15b-e which show dislocation direction not defined by theory. Partial dislocation direction can be influenced by the direction of the Burger vector. Indeed, partial dislocations lying on the [110] direction can have Burger vectors at 30° and 90° with respect to the direction of the partial dislocation. Within TEM investigations it has been observed that PDs can have unconventional directions such as [112], [123], [134], so that two beams TEM analyses were performed to ascertain the relationship between the Burger vector and the dislocation line direction. Bright-field images of a SF is reported in Figure 16a.

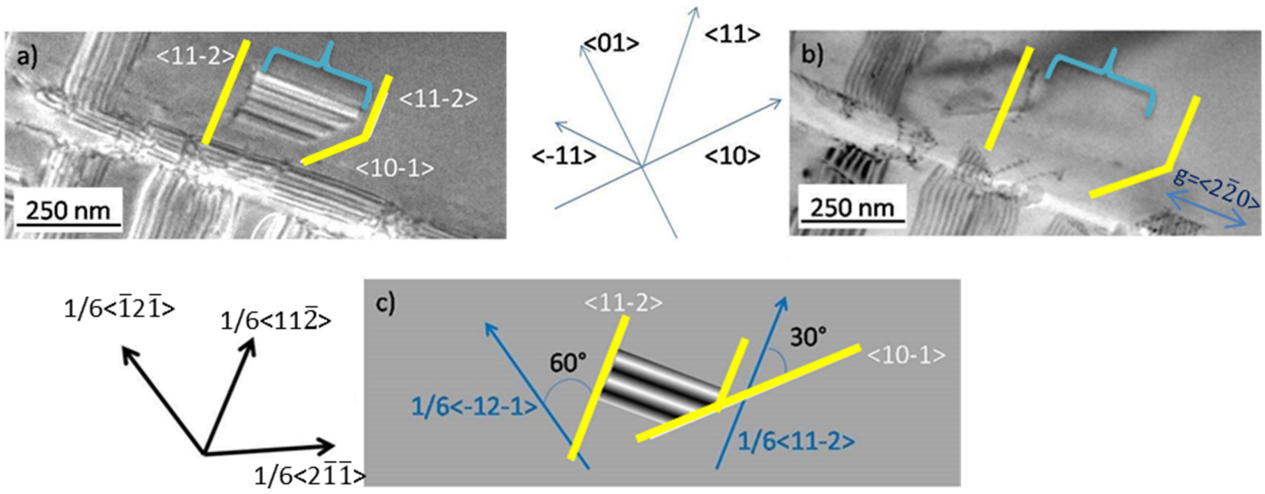

Figure 16. a) Bright-field images of a SF. Yellow lines are parallel to the partial dislocation lines and brace individuate the position of the SF, b) same area acquired in Weak Beam Dark Field using forward beam and the {2$\bar{2}$0} diffracted beam, c) SF with dislocation lines and Burgers vectors. Yellow and blue lines are PDs and Burgers vectors respectively.

In this figure the yellow lines appear parallel to the dislocation and brace points the SF location. On the left the direction of the partial dislocation <11$\bar{2}$> is highlighted, while on the right it is noted that the dislocations lie on the directions <10$\bar{1}$> and <11$\bar{2}$> . By exploiting the g·b criterion in the two-beam TEM technique, it is possible to identify partial dislocations Burger vector. The invisibility criterion attests that by selecting the transmitted beam and another beam with a known diffraction vector g, it is found that in the case of perpendicularity between the vector g (translation vector of the SF) and the Burger vector b of the dislocation, the dislocation (SF) has a very weak contrast and it is not visible [78].

In Figure 17 we report the diffraction pattern with the g1, g2, and g3 vectors used in the analyses define by red arrows.

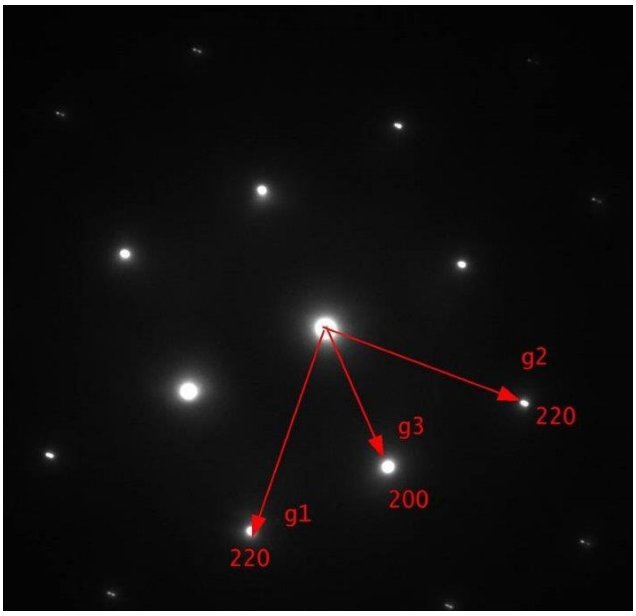

Figure 17 3C-SiC sample diffraction pattern under [001] zone axis together with the g1, g2, and g3 vectors used in the analyses

Moving back to Figure 16b we can see how this image was acquired in double beam condition using the transmitted beam together with the diffraction point $\{2\bar{2}0\}$. The image acquisition region is the same as in Figure 16a, but unlike the latter the SF is invisible and only the dislocation on the left of the SF is visible (in the $<11\bar{2}>$ direction), while those on the right are invisible as well as the SF. In Figure 16b the invisibility of the SF arises from the perpendicularity of the diffraction vector $<2\bar{2}0>$ and the translation vectors $<11\bar{2}>$. The disappearance of the SF is motivated by the fact that the partial dislocations in the (111) plane of an FCC crystal are individuated from one of the vectors b between $1/6<11\bar{2}>$, $1/6<\bar{2}11>$, and $1/6<1\bar{2}1>$ [79], as shown on the left of Figure (16). Due to perpendicularity to g it follows that the burger vector of the dislocation is therefore $1/6\ <11\bar{2}>$.

It is possible to observe that the angle between the line and Burger vector is 30° for $<10\bar{1}>$, as commonly found in partial dislocations and 0 ° for $<11\bar{2}>$. Instead, we can deduce that, due to its visibility, the Burger vector for the left partial dislocation can be either $1/6<\bar{2}11>$ or the $1/6<1\bar{2}1>$. Assessing which of the two Burger vectors is allowed appears to be forbidden since they are tilted by 60° with respect to the direction $<11\bar{2}>$. It follows that the partial dislocation $<11\bar{2}>$ is characterized by a mixed character. To provide an illustrative example Figure 16c displays an SF image. The yellow lines and the blue lines correspond to PDs and g. On the left, the partial dislocation has a Burger vector equal to ($1/6<11\bar{2}>$) as well as direction ($<11\bar{2}>$) at 60° which is an uncommon angle. The partial dislocation on the right is defined by two segments rotated at 30°

(<10$\bar{2}$>) and 0° (<11$\bar{2}$>) and Burger vector (1/6<11$\bar{2}$>). The existence of <121> line direction may also be preferred by screw character, in fact, compared to edge dislocation, presents a reduced line energy. Therefore we observed 60° and 0° as (uncommon) angles among dislocation and Burger vector.

We now have to understand why the other partial directions [123], and [134] are found experimentally. In order to shed light on this aspect, we have simulated the specific structure of partial dislocation in 3C-SiC. In particular, we have studied the behaviour of partial dislocations with <132> and <143> dislocation line directions (lying in the (1$\bar{1}$1) plane observed experimentally) with molecular dynamics tools. In Figure 18a, (green line) pairs of partial dislocations having opposite Burgers vectors with stacking faults formed naturally between them have been inserted in the (1$\bar{1}$1) plane inside the simulation cells oriented in such a way that the y-axis is the vector <132>. Note that we choose a direction and a Burgers vector oriented about 10° off. This value is intermediate between 30° and 0° that are observed in the right dislocation of Figure 16. A similar image for the <143> direction is reported in figure Figure 18b . The systems have been allowed to evolve at 2000 K for 15 ps. To avoid the influence of the stacking fault energy on the evolution of dislocation pairs, all MD simulations have been performed only with analytical bond order potential (ABOP). This potential is parameterized in such a way that only atom interactions between the first nearest neighbours are taken into account. Therefore, ABOP makes no difference in energy between various SiC polytypes, and hence, the stacking fault energy is equal to zero. Results of simulations presented in Figure 18a(b) and in Figure 18b(b) for the <143> direction demonstrate that the <132> and <143> direction of the partial dislocation lines are not stable and experience transformation during annealing. In particular, it acquires a zig-zag shape made up by the segments aligned in the <011> direction (known to be preferential for the partial dislocation lines from the crystallographic point of view), in alternation with the segments aligned in the <121> direction. The presence of <121> line direction is favoured by the screw nature of the formed dislocation segments along this direction, which has smaller line energy as compared to other directions. With such segments of the dislocation line along equivalent [011] and [121] directions, the effective <132> segment is formed by <011> + <121> and the <143> segment by <121>+ 2 <011> segments. Thus dislocation line alignments are expected to be observed experimentally. We may conclude therefore that the observed experimentally dislocation lines effectively visible to be oriented along <132> and <143> directions are the step-like lines formed by the segments with alternating directions <011> and <121> corresponding to the minimum dislocation line free energy.

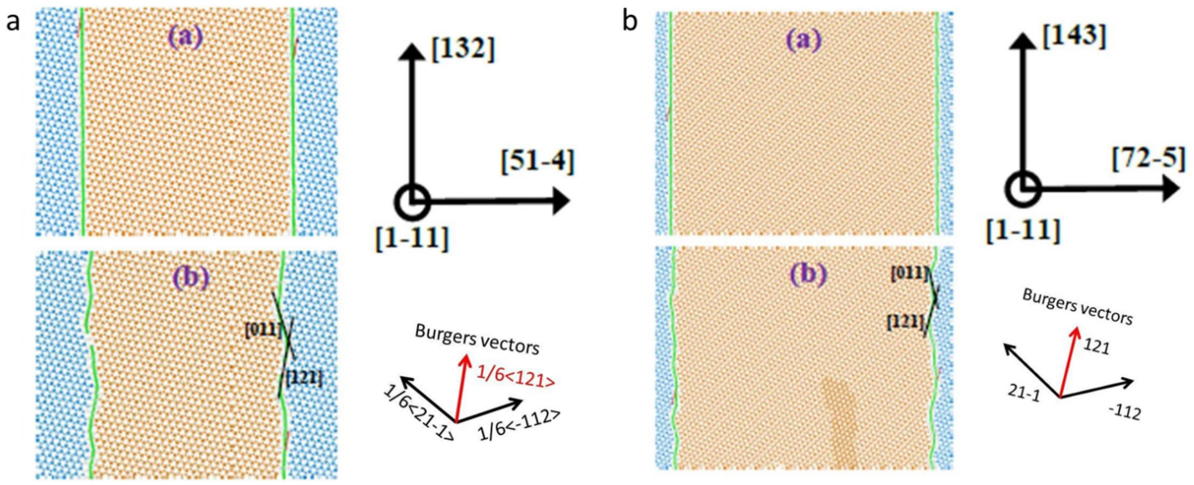

Figure 18. a) Molecular dynamics study of a) [132] and b) [143] partial dislocation before (a) and after (b) T=2000 K annealing for 20 ps.

One may consider a general concept of the appearance of visible <132>, <143> alignments of the dislocation lines by shortening of the dislocation line length by the formation of segments with equivalent <011> and <121> orientations. For the sake of completeness, we consider a partial dislocation loop enclosing a stacking fault, in the 3C-SiC film. It is shown schematically in Figure 19a. For a small loop, it is expected to be formed by six segments aligned in the equivalent <011> directions corresponding to the preferential dislocation line alignments. Increasing the loop size, we expect an increase in its free energy due to the elongation of the dislocation line. At a certain size of the loop, it is possible to shorten the dislocation length by the formation of the segments different from <011> alignment. Based on the results obtained above, these new alignments should be along with equivalent <121> directions. This means that [112] directions are “preferred” directions other than the [110]. The loop shape turns therefore to the one schematically shown in Figure 19b composed of the segments in the <011> and <121> directions. It has now the shape of a dodecagon. Increasing the size (larger loop) it is finally expected to produce visible <132> and <143> dislocation line directions observed experimentally (see Figure 19c), shortening of the dislocation line length at later evolution stages. In general, the formation of unusual dislocation line alignments upon the increase of the dislocation loop can be compared to the formation of the equilibrium Wulff shape during crystal growth.

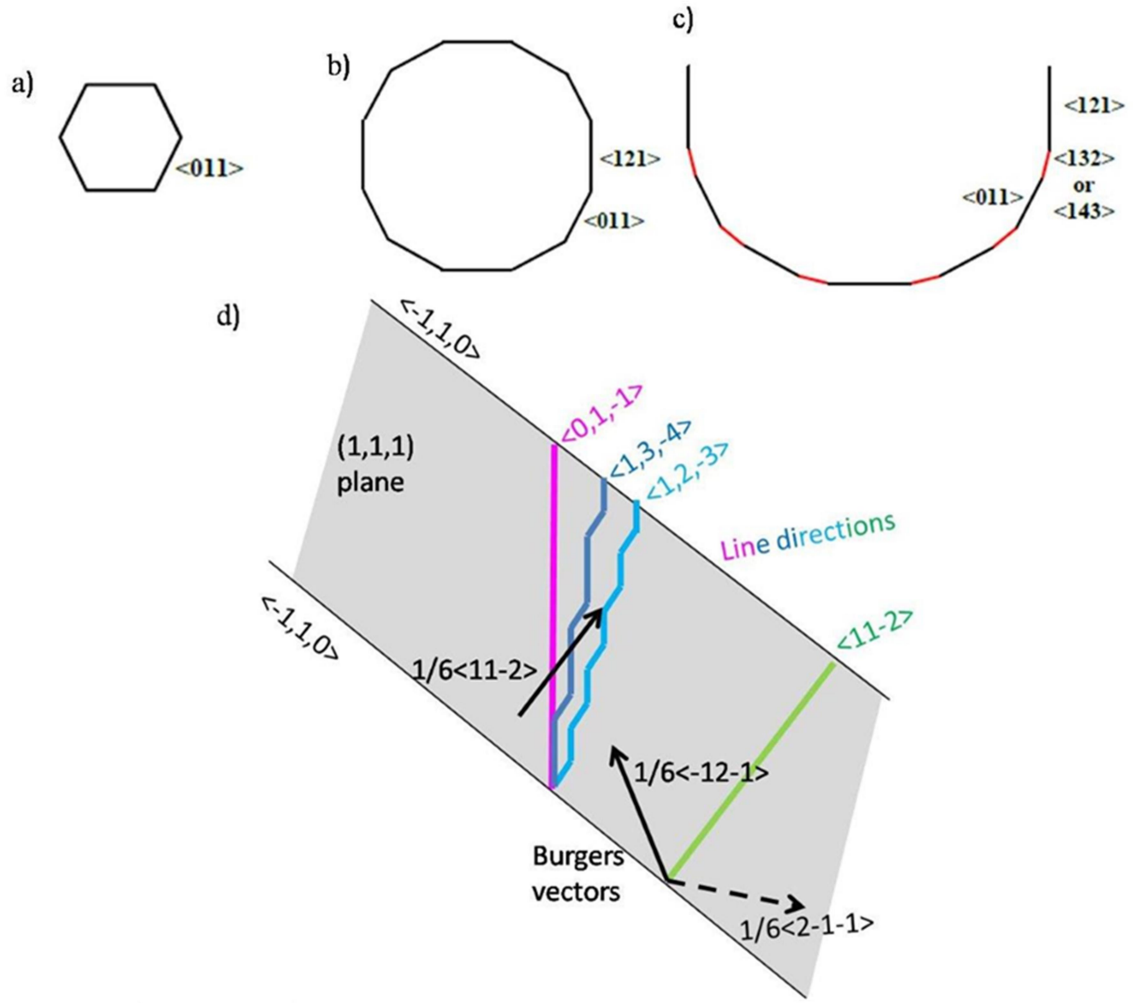

Figure 19 Preferential dislocation line alignments for small dislocation loop; b) when increased dislocation loop size it is possible to minimize its dimension by inserting segments different from <011> one; c) further increasing the size the dislocation loop shows <132> and <143> directions. d) schematic of dislocation directions and burger vectors detected.

Let's now come back to our case in which the PD directions are lines (and not circle or loop). We draw the Figure 19d a schematic of our situation on the plane (111). Black <-110> lines are the intersection of the lamellae face with the (111) plane. Green, light blue, dark blue and magenta lines are the PDs that lie along the $<11\bar{2}>$, $<12\bar{3}>$, $<13\bar{4}>$ and $<01\bar{1}>$ direction respectively. Black thick arrows are the three possible Burgers vectors in the (111) plane ($<\bar{1}2\bar{1}>$,$<11\bar{2}>$,$<2\bar{1}\bar{1}>$). The PD on the right (green) has the shorter line connecting the lamellae faces along the (111) plane. This PD can have one of the two Burgers vectors: $1/6<\bar{1}2\bar{1}>$ or $1/6<2\bar{1}\bar{1}>$. Both vectors are tilted 60° respect to the $<11\bar{2}>$ line direction. The other PD, on the left, has Burgers vector of $1/6<11\bar{2}>$ and line direction on $<01\bar{1}>$. As above reported, it can lower his length (and thus the strain energy) by using the <134> or <123> directions by realizing a zig-zag structure by combining the $<11\bar{2}>$ and $<01\bar{1}>$ segments.

Antiphase boundaries

A further investigation has been performed to define IDBs morphology and provide a detailed characterization. First of all, we show the structure of the domain boundaries found in the 3C-SiC grown on Si (001). In Figure 20, we show high-resolution images of a domain boundary in a place where the boundary is perpendicular to the observation plane (110). Thanks to high-resolution STEM images acquired using low, medium and high angle annular dark field detectors, we were able to reveal both the nature and the atomic structure of DBs. The images, in Figure 20, can disclose the structural information revealing the carbon position in the Si-C doublet.

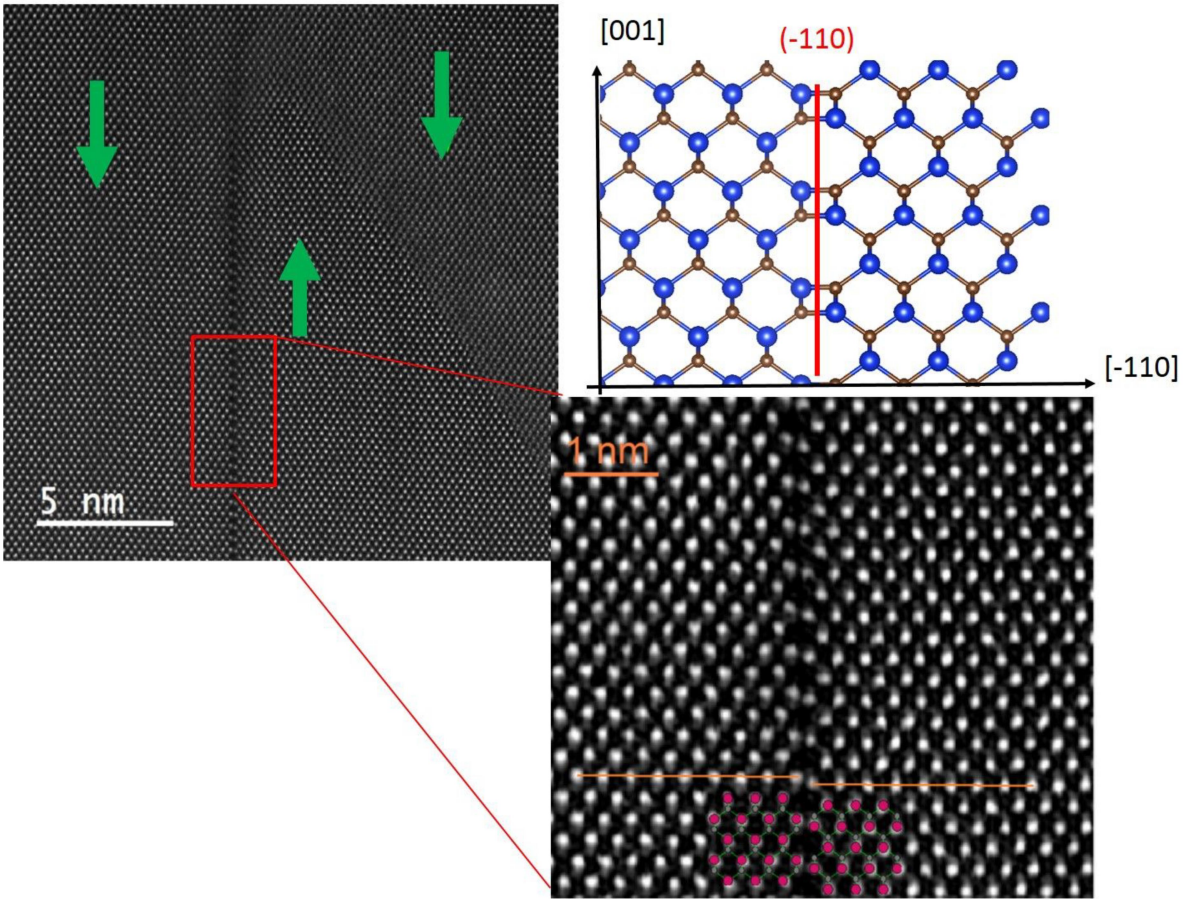

Figure 20. STEM of a coherent semi-polar (-110) inverted domain boundary (IDB). The green arrows point to the position of the Si-C doublet. C atom is above or below Si according to the arrow direction. The inset enlarges the structure of the IDB. The lattice reconstruction of the coherent semi-polar IDB is shown at the top of the figure. It shows in detail the bonding configuration along the (110) plane.

So, we were able to have a direct experimental detection of the nature of the boundary. Figure 20, also shows (top image) a lattice reconstruction of the two domains (bicrystal). The two domains, delimited by the boundary, are aligned coherently. They appear rotated of 180° around [110]

direction, thus generating inverted Si-C doublets across the boundary. It is worth noting that thanks to the crystal symmetries, a rotation of 90° around [001] with an additional shift of a/2 [001] (where a is the lattice spacing,) is equivalent to flip the crystal upside down i.e. rotation of 180° around [110]. Thus, the STEM image in Figure 20 shows the formation of an inverted domain boundary (IDB) aligned with the {110} planes. To the best of our knowledge, this is the first atomic resolution image of an IDB in the (-110) plane. The alignment of the Si-C doublet across the two domains not only reveals the coherent nature of the boundary but also the peculiar structure: it is composed of a Si-C distorted bond forming a square and a semi-octahedral structure with undistorted bonds as shown in the reconstruction of Figure 20. In the same figure, another boundary can be individuated in the upper-right part. It is much more difficult to visualize because the boundary lying plane is tilted with respect to the observation plane. Nevertheless, it can be individuated because the Si-C doublet is inverted (rotated upside down) in each domain. In the image, three domains can be identified and the green arrows indicate the position of the Si and C atom in each domain. It is worth noting that, after a deep investigation we can state that all the boundaries investigated up to now in the 3C-SiC (001) growth on (001) Si are IDBs.

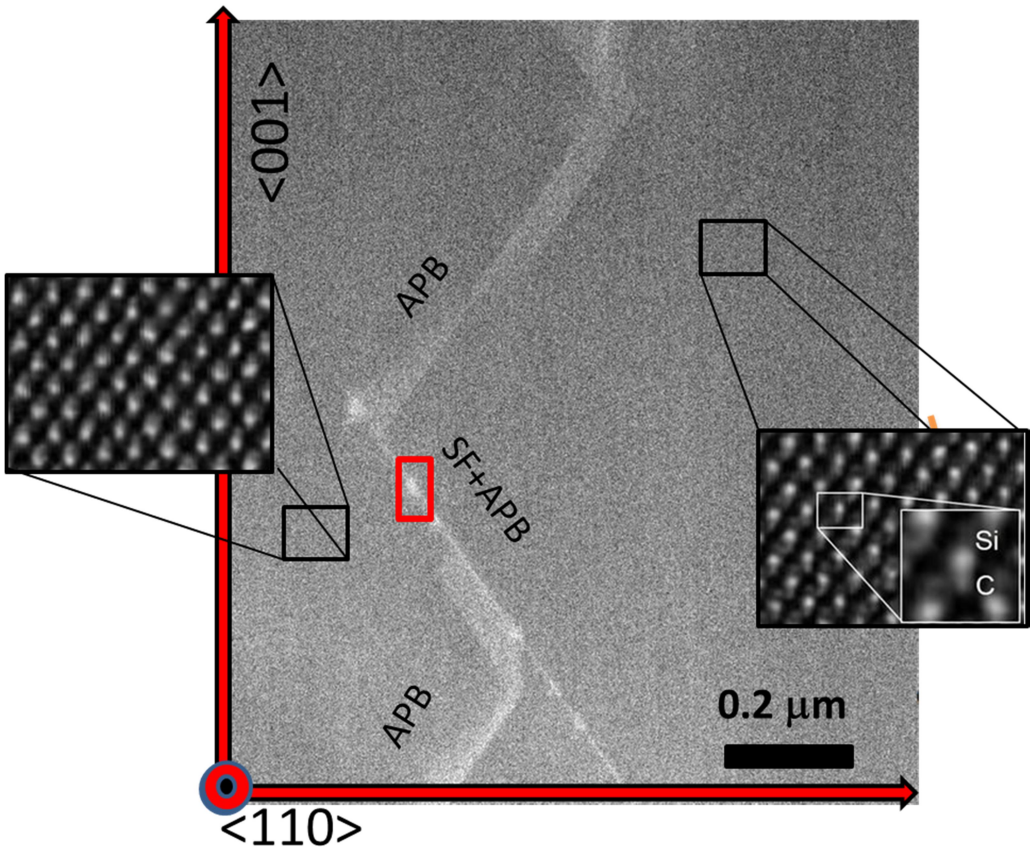

Figure 21 XSTEM image showing the intersection of an APB and a SF. In the insets HRSTEM images display the Si-C configuration in the two domains typical of Anti Phase Boundaries. Red square shows the position of HRSTEM analysis discussed through the next figure.

In 3C-SiC lattice stacking faults lie along {111} planes as evidenced by a low and high resolution survey. XSTEM in Figure 21 boxes showing the high resolution of the crystal allow an overlook on Si-C doublet configuration (in which the Si is bright due to the greater scattering cross section). It is possible to demonstrate that the two domains have a reversed configuration between each other.

The border among the two domains involves APB formation. In particular, it is noted how the APB during its path intersects an SF<1>,thereafter sharing its storage plane along the plane $(1\bar{1}1)$ and then splits from the SF<1> for energetic reasons and lies along the direction $<\bar{1}12>$. The shaded regions in the image show how the APB is able to proceed in a non-orthogonal way to the zone axis [110] by rotating around the <-112> direction. Inside the image it is possible to see a red square. In this square an HRSTEM analysis was performed as shown in Figure 22. In this image we can understand the atomic structure of the crystal. The structure of the APB displays its coherent structure characterized by a Si-Si bond and a SF <1>. In fact the atoms of C appear shifted by 1/6 [112] inside the boundary.

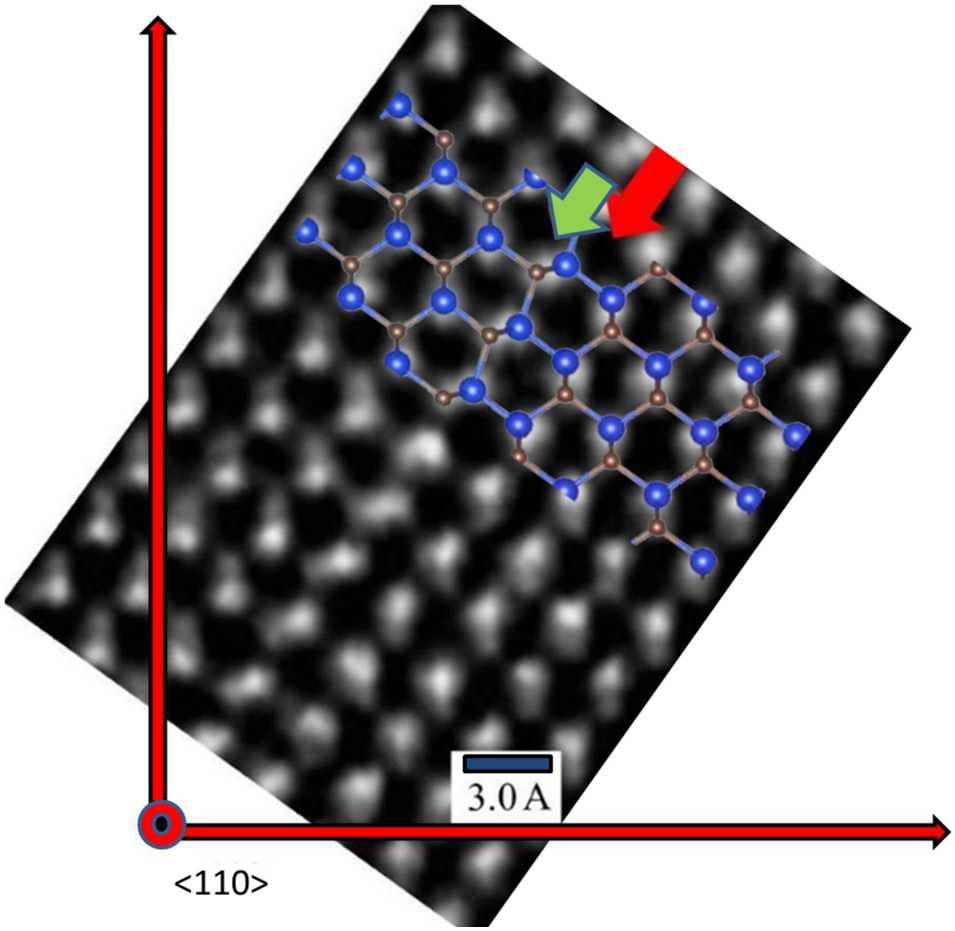

Figure 22 HRSTEM under [110] zone axis showing SF<1> and APB sharing the same plane. Cristallyne configuration is highlighted by VESTA simulation superimposed. Red arrow displays the boundary plane between the tho domains while green arrow shows the SF plane

The angle between the two diatoms is 70° and there is no distortion in the bond. The red arrow indicates the boundary plane while the green arrow denotes the SF plane. Inside Figure 23 we can anticipate the topic of the next paragraph regarding the interaction between APB and SF. It shows, in fact, a high resolution of a region in which an SF <2> and an APB are present. Within the epitaxial growth process the SF lying along the plane (1-11) intersects an APB lying on the opposite plane. The SF is closed by the APB involving a crystal shift of 1/3 [112] along the growth direction. This mismatch results in a stress condition inside the crystal highlighted by the confusion zone in Figure 23 caused by the local loss of alignment of the atoms along the crystalline matrix in the zone axis [110]. This condition implies that the storage plane ($\bar{1}11$) loses its energy convenience, so the APB changes its direction to lie along the plane (110).

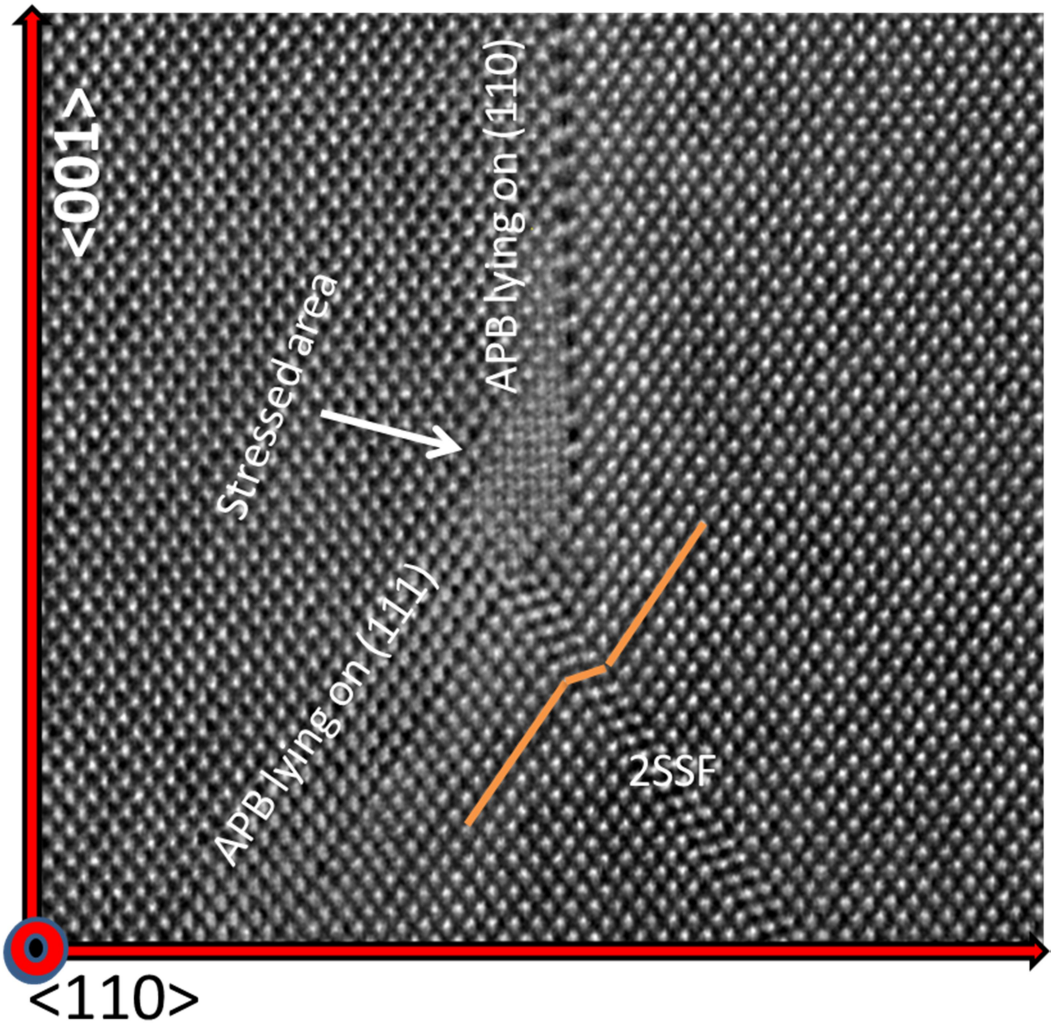

Figure 23 HRSTEM under [110] zone axis showing intersection between SF<2> and APB. APB change direction due to change in stress configuration. SF introduces a ½[1$\bar{1}$2] shift which induces APB to switch plane from ($\bar{1}$11) to (110).

.

IDB and SFs interaction

Several authors have also observed that a high density of SFs exist in regions of the material where grain boundary are found [80], implying that a relationship between them exists. While it is known that an IDB can terminate a SF [81], the details of the relationship between IDBs and SFs have not been studied for SiC and even more interestingly the generation of SFs from IDB has never been reported in 3C-SiC.

In order to understand the interaction between IDBs and SFs, we followed one of these boundaries through a series of cross-sectional view STEM images as shown in Figure 24 on the right. The growth direction ([001]) is indicated in the lower part of the image same figure. The SFs always lie in the {111} planes and in cross-view STEM images (as in Figure 24 right side) the SFs lying in the (1-11) and (-111) plane are observed as lines in the <1-12> and <-112> directions, respectively, while SFs in the (111) and (-1-11) are observed as almost trapezoidal-shaped bright zones. In the same figure, an IDB is apparent. The IDB has different lying planes: the IDB lies in the (1-11) plane in the bottom image of the series then it changes to the (-111) plane in the third image of the series, in the fourth image the IDB lies in the (011) plane and in the top left image it lies again in the (111) plane.

Additionally, in Figure 24 we included a STEM plane view of an IDB "running" through the surface and interacting with SFs. The plane and cross-view images show IDBs changing their lying plane. A detailed inspection of the image shows that the IDB lying planes seem to lie only on specific planes (i.e. the {111}, {011} and {001}) and a process of faceting occurs when an IDB curves. In such a way, at low magnification, it is able to "curve" through the sample.

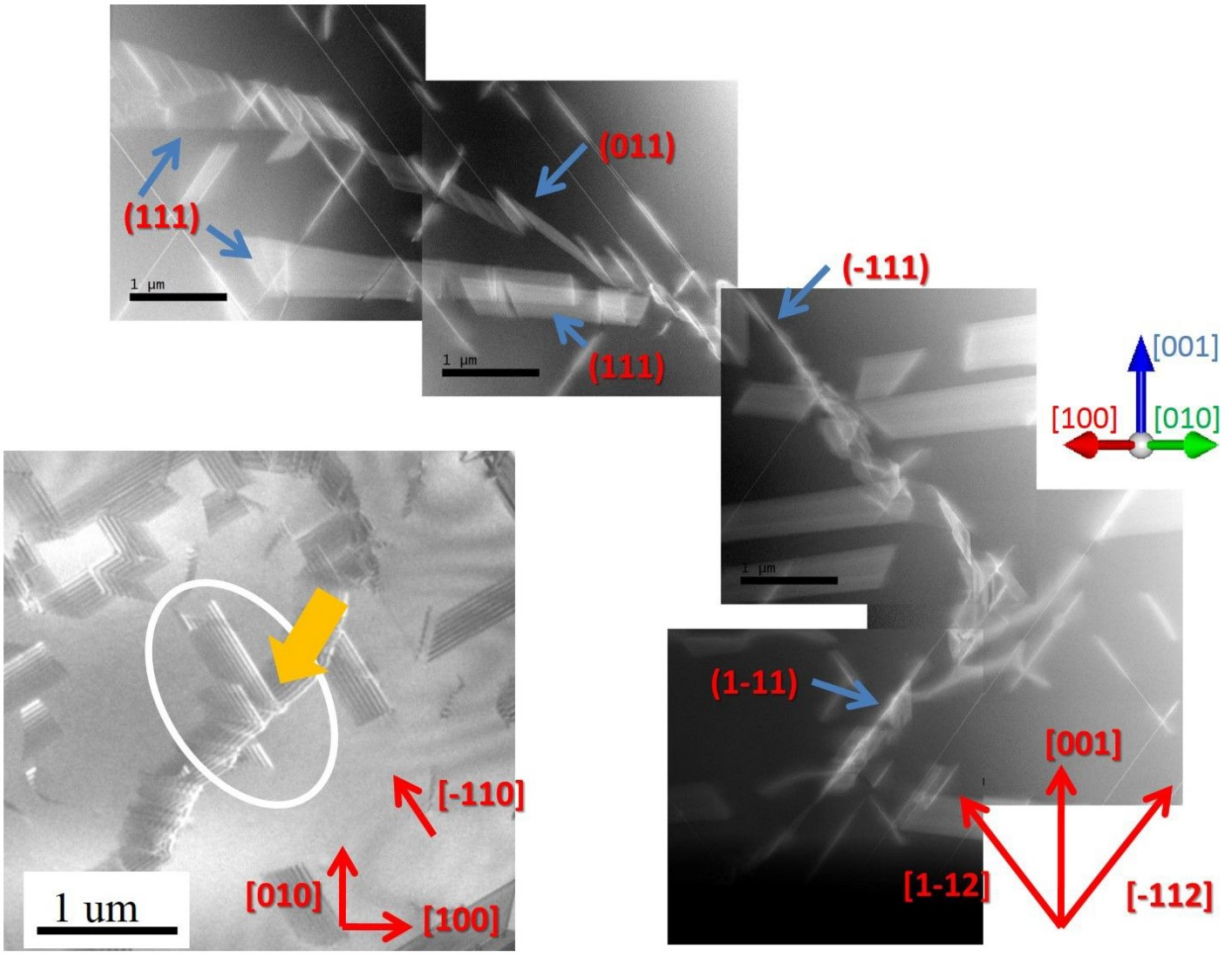

Figure 24. The sequence of STEM images shows an IDB and its effect on SFs. The image is the projection of the TEM lamellae in the (110) plane. The growth direction ([001]) is indicated at the bottom, the lying plane of the boundary for each image is also indicated, and the scale bar is the same for all images. The growth was performed in the [001] direction. In the bottom left, a plane view STEM image showing a boundary interacting with SFs in the highlighted region.

Another very important fact, that is evident from these images, is that IDBs and SFs strongly interact as highlighted with the white circle in the bottom left image.

In order to understand and recognize the plane of the IDBs and explore the interaction between IDBs and SFs in detail, we reconstructed in 3 dimensions the structure of the boundary observed in one of the images from Figure 24 (the second image from the top). We report this image in Figure 25a with hits 3D reconstruction in Figure 25b.

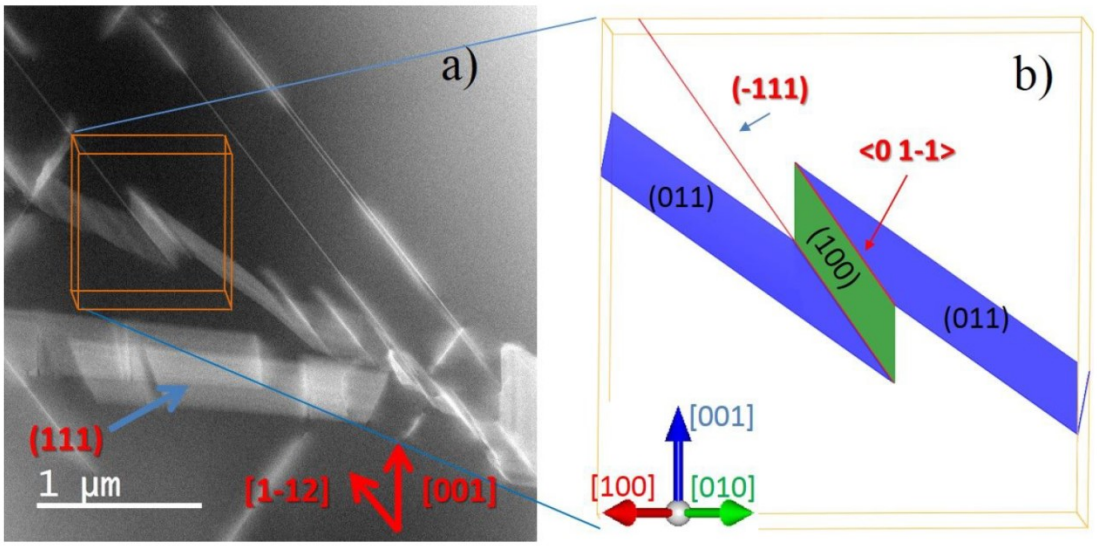

Figure 25 a) One of the images in the sequence of figure 24 (white circle) showing the cross-view STEM projection along the (110) plane. The highlighted region shows a large step-like defect and a line "coming out" from it. The line is individuated to be SF while the large defect is a boundary. The image shows the generation of an SF from an IDB. b) 3D reconstruction of the lattice planes involved in the highlighted region. The yellow boundary in b) is the lamella of the STEM sample.

We summarize here briefly the procedure able to individuate the lying plane of the IDB. Firstly, note that:

1) domains are oriented in the same way with respect to the Si wafer (001) because the growth is epitaxial as it is confirmed by the diffraction pattern of Figure 20.

2) the beam is perpendicular to (110) plane of the domain (thus it is perfectly parallel to [110] direction of the crystal

3) SFs lie on the {111} planes. Starting from these considerations, it is possible to detect a very small misorientation of the lamella face with respect to the (110) plane. So, it is possible to reconstruct a lamella with the same geometry as the real lamellae. We start by drawing {011} and {111} planes in a 3D reconstruction by using the crystal visualization program VESTA [82]. Thus, we can reconstruct the intersection between the studied plane and the lamellae boundary i.e. the "intersection lines". In Figure 25, the obtained 3D reconstruction by using the same perspective of the experimental STEM image is shown. We find that two (011) planes (blue) are connected with a (100) plane (green). From the right side of the image, it can be seen that when the (011) IDB plane (blue) changes into the (100) (green) a linear step-like IDB defect along the $<01\bar{1}>$ direction (labeled in red) is generated. In the same image, when the (100) IDB plane (green) changes into the (011) plane (blue) a defect lying along the (-111) plane (visualized in the $[1\bar{1}2]$ direction) is observed, indicating the correlation between of IDBs and SFs.

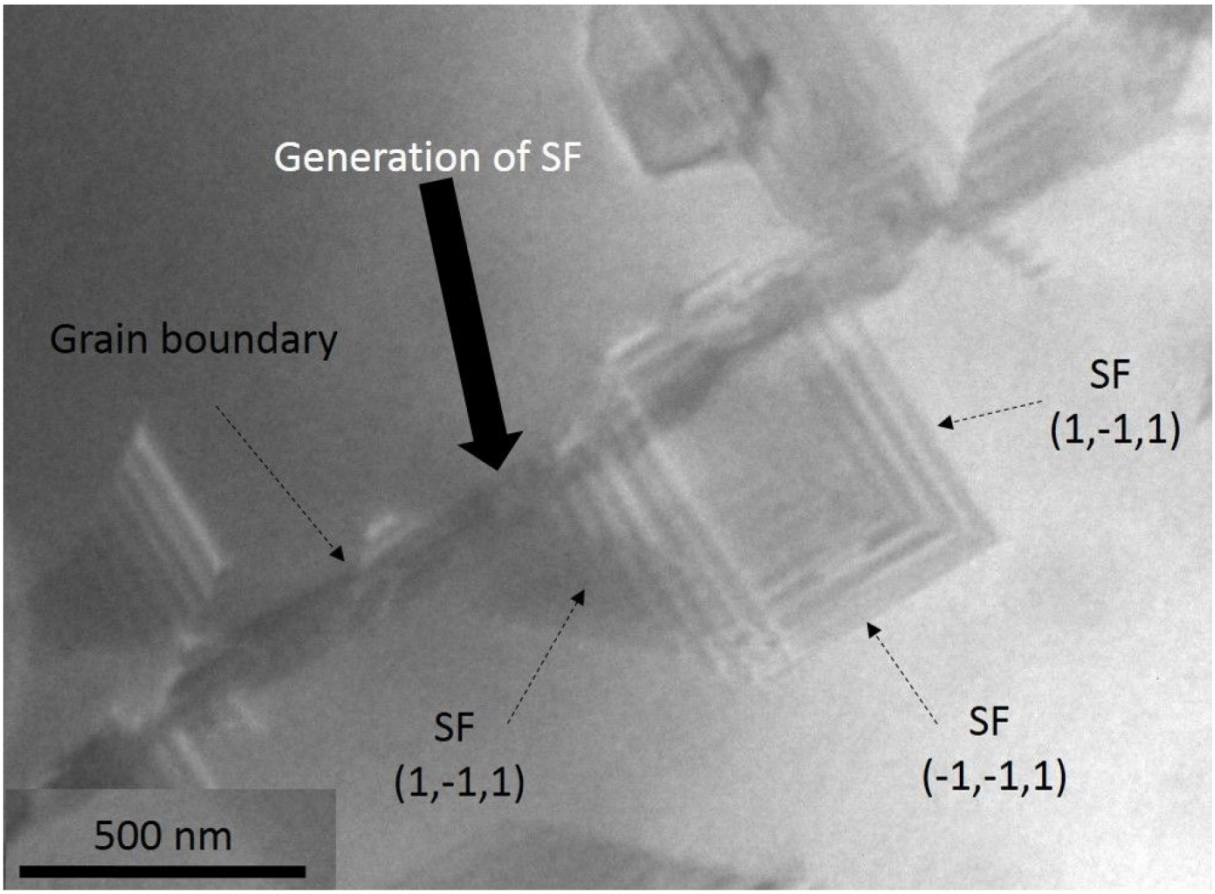

Figure 26. Plan view of a DB and SF interaction. A series of SFs are shown in the figure: a (-1-11) and two (1-11) are observed and highlighted in the figure. The SFs interact with the boundary in the position indicated by the black arrow. The (-1-11) SF is limited by two (1-11) SFs. The (1-11) SFs are limited on one side by the (-1-11) SF and by the boundary on the other side.

Another very interesting example of SF generation from IDB is shown in the plane view STEM image of Figure 26.

In these images, IDB and SFs are indicated. In particular, we focus our attention on three of these lying in the (1-11) and (-1-11) planes. Interestingly the SF in the (−1−11) is limited by two SFs in the (1−11) planes. They, in turn, are limited by the SF in the (−1−11) plane on one side. The intersection between SFs is called Lomer-Cotrell dislocation and has a Burgers vector of a/6[011]. The intersection between the IDB and the (−1−11) SF is the place where the SF is generated. From images, it is evident that a boundary is able to generate SFs. The second behavior evidence in Figure 24 regarding SFs and IDBs lying in the (1-11) and (111) planes, respectively: the termination of a SF with an IDB resulting in the formation of a step. In Figure 27 a) an IDB lying in the (111) plane is observed. Reconstruction of the plane was performed similarly to what was reported above. Figure 27 b) shows a 3D simulation of the highlighted region in Figure 27 a) generated using the VESTA program.

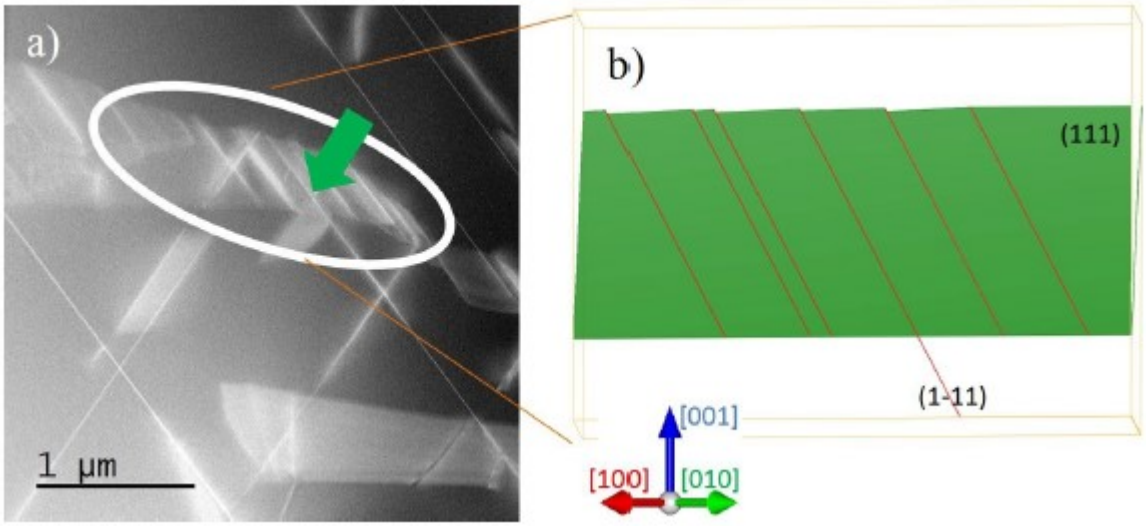

Figure 27 a) Part of the sequence of the STEM images from figure 3 showing the termination of SFs. b) 3D reconstruction of the highlighted zone. Green planes are (011) and red lines are SF. The yellow boundary in b) is the lamella of the STEM sample.

The IDB in the (111) plane is shown in green and is punctuated by a series of small steps. Moreover, the SFs interacting with the IDB is terminated with the creation of a small step. In the present example, we observed an SF interacting with an IDB associated with a step. Dislocations lying on a domain boundary associated with small steps are called disconnections.

To give more insight into the interaction between SFs and IDB, we performed 3C-SiC growth kinetic simulations by using a Monte Carlo super-lattice approach.

Simulations of the 3C-SiC growth in presence of extended defects such as IDB can be useful to understand if the generation of the SFs (and PDs) are possible during the growth of the crystal and in such cases what is the nucleation site and what are the growth condition favoring the nucleation site formation. In this way, the simulation can give a boost in the understanding of the IDBs and SFs interaction. Our KMC code allows simulation of the deposition and/or evaporation of Si and C atoms on a substrate surface. Atoms can locate on cubic lattice sites ("k" sites with zinc blende structure) or hexagonal lattice ("h" sites with wurtzite structure) sites both characterized by sp^3 bond symmetry. By adding Si and C atoms on the surfaces, the code can simulate the epitaxial evolution (growth or etching) of the surface together with the formation of point-like and extended defects such as dislocations and stacking faults [54]. The code is also able to simulate the diffusion of Si and C atoms in bulk and allows the study of the formation of clusters or aggregates. In our code, we implemented a cubic box with a size of 740.8 Å. The box contains about 8 x 109 lattice sites. We started the KMCsL run from a slab thick 137.8 Å thick slab of 3C-SiC. The initial active KMC particles lying at the (001) surface consists of 51200 under-coordinated atoms. We include also four IDB which, considering the periodic boundary conditions imposed in the simulation box,

reproduce a space distribution of IDB with alternating phases. The edge of the domains were set along {110} crystal planes. More details of the simulations can be found in ref [83]. In Figure 28a and 13b, we show two side views of the same 3D IDB structure obtained with the Monte Carlo simulation.

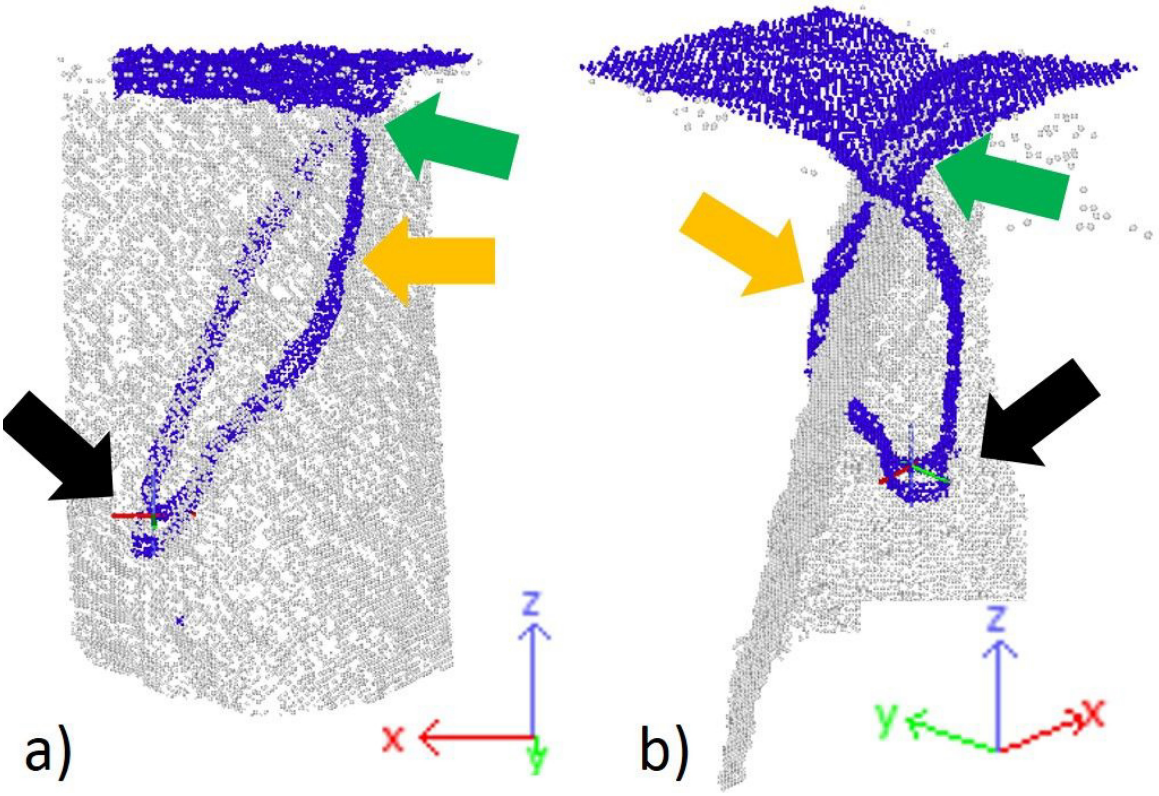

Figure 28 Snapshot of a Monte Carlo simulation showing the "evolution" of IDBs during a 3CSiC growth process. Gray atoms belong to the IDB while partial dislocation, contouring the SF, and the under-coordinated surface atoms are highlighted in blue. Arrows (black) indicate the SF nucleation site (black), the intersection of SFs and the surface (green) and the place where IDB hinders the SF evolution and terminates the defect (red)

The DBs observed in (001) 3C-SiC grown on (001) Si are inverted domain boundaries (IDBs). The rotation described in the last section (180° around the [110]) results in two crystal domains that are inverted with respect to each other. The literature referred to IDBs as antiphase boundaries (APBs), because the same boundary can be formed by rotating two domains 90° with respect to the [001] direction with an additional lattice shift along the [001] direction. Due to the crystal symmetry, the two rotations (90° around the [001] and 180° around [110]) produce in 3C-SiC exactly the same atomic arrangement. It should be obvious that the relative orientation and shift of the two domains and the coherent nature of the boundary is retained even when a IDB changes its lying planar orientation.

IDBs form during carbonization and “propagate” during the epilayer growth. On the contrary, generation, propagation, and termination of SFs in 3C-SiC are still a mattered of debate. SFs are clearly related to their boundary that is constituted by the partial dislocations (or disconnection(s)). The fate of a SF is determined by the PD bounding the SF. A partial dislocation (and SF) can form in three different “moments”: 1) during the carbonization when the first seeds of SiC on Si form to relax the lattice mismatch 2) during the growth to relax the stress related to the growing surface 3) during the “cool down step” after the growth to relax the stress related to the different expansion coefficients. Two of these “moments” are connected to the growth front while the third one is a post-growth process. It is impossible to state if the SFs form during the growth together with the IDB or during the “cooling down step” when the IDB is formed, nevertheless, it is apparent that the presence of the IDB can trigger the presence of SFs. For strictly topological reasons, dislocations and PDs have to “start” and to “end” from external or internal (IDB) crystal surfaces or lattice defects or forms loops. Once partial dislocations are formed, they can propagate into the crystal increasing the size of the associated SF and relaxing the stress. It is known that grain boundaries oriented along the <110> directions as described in the literature generate SFs in FCC metals other than SiC [84,85]. It was shown that a grain boundary can adsorb [86,87,88,89] or emit [90,91,92,93,94,95] lattice dislocation through a process involving disconnections. Disconnections are a particular kind of dislocation lying in the grain boundary and associated with steps in the boundary. As reported by Han et al. and the references therein, lattice partial dislocations (with an associated SF) can be emitted from GBs under applied stress leaving a disconnection on the grain boundary [60]. In Figure 25, we report, SFs that connect an IDB and the top surface leaving step(s) in the IDB in the (011) plane. In this case, considering that 1) 3C-SiC hetero-epitaxially grown on Si contains high stress after cooling down 2) it has a high degree of mosaicity related to the high presence of IDB, it is reasonable that the emission of partial dislocations with the formation of steps in the boundary occurs. According to the “Burger’s vector” conservation law, an emission of PDs (and the associated SF) from the IDB creates a disconnection on the IDB with the “burger vector” as opposed to the emitted partial that has to be of the type a/6[112]. The formation of disconnections changes the IDB profile, indeed, according to the “step heights” conservation law, more than one step can be formed. The net result of PD emission is the presence of SFs and a change in the IDB profile (due to the introduction of the steps associated with disconnections). This mechanism can be associated with what is observed in Figure 25. The emission mechanism has been also demonstrated in Σ9 [110] (221) Cu bicrystals [96] where, under applied tensile stress, lattice PDs (associated with the SF) were emitted from the grain boundary. The emission of SFs can happen if the strain energy overcomes a defined value. This, indeed, could be one of the

mechanisms for stress relaxation in 3C-SiC. In the same interpretative paradigm, we can understand how in Figure 26 four SFs are generated from an IDB. These are generated at the intersection line between the $(\bar{1}\bar{1}1)$ SF and the IDB. Moreover, the $(\bar{1}\bar{1}1)$ SF is limited by the two SFs in the $(1\bar{1}1)$ plane realizing a 3D structure resembling an inverted pyramid. Considering the presence of disconnections, it is possible to interpret also the termination of SFs on the IDBs as shown in Figure 27. In Figure 27, we report a SF that "came out" from the Si/SiC hetero interface (bottom) and then merge with the IDB. When a SF and the associated PD come in contact with the IDB, the trapped dislocation form disconnections along the IDB conserving the total Burgers vector. The disconnection can also evolve realizing steps at the domain-domain interface. Since each disconnection has an associated step height, their formation leads to local IDB migration (or the change of the IDB profile) that concur with the stress relaxation. The termination of SFs with IDBs was also observed in the work of Mantzari et al. [97] and Elkajbaji et al.[98]. A second model framework that can explain the features of figures 3-6 involves superdislocations.

Super-dislocations (SD) are dislocation defined by the Burger's vector bs = a <110> which is twice the perfect dislocation in an FCC material: b= a/2 < 110 > [99]. The action of bs and b are related in an FCC material [84, 100], though their energies are different. Several peculiar mechanisms of dissociation have been proposed in the literature based on the dissociation of SDs to form GBs, whereby, both can further dissociate [49, 27, 28, 50]. The applicability of these models depends on the formation energy of SFs versus the formation energy of GBs. In one particular model, the glide of a perfect dislocation results in the production of a boundary, which is bounded by another perfect dislocation [49]. The perfect dislocations at the edge of the boundary have the same Burger's vector and dissociate into Shockley PDs, which form SFs in 3C-SiC [101, 102], according to the following reaction: $a/2[1\bar{1}0] \rightarrow a/6[2\bar{1}\bar{1}]+a/6[1\bar{2}1]$ [53,103, 104]. Furthermore, it has been noted that SFs formation can occur through the mechanism of cross-slipping [105]. Since it is well known that the formation energy of SFs in 3C-SiC is three orders of magnitude lower than IDBs [76], the IDBs may generate SF due to the dissociation of dislocations at the edge through a mechanism of cross-slip. In particular, as IDBs try to minimize their total energy through a mechanism of cross slipping [106], each time the IDB "changes" direction it generates boundary dislocations, which help to minimize stress [107].

We now want to discuss briefly the findings of the KMC simulations and how it fits with the experimental evidence of generation and termination of SFs. First of all, we want to point out that the simulation qualitatively reproduces the experimental observations depicted in Figure 24 and in Figure 27. In particular, SFs generated from an IDB reported experimentally in Figure 26 can be associated with that obtained in Figure 28. In particular, the black arrow of Figure 26 and Figure 28

are both associated with the place where the SF is generated. Orange arrows of Figure 24 and Figure 28 describe the place where the IDB interact with the SF limiting its propagation and green arrows of Figure 27 and Figure 28 show the place where the SF is terminated by the IDB. Therefore we find that the theoretical simulation can describe the experimental results. Moreover, from simulations, we can depict the kinetics of the interactions between the SFs and the IDBs. In particular, we can investigate the mechanism of PDs and SF generation and termination. The simulation (as is apparent in Figure 28b) and the experimental results evidence that during the growth, a furrow is formed on the surface in correspondence with the IDB.

This furrow exposes prevalently {111} faces that are the lowest growth rate planes. The statistical surface instability on this furrow leads to the nucleation sites for the PDs and a SF is generated. Once nucleated on the IDB, the PDs evolve on {111} independently from the generated IDB. For topological reasons, the PDs bounding the SF have to be terminated in a surface of the crystal so the SF grows together with the crystal until it collides with an IDB and thus can shrink or be terminated as reported in the figure. Therefore, we can speculate that domain boundary manipulation could be used to block SFs coming out from the hetero-interface and reduce the stress related to the hetero-interface. A comprehension of these issues can help in improving the quality of the hetero-epitaxial layer and reducing the leakage current observed in the devices [108].

Stacking Faults and doping interaction

3C-SiC SFs' concentration is highly dependent on the grown layer thickness. A usual exploited strategy concerns the increase of grown thickness to allow a physiological reduction towards a saturation value. Indeed, at the Si/SiC interface, where a very dense defectiveness network is observed, SFs are annihilated at a high rate and the mutual closure mechanism is stimulated. When the number of SFs decreases, the SFs extinction rate falls and their density tends to a saturation value. However, despite the strategies used so far, the concentration of stacking faults is still not compatible with the development of VLSI technology owing to their high electrical activity [109,110].

In order to minimize the density of SFs, their formation and development inside the material must be understood. Stacking faults in 3C-SiC can be treated as random mixing of polytype unit structures, such as 6H and 4H. Theoretical calculations and experimental analysis methods are really important for spatial profiling of SFs in SiC wafers. Different techniques can be utilized, such as transmission electron microscopy (TEM), cathode-luminescence, KOH etching, X-ray topography, and micro-photoluminescence (micro-PL) mapping [111]. However, a technique such

as TEM does not allow to analyze large areas, and the others were generally applied for plan-view characterizations of the surface. In particular, for 3C-SiC, the SFs' density on the surface is investigated by etching epilayer in KOH, and then observing the sample by optical microscope. The etching of the material is heterogeneous, especially through localized defects, rather than uniform on the whole surface. In this way, it is possible to observe the total number and the shape of the SFs, but it is not possible to discriminate the type.

Raman spectroscopy is commonly used for SiC analysis as it is non-destructive and does not require any sample preparation. This technique provides spatial resolution suitable for studying defects in thin films. Hence, it can be considered as a complementary method to photoluminescence (PL) analysis for SiC characterization, one of the most used methods to detect and study crystallographic defects in the material [112,113].

In this work, we report the study of the stacking faults (SFs) in the 3C-SiC cross-section epilayer. Structural characterization as well as SFs' distribution was performed by μ-Raman spectroscopy and room-temperature μ-photoluminescence. Two kinds of SFs, 4H-like and 6H-like, were identified near the removed interface with silicon. Each kind of SF introduces a characteristic photoluminescence emission of 4H-SiC and 6H-SiC located at 393 and 425 nm, respectively. 4H-like and 6H-like SFs show a different distribution along the thickness of the film. The reported results were discussed in relation with the experimental data and theoretical models present in the literature.

Micro-Raman and micro-photoluminescence maps were performed at room temperature using an HR800 integrated system by Horiba Jobin Yovin in a backscattering configuration. For the Raman analysis, the excitation wavelength was supplied by a continues He-Ne laser (632.8 nm), which was focalized on the sample by a x40 objective, with numerical aperture (NA) of 0.5. The scattered light was dispersed by an 1800 grooves/mm kinematic grating. For the PL analysis, the excitation wavelength was supplied by a continues He-Cd laser (325 nm), which was focalized on the sample by a x40 objective, with numerical aperture (NA) of 0.5. The emitted light was reflected onto a 300 grooves/mm kinematic grating.

3C-SiC film was synthesized by CVD adding a constant nitrogen concentration of 1600 sccm inside the chamber. Thus, 3C-SiC film shows a nitrogen concentration of $1 \cdot 10^{19}$ at/cm^3 (the nitrogen concentration in the layer was measured by Van der Paw structures). Figure 29 shows some free-standing 4 inch wafers of 3C-SiC synthesized in accordance with the process scheme reported in Figure 12.

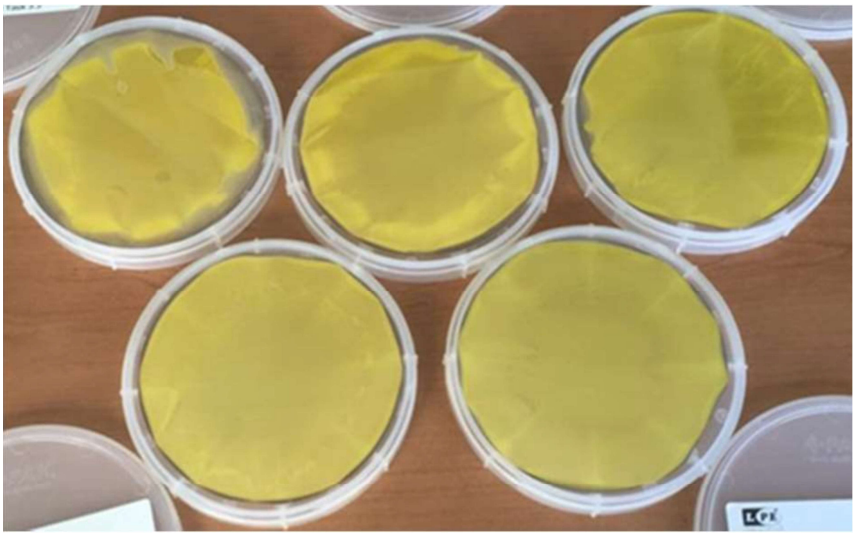

Figure 29 Free-standing 4 inch wafers of 3C-SiC. The growth was performed in a horizontal hot-wall chemical vapour deposition (CVD) reactor supplied by LPE.

We chose to dope the material with a high nitrogen concentration, because N-doped 3C-SiC has a direct band gap character that exhibits good emission properties. Moreover, it has more electrons near the Fermi level that contribute to increasing band-to-band transitions [114], and thus to increasing the intensity of the detected signals. Figure 30 shows the room temperature micro-PL map at 540 nm acquired on a 3C-SiC cross-section sample (Figure 30a), and relative PL spectra extracted at different thicknesses (Figure 30b).

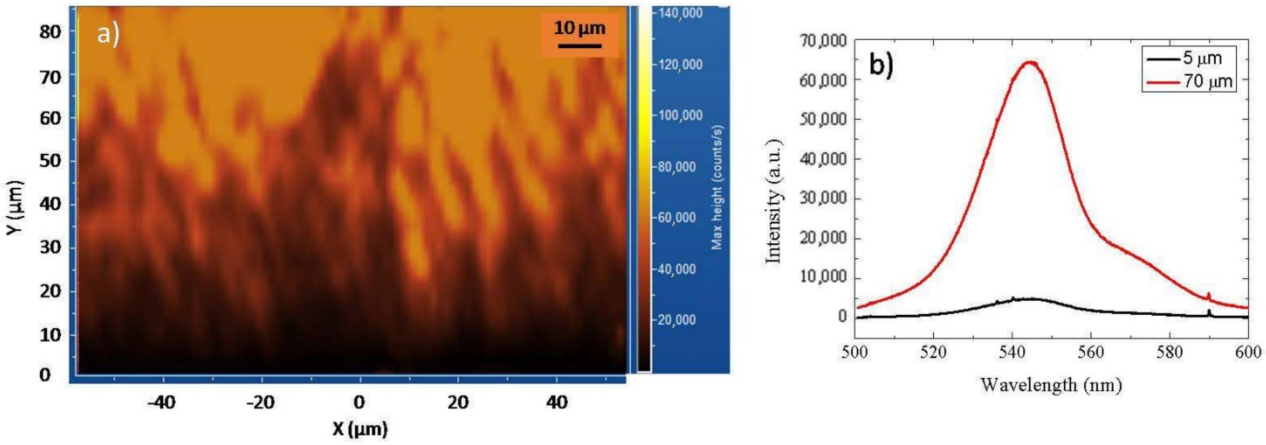

Figure 30. a) Micro-photoluminescence (PL) map at 540 nm of a 3C-SiC cross-section. The point 0 on the Y axis indicates the interface removed with the silicon. b) PL spectra extracted at various thicknesses. The interface with the removed silicon substrate is placed at 0 µ m.

We can observe that the region next to the removed silicon substrate (point 0 on the Y axis) appears

darker (Figure 30a), owing to a lower intensity of the band-edge peak, about 5000 counts/s (Figure 30b, black spectrum). As we approach the surface, the intensity of the map intensifies, revealing a greater band-edge peak emission, of about 65,000 counts/s (Figure 30b, red spectrum). It is known that, for 4H-SiC, the intensity of the band-edge emission is decreased by the non-radiative recombination via defect levels and surface/interface recombination [115]. However, SFs in 3C-SiC do not produce a PL peak, usually in the range between 450 and 900 nm, because they do not introduce levels inside the bandgap [113,116].

Nevertheless, we think that the variation of the band-edge peak intensity in the map provides a distribution of crystalline quality, and thus of defects, along the sample section. This difference suggests a high concentration of defects in the first 20 μm of 3C-SiC. These defects decrease moving to the surface.

To better understand this result and the possibility to detect the presence of SFs in 3C-SiC film by μ-PL and/or μ-Raman analysis, we focused our attention on the first 30 microns of the 3C-SiC cross-section. In Figure 31(a-c), we report (a) μ-PL map at 540 nm and μ-Raman map at (b) 778 cm^{-1} and (c) 784 cm^{-1} acquired in the cross-section in the same area.

We can observe that the μ-PL map (Figure 31a) shows the same intensity distribution reported in Figure 30. The band-edge peak intensity increases moving from the silicon-removed interface to the surface (from 0 μm to 85 μm). In Figure 31b,c, μ-Raman maps show some localized zones near the original 3C-SiC/Si interface, which show a higher intensity of the signal acquired at 778 cm^{-1} and 784 cm^{-1}, respectively. In particular, the 778 cm^{-1} signal is visible in a very large area (about 80 μm in width and 25–30 μm in depth) (Figure 31b). Instead, the 784 cm^{-1} signal extends to a smaller area (about 20 μm in width and 20 μm in depth) (Figure 31c). However comparing the two figures, we observe a coexistence of the two signals in a portion of the image. The average Raman spectra acquired in regions (1), (2), and (3) were reported in Figure 31d–f. The average Transversal Optical TO Raman mode of 3C-SiC is localized at 796.5 ± 0.2 cm^{-1}, 796.3 ±0.2 cm^{-1}, and 796.5 ± 0.2 cm^{-1}, respectively. At the same time, the average full width at half maximum (FWHM) is 5.6 ± 0.2 cm^{-1} at point (1), 5.3 ± 0.2 cm^{-1} at point (2), and 5.2 ± 0.2 cm^{-1} at point (3).

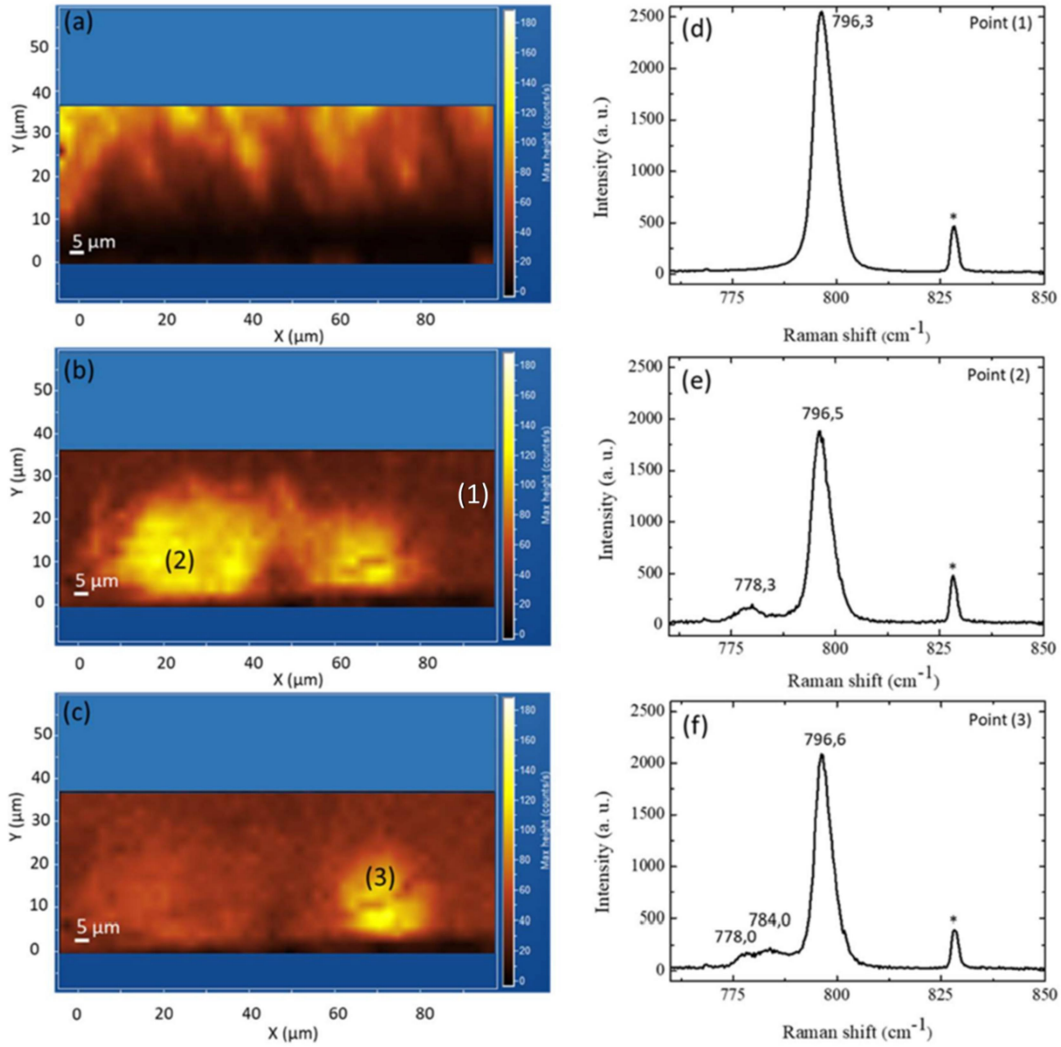

Figure 31 Micro-PL map (a) at 540 nm and micro-Raman map at (b) 778 cm^{-1} and at (c) 784 cm^{-1} of a 3C-SiC cross-section. The point 0 on the Y axis indicates the interface with the removed silicon. Average Raman spectra acquired in (d) region (1) on the map (b), (e) region (2) on the map (b), and (f) region (3) on the map (c). The peak localized at 828.37 cm^{-1} (*) is the result of the laser.

The average Raman spectrum acquired in point (2) shows an additional peak at 778.3 cm^{-1}, and the average Raman spectrum acquired in point (3) shows two additional peaks at 778.0 cm^{-1} and 784.0 cm^{-1}. The stacking sequence of the 3C-SiC polytype includes an intrinsic, extrinsic, and double-extrinsic stacking faults. SFs are wrong sequences of the double layers and they can be seen as inclusions of a few layers of a SiC polytype in the perfect layer stacking of another polytype [117]. It is known that the TO mode for 4H-SiC lattice is located at 778 cm^{-1} [118]. Thus, we think that the area of the µ-Raman map (reported in Figure 31b) characterized by the presence of the peak at 778.3 cm^{-1} is an area with a high density of defects. In particular, these extrinsic stacking faults recall the structure of the 4H-SiC [117]. In the same way, the TO mode for 6H-SiC lattice shows two components at 764.4 cm^{-1} and 789.4 cm^{-1} [119]. Thus, it is possible that the area of the -Raman map (reported in Figure 31c) characterized by the presence of the peak at 784 cm^{-1} is an area with a

high density of double-extrinsic stacking fault, which recall the structure of the 6H-SiC [117]. The component at 764.4 cm^{-1} cannot be discriminated in our spectra because it is too close to signals from the laser.

To confirm this hypothesis, we acquired (in the same area) some linear μ-PL maps along the entire thickness of the cross-section, from the removed interface with Si (0 μm) to the surface (85 μm). Figure 32 shows the linear μ-PL map acquired crossing area (3) in Figure 31c and centered at 390 nm (Figure 32a).

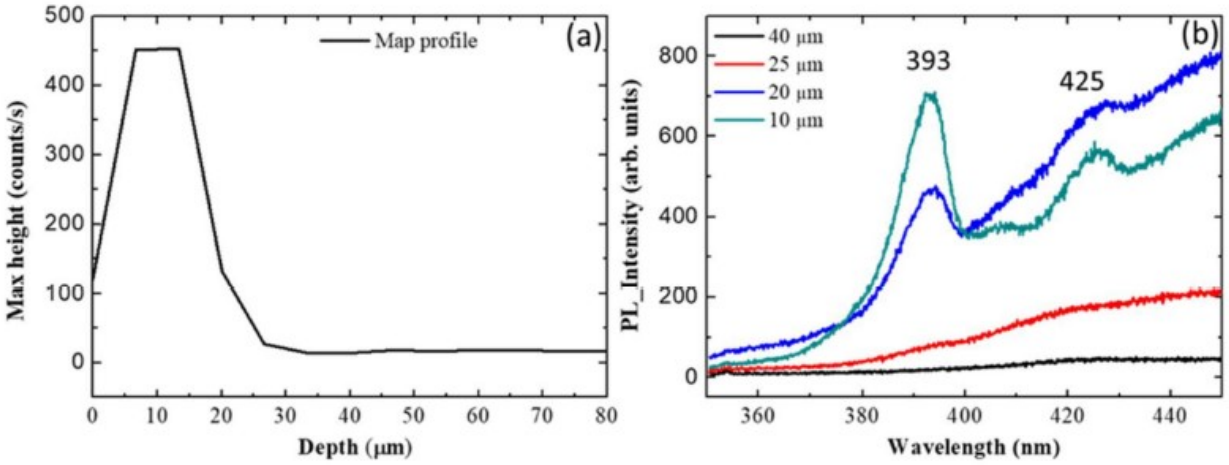

Figure 32 a) Profile μ-PL linear map at 390 nm and b) spectra extracted at various thicknesses. The point 0 on the X axis (in left panel) indicates the original silicon interface.

Linear μ-PL maps were acquired in the range between 350 and 450 nm. In particular, the map profile centered at 390 nm shows the absence of the signal for thickness greater than 25 μ m (Figure 32a).

Instead, for thickness lower than 25 μm, the signal increases until a value of 450 counts/s in the range between 5 and 15 μm. The relative spectra extracted from the map profile at various thicknesses are shown in Figure 32b. For thickness greater than 25 μm, in the range between 350 and 450 nm, the PL spectra do not show any particular peak (black and red spectra in b). For thickness of 20 μm, the PL intensity increases in the same range. In particular, we observe the presence of a new peak at 393 nm (blue spectrum in Figure 32b), which is very close to the band-edge emission of the 4H polytype, reported at 390 nm [120]. For thickness of 10 μm, the intensity of the peak at 393 nm increases and another peak appears at 425 nm (green spectrum in Figure 32b), which is very close to the band-edge emission of the 6H polytype, reported at 423 nm [121].

So, combining the results obtained from μ-PL and μ-Raman maps, the presence of 4H-like and 6H-like staking faults was ascertained. In particular, they allowed us to detect the distribution of

defects along the cross-section of a sample. Comparing these results with those present in the literature and obtained with different experimental techniques and theoretical simulations, two aspects are most striking.

First, to our knowledge, there are no reports in the literature that highlight a distribution and discrimination of SFs over large areas in the cross-section. Even if TEM analysis allow to discriminate the typology of defects, the analysis is often carried out on very small areas (some micron) [104,122]. Meanwhile, the other techniques are used to characterize surfaces. In particular, the most common technique to study and highlight the presence of SFs on the surface of the 3C-SiC is to attack the sample in KOH. The attack takes place selectively, mainly affecting areas with defects. For an etched sample [123], the TO mode becomes asymmetric into the low frequency side. At the same time, the intensity of the TO band increases. Nevertheless, it is not possible to discriminate the type of SFs dispatched by the attack itself. Our approach is not destructive, so we observe the formation of new distinct peaks in Raman spectra (see Figure 31e,f) at a lower frequency with respect to the TO mode of the SF-free 3C-SiC (see Figure 31d), but we do not observe a greater intensity of the TO peak. This difference is related to the different crystallographic planes exposed during the Raman acquisitions. In the results reported in the literature [123], the KOH etch and the relative Raman analyses are conducted along the (001). As the TO mode is forbidden for a perfect 3C-SiC crystal in a backscattering geometry for {001}, the increase of the TO intensity indicates that stacking disorder breaks the k-selection rule [123].

In our case, the sample is placed in cross and the Raman spectra were acquired along the (110). In accordance with the above configuration, we observe a more intense TO peak outside the defective zone (Figure 31d) and a less intense TO peak in the presence of the signal associated with the defects (Figure 31e,f). The average FWHM of the TO peak shows a constant value between the region with (Figure 31e,f) and without the defects (Figure 31d).

The second point concerns the type of defects and their distribution along the thickness. The literature on the thermodynamic stability and polytypes of SiC is rich. Many theoretical works were carried out to explain the band structure and total energies of the various polytypes of silicon carbide [124,125,126], showing that, at a high temperature, the 6H- and 4H-SiC polytypes become thermodynamically more stable than 3C-SiC [117]. In particular, the formation energies of SFs in 3C-SiC decrease with the temperature (particularly for ESFs). Even though 6H-like SF shows a lower formation energy than 4H-like [117], and it is considered the most common inclusion of other polytypes in 3C-SiC [127], we clearly observe the peak related to the presence of 6H-like SFs only in the first 15 μm of the film (from the removed Si interface to the surface, Figure 31c). Meanwhile, it was possible to detect the peak attributable to 4H-like SFs in the first 20–25 μm of the film

(Figure 31b). Another interesting aspect is that the 6H-like signal appears coupled to the 4H-like one, while it is possible to observe large areas where only the 4H-like signal is visible (Figure 31b,c). Furthermore, moving along the cross section of the samples, for thicknesses greater than 25 μm, we observed the 4H-like signal in small areas, but not the 6H-like signal (spectra not shown here). It is important to underline that, to detect the signals related to SFs along a cross-section, the defects must have high density and be sufficiently superficial with respect to the exposed section. In particular, for PL measurements. In fact, the penetration length in the 3C-SiC of the laser source used to acquire the PL spectra is about 3 μm. As the film was grown at a constant temperature (1400 °C), the distribution of SFs along the thickness of the film cannot depend on the formation energy alone. The cause could be ascribed to the stress profiles that vary by moving from the interface to the surface. For example, at the interface where there is a large residual strain, both types of SFs may be needed. However, factors such as crystallographic orientation of substrate and/or the carbonization process of silicon can influence the formation of defects at the interface. Therefore, one type of SF can be privileged over another. Another possibility could be the high concentration of nitrogen, which could facilitate the closure of one type of SF rather than another. The first results on 3C-SiC samples attached in KOH showed that the concentration of surface defects depends on the nitrogen concentration. In particular, the density of SFs decreases with increasing nitrogen concentration.

To assess SFs trend in relation to N doping, CVD growths were carried out at different N concentration and molten KOH etching methods were adopted for SF evaluation. The etching in potassium hydroxide (KOH) was performed at 500 °C for 3 min. The densities were calculated based on the observation under fully automated (X, Y, Z) optical microscopy. With powerful software for the image analysis coupled with high-resolution optical microscope, a detailed SFs count and classification were obtained.

From Raman analysis performed with He-Cd laser (λ=325 nm) it was verified the dopant value activated within the sample through fitting experimental longitudinal optical plasma coupled modes with theoretical formulas [128]. The three N_2 fluxes led to concentrations of $1.2 \cdot 10^{19}$, $2.9 \cdot 10^{19}$, $5.8 \cdot 10^{19}$ N^+/cm^3. In Figure 33a are reported the images of samples subjected to selective KOH etching. The etching rate of the C-face SFs, lying on (-111) and (1-11) crystallographic planes, is uniform to the (001) plane, while the etching rate of the Si-face SFs is lower displaying their distribution. Off-axis growth favors SFs surface propagation lying along the (111) plane, while (-1-11) SFs opposite to the growth step are forbidden. In the absence of the annihilation mechanism Si face SFs propagation from 3C-SiC/Si interface towards surface is favored. The distribution shown

in Figure 33b therefore constitutes a good approximation of the total SFs distribution, at least for SFs longer than 1 μm (our detection limit).

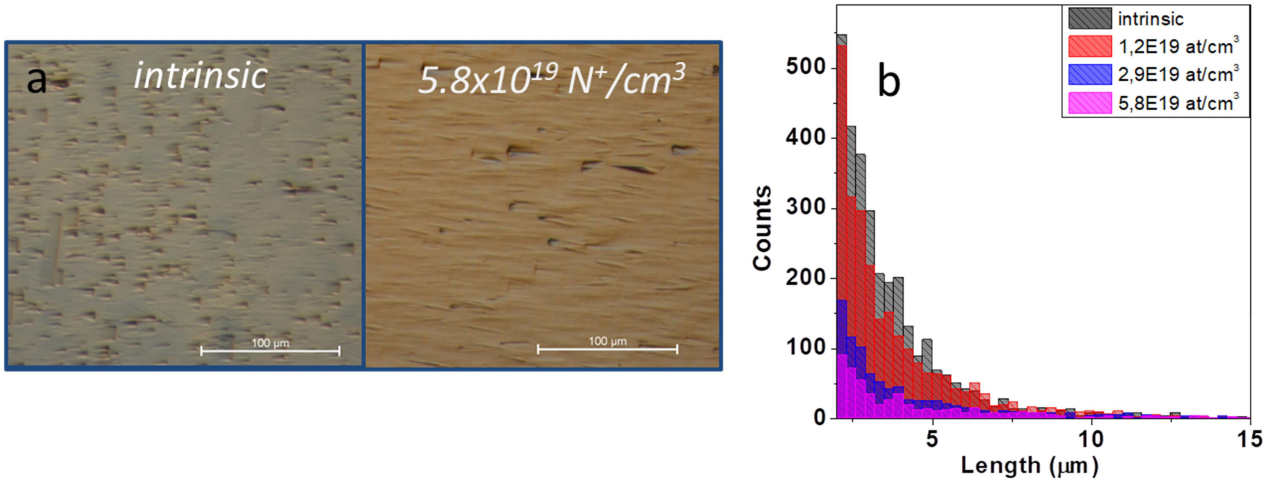

Figure 33 a) Optical microscope image of the intrinsc and 5.8·1019 N^+/cm^3 after the molten KOH etching at 500 °C for 3 min. b) SFs size distribution histogram acquired by optical microscopy;

This graph shows a drastic reduction in SFs concentration and average size obtained from investigation. Such framework is summarized in Figure 34a as a function of the active doping concentration. This trend is consistent with ab initio DFT calculation which establishes that nitrogen doping around a SF increases SF formation energy [129]. Nitrogen suppresses the SF formation only when very close to the SF. Experimental estimation confirms to be more certain about the range of the influence of the dopant. It is evident that if for the intrinsic sample the average SFs density is $2.2 \cdot 10^2$ cm^{-1} and by increasing doping to $2.9 \cdot 10^{19}$ N^+/cm^3 and $5.8 \cdot 10^{19}$ N^+/cm^3 such value is notably reduced.

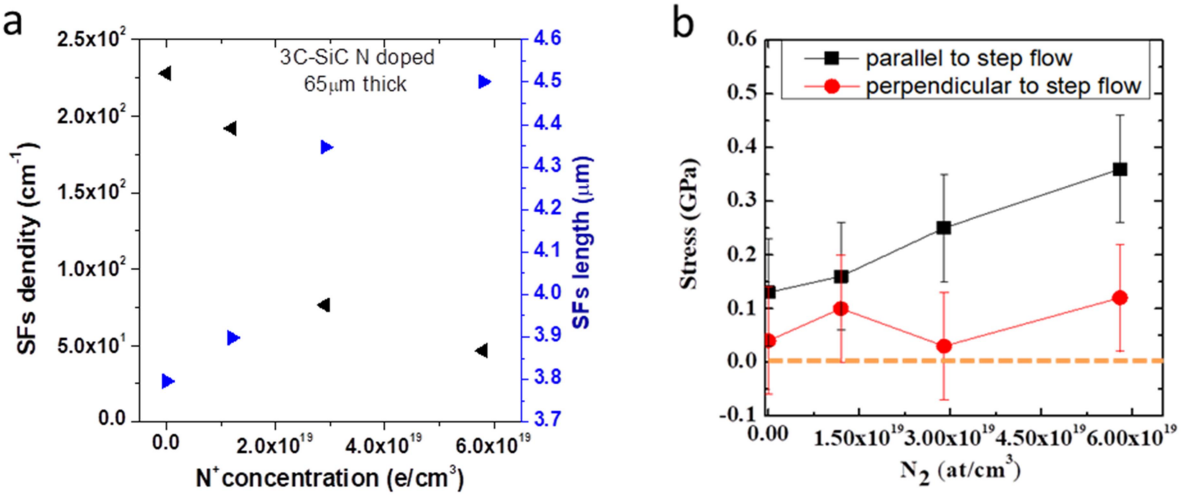

Figure 34 a) Average SFs density and length as a function of doping; b) Raman extracted stress distribution parallel and normal to step flow direction.

A further investigative approach was aimed at the characterization of the 3C-SiC layer grown in homoepitaxial mode as a function of growth temperature to find a convincing alternative to the 3C-SiC/Si hetero-epitaxial system. In order to grow four and six inches 3C-SiC bulk material, a new epitaxial reactor chamber has been designed and tested. The main idea is to grow a hetero-epitaxial layer as seed, melt the silicon substrate, and continue the growth at a high temperature. In this way, it is possible to grow a bulk substrate of 3C-SiC with a low density of SFs and low wafer bow. In fact, the bow can be strongly decreased, because by removing silicon, one of the main components of the stress due to the different thermal expansion coefficient between the two materials is completely eliminated. The removal of silicon also gives the possibility of a large increase in the growth temperature and in the growth rate, and then thicker wafers and better material can be grown.

The first structural investigation of the entire 200 μm thickness film was performed by SEM. in cross section, where the 3C-SiC film (seed and homo-epitaxial layer) is observed (Figure 35). The Figure 35a shows different layers within the film: starting from the bottom, first the seed of 90 μm and next, the homo-epitaxial layer grown after the fusion of Si. The seed shows different layer with different growth rate, with more defects close to the old Silicon interface. The seed shows the decreasing of defects increasing the growth rate. The second step is made-up of the homo-process that reveals a lower thickness value (around 120 μm) compared to the predicted one (150 μm of Figure 35b). From the figure, the change of the doping concentration is also visible close to the film surface (10 μm thickness layer with low doping concentration close to the surface).

The investigation of the temperature influence on the homo-epitaxial process was evaluated by X-ray diffraction analysis (Figure 36). The full width of half-maximum (FWHM) on the X-ray rocking curve of the 3C-SiC (002) peak is related to the crystal quality and defect density (decrease the FWHM, increase the crystal quality). Figure 36 shows the trend of FWHM as a function of film thickness for different sample growth, also in different conditions.

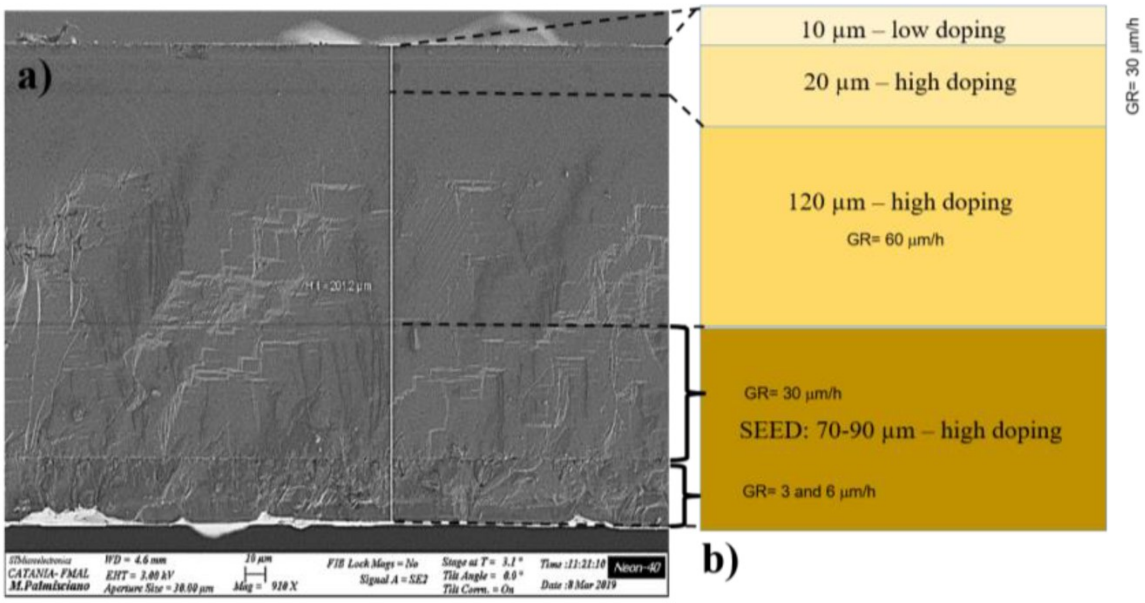

Figure 35 a) Cross section SEM image of the 3C-SiC wafer (about 200 µm); (b) schematic representation of the structure: hetero-epitaxial seed and homo-epitaxial layer. Layers have a different doping concentration and growth rate.

It is well known that by increasing the film thickness, the quality of the material increases [130]. The first part of the curve (from 0 to about 20 µm of thickness) shows the 3C-SiC sample growth with the Si substrate. For such samples, the crystal quality is limited by the presence of silicon substrate that, starting from about 20 microns of thickness, introduces many cracks and extended defects during the cooling down after the growth [110]. The three points at 60 µm are the 3C-SiC samples without silicon substrate (after Si fusion) with a good crystal quality (around 200 arcsec), comparable with an old two-inch 3C-SiC wafer provided by Hoya corporation (dotted line). These samples are the substrates used as the template for the homo-epitaxial process of this experiment. The starred points (three at 200 microns) are the samples that grew using the new melting technique described in the present work. They were grown at three different temperatures (1600 °C, 1640 °C, and 1700 °C). The graph clearly shows that the sample grown at 1600 °C is significantly better than the other two. Indeed, it has an FWHM value of around 100 arcsec that is very promising, also compared to a thicker sample (about 400 microns) grown by sublimation epitaxy (PVT reactor) at high temperature [131].

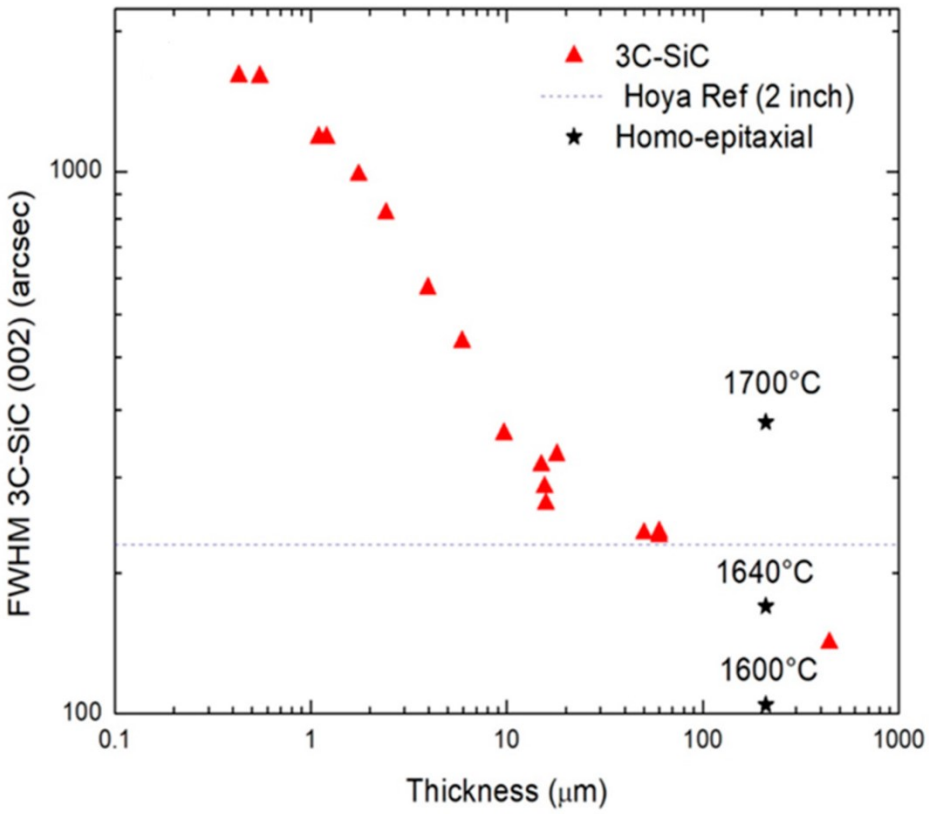

Figure 36 The full width of half-maximum (FWHM) of the X-ray Rocking curve as a function of film thickness for different values of temperature and compared with other reference samples [110].

In the 3C-SiC, the micro-Raman signal of the transversal optical (TO) mode in our experimental conditions (back scattering configuration and (001) oriented samples) should be forbidden [132] due

to selection rules. In the "perfect" cubic structure (001)-oriented, the TO Raman peak is not allowed, for this reason, the TO peak could be considered as a marker of the quality of the material. Nevertheless, the defects and stress produce a loss of periodicity, reduction of crystal symmetry, and topological disorder of crystals. Therefore, they induce a breakdown of the selection rules and the appearance of such a peak in the experimental spectra. Figure 37 shows the TO intensity peak for samples grown at different growth temperatures. The decreasing signal intensity means a decreasing of crystal "disorder". Lower intensity was recorded for samples grown at 1600 °C. Moreover, the FWHM of the TO mode is related to the crystal quality of the film. In Figure 37b the FWHM of the TO mode (reported in Figure 37a) as a function of growth temperature is reported. The graph clearly shows that the quality of the material improves when lowering the growth temperature. These results confirm the XRD result reported in Figure 36.

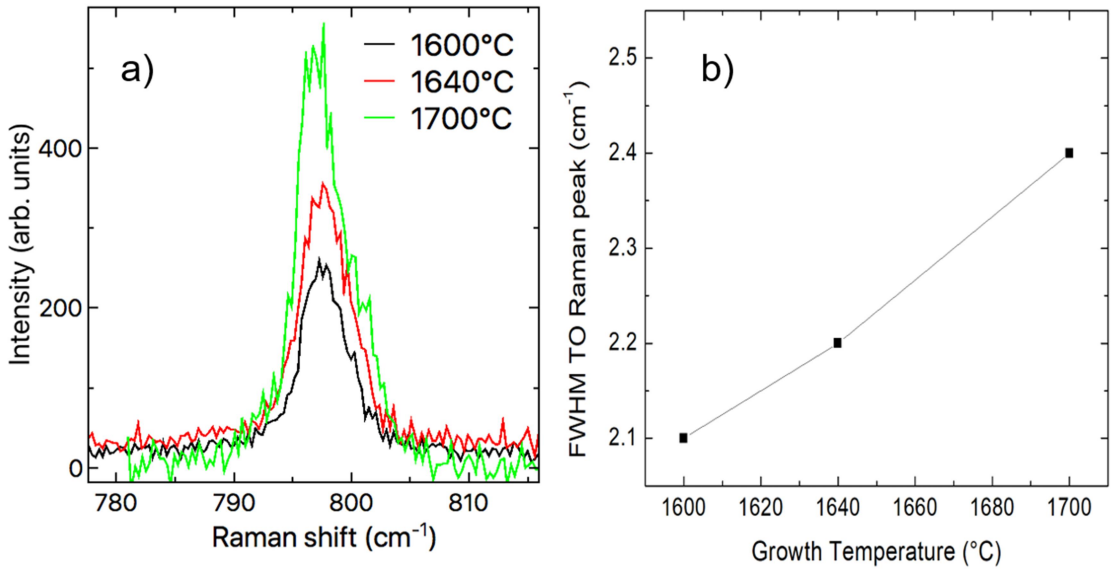

Figure 37 a)The intensity of the Transversal Optical (TO) Raman mode peak for the different growth temperatures studied; b) FWHM of the TO curve as a function of the growth temperature.

The Stacking Faults (SFs) density on the surface was investigated by etching epilayer in molten KOH and observed by a fully automated optical microscope. Image analysis software allows to count and classify SFs. Figure 38 shows the optical microscope image of the sample growth at 1600 °C (left) and 1700 °C (right). The figure shows the shape of the stacking faults after the etching (line-like). By comparing the figures, we can observe that the total amount of SFs is lower for the low-temperature sample and the low temperature also shows the lower SFs length. At high temperatures, the number of short SFs decreased and, at the same time, the SFs became longer.

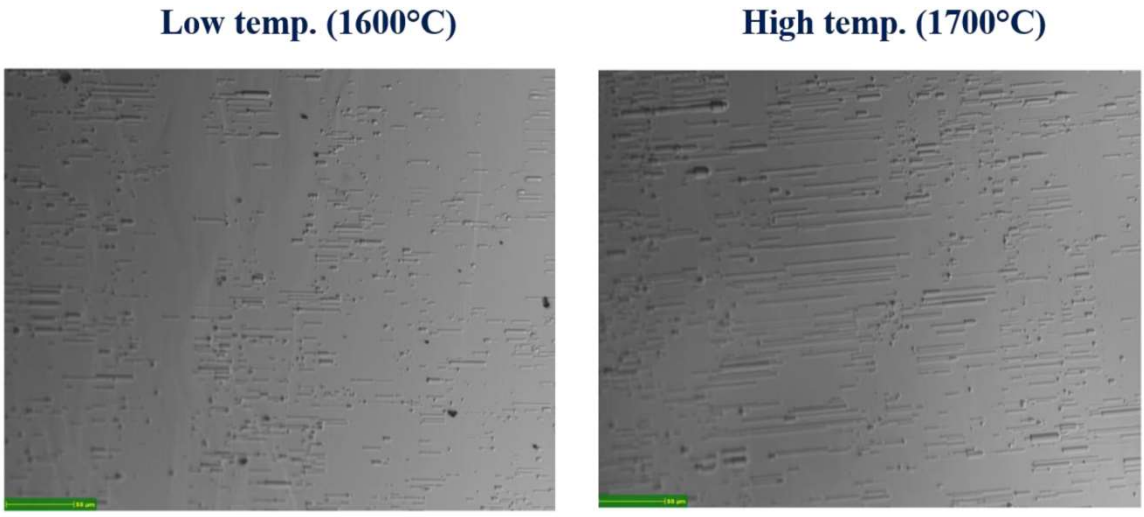

Figure 38 Optical microscope image of the sample growth at 1600 °C (left) and 1700 °C (right) after the molten KOH etching at 500 °C for 3 min. The figure shows the shape of the stacking faults after etching.

The increased amount of SFs at high growth temperatures is the reason why both the XRD and micro-Raman defect evaluation analysis shows better crystal quality at lower temperatures.
In Figure 39, the results of the SFs analysis, based on the previous images, on the 3C-SiC film as a function of deposition temperature, are reported. From the SFs data analysis, an increase of both the SF density (see Figure 39a) and SF length (see Figure 39b) was observed with increasing temperature.

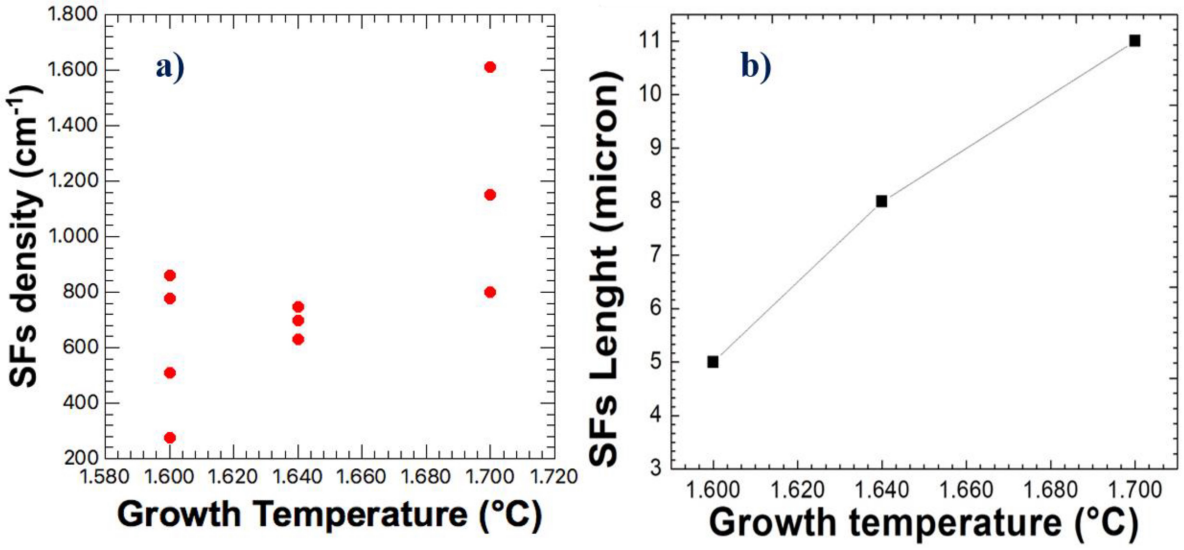

Figure 39 a) Stacking Faults density as a function of the growth temperature obtained by optical observation of the 3C-SiC layer; b) Stacking Faults length as a function of growth temperature. The data were obtained after the molten KOH etching of the 3C-SiC wafer at 500 °C.

In a previous paper [133], it was observed that two kinds of SFs could be distinguished in 4H-SiC. A kind of stacking faults can be "closed" by using high temperature and low growth rate, while the other kind can be closed by using a low temperature and high growth rate. This kind of study has not been performed in the case of 3C-SiC growth, but from these measurements, it seems that the low temperature can help to close the SFs observed in 3C-SiC [133]. Probably for kinetic reasons, the combination of 30 μm/h with 1600 °C allows for a reduction in SFs density with respect to the 1700 °C growth. At a lower temperature, the kinetics of the system produces growth of the defect-free material (without SF) surrounding the SF and allows the closure of the SF on itself. For this reason, at a lower temperature, we observe a lower "long SF" density and the closure of short ones. Probably, by increasing the growth time, in these conditions, we could observe a further decrease of the SFs density. In Figure 40, the PL spectra of the different samples in the wavelength range 1100–1600 nm, are reported. The PL spectra in the usual range between 450 and 900 nm do not show any particular peak structure with the exception of the band-band peak at 540 nm. As reported in previous papers, the SFs in 3C-SiC do not produce a PL peak [113], as in the case of 4H-SiC,

because they do not introduce levels inside the band-gap [116]. Then, the emission in this wavelength range of Figure 40 close to the mid-gap of 3C-SiC, is attributed to points defects, as reported in a previous paper where 3C-SiC had been implanted with different ions and annealed at different temperatures [134]. It can be observed that the signal at 1300 nm is extremely high in the seed layer (standard hetero-epitaxial growth process at a low temperature, 1370 °C, with silicon substrate) without the homo-epitaxial layer on top.

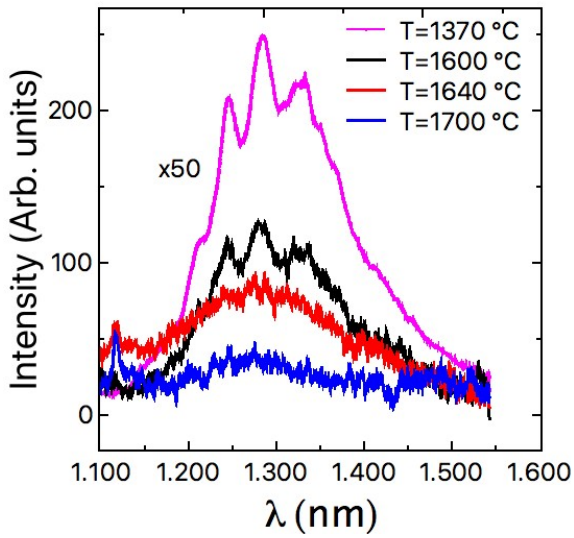

Figure 40. Infrared PL spectra for different grown temperatures. For the seed sample grown at a lower temperature (1370 °C), point defects peak is 50 times reduced in intensity when shown in the same scale.

The PL emission decreases, increasing the growth temperature at a fixed growth rate. A similar behavior that confirms what was observed in Figure 40, has been reported previously also by Kinetic Monte Carlo Simulations (KMCS), and by Schottky diodes leakage current distributions in a previous paper on 4H-SiC [135]. It has been observed that the point defects density depends essentially on the growth temperature and the growth rate. Low growth rate and high temperature decrease the point defects density, while high growth rate and low temperature increase the point defects density.

Micro-Raman of Longitudinal Optical mode (LO) was also performed. From these measurements, it is possible to determine the doping concentration of both the 10 μm-thick low doped region and of the high doped region of the substrate. The obtained results are reported in Table 4. For a fixed value of N, the doping concentration of the fixed layer is $4 \cdot 10^{17}/cm^3$ for all the temperatures. The other LO peak reveals that the doping incorporation change as a function of the temperature, increasing with the temperature.

Growth Temperature (°C)	Low Doping (cm^{-3})	High Doping (cm^{-3})
1600	4×10^{17}	2.1×10^{18}
1640	3.6×10^{17}	3.3×10^{18}
1700	4×10^{17}	6.2×10^{18}

Table 4 Doping concentration.

The interaction between electron collective excitations with the longitudinal optical phonon leads to LO phonon-plasmon coupled (LOPC) mode whose Raman lineshape is particularly sensitive to ionized dopant concentration in inspected material. By fitting Raman LO peak with its intensity equation

$$I(\omega) = S(\omega) Im\{-1/\varepsilon(\omega)\} \tag{7}$$

where ω is the Raman shift, S is a proportionality constant, ε is the dielectric function and $A(\omega)$ is given in ref [136] we were able to estimate samples carrier density. In fact, by entering the nominal 3C-SiC TO and LO vibrational frequency, namely ω_T and ω_L, in the dielectric function expression

$$\boldsymbol{\varepsilon(\omega) = \varepsilon_\infty\{1 + [\omega_L^2 - \omega_T^2/(\omega_T^2 - \omega^2 - i\omega\Gamma)]\} - [\omega_p^2/\omega(\omega + i\gamma)]} \tag{8}$$

where ε_∞ is the infinite dielectric constant, Γ and γ are the phonon and electron damping factor respectively. It is possible to extract the electron carrier density from the expression of plasma frequency

$$\omega_p = \sqrt{4\pi ne^2/\varepsilon_\infty m} \tag{9}$$

where m is the electron effective mass. This technique provides a non-destructive immediate way for electrical sample characterization [137].

Compliance substrates

ISP substrate

The most crucial issues that hinder the use of 3C-SiC are the high number of defects in both bulk and epilayer (such as stacking faults and grain boundaries) and the high bow of the Si wafer after the growth of the SiC. These issues arise from the different lattice parameters and the difference in the thermal expansion coefficient [138,139]. Several different approaches have been proposed to alleviate the above-cited problems. One of the most interesting techniques is the use of compliant substrates. The compliant substrate should be able to better adapt the SiC interface with the Si one and thus reduce the defectivity in the SiC layer grown on Si. Among these approaches, we cite the

use of the SiGe buffer layer [140] or the growth on a patterned substrate as inverted silicon pyramids (ISP) [141] silicon pillars [142] or the use of porous silicon (p-Si) as substrate [143].

The most important improvement in the 3C-SiC on Si quality is due to Nagasawa et al. in early 2000 [144]. They proposed to cover the (001) Si surface with an undulant structure aligned in the [110] direction. This structure is able to eliminate anti-phase boundaries and twins boundaries. Moreover, the same team used the switch-back epitaxy methods to grow a 200 μm thick 6-inch wafer with a remarkable quality [145], and further, they demonstrated a good performance of vertical and lateral MOSFET [146,147]. Nevertheless, despite the obtained improvements, the density of SFs remains quite high and cannot be reduced below 120 cm^{-1} [148,149].

We investigate a particular compliant substrate able to reduce the number of SFs in the epilayer surface. The SFs lie on {111} planes and can interact with each other in several ways. Some of these interactions stop the propagation of SFs in the epilayer and thus reduce the number of defects approaching the surface. We propose a compliant substrate able to promote the self-annihilation of the SFs' mechanism. In particular, we patterned the Si surface with an array of inverted silicon pyramids (ISP) having their squared bases along the [110] direction covering the whole 6-inch (001) Si wafer. We investigated the morphology of the surface and recognized the presence of extended defects, such as anti-phase boundaries (APB), related to the patterning structure. ISP were manufactured on 500 μm thick (001) Si wafer by Deep UV contact lithography. The structures were 700 nm wide square geometries with a 1.4 μm pitch. A thin layer of stoichiometric silicon nitride deposited by LPCVD with a thin layer of thermal Silicon dioxide as a buffer layer was used as a hard mask. The layer was etched by a fluorine-based plasma. The silicon substrate was anisotropically etched by a 45 wt.% KOH @ 70 °C solution.

To bring ISP structures as close as possible, the etching time was extended by exploiting the non-zero etching rate of the KOH on the <111> plane. The gap among the structures after the wet etching was between 60 and 100 nm on the whole substrate.

The growth process was performed at the NOVASIC (Nice France) CVD reactor, using silane (SiH_4), propane (C_3H_8), and H_2 as silicon, carbon precursors, and gas carrier, respectively. The carbonization step (or buffer layer) was performed at 1120 °C and with a C_2H_4 flow rate of 120 sccm while flowing the H_2 gas carrier at 100 slm [150]. Deposition temperature of 1380 °C, a C/Si ratio (the ratio between silicon and carbon atoms) of 1.6, and Si/H_2 ratio of 0.032% were used. The reactor chamber pressure was held at 100 mbar during the entire growth process. The growth rates used were maintained to 1 μm/h, if not specified. In a specific set of experiments, N_2 gas was introduced in the reaction chamber every 10 min during the growth. For a better evaluation of the impact of the ISP substrate on the resulting 3C-SiC films, each growth process was conducted

simultaneously on both ISP and conventional (001) Si. The film thickness was measured by Fourier transform infrared spectroscopy. Scanning electron microscopies SEM are performed with ZEISS SUPRA 35, (Carl Zeiss, Oberkochen, Germany). Scanning transmission electron microscopes (STEM) images are acquired on a ARM200F probe Cs-corrected TEM (Jeol, Tokyo, Japan), equipped with a cold field emission gun (FEG) and working at 200 kV with a nominal point resolution of 0.68 Å.

In Figure 41a, a Scanning TEM cross-section image of 3C-SiC grown on a flat silicon wafer is shown. A huge number of defects are evident near the interface, but moving away from the interface, the defectivity decreases. At about 150 to 200 nm from the interface, there are evident bright lines. The ones laying in the <112> directions are individuated, in literature, to be stacking faults while curved lines are grain boundaries [144,145,146,147,151]. SFs can interact with each other. They can (1) cross each other creating an X shaped defect called Forest dislocation, (2) self-annihilate creating a structure called Lomer dislocation, or (3) terminate on a pre-existing SF creating a "λ shaped defect" [104]. In the case of "λ shaped defect," or in the case of Lomer dislocation, the interaction of SF lead to a decrease in SFs number that finally reaches the surface.

The annihilation of SFs can be promoted by using ISPs as a substrate. In Figure 41b, we propose a pictorial cross-section view of this compliant substrate. Black and white regions indicate silicon and silicon carbide, respectively. Blue lines are SFs. SFs lying, for example, in the (111) plane cross the SF coming from the opposite sides of the pyramid (i.e., lying in the $(\bar{1}\bar{1}1)$ plane) and self-annihilate, reducing the defectivity of the material.

The SFs reduction rate follows a self-annihilation mechanism inversely proportional to SF density. The use of an ISP compliant substrate makes it possible to obtain an important reduction in SF concentration just in thin epilayer growth through its characteristic geometry, which is able to concentrate SFs in small regions, thus increasing the probability of SF annihilation as the mutual closure mechanism is stimulated. Therefore, the ISP substrate turns out to be particularly advantageous. Taking into account that the concentration of SFs reaches a saturation value (due to a trade-off mechanism in the generation/annihilation process) an ISP compliant substrate allows SFs to reach saturation density in shorter epilayer thicknesses with respect to (100), (111) flat substrates, or undulant silicon [141,147].

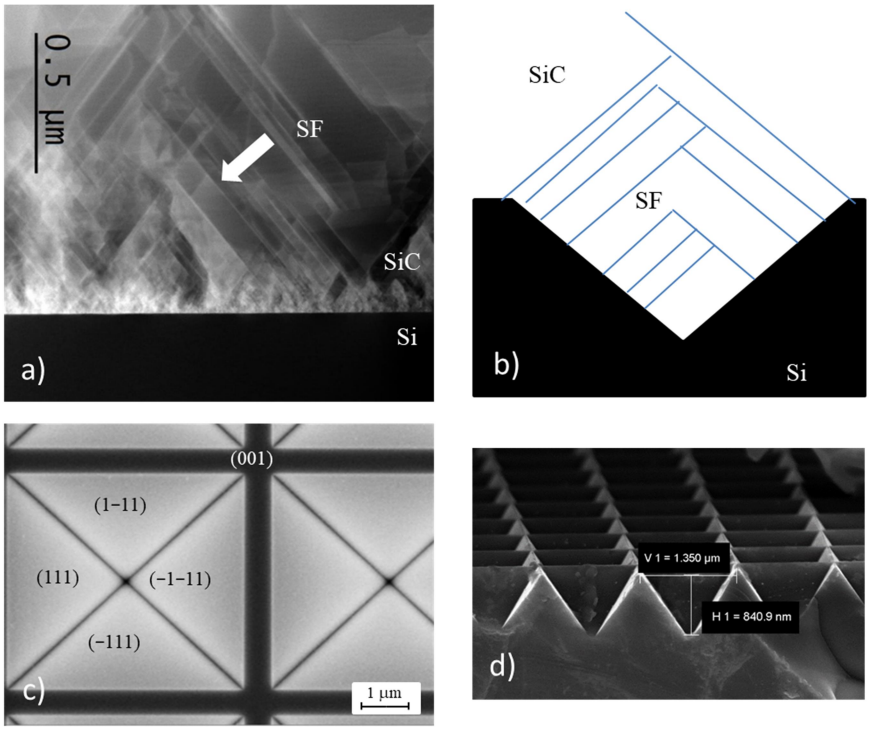

Figure 41. a) Scanning TEM cross-section image of cubic silicon carbide (3C-SiC) grown on a flat silicon wafer. Bright lines indicated by the arrow are stacking faults (SFs); b) pictorial cross-section view of SF self-annihilation mechanism. The black region represents silicon while white SiC. Blue lines are SFs; c) SEM plan view of the 5 · 5 µm^2 pyramid. The four (111) planes of the pyramid are indicated together with the (001) zone between two pyramids; d) Cross view SEM image of 1 · 1 µm^2 pyramid

Following this idea, we investigated the effect of ISP size and pitch on the 3C-SiC epilayer properties. In Table 5, the main structural features (size and pitch) of the manufactured pyramids are tabulated, and in Figure 41c,d, plan and cross-view of the ISP are shown respectively. In Figure 41c, we show, as an example, the plan view of a 5 × 5 µm^2 pyramid. The four (111) faces of the pyramid are highlighted. In the same figure, the (001) zone, between two pyramids, is clearly observed. In Figure 41d, a cross view of a 1 × 1 µm^2 sized pyramid is shown. The thin layer hard mask has been removed by a 15% HF solution. After the long over etching by KOH, the gap among the ISP structures is lower than 100 nm.

Pyramid size	Pitch
5 × 5 µm^2	6 × 6 µm^2
3 × 3 µm^2	4 × 4 µm^2
1 × 1 µm^2	1.4 × 1.4 µm^2

Table 5. Size and Pitch of the Manufactured Pyramids.

Figure 42a shows a plan view SEM image of the 3C-SiC film grown on ISP. The thickness of the SiC layer was 2 µm, and the pyramid size was 5 × 5 µm^2. In this experimental condition, the silicon carbide layer was thin and did not fill the pyramid; thus, a structure with holes formed. In this image, the presence of small black wavy lines between pyramids can be noted. These lines create

small domains or grains between pyramids. As an example, two grains are highlighted in light blue in the same figure. The contour of the grain is a grain boundary (GB).

It is worth noting that the GBs (dotted blue lines) are always connected to the edges and the vertex of the pyramid. A very interesting feature that is depicted in Figure 42a is that the grains contain the (1−11) and (−111) planes (up and down pyramid faces) or (111) and (−1−11) (left and right faces). We are not able to report a domain that contains two adjacent sides of the pyramid as, for example, the (111) and (1−11) planes (left and top faces). The adjacent domains have clearly different natures that have to be related to the mechanism of grain formation.

To give more insight into the nature of the domains, we first consider that in the silicon crystal, where pyramids are fabricated, the four {111} planes ((111), (−111), (1−11), (−1−11)) are equivalent while in 3C-SiC crystal they are not. They, indeed, have different polarities. In 3C-SiC monocrystal, (111) and (−1−11) faces expose (for example) silicon atoms and are called "silicon faces" while (1−11) and (−111) expose carbon atoms and are called "carbon faces".

This means that in a Si-SiC bi-crystal, the silicon pyramid in (111) plane should "couple" with carbon face of 3C-SiC while silicon (1−11) face should "couple" with silicon face. These two interfaces are clearly different in nature and are expected to have different properties as, for example, growth rate.

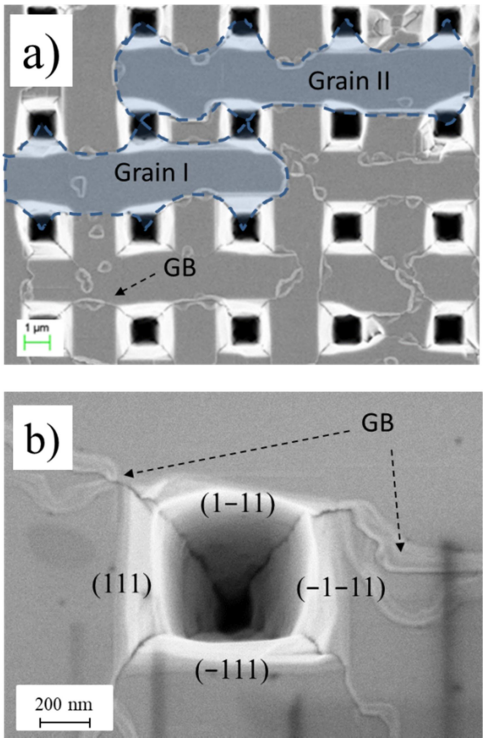

Figure 42 a) Plan view SEM images of 2 µm 3C-SiC film grown on 3 · 3 µm² inverted silicon pyramids (ISP). As an example, the contour of two grains is highlighted in blue; b) High magnification image of the pyramid showing GBs and pyramid faces.

To make it clearer, Figure 43 is drawn. In Figure 43a, the SiC/Si bi-crystal projected along the (110) plane is represented. Here, the interface between SiC and Si realizes a Si-C bond perpendicular to the (1−11) plane (red line). In Figure 43b, the same bi-crystal is projected along the (1−10) plane; here, the interface is realized by a Si-Si bound perpendicular to the (111) plane (red line). It is worth noting that the bi-crystal is the same, and the only difference between Figure 43a,b is the projected plane (i.e., SiC is a monocrystal inside the pyramid).

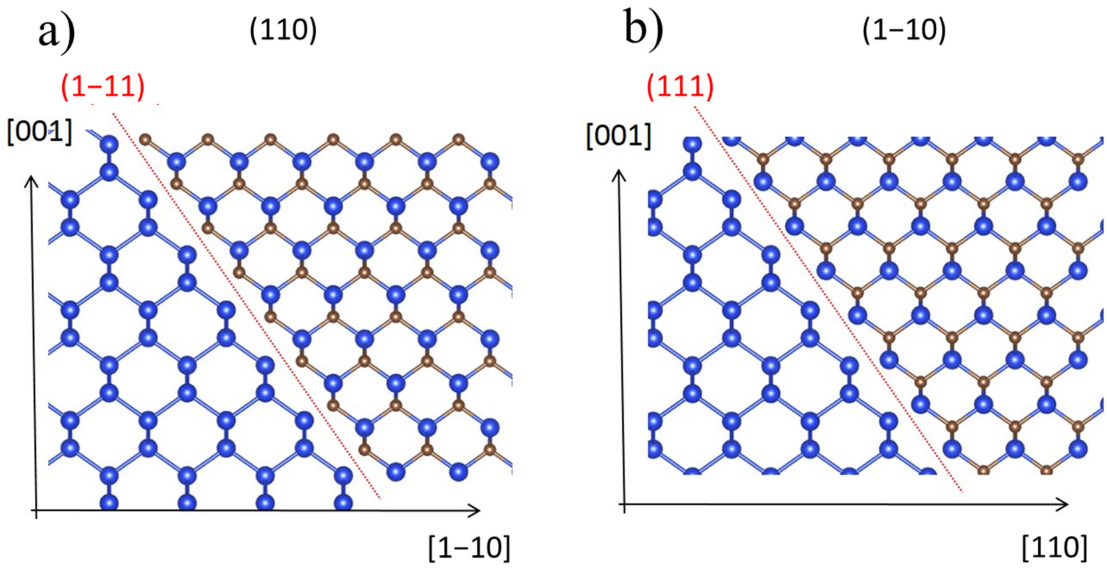

Figure 43. Projections of Si/SiC bi-crystal interface on (110) a) and (1-10) b) planes. The red line represents the [111] plane and interface between Si and SiC crystal.

Interestingly, a closer inspection of Figure 42 reveals that the grains in adjacent faces of the pyramid have similar properties: the morphology of the SiC grown on the (111) and (1−11) are very similar although the two faces should have different polarity and growth rate. It indicates that the growth rate along the two adjacent (left and top) faces was equal (within the experimental errors). The surface free energy of the C faces (300 erg/cm^2) is known to be lower than the free energy of Si faces (2200 erg/cm^2) [152]. Thus, we should expect that the C-face grows faster than the Si-face, and we should expect an asymmetry in the pyramid morphology if a monocrystal is grown on a pyramid. On the contrary, symmetric pyramids with grain boundaries were experimentally observed.

This fact corroborated the speculation that the two adjacent faces ((111) and (1−11)) have the same polarity. Now, we need to be reminded that in 3C-SiC grown on “on-axis“ flat silicon, Si-C diatom can orient in two different ways. This leads to two different grain orientations: rotated 180° around

the [110] direction (flipped upside down). Grain boundaries separating grains having the above-cited property are called anti-phase boundaries (APBs). It is one of the most common extended defects in 3C-SiC grown of Si [153,148,147].

As evidenced in Figure 42, face (111) and face (1−11) belong to different crystals (a grain boundary between these two regions is apparent from SEM image) and have the same polarity (they have the same growth rate). Therefore, APB develops between adjacent pyramid sides.

In this case, at the Si/SiC interface, we should have only one kind of configuration shown in Figure 43. Nevertheless, at this stage, we are not able to distinguish if the interface structure is similar to Figure 43a or Figure 43b. Thus, we performed cross-section STEM images of the interface between SiC/Si on the faces of the pyramid.

High-resolution STEM investigation was performed, and, as an example, an image of the hetero-interface is shown in Figure 44. In this image, the hetero-interface is indicated with a dotted line. On the left, the Si-Si doublet is apparent while on the right typical 3C-SiC ABAC stacking under [110] zone axis is shown, and the Si-C diatom is evident. In the lower right part, a magnification of the Si-C diatom is reported.

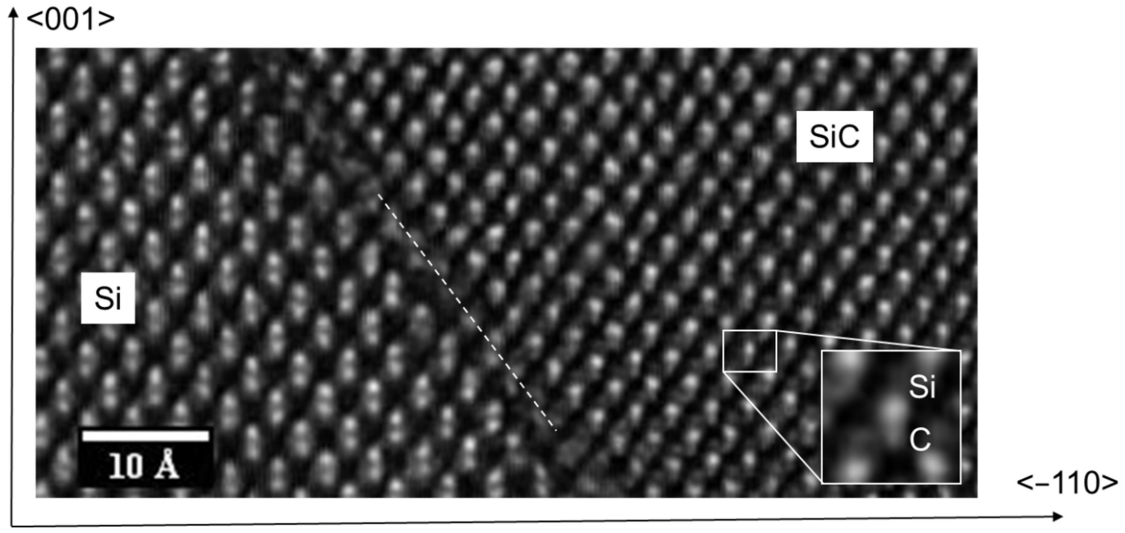

Figure 44. High-resolution STEM image of the heterointerface along the pyramid face. Si/SiC interface is projected on (110) plane. The white dotted line represents the interface between Si and SiC crystals. In the lower right part, a magnification of the silicon and carbon diatom is shown.

This image sheds light on the (111) SiC orientation near the interface and the polarity of the exposed faces on the pyramid. As observed, the more favourable configuration is that shown in Figure 43a. The Si/SiC interface, in both adjacent sides of the pyramid, exposes a carbon face at Si/SiC interface, and thus, we have a Si–C bond perpendicular to the (111) (red line) plane. We can also extrapolate that at the (111) SiC/air interface always expose a “silicon face” when SiC is grown on silicon.

The morphology of the SiC grown on ISP is dependent on both the thickness of the epilayer and the size of the pyramid. After eliminating the holes, the quality of the epilayer was limited by the presence of APB. Indeed, APB is known to be a device killer defect in 3C-SiC [153]. Thus, we focused our efforts on the reduction of APBs. To eliminate these boundaries, we changed the growth conditions. In the first trials, we modified the C/Si ratio during the growth step between 1.2 and 3.15. A sample with less GB density was grown by using a C/Si ratio of 1.6. It is worth noting that for 1.2 and 1.6, the morphology is almost unchanged, but for C/Si = 3.15, a high concentration of GB and small holes were apparent. Raman and XRD results (not showed here) suggest that a high C/Si ratio created carbonic features on the surface that reduces the morphology quality. C/Si ratio of 1.6 was chosen to be the optimized one.

In a second attempt to reduce the grain boundary density, we changed the growth pressure from 80 to 150 mbar, but no remarkable difference could be observed.

Grain boundaries can be highly reduced, increasing the film thickness. It is apparent that the 2 μm thick layer had a higher value of grain boundary length (for unit surface) with respect to the 6 μm thick layer. From plan view SEM analysis, we estimated the APBs covered area as a function of the layer thickness (Figure 45). Although the ISP compliant substrate generates APBs (from the coalescence of 3C-SiC, coming from orthogonal {111} faces), a rapid exponential decay in APBs concentration was achieved after a few microns of growth. In particular, it can be noted that in a 12 μm epitaxy, the APBs coverage was reduced by a factor 20 with respect to the initial layers. This suggests that increasing the layer thickness is an efficient way to lower the APBs concentration leading to uniformly smooth surface sample morphology.

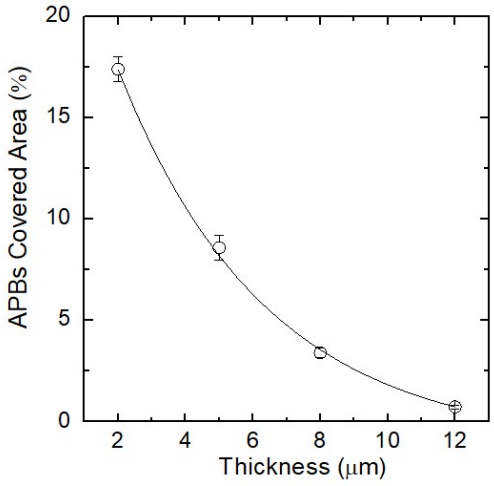

Figure 45. Anti-phase boundaries (APBs) covered area percentages for different thicknesses of epitaxial growth.

Although the quality of the epilayer can be greatly increased by increasing the thickness, the ISP morphology induced the formation of buried voids in the epilayer. These voids are observed in

STEM cross images in a high thickness epilayer and are related to the holes observed in the low thickness epilayer. In Figure 46, we show a cross-section STEM image of 12 µm-thick sample growth on ISP 1 × 1 μm^2. Si pyramids are shown in the bottom of the image in black, while SiC is related to the brighter region. Several straight lines inclined at about 57° are SFs, while curved bright lines are grain boundaries. On top of the vertex of each silicon pyramid, the presence of a void is apparent. On the one hand, the role of the void can be beneficial for the epilayer quality, and it could, in fact, relax the stress related to the Si/SiC hetero-interface and more importantly, can annihilate the SFs nucleating on the Si pyramid side. Indeed, the SFs that nucleated in the {111} planes of the Si pyramid collided with the void and were eliminated. Nevertheless, SFs that nucleated in the top part of the pyramid and in the (001) zone were able to surmount the void and propagate in the sample. As an example, some of these SFs are highlighted in Figure 46. Unfortunately, these SFs can reach the surface.

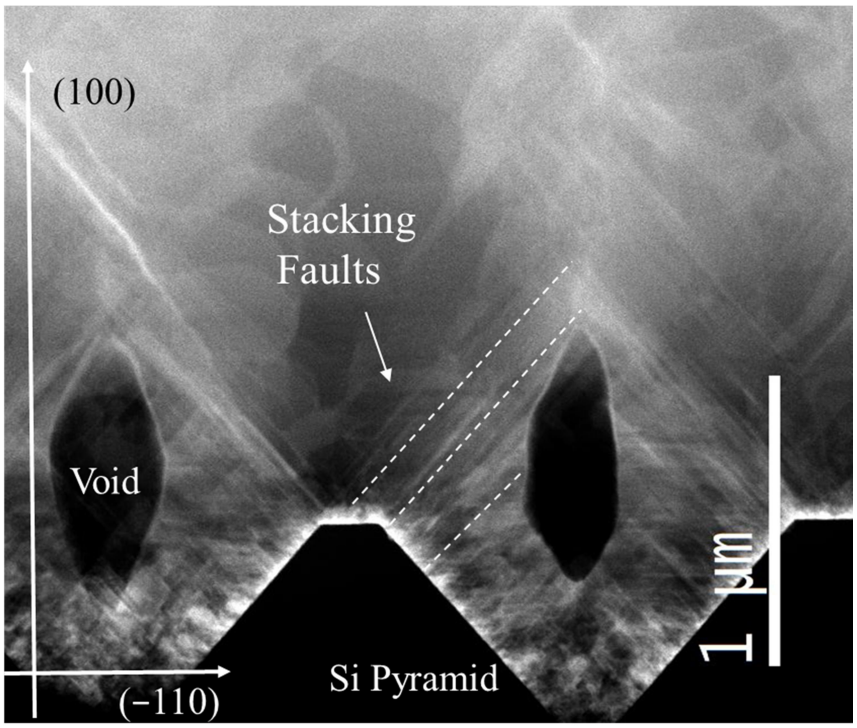

Figure 46. TEM plan view of a 12 µm-thick sample. Stacking faults are indicated together with major crystallographic directions. Si pyramid, voids, and SFs are indicated.

To give more insight into the structure of the void and into the motivation of this formation, a series of new experiments was performed. In such experiments, N_2 gas was introduced into the reaction chamber every 10 min during growth. This creates highly doped markers and allows the reconstruction of the surface front during growth. In Figure 47a, an SEM cross-section of the

pyramid showing the void, and the N^+ markers are shown. Red lines follow the N^+ profile, and they are drawn as a guide for the eyes. In the same image, three black straight lines are drawn: Line 1 is related to the growth of (001) SiC plane, while lines 2 and 3 refer to the growth on (111) plane in two different positions of the pyramid.

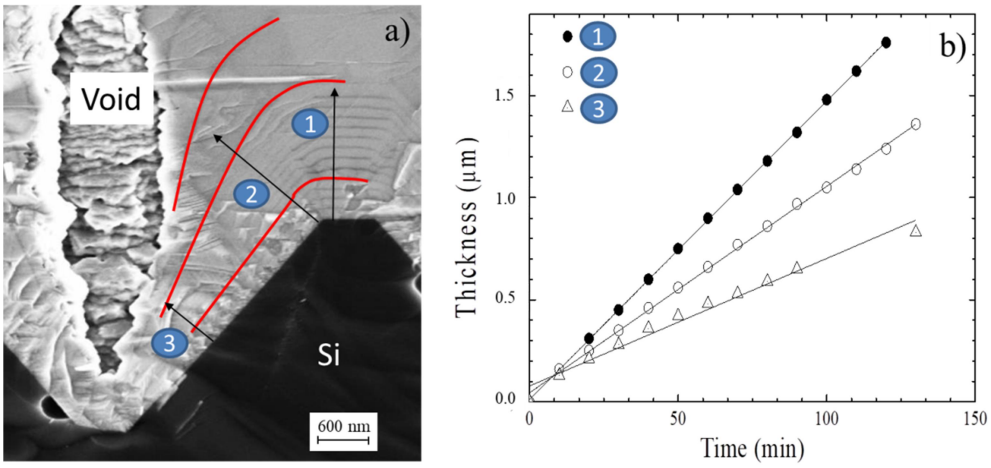

Figure 47. a) SEM cross-section of the pyramid showing the void and the N^+ markers. Red lines are drawn as a guide for the eyes. In the same image three black straight lines are drawn: Line 1 is related to the growth of (001) SiC plane, while lines 2 and 3 refer to the growth of (111) plane in two different positions of the pyramid; b) The thickness of the epilayer as a function of growth time for line 1, 2, and 3 of the figure a).

It is worth noting that it is possible to measure the growth rate along with the 1, 2, and 3 lines. In Figure 47b, we show the thickness of the film as a function of growth time along these lines. The growth rates were 860 ± 4, 600 ± 4, and 370 ± 4 nm/h for 1, 2, and 3 lines, respectively. The growth rate of the (001) was about 40% higher than the growth rate of the (111), as expected. The extremely interesting fact is that the growth rate depends on the position on the (111) plane if it is measured on line 2 or 3. From easy geometrical considerations, a conformal growth could be observed if the ratio between (111) and (001) growth rates is about 0.81. Higher values of this parameter lead to the filling of the pyramid while lower values, to the formation of voids. In our case, the ratio was 0.69 (< 0.81) for line 2, so the formation of voids was geometrically allowed. Moreover, the growth rate in the (111) plane depended on the distance from the vertex; indeed, the nearer the pyramid vertex, the lower the grown rate. (0.69 and 0.43 for line 2 and 3, respectively). This fact could be explained considering that deeper structures suffer from lower gas diffusion, and a reduction in the growth rate is possible. It is also worth noting that at the pyramid edges, APBs develop, and four APBs meet in the vertex of the pyramid (as shown in Figure 42b). It is going to be demonstrated in a separate paper that the growth rate near an APB is highly reduced, creating a furrow on the surface. This should happen even near the vertex of the pyramid, where four GBs

meet. Here, a large reduction in the growth rate is probable. This, thus, increasingly reduces the (111)/(001) growth rate ratio forming the void.

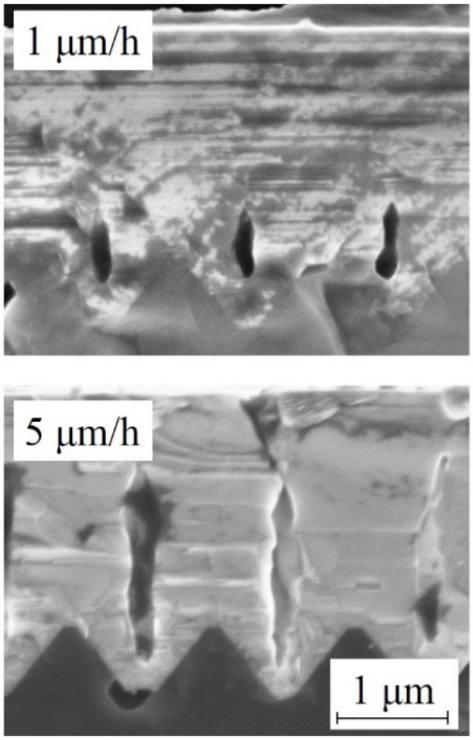

Figure 48. Cross SEM images of the SiC layer grown on 1 · 1 µm^2 ISP obtained with different growth rates. Scale bar is the same for both the images.

As already reported, the formation of the void can be beneficial for the reduction of the defectiveness of the epilayer. Voids, in fact, can annihilate SFs. Control of the void height and width is needed to reduce the SFs. In a new series of experiments, the growth rate was changed, acting on the gasses fluxes. In Figure 48, we show cross SEM images of the SiC layer grown on 1 × 1 µm^2 ISP obtained with different growth rates. This figure demonstrates that we are able to control the void height changing the growth rate. As an example, films grown at 1 and 5 µm/h had a void height of 0.6 µm and 1.6 µm, respectively. In the last case, all the SFs "starting" from the Si/SiC hetero-interface were eliminated.

SiGe Buffer Layer

Another methodology explored refers to the use of a buffer layer between Si and SiC that minimizes the Si and SiC lattice parameter difference and should be able to reduce residual stress in the wafer. Among the different kind of buffer layers, $Si_{1-x}Ge_x$ layer promises to be the most effective [154,155,156,157,158,159,160]. The use of this buffer layer implies that the growth conditions need to be specifically optimized considering the peculiarity of the chosen substrate. Thus, it is necessary to modify the process parameters such as temperature, pressure, ramp time for each step in the

process. Indeed, SiC hetero-epitaxy on Si is a complex process that involves several steps such as etching, carbonization, growth and cool down. Each of these steps must be modified with respect to the standard process. We choose the $Si_{1-x}Ge_x$ composites for several reasons. First, Si and Ge are perfectly miscible and several different composites can be easily achieved. Second, regarding correcting the ratio 4/5, at growth temperature, only a small mismatch on the order of 2% remains between the 4 layers of Si and 5 layers of SiC. Third, for reducing the stress in the SiC epilayer induced by the difference in the thermal expansion coefficients.

Samples comprised a 300 μm silicon (0 0 1) substrate with 2 μm of Si1-xGex grown on top and a final 10 nm thick Si cap. The Si capping layer was needed for the initial carbonization step. From simulations [161], the value of [Ge] for an ideal lattice match at growth temperature was calculated to be around 12% and thus three germanium concentrations were used at 10%, 12% and 15% After the deposition of the Si1-xGex layer and the capping layer, the substrates were diced into 1.5×1.5 cm^2 squares. The growth of the 3C-SiC films was realized using a hetero-epitaxial chemical vapor deposition (CVD) process in a horizontal hot-wall reactor [24] on the 1.5 cm^2 substrates by NOVASIC Silane (SiH_4) and ethylene (C_2H_4) were used as silicon and carbon precursors, respectively, and hydrogen (H_2) was used as a gas carrier. The entire deposition process constituted several steps: “etching”, “carbonization” and “growth”. Each of these steps were further composed of several sub-steps. The etching and carbonization steps were performed at a lower temperature of 900 °C and about 1000–1150 °C, respectively, using a hydrogen flux during etching, and hydrogen and ethylene flux during carbonization. Epilayer growth was performed for 1 h at 1290 °C, which is lower than the melting point of the highest Ge concentration.

In Figure 49a, a schematic of the sample structure is shown. Silicon capping layer thickness is lower than the critical thickness for the formation of interfacial defects at the $Si/Si_{1-x}Ge_x$ interface, because the capping layer is strained and thus matches the $Si_{1-x}Ge_x$ lattice parameter. The strained Si capping layer with the larger lattice parameter of $Si_{1-x}Ge_x$ is used as a seed for the carbonization step, thus reducing the lattice mismatch between Si and SiC. An FTIR spectra of sample 1000 °C, 10% is shown in Figure 49b. The spectrum consists of interference fringes in the spectral region between 1000 and 4000 cm^{-1} and a peculiar peak at wavenumbers lower than 1000 cm^{-1}. From the fitting of the spectra (red line), it is possible to infer information about the SiC layer thickness and its doping. In particular, from the maximum and minimum spectral interference position (for wavenumber higher than 1000 cm^{-1}) we can extract the thickness, while from the shape of the peak at 800 cm^{-1} it is possible to extract the doping concentration.

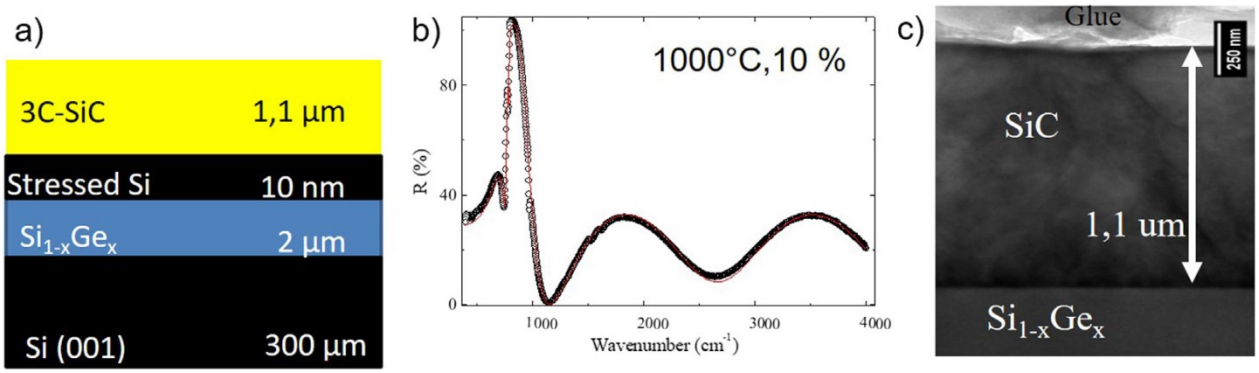

Figure 49. (a) Schematic of the sample structure. It comprises a Si (0 0 1) substrate, Si1-xGex buffer layer (2 µm), Si capping layer (10 nm) and a 3C-SiC layer (1.1 µm). Image is not in scale. (b) FTIR spectra of 1000 °C, 10% in the range between 400 and 4000 cm^{-1}. Fit is also shown in red. (c) Low magnification cross section TEM image of the previous sample. A well defined interface is apparent between Si and SiC. Dark regions near the interface are due to large amount of defects. (For interpretation of the references to color in this figure legend, the reader is referred to the web version of this article.)

Doping concentration results to be lower than 1E17 cm^{-3}. A low magnification cross section TEM image of the sample showing the Si1-xGex interface and the SiC film is presented in Figure 49c. Well-defined interfaces are apparent in the image. Dark regions near the $Si_{1-x}Ge_x$/SiC interface are due to a large defect density, such as stacking faults, twins, dislocations and anti-phase boundaries. Away from the interface, defects reduce and the TEM image becomes brighter. Figure 50 shows the optical microscopy images of samples 10% and 15% grown at temperatures of 1000 and 1150 °C. The 1150 °C, 10% sample surface is covered uniformly with small black dots and unresolved white dots, while sample 1150 °C, 15% has large black dots of diameter 20–40 µm with a peculiar internal structure. White dots are related to the well-known silicon voids at the SiC/Si interface. Samples grown at 1000 °C present very different morphologies. 1000 °C, 15% is quite rough and resembles a polycrystalline sample, while 1000 °C, 10% has a smooth and uniform surface structure. Nevertheless, unresolved white dots are still apparent in both samples at 1000 °C.

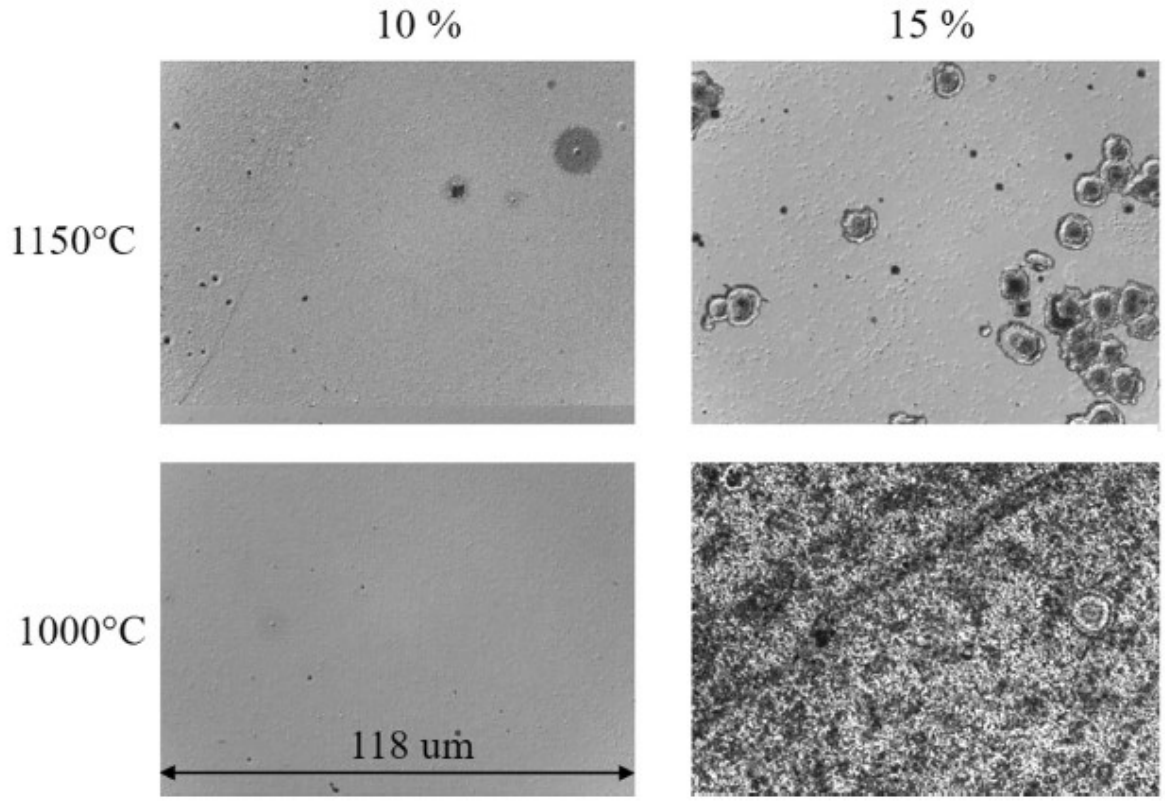

Figure 50. Example of surface morphology optical images. Ge content and carbonization temperature are shown at the border of the image.

A close inspection of 1000 °C, 10% reveals the presence of vertical and horizontal stripes, probably due to extended defects. Sample 1150 °C, 10% has small areas with relatively good epitaxial film and areas where the film is polycrystalline and rough. The sample 1150 °C, 15% presents similar features, but with small grain coarsening. Samples grown at lower temperature (1000 °C) present very large grains for high germanium concentration (15%) and a polycrystalline nature, while a regular and smooth surface for the low (10%) concentration is seen. Micro Raman spectroscopy analyses were conducted in order to understand how the morphology observed by SEM is related to the quality of the samples. We focus on the position of the transverse optical (TO) peak of Si at about 520 cm^{-1} and on the TO and longitudinal optical plasma coupled (LOPC) peaks of SiC at 796 cm^{-1} and 972 cm^{-1}, respectively. Spectral position and intensity of the TO peak in SiC gives information about the quality of the epitaxial film [161]. The TO Raman peak is forbidden for 3C-SiC grown on (001) substrates (in back scattering configuration) due to the selection rules, thus its presence is associated to defects, in particular, twins and poly-crystals. Moreover, a spectral shift of this peak is related to lattice strain caused by intrinsic or extrinsic stress. The inset of Figure 51 shows the TO peak for samples carbonized at 1000 °C. A negligible spectral peak shift was observed and thus a negligible stress was observed for all samples. The same results were observed

for the 1050° and 1150 °C samples. In Figure 51, the TO intensity as a function of Ge concentration is shown for different carbonization temperatures.

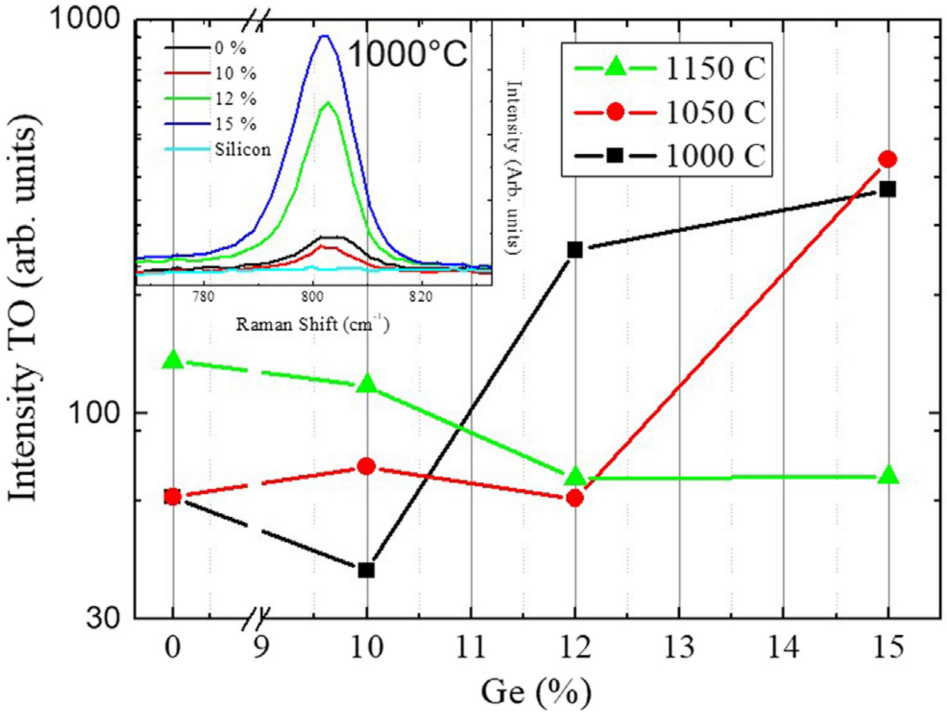

Figure 51. Intensity of the 3C-SiC TO peak as a function of nominal Ge concentration for various carbonization temperatures. Results obtained on bare silicon are also reported. In the inset, spectra of samples carbonized at 1000 °C are reported.

Note the logarithm scale on the y-axes. The samples grown at higher germanium concentration and low temperature (1000 °C, 15%, 1050 °C, 15% and 1000 °C, 12%) have a high TO intensity (approximately 300–400 a.u.). This high intensity is related to the polycrystalline nature of the layer, whereby, the selection rules are broken with increasing TO intensity. For the same three samples a rough surface was observed in SEM images. On the contrary, by using higher temperature and high (15%) Ge concentration, the 1150 °C, 15% intensity decrease to 70 a.u. and higher wafer quality was achievable. Nevertheless, the overall quality of the sample is relatively low due to the presence of “black dots” as observed in the previous SEM images. The best results were obtained for low Ge content, in particular, for low carbonization temperature (1000 °C, 10%) the lowest intensity (40 a.u.) was achieved.

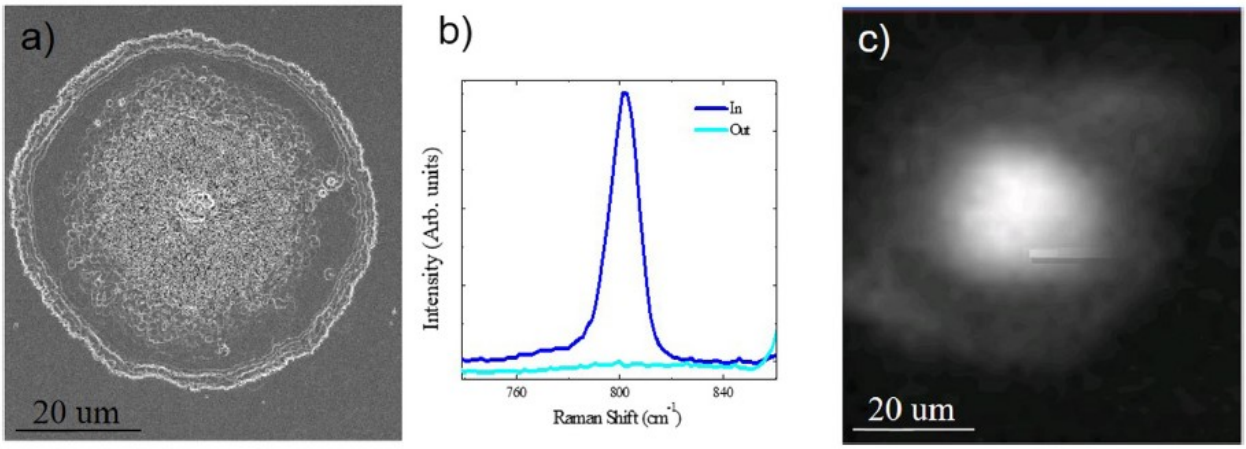

Figure 52. a) High magnification SEM image of a dot observed in the 1150 °C, 15% sample. b) Raman spectra of TO peaks measured inside and outside the dot. c) Raman map of the TO intensity peak (range 790–810 cm^{-1}) for the same dot observed in a).

For the sake of clarity, we show the TO intensity of the SiC grown on bare silicon substrate in the same Figure 51: indicated as 0%. It is worth noting that the TO intensity of the samples grown on bare Si have a larger intensity (about 60 a.u) with respect to the Si counterpart making the sample grown on $Si_{1-x}Ge_x$ of higher quality. Moreover, the 1000 °C, 10% sample shows improvement with respect to all samples fabricated with 0% [Ge]. Information about the electron mobility can be inferred by analyzing the Raman LOPC peak, indeed the spectral position and broadening are sensitive to the free electrons and to the mobility. Considering an electron density lower than 1e17 cm^{-3}, as measured by IR reflectivity spectra, we fit the spectra with the formula reported in [162] in order to evaluate the carrier mobility. Whilst the mobility exhibits low values for 12 and 15% Ge concentration, it is higher than 130 $cm^2/V/s$ for the 1000 °C, 10% sample. This value is also higher than that observed by using a bare silicon substrate, validating the results acquired from the SEM images and the TO Raman spectra. In the same figure, in the inset, we show the LOPC spectra for the samples grown at 1000 °C.

From the preceding analyses it is apparent that best results are obtained for the 1000 °C, 10% and the 1150 °C, 15% samples. Nevertheless, the overall quality of the film for 1150 °C, 15% is decreased due to the presence of the black dots evident in the optical microscopy and SEM image. In order to understand the nature of the black dots, we performed spatially resolved micro-Raman analysis. Figure 52a, we report, as an example, a SEM image of a black dot observed in Figure 50 for the 1150 °C, 15% sample. The image shows a corona encasing a circle with high roughness. In Figure 52b, the Raman TO peaks measured inside and outside the circle are shown and in Figure 52c a spatially resolved image map of the intensity of LOPC peak (acquired in the range 790–810 cm^{-1}). The intensity of the TO peak is higher inside the circle indicating the presence of poly-crystals. The position of the peak has negligible spectral shift with respect to the theoretical value

and thus a negligible stress was observed. An interesting behavior connected also with the presence of dots, is found by analyzing the spectral position of the Si-Si peak (520 cm^{-1}) from the Raman spectra. In Figure 53, we show the spectral position of the Si-Si peak (Si TO mode) as a function of the Ge concentration for different carbonization temperatures. In the same graph, the position of the peak before the growth of the SiC (named before growth) is plotted and the inset reports the spectra recorded for samples carbonized at 1000 °C. It is interesting to note that sample obtained at a lower carbonization temperatures 1000 °C, 12%; 1000 °C, 15% and 1050 °C, 15% show a peak shift more pronounced with respect to what is observed for the "before growth" samples. As an example for 1000 °C, 15% we observe a 502 cm^{-1} peak, while the peak position of the "before growth" 15% is at 510 cm^{-1} and the samples carbonized at 1150 °C (green dots) follow the same trend observed for the "before growth" samples. A shift in this peak can be related to an increased Ge concentration in the surface or to the presence of stress in the Si-Ge layer [163]. It is worth mentioning that samples with a higher Si TO shift (1000 °C, 15%; 1000 °C, 12%; 1050, 15%) have a rough morphology (SEM images, Figure 50) and a high SiC TO intensity (as reported in Figure 51). Furthermore, it is a remarkable fact that a similar shift is found in the micro-Raman maps of the black dots presented in Figure 52. As earlier mentioned, the position of the Si peak can be related to the germanium concentration in the sample and a shift could be interpreted assuming a Ge segregation near the $SiC/Si_{1-x}Ge_x$ interface.

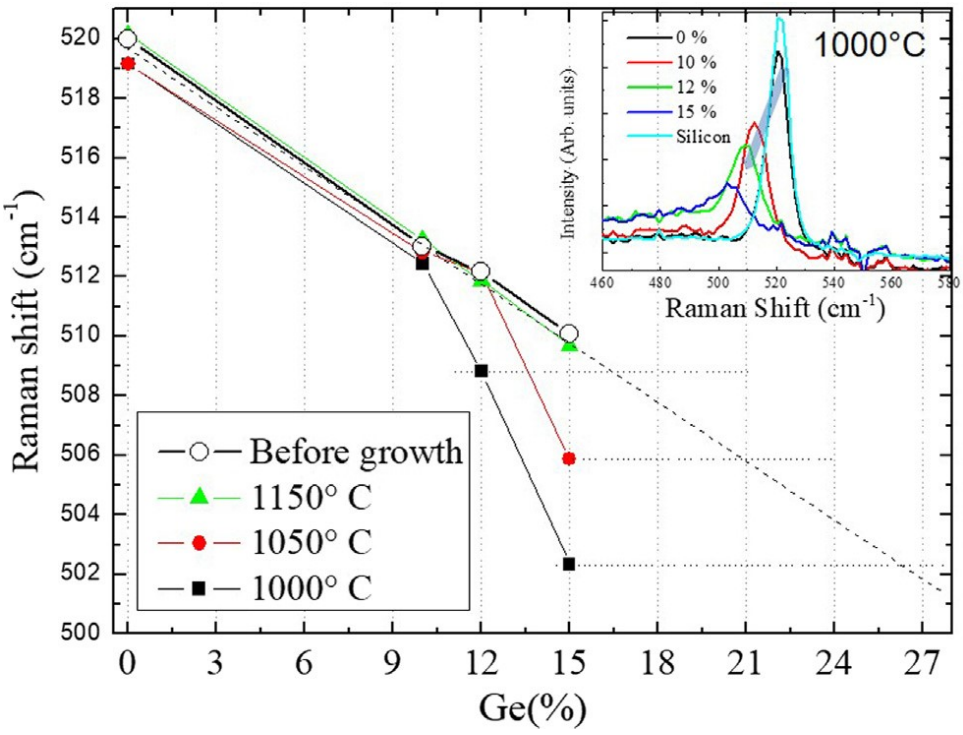

Figure 53. Spectral position of the Si peak (TO mode) as a function of the Ge concentration for different carbonization temperatures. The 1000 °C and 1050 °C (black and red dots) samples shift more than what observed for the "before growth" samples while at 1150 °C (green dots) samples follow the same trend observed for the "before growth" samples. In the inset, spectra recorded for samples carbonized at 1000 °C are showed.

Assuming that segregation occurs, it is possible to calculate the amount of Ge segregated at the interface: it ranges from 17% at the 1000 °C, 12% sample interface to 26% for the 1000 °C, 15% sample. The intersection between the horizontal lines in Figure 53 and the extrapolated dotted line represents the amount of segregated Ge. In order to investigate further the Ge segregation at the SiC/$Si_{1-x}Ge_x$ interface, we performed scanning TEM analysis at the interface.

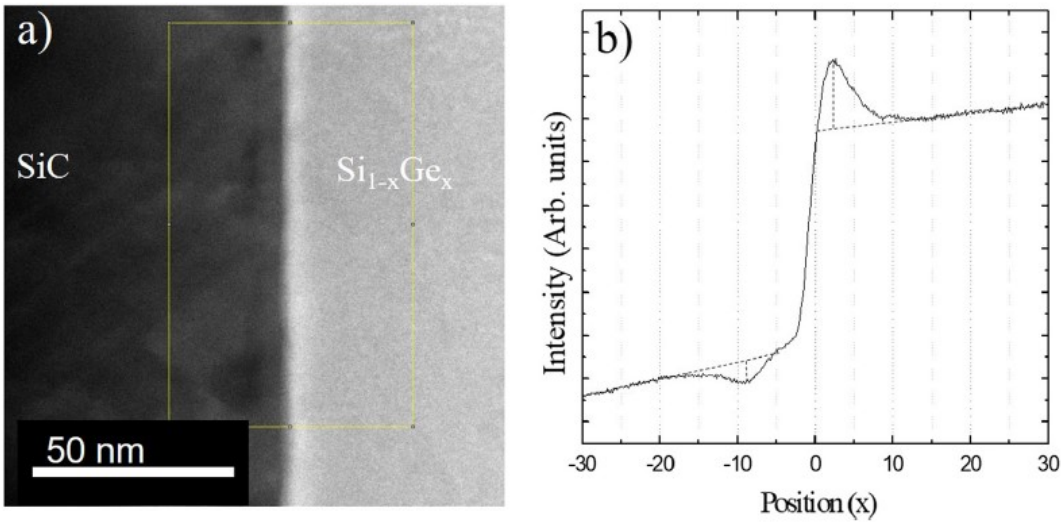

Figure 54. a) STEM cross section of the SiC/Si1-xGex interface for 1150 °C 10%. (b) Intensity profile across the yellow rectangle drawn in the figure (a).

The image is acquired in dark field where the image contrast is mainly related to atomic scattering intensity, i.e to the square of the atomic weight. Thus, dark zones are related to C while brighter zones are related to the presence of Si or Ge. It is worth recalling that these samples have a rough morphology and are polycrystalline. We investigated the Ge content near the interface between $Si_{1-x}Ge_x$ and SiC in samples with low Ge content (10%). A STEM image of sample 1150 °C, 10% is shown as an example in Figure 54a. A brighter zone is recognizable at the interface while a darker region is observed 10 nm under the interface. In Figure 54b, the intensity profile obtained by scanning inside the yellow rectangle of Figure 54a is shown. The Ge content in SiC is negligible, but a brighter region near the interface (on the side of $Si_{1-x}Ge_x$) is apparent. Ge segregation at the interface is thus recognizable in a region that extends less than 10 nm from the $Si_{1-x}Ge_x$/SiC interface. It is possible to give a rough estimation of the amount of germanium content at the interface assuming that the Ge concentration far from the interface is the nominal one (10%). We assume that the contrast in the image (due to scattering) should be the sum of the Si and Ge contributions. Scattering intensity is proportional to the amount of the considered element (Si or Ge) and to the molecular weight squared. Following simple math, we obtained the equation:

$$x_{intf} = \frac{x_{bulk}}{\beta} + \frac{1-\beta}{\beta(\gamma^2-1)} \quad (10)$$

where

$$\gamma = \frac{Z_{Ge}}{Z_{Si}} \quad (11)$$

$$\beta = \frac{I_{bulk}}{I_{intf}} \quad (12)$$

where x_{bulk} and x_{intf} are the extrapolated concentration of Ge in $Si_{1-x}Ge_x$ bulk and at the interface. I_{bulk} and I_{intf} are the intensity observed in the bulk and at the interface, Z_{Ge}, and Z_{si} are the molecular weights of Ge and Si. This formula allows us to estimate the amount of germanium segregated at the interface to be 14% in the 1150 °C, 10% sample (Figure 54) and only 11% in the 1000 °C, 10% sample.

The above results allow us to gain more insight into the growth process. Let's first consider the effect of the Ge concentration in the $Si_{1-x}Ge_x$ layer. High nominal Ge contents (i.e. 15%) lead to the formation of poly-crystals: poly-crystal dots are found at high temperatures (Figure 50, 1150 °C, 15%) while a full poly-crystal surface (Figure 50, 1000 °C, 10%) was observed at low temperature. Decreasing the Ge concentration from 15% to 10%, the morphology improves irrespective of the carbonization temperature as evidenced by the reduction of the polycrystalline area and the reduction of the TO intensity. This behavior can be ascribed to the carbonization process. During carbonization, a high flux of carbon precursor reaches the surface of the $Si_{1-x}Ge_x$ substrate forming a thin and very defective layer of SiC: the carbonized layer. While Si and Ge are perfectly miscible, Si and C have SiC as the only stable phase and Ge results immiscible (solubility is on the order of 10^{16} ion/cm^2) in SiC. Thus, as SiC is formed on the surface of the wafer, the germanium contained in the first carbonized layer is "pushed down" into the $Si_{1-x}Ge_x$ layer giving rise to the segregation observed with TEM and Raman. Segregation is more efficient as the Ge amount is increased.

As segregation reaches a critical value poly-crystals come out. This phenomenon appears on the entire surface for the 1000 °C, 15% sample while it is confined to polycrystalline dots in the 1150 °C, 15% sample. The difference between these two samples is due to the dependence of the critical Ge concentration at interface with the carbonization temperature. More complex is the effect of the carbonization temperature because of the interplay between contrasting effects that affect the amount of Ge segregated at the interface. The higher carbonization temperature enhances the specimen diffusion and it can:

(1) allows the diffusion of Ge inside the $Si_{1-x}Ge_x$ layer, thus decreasing the segregation at the interface.

(2) enhances the diffusion of C in the carbonized layer, thus realizing a thicker carbonized layer and "pushing down" more Ge in the $Si_{1-x}Ge_x$ layer and thus increasing segregation. The result depends on the interplay of these two contrasting effects.

Let's now discuss this effect on the 15% samples. Increasing the temperature, the sample morphology improves, indeed samples have a complete polycrystalline surface at 1000 °C and only polycrystalline dots at 1150 °C. This behavior can be explained considering that at low temperature (1000 °C) Ge diffusion is inhibited (the diffusion coefficient of Ge in Si is 10^{-8} $\mu m^2/s$ [28]) while high temperature (1150 °C) allows Ge to diffuse (the diffusion coefficient 10^{-6} $\mu m^2/s$ [29]) into the $Si_{1-x}Ge_x$ layer reducing segregation at the interface. A reduced segregation induces an improvement in the sample quality and a reduction of the amount of polycrystals realizing only small polycrystalline dots (black dots of Figure 50, sample 1150 °C, 15%). Once segregation occurs, the polycrystalline SiC seeds are formed at the interface and during SiC growth (at 1290 °C) Ge is allowed to diffuse among SiC grains forming Ge nanocrystals. The shift in the Raman peak observed in Figure 53 is ascribable to the high content of Ge (and Si) in the SiC layer. A different behavior is observed in the 10% samples. In these samples segregation is less pronounced and an opposite behavior (with respect to the 15% ones) is observed: segregation occurs at higher temperature (1150 °C, 10%) while at low temperature (1000 °C, 10%) it is negligible. Indeed, Ge content, at the interface, is estimated to be 14% or 11% for high and low carbonization temperature. We can consider that higher temperatures enhance the diffusion of C in the carbonized layer making the carbonized layer thicker [30]. This effect increases the Ge concentration "pushed down" (segregated) at the interface. Sample carbonized at high temperature (1150 °C, 10%) have small black dots, rough surface (Figure 50), higher TO intensity (> 100 a.u.) and low mobility (< 100 $cm^2/V/s$) than the lower temperature counterpart (1000 °C, 10%). Here diffusion of Ge in $Si_{1-x}Ge_x$ layer is less important being driven by a concentration gradient that is negligible in this case.

In conclusion, the effect of the SiGe buffer layer on SiC growth was investigated. Morphology and the overall film quality strongly depends on the carbonization temperature and the Ge concentration. In particular, we found that these two parameters affect the Ge concentration in a region ten nm from the interface because of a segregation process. We found that non-optimized Ge segregation gave rise to polycrystalline dots or a full polycrystalline surface. Nevertheless, good crystal quality was observed for 3C-SiC grown on a 10% $Si_{1-x}Ge_x$ buffer layer and at low carbonization temperature (1000 °C). Moreover, by finely tuning the carbonization temperature and the Ge amount in the bulk, it was possible to achieve superior quality with respect to a film grown on bare silicon. This approach demonstrates the use of a buffer layer can be a real methodology to achieve high quality 3C-SiC epi-layers on silicon.

Chapter 3. Furnace annealing and laser annealing strategies on high dose ion implantations

In this chapter an analysis on P implanted 4H-SiC samples undergone furnace annealing as well as innovative nonequilibrium annealing techniques will be presented. A particular attention is given to the implanted dopant concentrations of interest for the fabrication of 4H-SiC MOSFET device and in this sense an analysis on source P implanted 4H-SiC samples undergone double step annealing will be presented. Dislocation loops, the main type of extended defects, will be investigated together with stress phenomena recorded after the post implantation annealing. Pioneering Excimer pulsed laser annealing results on implanted epitaxial layers with single P implantation and double P and Al implantations will be delivered and compared with the thermal annealing treatments.
A detailed portrait of the laser energy recovery thresholds will be reported with particular care on surface damage minimization strategies. Electrical tests accompanied by temperature profile simulation will prove remarkable P activation on irradiated site.

Introduction

Powere semiconductor devices are key components for powere conversion systems. Silicon carbide (SiC) has received increasing attention as a wide-bandgap semiconductor suitable for high-voltage and low-loss power devices. Through new improvements in the crystal growth and SiC processing technology, the manufacturing of medium-voltage (600–1700 V) SiC Schottky barrier diodes (SBDs) and powere metal–oxide–semiconductor field-effect transistors (MOSFETs) has begun. However, dopant diffusion rates are slow even at temperatures as high as 1800 °C so that SiC cannot be doped effectively by thermal diffusion. Therefore, selected doped areas can be created through ion implantation. However, the common drawback of ion implantation is the generation of lattice disorder. Typically, post-implantation annealing at high temperature (T > 1600 °C) is used to activate the dopant and decrease the defectiveness of the ion implanted area, thus increasing the crystal quality. Dopants activation in SiC is a very debated topic. Although in literature it is not rare to come across high activation values, these processes are strongly dependent on dopant solid solubility [164] so that high dose implants result in low activations percentages after thermal equilibrium processes [165]. The realization of MOSFET selected doped areas, such as the source

and body region, are achieved through ion implantation. In particular MOSFET's n-type source region occurs through P ion implantation, while the p-type body region is obtained using Al. The use of these processes involves the generation of a considerable implantation defectiveness, which is only partially recovered by conventional thermal treatments. Thermal annealing is also involved in V_C generation under standard thermal equilibrium processes so that new non equilibrium methods based on short time annealing duration are required. In this work we will use Raman scattering and photoluminescence (PL) together with transmission electron microscopy to examine a series of P implanted 4H-SiC wafers that underwent a one step and a two step annealing processes and the doping activation from Raman spectra longitudinal optic mode will be extracted.

A comprehensive description of thermal annealing dynamics is provided by transient model activation [164], which states that the initial activation speed for both donor and acceptor impurities is extremely high and decreases rapidly with time. Indeed, rapid thermal annealing systems, are able to obtain high dopant incorporation eluding the usual impurity deactivation due to solid solubility lowering during cooling ramps.

Laser irradiation and the consequent annealing offer two fundamental new functionalities to the class of thermal processes: (a) the heating of localized regions of the specimen while the rest of the sample remains cold; (b) the access to far-from-equilibrium conditions allowing to overcome the limits imposed by solid solubility in pure and composed materials.

In particular, laser annealing technique counts on heating ramps as high as 10^9 K/s and allows to obtain much higher temperatures than conventional processes.

After first Hishida [166] and Ahmed's [167] laser annealing attempts on 4H-SiC, Tanaka [168] pointed out that 4H-SiC melt phase annealing was not a suitable post implant treatment due to the impossibility of obtaining full 4H-SiC epitaxial regrowth. Consequently excimer laser pulses under sub-melting condition were proposed to perform a sequence of rapid thermal annealings in the ns time regime. Boutopoulos [169] confirmed the viability of this method carrying out a structural micro-Raman analysis of multishot laser annealing on Al implanted 4H-SiC. He observed how Nd:Yag (355 nm) multiple irradiation method was able to significantly recover reflectivity signal intensity in the Restrahlen band. However, TEM analysis showed the formation of polycristalline structure after laser annealing process. Similar results are stated by Mazzamuto [170], who claims to obtain full epitaxial regrowth from SiC melting phase, though TEM analysis show polycrystalline lattice recovery after ion implantation.

The aim of this work is to offer a pioneering characterization of laser annealing effects on implanted SiC with particular concern to phase separation energy thresholds related to SiC non-congruent melting. We perform an effective study of the exploitable XeCl laser energies, as well as an atomic

scale characterization that confirms the complete 4H polytype maintenance under sub-melting regime. Electrical characterization will confirm the validity of this technique which allows to obtain low resistivity and high activation levels.

Experimental

A 6 μm epitaxial layer was grown on (0001) 4° off-axis 4H-SiC through low pressure hot wall chemical vapour deposition, and doped with N at a concentration of 10^{16} at/cm^3. P ion implantation was performed at 550 °C with energies between 20 and 200 KeV, and fluences ranging from 10^{13} to 10^{14} cm^{-2} in order to obtain an almost uniform doped layer, 200 nm thick, with a concentration of 10^{20} cm^{-3}. Following, isochronal (1 hour) thermal annealing were carried out at 1650 °C, 1700 °C, 1750 °C, followed by second thermal treatments at 1500 °C for times between 4 h and 14 h. During annealing processes graphitic capping layer was deposited on sample to avoid surface step bunching. In the double implanted sample a further multistep implantation was performed with Al doses between 10^{12} and 10^{13} cm^{-2} at 400 °C and annealed at 1650 °C for 30 min. The latter underwent a shorter annealing time with respect to single source implant samples to reduce the dislocation loop fractional area [47].

After ion implantation, the wafer was cut into several squares using a diamond tip to obtain different samples on which we performed the annealing tests. In order to eliminate any impurities on the surface, the samples were subsequently bathed in isopropyl alcohol and dried by compressed air jet. Laser treatments were carried out through a Lambda Physics LPX 300 XeCl pulsed excimer laser (λ=308 nm) with 40 Hz repetition rate, whose beam intensity is tuned by a MicroLas Lasersystem attenuator unit, which accomplishes the variation of laser pulse energy by almost two order of magnitude in steps of 1%. The beam is then sent to an homogenizer, which divides the laser beam into many sections (splitter optical element), superimposing them in a 2-D matrix of secondary beamlets that overlap in the focal plane of the condenser lens, called the focal plane, so that the final beam assumes the desired dimensions (condenser optical elements), local spatial fluctuations of the beam energy are averaged due to the overlap of different portions of the input beam. The samples were so irradiated by a 1 mm x 20 mm uniform intensity profile radiation inside a chamber under helium atmosphere at a pressure of $1x10^{-2}$ mbar. Substrate holder inside the chamber was heated at a temperature of 580 °C and a mobile stage allowed to implement an irradiation process until 1000 shots/point.

Further test were performed using a graphitc layer superimposed on SiC surface. Speciality Coating Systems model P6700 semiautomatic spin coater with a DV-1000 data access unit was used to coat the sample with the photoresist. The photoresists used were Microposit s1813+s1805. Soft baked at 90°C for 30 min was then performed. The resists were pyrolyzed in a closed tube furnace in a forming gas atmosphere 95% N_2,5%H_2 at 950 °C for 10 min to achieve on a group of samples 90 nm of graphite layer and on another 180 nm graphite layer. Some other samples underwent 1100 °C treatment for 20' with final graphite thickness of 180 nm. By means of optical interferometry final 90 and 180 nm thick layer formation was controlled on double P and Al implanted SiC epitaxial layer. For comparison, some samples were left uncoated and another one underwent heat treatment at 1650 °C for 30 min. Once irradiated by means of a XeCl laser source (λ =308 nm) with 40 Hz pulse and 1000 shots/point, graphite was removed through room temperature oxygen plasma attack. Electrical measurements using Circular Transfer Lenght Method (CTLM) allowed to obtain the sheet resistance values of treated samples. To asses samples sheet resistance, CTLM patterns with circular geometry (diameter of the inner circle was 200 μm, and the distance between inner and outer circles was , 10, 15, 20, 25 μm) were defined using photolithography. As a contact metal, 150 nm thick Ni was deposited on the patterned SiC substrate using an e-beam evaporator. After the lift-off process, rapid-thermal annealing (RTA) was performed at 950 °C for 1 min in N_2 ambient in order to stimulate a reaction between Ni and the 4H-SiC substrate. The effectiveness of laser treatments was verified by micro-Raman and Room temperature PL, carried out with a He-Cd laser source (λ=325 nm) and a Horiba Jovin Yvon LabRAM HR spectrofluorimeter with a 1800 l/mm grating. Structural investigation was performed using TEM microscopy on a JEOL JEM 2100 TEM-FEG operating at 200 kV microscope equipped with a Gatan image filter for electron energy loss spectroscopy (EELS) . SEM images are performed with ZEISS SUPRA 35.

Convectional Annealing Processes

The PL spectra (λ=325 nm, P=5 mW) of implanted samples after annealing at different temperatures are reported in Figure 55. These spectra show two peaks, a narrow one related to the 4H-SiC bandgap at 390 nm and another one coming from defectiveness and peaked at 488 nm with 175 nm full width half maximum (FWHM) . The bandgap signal is, in particular, lower by about a factor 6 with respect to the PL response coming from the sample not subjected to annealing treatment (pink curve). This consistent band to band signal reduction is due to recombination phenomena with the energy levels localized in the bandgap not present in the epitaxial sample.

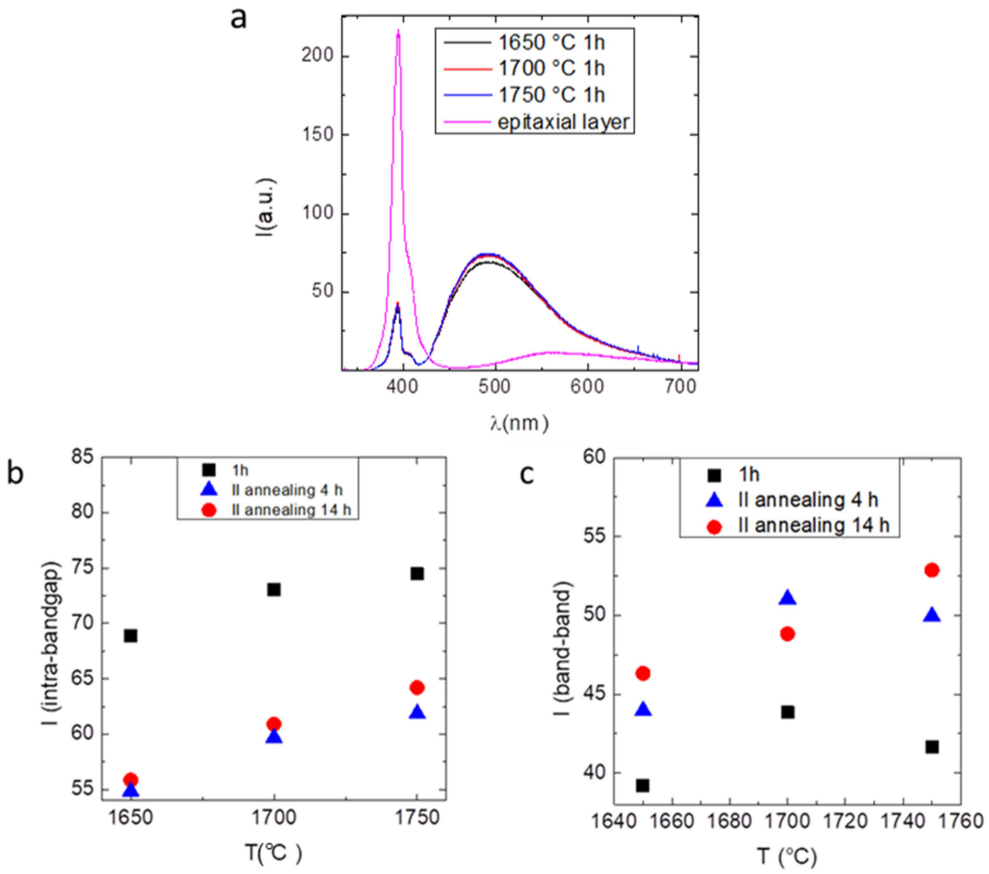

Figure 55 . PL spectra of the 1650 °C, 1700 °C and 1750 °C annealed P implanted samples, (b) PL intra-bandgap peak intensities, (c) PL band-band peak intensities for all annealed samples.

The presence of the defect peak can so be associated with crystallographic damage, which introduces optically active intra-bandgap energy levels [171].

The intensity of this peak increases with increasing the temperature of the first annealing process; in particular, at 1750 °C its intensity is 7% higher than at 1650°C. This behavior is mostly associated to a rise in the point defect density during the first annealing process [38], so that we can infer the defects density corrispondent to intra-bandgap energy level grows with temperature. Furthermore, the intensity of the PL peak changes after the second low temperature annealing, and in Figure 55b this intensity is reported versus the temperature of the first annealing for different values of the second annealing time. The second annealing process at 1500 °C (for times between 4 h and 14 h) lowers the intra-bandgap 480 nm PL intensity peak in a range between 13% (1650 °C) to 20% (1750 °C) with respect to that underwent 1 h trial. This might be due to a reduction in the carbon vacancies concentration [Vc] in the implanted region [172]. Indeed, according to defect kinetics, during high temperature annealing, thermal generation of Vc is the dominant process while at moderate temperature the recombination of Vc with carbon interstitials present in the implanted area or injected from the graphitic capping layer appears to prevail [38]. Moreover, this effect is accompanied by a slight enhancement of the band to band PL signal (Figure 55c) which confirms a recovery of the crystalline structure.

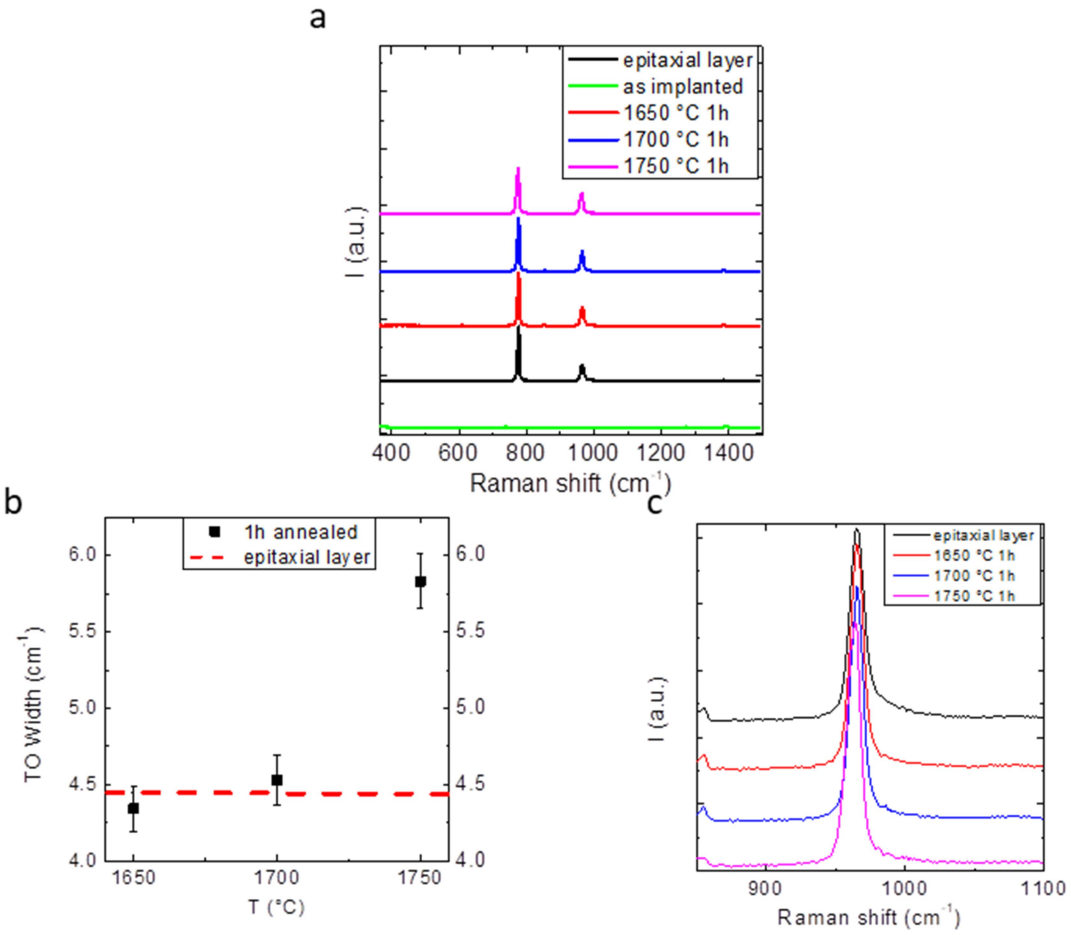

Figure 56. a) Raman spectra, (b) TO width and (c) LO Raman peaks for 1650 °C, 1700 °C and 1750 °C annealed P implanted samples.

In Figure 56a micro-Raman spectra from the three implanted samples after first HT annealing are reported: they show sharp Raman lines of tranverse optical (TO) modes at 776 cm^{-1} and longitudinal optical mode (LO) at 964 cm^{-1}. In Figure 56b TO mode Raman width versus post-implantation annealing temperature is reported.

The as grown sample TO curve shows a 4.4 ± 0.1 cm^{-1} width. After P implantation and annealing the TO width moves to 4.3 ± 0.1 cm^{-1} and 5.8 ± 0.2 cm^{-1} for 1650 °C and 1750 °C respectively. Furthermore, the broadening of the TO peak in the 1750 °C annealed sample highlights the worsening crystal quality due to point defect creation in the lattice and is accompanied by a downshift in the TO mode frequency, indicating an implantation induced tensile stress with respect to the supposed stress free as grown sample [173].

The persistence of an extended defect network of almost orthogonal traces made by extra-planes with dislocation loops (DLs) was also observed in the projected range of the implanted area Figure 57a. Most of extra-planes are aligned parallel to the surface while a smaller percentage exhibits a perpendicular habit plane. The formation of aggregates and extended defects is one of the consequences of the ion implantation process. This interstitial aggregation process can be observed

within the implant region and is correlated to the implant dopant concentration. In particular, within Figure 57a it is evident how the density of the defects increases in correspondence of the maximum concentration of the implant, as the overlap between the data coming from the Secondary Ion Mass Spectroscopy (SIMS) analysis and the cross TEM shows. The high resolution shown in Figure 57b reveals the structure of one of these extended defects as an extra-plane incorporated within the basal plane.

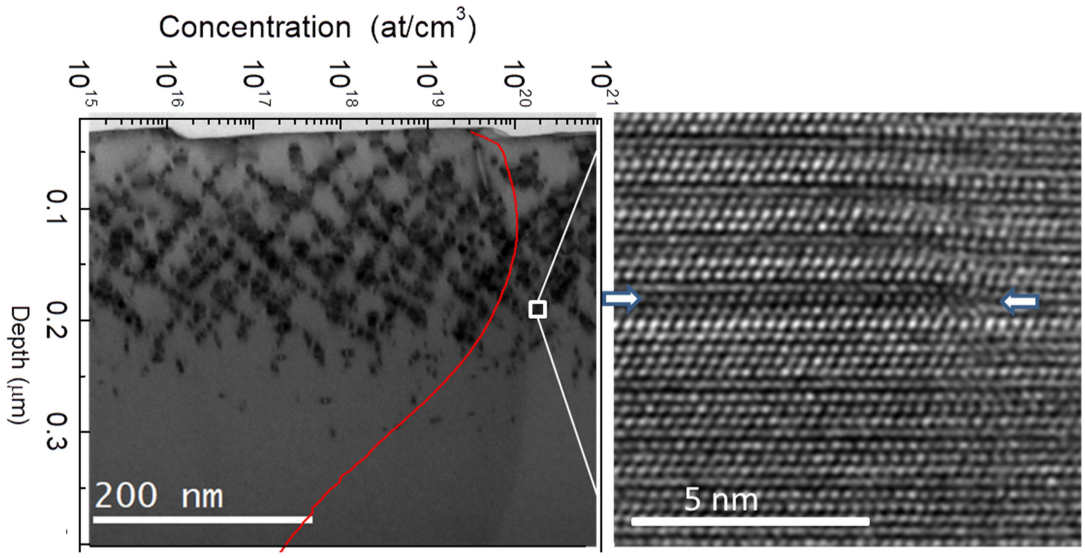

Figure 57 a) XTEM of 1750 °C annealed source implant sample undergone double step annealing acquired under Z.A=[11$\bar{2}$0]. B) HRTEM showing an extraplane inserted in lattice implanted area.

This behavior, frequently found within the implanted region, is consistent with definition of extrinsic loops characterized by a Si-C doublet which varies the normal stacking of the crystal by introducing 3C-like stacking portions together with stressed regions around it as shown in
Figure 57b. Several papers have previously reported (0001) prismatic loops in (0001) 4H-SiC crystals following post implantation annealing processes [174,175,176,177]. However, many defects lie on planes other than the basal plane and have been investigated in this work. To characterize extended defects morphology, an analysis was carried out using the invisibility criterion represented by the g·b rule.
Figure 58a shows the diffraction pattern under [10$\bar{1}$0] zone axis. This type of analysis is useful to provide a characterization of the burger vector and consequently a classification of the dislocation.

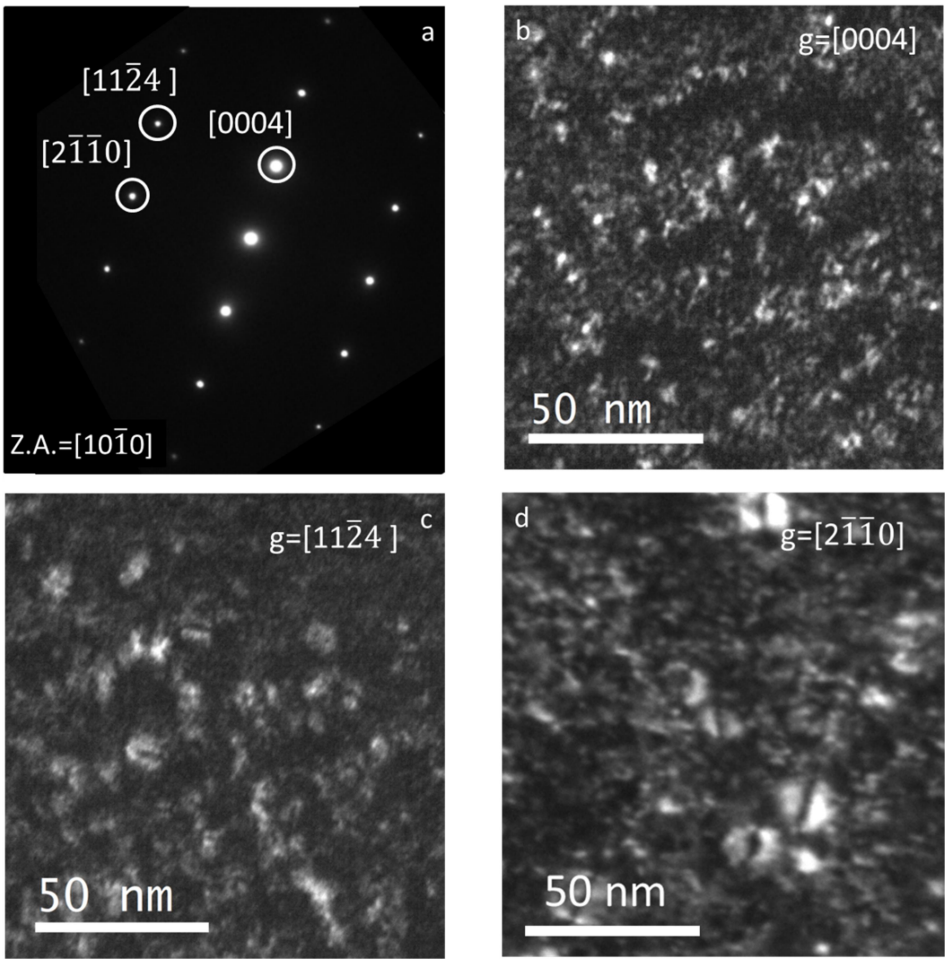

Figure 58. Weak beam XTEM micrographs on various diffracting conditions of (0001) 4H- SiC after implant and 1750 °C annealing for 1h, under the zone axis [10$\bar{1}$0]. b) g=[0004], c) g=[11$\bar{2}$4], d) g=[2$\bar{1}\bar{1}$0].

Figure 58 represents a defect network assembly taken from different diffraction conditions. When the weak beam dark field condition is realized under g = [0004] (Figure 58b), several regions with weak contrast can be seen along the whole implant. This contrast seems to come from portions of stressed regions and seems widespread throughout the implanted area and is related to crystal deformation surrounding extra plane lying in (0001) plane. When weak beam dark field analysis is performed on direction [11$\bar{2}$4] as in Figure 58c, a slight contrast is visible for some of the distorted regions with extra-plane lying on the basal plane. When the spot g=[2$\bar{1}\bar{1}$0] is used to acquire the image of the implant, a subtle signal comes from the dislocation loops with an habit plane normal to the basal plane (Figure 58d). To further configure defects, plan view analysis was performed. Figure 59 shows plan view sample under different diffraction conditions. The sample was subjected to wet oxidation under 10 hours at 1150 °C so as to remove most of the projected range of the system where the defects concentration is higher [178]. In Figure 59a the diffraction pattern with the directions in which the sample was investigated is reported. Note that when the sample is

investigated along the direction represented by the diffraction spot g = [11$\bar{2}$0] as in Figure 59b, only the distorted regions around the extraplane that shares the same direction are visible.

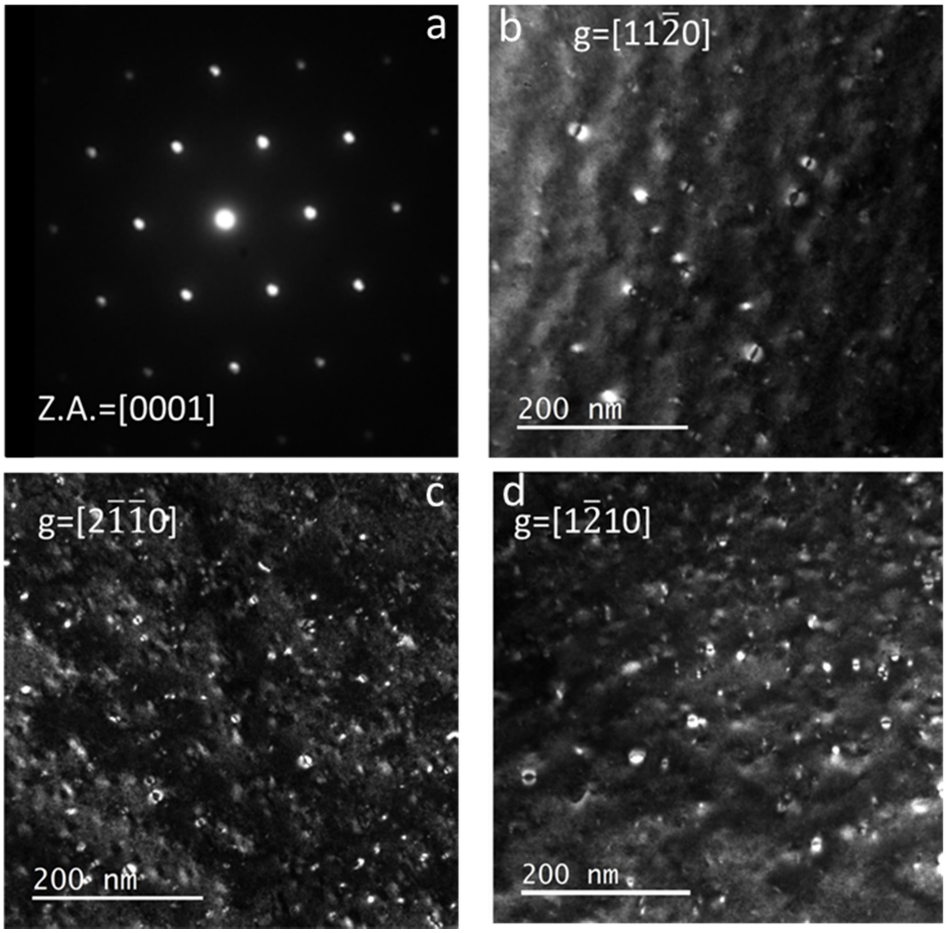

Figure 59. Plan view TEM extracted from 4H-SiC, Weak beam PVTEM micrographs on various diffracting conditions of (0001) 4H-SiC after implant and 1750 °C annealing for 1h, under the zone axis [0001]. b) g=[11$\bar{2}$0], c) g=[2$\bar{1}\bar{1}$0], d) g=[1$\bar{2}$10].

Figure 59c and d acquired with respect to the diffraction spots g = [2$\bar{1}\bar{1}$0] and g = [1$\bar{2}$10] show the same behavior, with a single direction of distortion selected with respect to the extraplane which remains invisible. From these TEM investigations it is evident that (0001) and (11$\bar{2}$0) loops are the dominant extended defects in all P implanted samples and are consistent with prismatic loops with Burger vector normal to the lying plane.

Using a theoretical analysis based on the Ising model it is possible to observe a stress configuration present within the implanted SiC layers. The total energy of a n-layer system can be written as

$$nE_0 = -\sum_{i,n} J_n \sigma_i \sigma_{i+n} \quad (13)$$

where E_0 constitutes the energy of a system without interactions between the layers and σ_i =+1 or -1 depending on the normal or twinned orientation of the tetrahedral layer. The terms J_n constitute the energetic interaction fields between n^{th} first neighbors. Considering negligible the value of the terms representing the interaction of neighboring planes beyond the third order, the equation (13) can be traced back to the following

$$nE = nE_0 - \sum_{i,n} J_n \sigma_1 \sigma_{i+1} + J_2 \sigma_1 \sigma_{i+2} + J_3 \sigma_1 \sigma_{i+3} \quad (14)$$

The energy of n layers containing an extrinsic prismatic fault in 4H-SiC in a layer (n + 1) / 2 can be calculated as

$$E_{fault} = nE_0 - J_1 + (n-6)J_2 - J_3 \quad (15)$$

By considering

$$A = \sqrt{3}\frac{a^2}{2} = 8.221 \cdot 10^{-20} cm^{-2} \quad (16)$$

as the area per atom on (0001) plane [179], extraplane energy can assume the form:

$$\gamma_{fault} = \frac{\Delta E}{A} = \frac{nE(faulted) - nE(perfect)}{A} \quad (17)$$

so that the extrinsic fault energy in 4H-lattice is

$$\gamma_{fault} = \frac{-J_1 - 6J_2 - J_3}{A} \quad (18)$$

Considering the values of $J_1 = 3.06 \cdot 10^{-20}$ mJ $J_2 = -3.6 \cdot 10^{-19}$ mJ, $J_3 = -6.31 \cdot 10^{-20}$ mJ [180] we obtain a value of 23.98 mJ/m^2, which confirms such configuration to be highly energetic compared to that obtained by usual (3,1) stacking fault in 4H-SiC equal to 14.7 mJm^{-2} [179] and 18 mJm^{-2} [181]. Thus it is deducible that interstitial basal plane generated in environments subjected to high temperatures annealings involves high stressed system contributes. Lattice forbidden evolution

towards more energetically convenient systems could be driven by the thermodynamic of treatment conditions not effective in post implantation annealings, leading to extrinsic type fault surrounded by stressed Frank partial loop with burger vector along [0001] and [11$\bar{2}$0].

Uncoated laser annealing process

Laser thermal processing was first inspected by Raman spectroscopy. This technique is widely used for SiC characterization since it is non-destructive, requires no special sample preparation and presents high sensitivity on structural changes, so that a survey methodology to verify crystal damage recovery can be obtained. Indeed, it is known that ion implantation process generates damage inside the crystal, and although implantation is carried out at 550 °C to avoid lattice amorphization, a decrease of first order Raman peaks intensities has been observed proportional to implantation dose [182].

With the increase in the number of laser shots it is possible to observe the recovery of the 4H-SiC characteristic phonon modes: E_2(TA) at 205.5 cm^{-1}, A_1(LA) at 612.1 cm^{-1}, E_2(TO) at 776.0 cm^{-1}, E_1(TO) at 798.6 cm^{-1} and A_1(LO) at 967.3 cm^{-1}. The increase in the intensity of these Raman peaks as a function of the radiation energy density shows how the laser is able to produce an annealing effect to recover sample crystallinity.

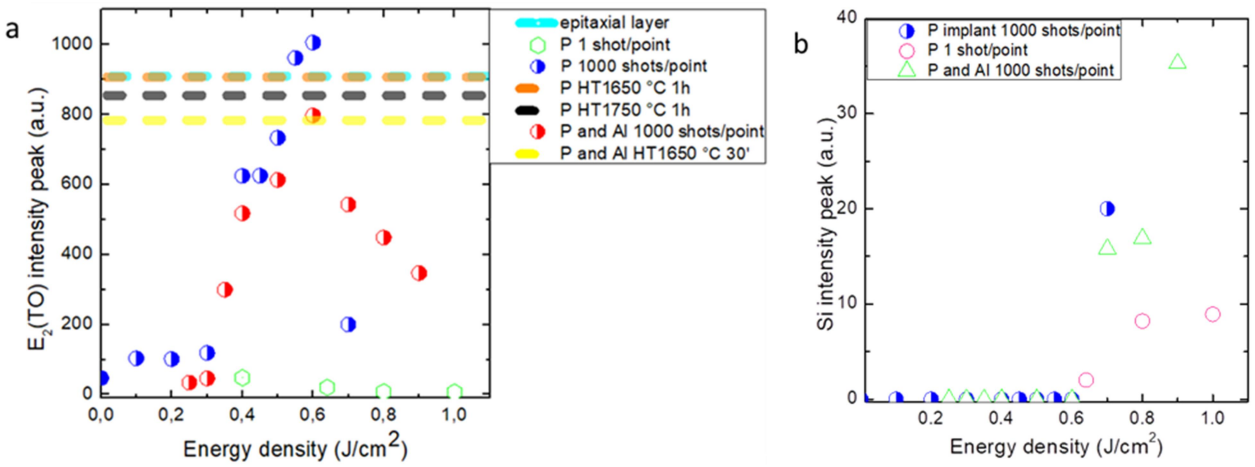

Figure 60. a) Raman E_2(TO) mode intensity peak, b) Si intensity peak vs laser energy density for single source implant and double source and body implants.

Transverse optic E_2(TO) mode signal intensities were extrapolated from Raman spectra and are reported in Figure 60a. In the case of 1 shot/point, crystal recovery is weak compared to as implanted sample signal. However, when the number of shots is increased up to 1000 shots/point, it can be seen that both samples with single and double implant exhibit E_2(TO) signal intensity enhancement and existence of 3 regions is found. Up to 0.30 J/cm^2 E_2(TO) peak intensity remains low. Between 0.30 J/cm^2 and 0.60 J/cm^2 the TO mode signal sharply rises up to its maximum, until the onset of phase separation, where 4H-SiC Raman signal E_2(TO) goes down and crystalline silicon peak at 520 cm^{-1} together with low carbon G band at 1592 cm^{-1} are detected. In thermally annealed samples, the attempt to increase the fraction of dopant activated by increasing the annealing temperature from 1650 °C to 1750 °C produces a 15% reduction in E_2(TO) signal intensity and broadening from 5.3 to 8.1 cm^{-1}, due to the increase in thermal generated defectiveness not only within the projected range of the system but throughout the entire sample, so that worsening of crystallinity is therefore deducible.

Raman signals coming from samples subjected to double implantation are slightly lower than the single implantation one. In this case, in fact, the presence of a second 550 nm deep layer involves an increase of damage and consequently a lowering of the Raman peak intensities.

When the sample is irradiated with an energy above the 0.60 J/cm^2 threshold, Raman spectrum shows a further peak at 520 cm^{-1}. This new vibrational frequency is associated with crystalline Si layers deposited on surface due to phase separation occurring when SiC melting temperature is reached. Figure 60b shows that the Si peak intensity increases linearly with the energy density exceeding 0.60 J/cm^2 for both types of samples analysed.

The identification of this energy threshold is consistent with the results coming from numerical solution of heat flow equation and expressed as

$$\frac{\partial T}{\partial t} = \frac{\alpha}{\rho C_p} I(z,t) + \frac{1}{\rho C_p}\frac{\partial}{\partial z}\left(k\frac{\partial T}{\partial z}\right), \tag{19}$$

$$I(z,t) = I_0(t)(1-R)\exp(-\alpha z), \tag{20}$$

where T represents the absolute temperature, ρ is sample density, C_p the specific heat, k is thermal conductivity, I_0 is laser energy density at the sample surface, R is surface reflectivity, α the optical absorption, z the depth from surface, $I(z,t)$ is the depth, at time t, of the absorbed laser energy density. According to equation (19) and (20), the melting threshold of as-implanted SiC irradiated with 30 ns XeCl pulse length stands over 0.60 J/cm^2 [183], while to induce phase separation in crystalline SiC a laser energy equal to 1 J/cm^2 is required. This prediction is based on the assumption that, when the implanted layer thickness exceeds 200 nm, optical parameters are in reasonable agreement with that of bulk amorphous SiC.

Samples subjected to thermal annealing also show a deviation from the nominal 4H-SiC vibrational frequency between 1650 °C and 1750 °C (Figure 61). The effect arising from such a high thermal budget results in the generation of a compressive stress particularly assessable along the planar component, since the E_2(TO) modes have an atomic displacement perpendicular to the c axis [184].

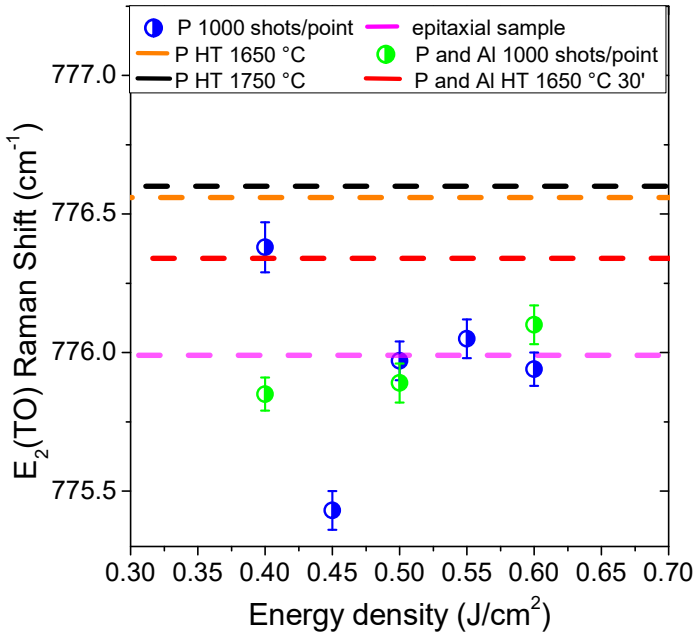

Figure 61. Raman E_2(TO) frequency mode vs Energy density for single source implant and double source and body implants.

From the equations

$$\Delta\omega_{E_2} = (2a_{E2} + b_{E2})P = 3.59P, \tag{21}$$

$$a_{E2} = -1.55 \text{ cm}^{-1}/\text{GPa}, \tag{22}$$

$$b_{E2} = -0.74 \text{ cm}^{-1}/\text{GPa}, \tag{23}$$

where $\Delta\omega_{E_2}$ is the phonon frequency shift, a_{E2} and b_{E2} are the phonon deformation potentials and P is the in plane pression, it is therefore possible to provide an estimate of the stress, which in the case of thermally annealed samples ranges from 130 to 172 MPa increasing with temperature. The usual thermal processes generate a strong stress contribution that is due to multiple factors. In small part this is due to the incorporation of the P or Al dopant responsible for opposing stress contributions and to the shear stress between the implanted area and the underlying epitaxial layer, while the predominant role is related to the creation of a high concentration of both point and extended defects in the implanted region [185].

Samples subjected to laser annealing show much smaller stress values. Especially in high recovery ranges between 0.50 and 0.60 J/cm^2, vibrational frequencies close to epitaxial mode were detected and calculated stress does not exceed 50 MPa, so that almost stress free samples resulted from laser annealing process.

The presence of an important crystal recovery effect is also visible by mean of the photoluminescence analysis. Figure 62a reveals through PL spectra (λ=325 nm, P=2.5 mW) how progressive irradiation at 1000 shots/point produces 4H-SiC band-gap signal recovery at 390 nm. The intensity value of the band-band peak is equal to that of the sample subjected to annealing for 1 h at 1650 °C (see Figure 62b). Thermally annealed samples exhibit a large peak centred at 490 nm with 175 nm FWHM, which can be related to the generation of a high defectiveness concentration and in particular to Vc generated in the implanted region and in the epitaxial layers [186,187]. In addition, interstitial aggregates present within the implanted layers provide an emission contribution to wavelengths corresponding to intra-band-gap emission signal. The PL results coming from laser annealed samples confirm the crystalline recovery trend as appeared from the Raman analysis. At 490 nm no large region of defectiveness is observed within the samples subjected to laser annealing.

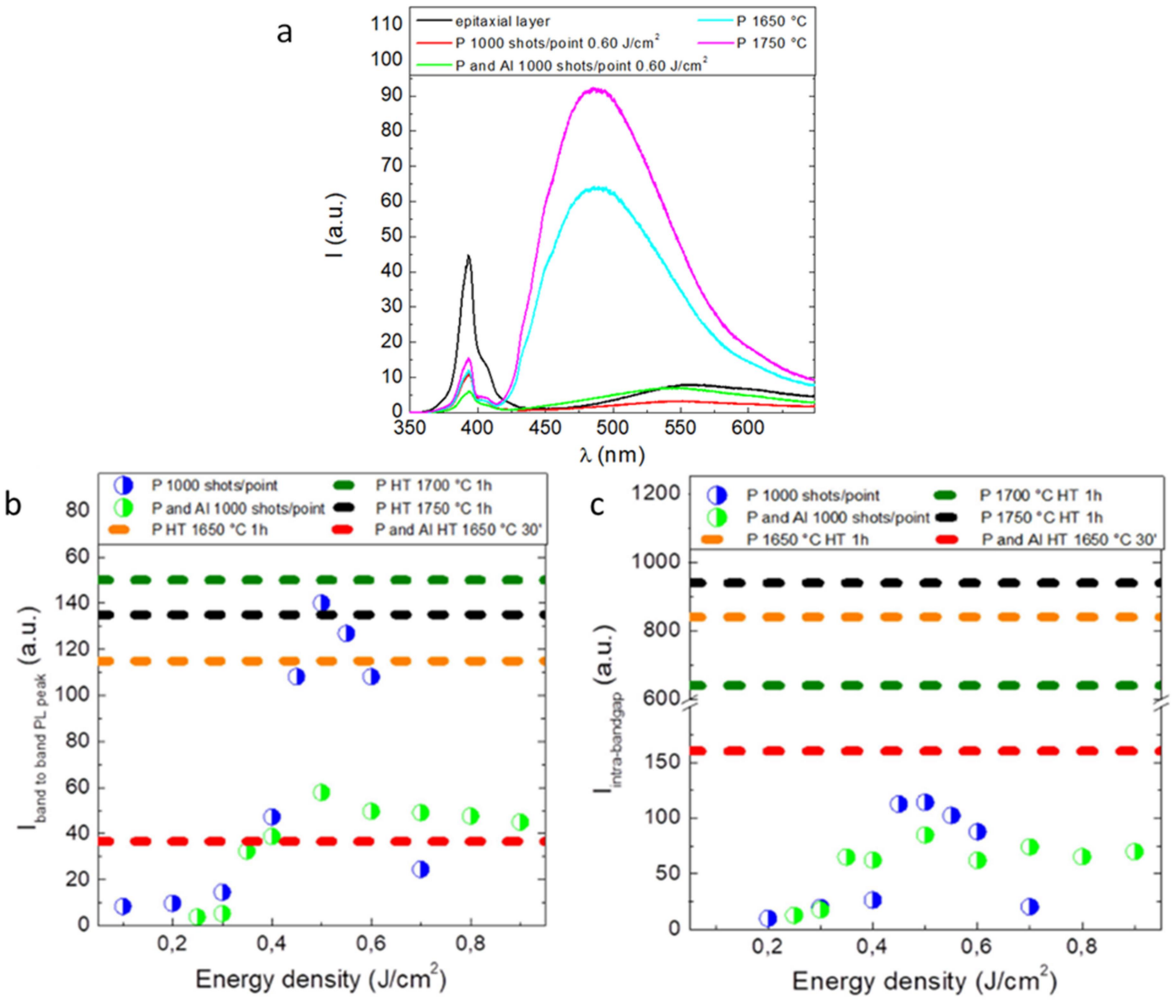

Figure 62 . (a) PL spectra or single source implant and double source and body implants for laser annennealed and 1 h thermally annealed samples. (b) band to band and (c) intra-band-gap PL intensity peak vs. laser energy density.

As shown in Figure 62b, these samples have, in fact, a band peak at 390 nm growing noticeably starting from 0.40 J/cm^2, reaching its maximum at 0.50 J/cm^2 and falling slightly at 0.60 J/cm^2, beyond which phase separation is detected. At 0.50 J/cm^2 the 390 nm peak exceeds the emission intensity of the sample subjected to annealing at 1750 °C. At 0.60 J/cm^2 the 390 nm peak intensity tends to decrease due to progressive enhancement of laser surface effects. The same trend is reported for intra-band-gap peak emission (Figure 62c). However, laser annealing leads to a 60 nm shift of intra-band-gap radiative recombination signal with respect to the corresponding thermal annealing values, making the emission peak to coincide with the epitaxial layer PL emission at 550 nm. Moreover, intra-band-gap emission peak intensity is definitely lower than that detected for thermally annealed samples: the ratio between band to band and intra-band-gap peaks in P implanted samples states on 1.2 between 0.50 and 0.60 J/cm^2 and decreases to 0.45 once the sample undergoes phase separation at 0.7 J/cm^2. Thermally annealed samples show much lower values

attested at 0.1. The PL analysis on double implanted samples confirms this trend. However, in this case the addition of Al further implantation to achieve the 550 nm thick body region results in sample signal attenuation due to the increase in defectiveness along the He-Cd laser penetration path. However it's worth noting that from 0.50 J/cm^2 the laser annealing effect on P and Al implanted samples leads to a higher band to band peak response compared to the corresponding thermally annealed samples. However, if on the one hand the deviation between the values obtained for laser and thermal annealing highlights how out of thermal equilibrium crystal recovery leads to a concentration of defects lower by a factor of 8-9, on the other PL contribute given by the underlying epitaxial layer cannot be disregarded due to implant partial etching and should be considered.

Bright field TEM analyses were performed to structurally characterize the effects due to laser irradiation. Several extended defects are detected inside the implanted area, as shown in Figure 63a in the case of the 0.60 J/cm^2 laser annealed source implant sample. The presence of these defects allows to quantify the portion of implant survived to laser interaction. It was possible to estimate that within the 0.40 J/cm^2 irradiated sample an implanted area of almost 130 nm was preserved (image not shown), while with the increase of laser energy density this fraction is thinned to 90 nm (see Figure 63a).

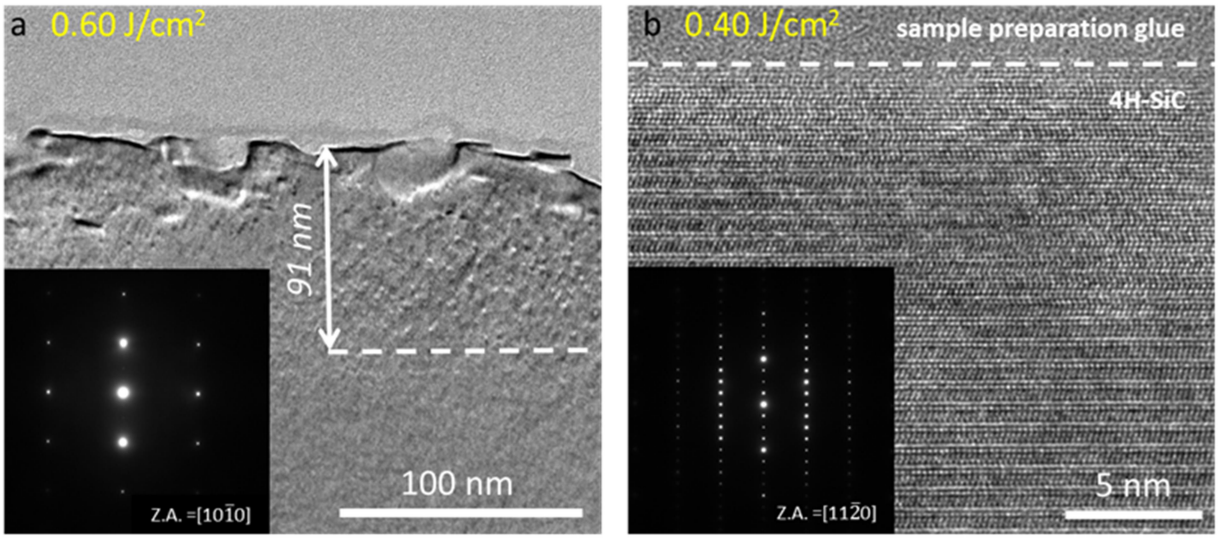

Figure 63. (a) XTEM Bright field image of the 0.60 J/cm^2 laser annealed source implant. The inset shows the 4H-SiC diffraction pattern under [10$\bar{1}$0] zone axis. (b) HRTEM of the source implant sample subjected to 0.40 J/cm^2 laser fluence showing periodic ABAC stacking sequence acquired in correspondence of the surface under the [11$\bar{2}$0] zone axis. The inset reports the related 4H-SiC diffraction pattern.

However, the cross section confirms the data obtained with Raman spectroscopy. In fact, in the inset of Figure 63a, the diffraction pattern acquired on the [10$\bar{1}$0] zone axis shows the full

crystallinity of the implanted area. From Figure 63a we can see that laser interaction gives rise to a certain degree of surface misalignment, although the crystal is kept under the 4H polytype. This is evident from the exclusive presence of the 4H-SiC diffraction spots under the zone axis Z.A. = $[10\bar{1}0]$ and from the absence of diffraction patterns coming from the nucleation of other SiC polytypes or from polycristalline areas, which would have returned circular areas on the sample. Figure 63b shows the 0.40 J/cm^2 irradiated sample HRTEM. It can be highlighted that inspected region maintained the ABAC stacking characteristic of the 4H polytype under the $[11\bar{2}0]$ zone axis up to the top. It is evident that the crystal did not undergo any melting process that would have produced 3C-SiC layer on surface [188] combined with the SiC columnar regrowth from the melt/solid interface [189]. However, since SiC (0001) is characterized by a relatively important surface energy [190], high temperature treatments commonly promote surface desorption of silicon atoms and consequent micro-step formation. Nevertheless, the presence of a further contribution to surface misalignment on many samples is visible in Figure 64a. Spherical aggregates with average size of 131 nm and with 21% of surface coverage are, in fact, detected on the sample. A first structural analysis was carried out by performing a selected area diffraction (SAD) relative to the area marked by the green circle in Figure 64a. Figure 64b highlights the presence of the resulting 4H-SiC diffraction pattern under the zone axis, as well as the presence of circles indicating amorphous material within the investigated area.

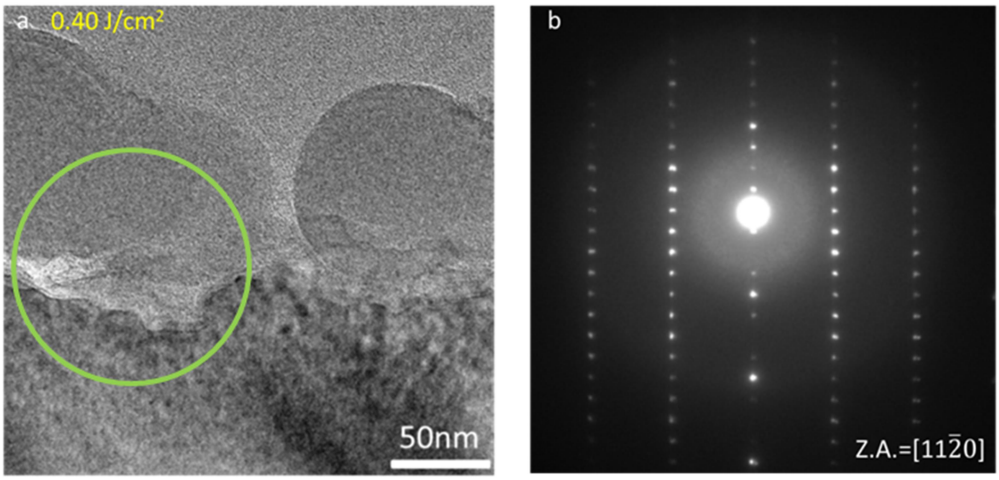

Figure 64. a) Bright field X TEM image of 0.40 J/cm^2 source implant annealed sample surface. Green circle indicates the area where (b) SAD has been acquired.

To perform an elemental analysis the sample was analyzed using STEM-EELS spectrum imaging. In Figure 65b we reported the EELS spectra acquired in correspondence of the region 1

and 2 of the sample, as indicated in Figure 65a. In the EELS spectrum corresponding to region 1, we can easily recognize the characteristic SiO_2 spectrum, where it is possible to identify the Si-L_1, Si-$L_{2,3}$ and O-K edges. The less intense signal coming from C is due to the epoxy glue employed during sample preparation, composed of $(C_6H_6O{\cdot}CH_2O)_x$ and $C_3H_4N_2$. In the EELS spectrum corresponding to region 2, instead, shows the typical SiC signal coming from bulk SiC.

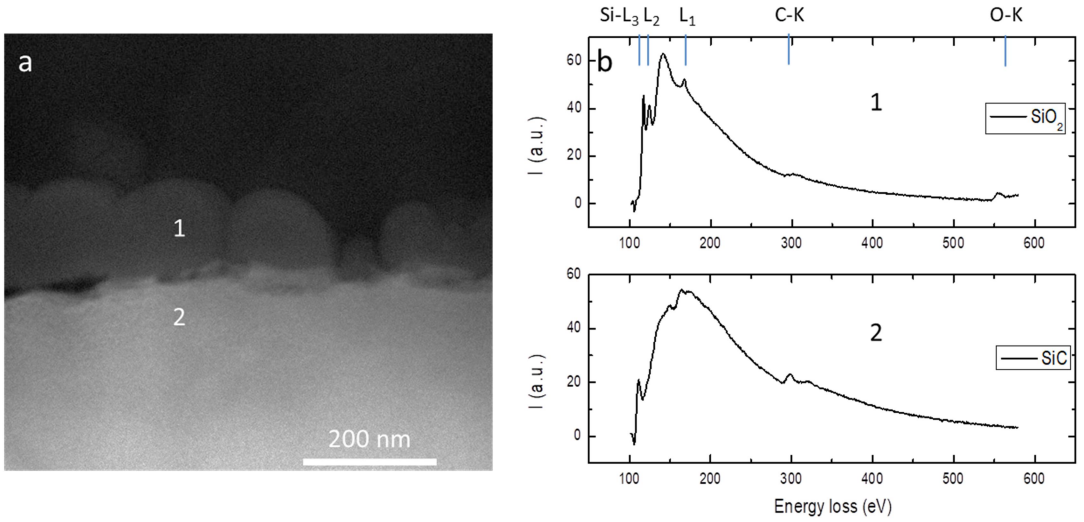

Figure 65. (a) STEM image of 0.40 J/cm^2 treated source implant surface. (b) EELS spectra coming from surface aggregates and from implanted area.

Therefore, once identified surface aggregates as SiO_2 compounds, it is possible to attribute their formation to the presence of residual O in the chamber as an etching source. Studies of the reaction between O and SiC [191] allow, in fact, to state that the interaction between O and SiC at high temperatures is not only present in the form of passive oxidation, but at low pressures it results in phenomena of active oxidation, leading to surface etching and contextual important role in C surface segregation. It can therefore be inferred that O presence in chamber may have played a role in superficial roughness while etching contributions of the sample are due to the local temperature rising at the surface layers and to the presence of photochemical effects inherent to the interaction with the environment inside the chamber during irradiation.

Therefore, once tested the effectiveness in crystalline recovery, the current challenge in the field of laser annealing goes through strategies aimed at improving surface protection and limiting roughening factors.

Coated laser annealing process

Although this technique has proven effective activation results, it has not yet reached an involvement in industrial processes due to the scarce control over the surface damage caused by laser-SiC interaction [3]. Indeed, unlike silicon, 4H-SiC does not favor post-melting epitaxial regrowth. This work, therefore, shows a pioneering method to acquire a substantial control over irradiated surface quality, allowing to implement implanted 4H-SiC crystalline and electrical properties. The technique exploits irradiations over an absorber layer obtained from the 950 °C bake of a spinned resist on SiC wafer surface. Thanks to its 3800 °C melting temperature and high absorption coefficient, graphite is, in fact, the best candidate to fully absorb laser radiation, allowing a heat diffusive regime along the underlying layers. Figure 66a shows two representative spectra in two different regions: at the border of the irradiated zone and in the non-irradiated area. The main feature in the shown Raman spectra of carbons are the so called G and D peaks, which usually lie at around 1560 and 1630 cm^{-1}. Raman spectra of carbon films are dominated by sp^2 sites, as the laser excitation source always resonates with the π states[192]. The cross section for the amorphous sp^3 C-C vibrations is negligible for visible excitation, thus its Raman signature can only be seen under UV excitation. The assignment of peaks D and G is immediate in polyaromatic hydrocarbon materials. The G peak is due to the bond stretching of all pairs of sp^2 atoms in both rings and chains and is related to the allowed phonons. The D peak is due to the breathing modes of sp^2 atoms in rings and is also associated with disordered graphite linked to the breakdown of the selection rules [193]. The as deposited graphite has a G and a D peak broadened and convoluted resulting in band shift to higher values (from 1584.2 ± 0.1 cm^{-1} up to 1592.1± 0.1 cm^{-1}), indicating that the bonding shows ordering behavior and increasing sp^2 content. It is well known that the in-plane crystalline size of graphitic domains can be calculated by using the following Tuinstra and Koenig relation [194]

$$\frac{I(D)}{I(G)} = \frac{C(\lambda)}{L_a} \tag{24}$$

where $C(\lambda) \sim 2.4 \cdot 10^{-10} \lambda^4$ using I(D)/I(G) as integrated area ratio. This expression was developed for disordered graphite with 100% sp^2 bonded atoms and it is valid down to a critical cluster size of 2 nm. In highly disordered carbon materials, the presence of defects and the possible decrease of crystallite size L_a below 2 nm point out a lower number of carbon hexagonal rings in the network. Consequently, the intensity of the mode and the ratio tend to decrease and the T-K approximation is

no longer valid. Approaching towards the laser annealed area, the results show an evolution of the average graphite cristallite size which increases from <2 nm far from the irradiated area to ~8 nm in the region presented in Figure 66c . Figure 66b shows the overlap of peaks average values relating to the G and D modes for graphite extracted from acquisition regions 3 mm x 3mm wide in the irradiated area center. Indeed inside the treated area a localized high temperature region around graphite is formed and laser induced photothermolysis of graphite appears [195]. Heated by high energy laser beam, the van der Waals contact between layers are broken, leading to graphite exfoliation as visible in Figure 66d where a SEM image acquired the center of an irradiated region, displays such process. From the data it is evident that the sample shows a reduction in the intensity of the peaks G and D as consequence of erosion phenomena which during irradiation induce a lowering in deposited graphite thickness. It is noted that the thickness decreases up to 0.6 J/cm^2. At higher energies it is possible to notice that with the same rate of irradiation at 1000 shots/point an increase in the signal intensity of the graphitic peak emerges. The increasing of such peak can be linked to the onset of SiC surface damage which, by means of phase separation, shows an enhancement in the carbon phase signal stratified on the surface from 0.7 J/cm^2.

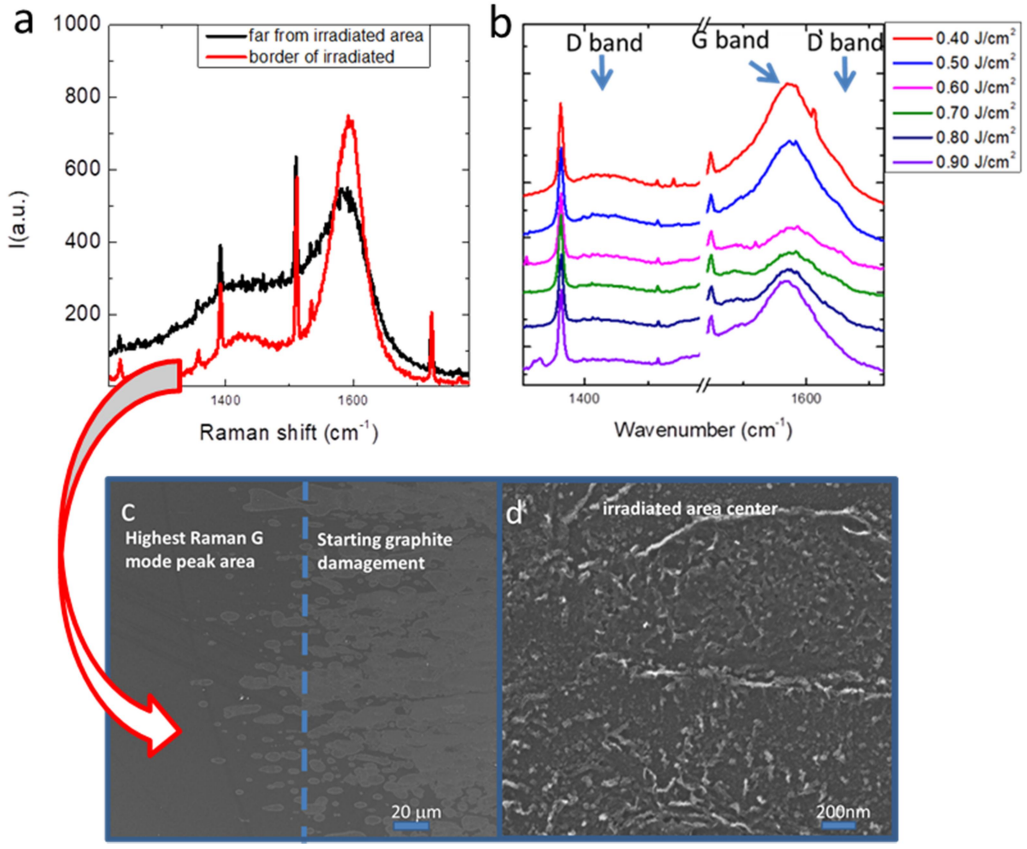

Figure 66 a) Raman G and D modes from not irradiated area and from the edge of the irradiated, b) Raman G and D modes extracted from Raman spectra in the irradiated sample center , c) SEM extracted area from damaged graphite border d) exfoliated graphite within the center of irradiated area.

The phase composition and structure of the samples was determined by X-ray diffraction using a D8 Discoved (Bruker AXS) diffractometer with a Cu-Kα source (instrumental broadening 0.07°). Probed area = 0.2cm^2.

From XRD investigation graphite 3R-(003) plane contribution is detected after alignment on the 4H-SiC substrate (4°off) (Figure 67a). This implies that 4H-SiC and graphite materials are aligned. The intensity distribution of graphite peak along the x-axis does not highlight pronounced differences between the center (namely the irradiated zone) and the edge of irradiated (+/-4mm). We limitedly notice a slight dip at the centre of the profile that could be simply due to statistics.

By involving the use of the Scherrer equation

$$L = \frac{K\lambda}{B\cos\theta} \tag{25}$$

which connects the FWHM B, the diffraction peak position θ to the physical size of the crystallite L, via the wavelength, λ and a dimensionless constant K, it is possible to determine graphite domains average size. Considering the FWHM coming from the signal in 2θ scan shown in Figure 67a it was possible to extract an average value of 7.6 nm ± 0.1 nm which is consistent with the value extracted from the Raman analysis.

Rocking curves in Figure 67b display an high degree of texturing both inside and at the edge of the irradiated area in the graphite layer without remarkable structural differences between the center of the spot and the border at 4 mm from the center.

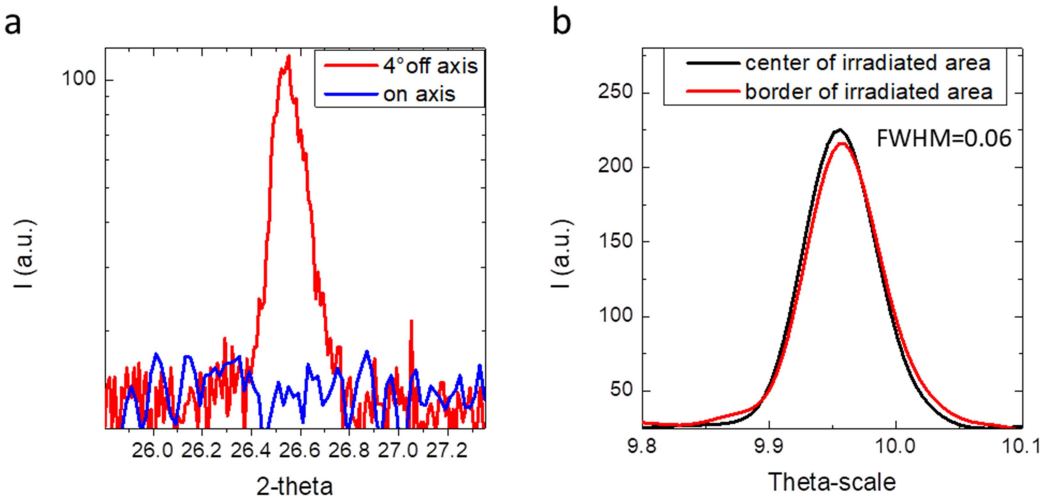

Figure 67 a) XRD diffraction pattern of graphite along 3R (003) peak on axis and 4°off axis b)XRD Rocking curve at the center and at the border of the irradiated area.

Raman spectra for the laser annealed samples are shown inside Figure 68. These samples show the progression of crystalline recovery as a function of irradiation energy. With the application of 90 nm graphite layer Raman spectrum shows the appearance of the crystalline Si peak at 520 cm^{-1} starting from 0.60 J/cm^2 (Figure 68a). This type of behavior demonstrates how graphite is mostly eroded by the sample and determines annealing regimes not yet sustainable by SiC leading to surface Si layering. As the energy density increases, Si signal increases. The enhancement is noted also from the E_1(TO) peak rising at 796 cm^{-1}. This peak constitutes a prohibited peak and is attributable to the laser probe exposure to planes different to (0001) following atoms desorption and consequent surface roughening. The activation of this mode is also related to the E_1(TO) FWHM broadening.

A 180 nm graphite layer is therefore ideal to remove sample damagement. The use of greater thicknesses of graphite is necessary to reduce the implanted material optical extinction coefficient and consequently lowering absorption coefficient.

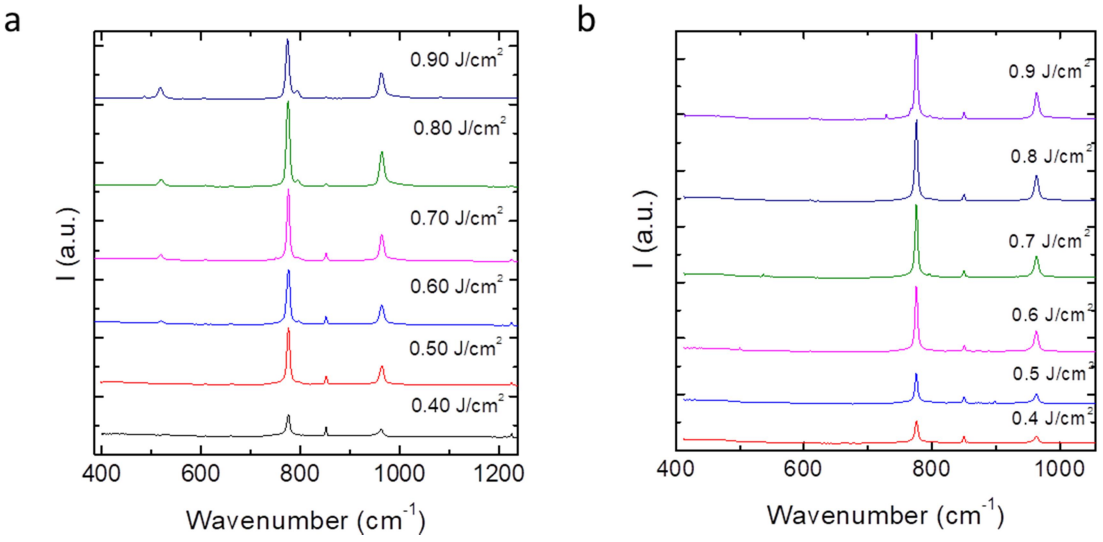

Figure 68 Raman spectra from laser annealed graphite coated samples with initial a) 90 nm and b) 180 nm thick graphite layer.

Indeed, in Figure 68b Raman spectra exhibit no Si related peak in the whole range of energies investigated as well as any increase in intensity of the E_1(TO) mode. As reported in Figure 69a Raman investigation focused on the E_2 (TO) peak points out a linear trend with the increase in laser annealing energy. There is therefore a recovery of crystalline damage proportional to the irradiation

strength. From FWHM E_2(TO) modes analysis in Figure 69b, it can be seen how graphitic thickness superimposed on the SiC implanted layer before irradiation induces beneficial effects on the crystal quality. Both in the case of the sample with 90 nm graphite coated and of the sample without coating there is a reduction of the FWHM with the increase of the irradiation energy. In this context, although it is difficult to establish the exact contribution of the epitaxy underlying the implant, it is noted that the FWHM combines values of 5.3 cm^{-1}±0.1cm^{-1} and 4.7 ±0.1cm^{-1}. Together with laser energy growth, FWHM increases its value as a consequence of crystalline quality degradation in the investigated area, reaching a value equal to 6.6 cm^{-1} and 7.5 cm^{-1}. The mode broadening is avoided with the application of 180 nm graphitic layer. FWHM values oscillate around 4.5 cm^{-1} and reach 4.35 cm^{-1} at 0.7 J/cm^2, lower than the 4.9 cm^{-1} value measured in traditional annealing. The analysis of the in plane stress provided by E_2(TO) mode deviation with respect to its nominal position (Figure 69c), involves a 78.1 MPa and 65.1 Mpa tensile stress respectively for 90 and 180 nm of graphite deposited with an equal radiation energy at 0.4 J/cm^2 and move towards stress free values at 0.50 J/cm^2 for 90 nm graphite layer and at 0.60 J/cm^2 for 180 nm graphite layer which are lower than the value of 140 MPa recorded for the sample subjected to thermal annealing. These values constitute, as mentioned, a border between a crystal recovery regime system and damage generation connected with the erosion of the implanted region. The removal of the P implanted region results in growing optical signal related to the body region. This area responds to tensile stress due to the activation of the Al ions placed in Si substitutional position. It is clear from the FWHM that the sample does not suffer from an important damage as in previous cases and that the non-thermal equilibrium regime contributes to crystalline recovery.

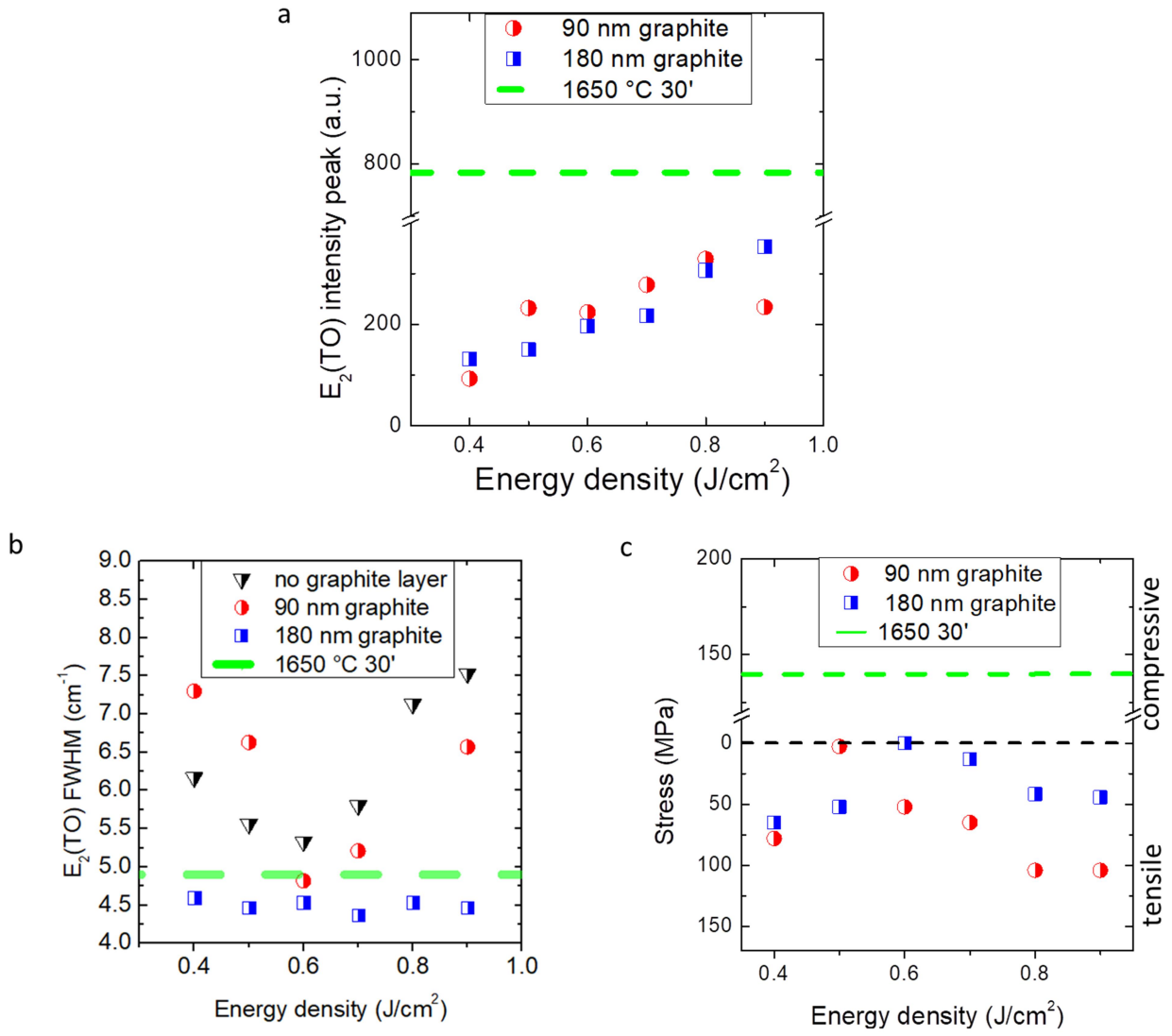

Figure 69. 90 nm, 180 nm graphite coated laser annealed sample and 1650 °C 30 thermally annealed Raman extracted a) E_2(TO) mode peak intensity b) FWHM c) in plane stress values.

Figure 70 shows in-plane SEM images for two samples irradiated at 0.6 J/cm^2. It is shown how the exposed surface underwent Si desorption and formation of silicon oxide spheres due to active oxidation phenomena during irradiations. Surface damage was prevented in graphite assisted laser annealing process resulting in smooth surface. With the application of 90 nm of graphite a slight damage effect is also present at 0.50 J/cm^2. In this case it is noticed how the sample manifests an irregular surface consequent to the desorption of the surface atoms.

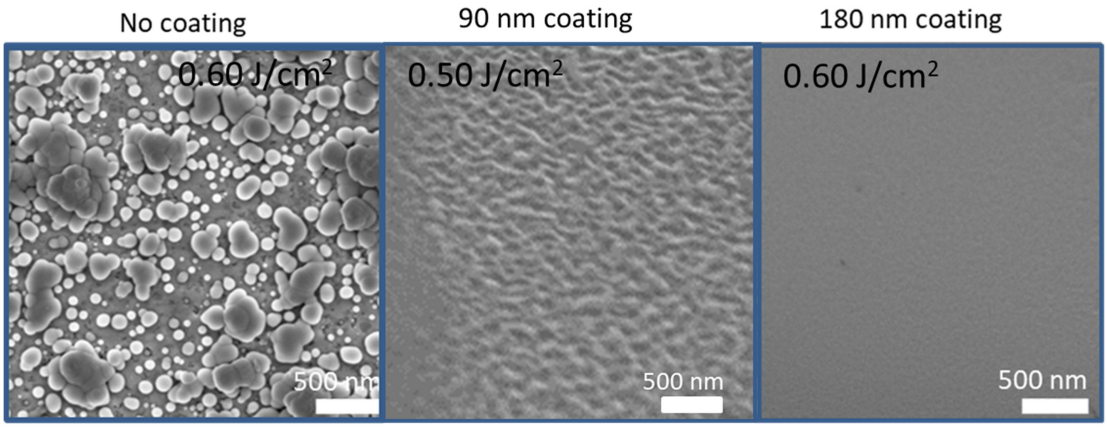

Figure 70. SEM investigation from laser annealed SiC surface sample with no coating and with 90 nm graphite and 180 nm graphite thick layer.

At 0.50 J/cm^2 the 90 nm graphite coated samples are thus eroded and SiC surface remains uncovered. Instead, at 0.60 J/cm^2 the 180 nm graphite coated sample remains intact despite, as attested by optical microscopy investigations, graphite has been removed during laser irradiation. It is evident that the greater initial graphite thickness deposited on the implanted region was effective in damage prevention, as it allowed SiC absorption coefficient shift towards values closer to crystalline one. From the absorption coefficient expression as a function of temperature

$$\alpha(T) = A\left[\frac{(h\nu - E_g(T) - k\ )^2}{1-\exp\left(-\frac{\theta}{T}\right)} + \frac{(h\nu - E_g(T) + k\theta)^2}{\exp\left(\frac{\theta}{T}\right)-1}\right] \tag{26}$$

where absorption of the incident photon $h\nu$ is assisted by emission or absorption of momentum conserving phonons of $k\theta$ energy, it was possible to follow $\alpha(T)$ during a single shot. In view of the fact that $E_g(T)$ is strongly nonlinear at low temperatures, the band-gap shift with temperature in Eq. (26) was approximated by the semi-empirical Varshni equation

$$E_g(T) = E_g(0) - aT^2/(T+b)$$

with a and b parameters taken from [196].

It can be understood from Figure 71 how the absorption coefficient undergoes a variation dependent on crystallinity as well as on temperature and consequently constitutes a key parameter within the single laser shot. Indeed it can be seen that the absorption coefficient passes from 1667 cm^{-1} up to $3\cdot10^5$cm^{-1} at 2500 K while for an as implanted sample, whose optical behavior is assimilated to an amorphous one, it assumes a value of $6\cdot10^5$ up to $2.4\cdot10^6$ cm^{-1}. The layers involved in SiC laser irradiation following graphite erosion are thus variable according to the degree of crystal recovery.

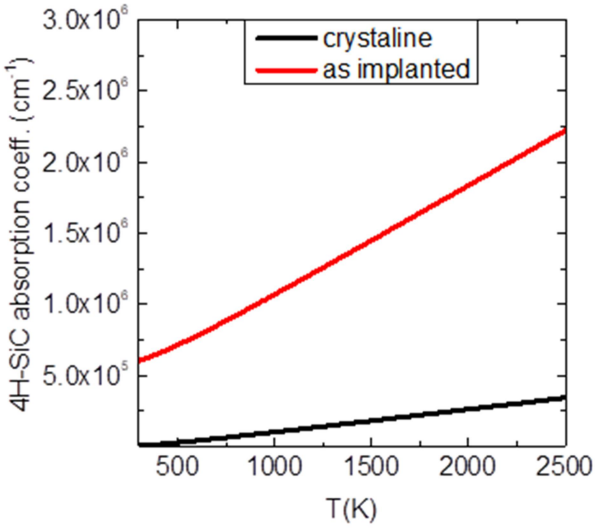

Figure 71. 4H-SiC absorption coefficient temperature dependence for as implanted and full crystalline sample.

The samples with 180 nm graphite suffered less damage than the samples with 90 nm and this process is referable to the greater optical parameters recovery in the irradiated samples.

Crystal recovery through laser annealing process mediated by a 180 nm thick graphite layer allows SiC to tolerate radiation at energies equal to 0.60 J/cm^2.

To perform a study on the variation of the number of pulses and therefore of the annealing time, tests were carried out with different number of shots/point. For this new set of samples graphite pyrolysis process took place at T = 1100 °C for a duration of 20 minutes. This system allowed a higher graphite quality gain. From Raman investigation, as deposited graphite crystallite size was 3 nm with G peak FWHM going from 75.6 ±0.9 cm^{-1} in the case of 950 °C annealed graphite to 62.8 ±0.7 cm^{-1} for graphite annealed at 1100 °C. Raman results are reported in Figure 72. It can be determined that samples displays an higher crystalline recovery than the previous one at already 1000 shots/point (Figure 72a). Through the number of shots variation, Raman spectra displays intensity oscillations in the E_2(TO) mode presumably due to small variations in the deposited layer thickness. Only at 0.6 J/cm^2 sample exhibits a slight increase with the number of shots applied. The FWHM data (Figure 72b) confirms the increase in crystalline quality compared to the sample subjected to conventional annealing and shows a further trend of FWHM reduction in the passage from 1000 to 10000 shots/point under the investigated energies. The variation is very evident in the sample irradiated at 0.4 J/cm^2 where with the increase in the number of shots it was observed FWHM passage of from 4.5 to 4.0 cm^{-1}. Beyond some fluctuation present at 0.50 J/cm^2 it is possible to notice how FWHM values tend to 4 cm^{-1} with the maximum number of shots/point. This implies that the increase in the annealing time towards 10000 shots/point induces a further improvement in the implanted lattice. As reported in Figure 72c the increase in the irradiation time does not entail a change in the stress recorded on the sample.

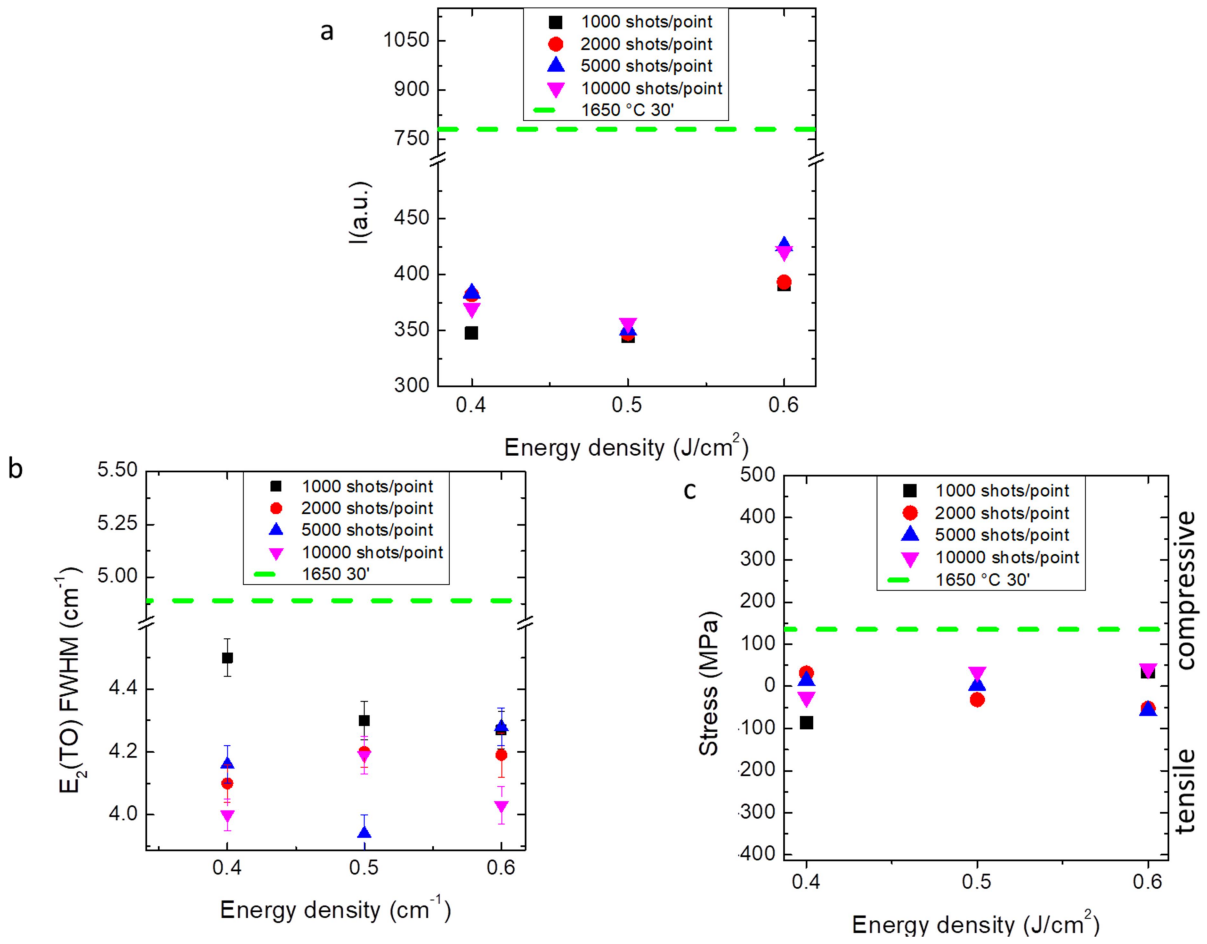

Figure 72. 180 nm graphite coated laser annealed sample with 1100 °C pyrolyzed photoresist Raman extracted a) E_2(TO) mode peak intensity b) FWHM c) in plane stress values.

The photoluminescence spectra (λ=325 nm, P=5 mW) show the degree of the sample recovery from implantation damage. In Figure 73a it is noted how samples show a different PL signal recovery degree for samples subjected to conventional annealing and laser annealing with 180 nm thick graphite treated at two different temperatures. At 390 nm we note the bandgap re-combination signal characteristic of 4H-SiC. This signal constitutes a fingerprint of the crystallinity and shows how the sample subjected to conventional thermal annealing displays still a greater degree of recovery with respect to both laser annealed samples. The laser annealed sample with higher pyrolyzation temperature demonstrates at the same number of shots twice the bandgap signal strength compared to the pyrolyzed sample at lower temperature. The latter displays a large defect band centered at 540 nm. The present defect target appears close to epitaxial sample point defects

signal recorded in the PL spectra shown previously. As shown by Figure 73b the bandgap peak tends to grow with the increase of the irradiation energy for the whole range of energies investigated. Damage phenomena detected from 0.8 J/cm^2 do not affect this trend since λ=325 nm laser wavelength mediates the signal of the underlying SiC epitaxial layer. The intrabandgap band shows an increase up to 0.6 J/cm^2. Starting from 0.7 J/cm^2 this signal undergoes a reduction in intensity due to the greater annealing contribution. The signal then appears stationary around 0.80 and 0.90 J/cm^2. On the other hand, the variation of the pyrolyzation temperature contributes to a greater recovery in PL.

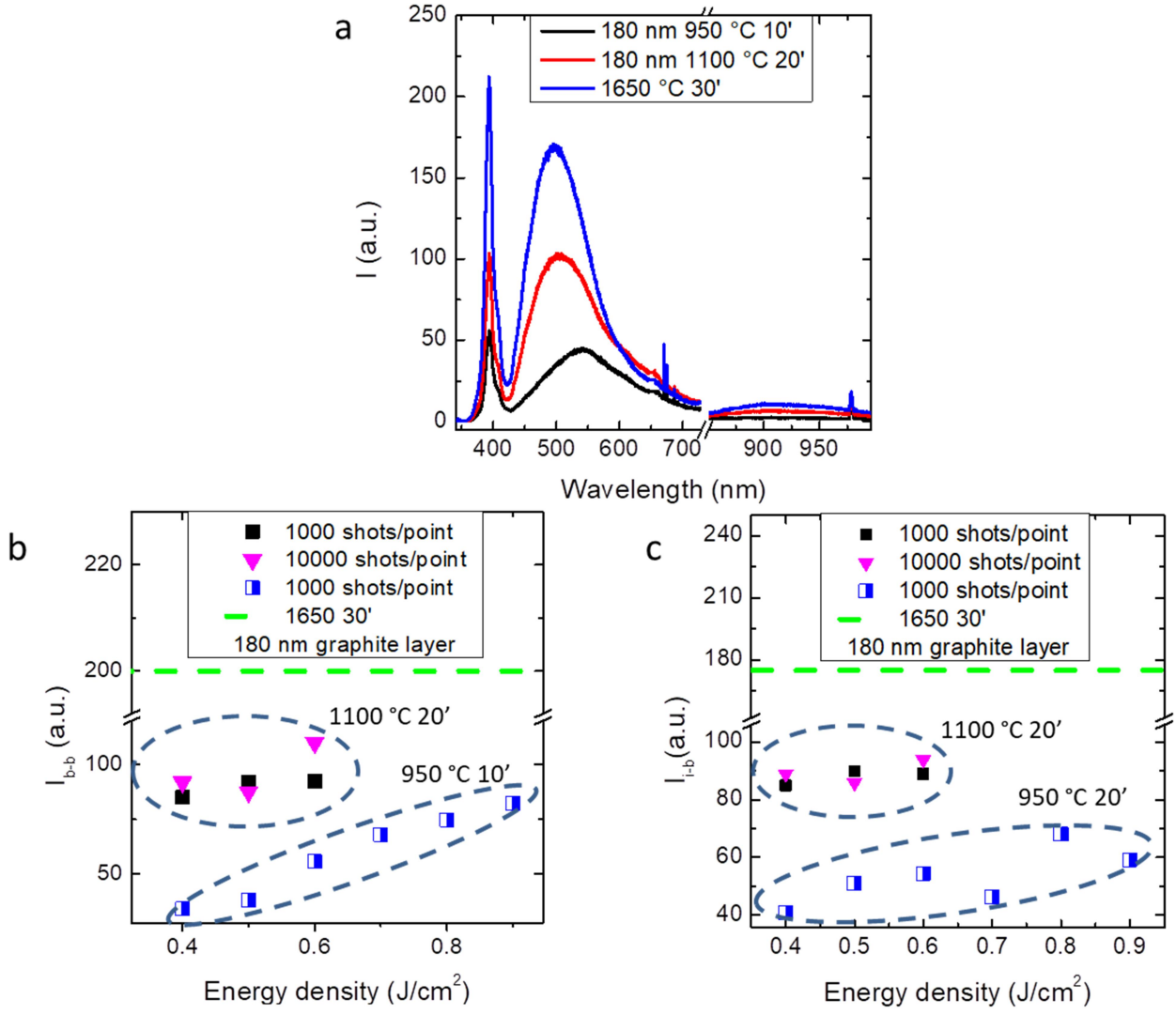

Figure 73. a) PL spectra b) band to band peak intensity and c) intrabandgap peak intensity from laser annealed sample with 950 °C and 1100 °C photoresist pyrolization temperature and 1650 °C thermally annealed samples.

The increase in the number of shots is appreciable at 0.6 J/cm^2 where the higher thermal budget involves band-to-band signal and a consequent increase in the intra-band signal which is shifted to

505 nm. We could speculate that the different quality of graphite has changed single shot annealing duration so in addition to the typical intrabandgap contribution of the laser annealed samples, another emission contribute was added. Exposure to more prolonged thermal treatments could have caused an increase in the thermally generated fraction of point defects such as carbon vacancies with the consequent shift of the wavelength band close to thermally annealed sample at 495 nm and the contextual presence of the 910 nm band linked to Si divacancies [197].

Figure 74 displays the XTEM acquisition from two samples subjected to furnace annealing and graphite assisted laser annealing at 0.6 J/cm^2. The sample processed at 1650 °C for 30' (Figure 74a) shows dislocation loops network related to the 200 nm thick source region as a consequence of point defects aggregation stimulated by high temperature annealing under thermal equilibrium conditions. The 550 nm thick body region, is affected by rear aggregates and follows the lower Al implant concentration. Laser annealed sample (Figure 74b) presents limited source region defectiveness and body region is remarkably free from dislocation loops. It can be deduced that, if on the one hand the shorter diffusion times result in smaller dislocation loops size distribution, on the other it is known that thermal non-equilibrium regime does not allow C interstitials diffusion times suitable for prismatic dislocation loops nucleation. From HRTEM investigations no extra-planes were identified within the implanted lattice along the [0001] direction and nor along [11$\bar{2}$0] as seen in the samples subjected to conventional thermal annealing.

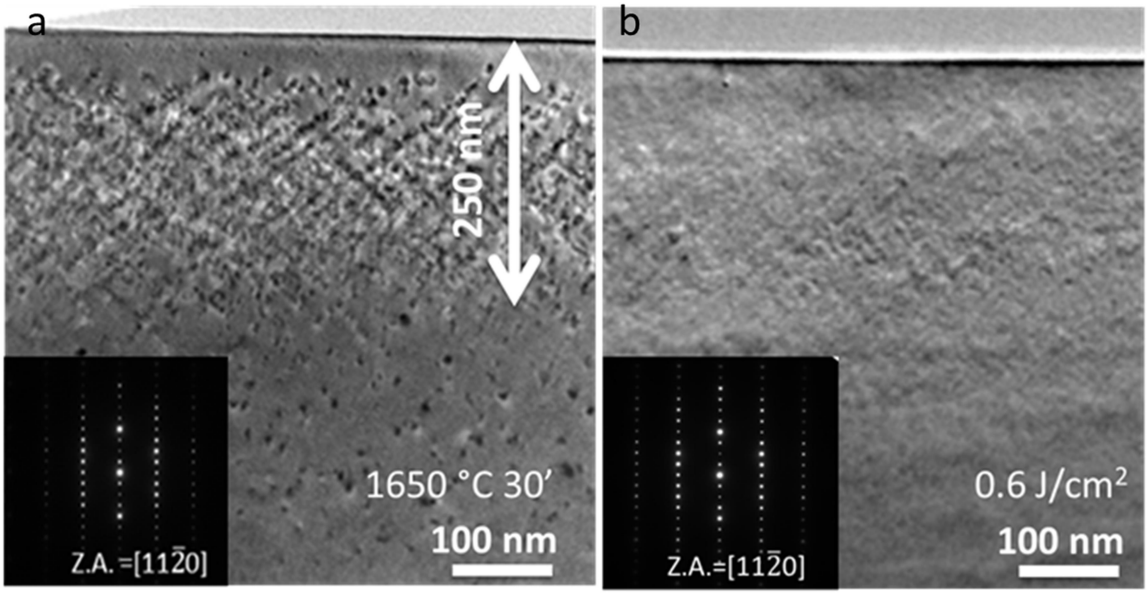

Figure 74. Source and body area Bright Field XTEM images from a) 1650 °C 30' thermally annealed sample and 0.6 J/cm^2 1000 shots/point laser annealed sample.

To perform a sample electrical characterization CTLM measurements have been performed. Through such structures the contact resistance as well as sheet resistance can be determined through the linear relationship between the resistance and the gap spacing between the contacts.

This technique turns out to be advantageous over the linear TLM technique as the latter tends to suffer from the fact that currents from one contact to another contact may spread due to current crowding.

In this adopted circular configuration the resistance *R* between the contacts follows the equation:

$$R = \frac{R_{sh}}{2\pi}\left[ln\frac{R_2}{R_2-s} + L_T\left(\frac{1}{R_2-s} + \frac{1}{R_2}\right)\right] \quad (27)$$

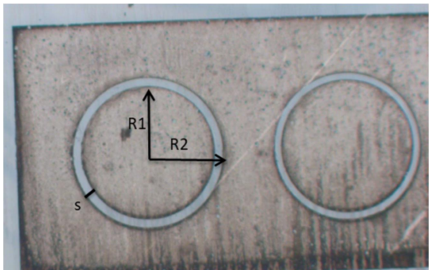

Figure 75 SEM plan view of a CTLM NiSi ohmic contact on laser annealed sample

where R_{sh} is the sheet resistance of the high doped semiconductor material on which the contact is made, R_2 is the radius of the outer circular contact, *s* is the gap spacing as reported in Figure 75 and L_T is the transfer length.

Many samples 90 nm graphite laser annealed together with uncoated laser annealed samples were so electrically characterized by CTLM measurements. An energy density threshold emerged in 90 nm graphite coated samples at energies greater than 0.4 J/cm^2: in this sample graphite permanence after laser annealing treatment was denoted. Here sheet resistance as high as $7.735 \cdot 10^3 \pm 481$ Ω/sq was measured and consequent high resistivity compared to a conventional annealing was associated as reported in Figure 76a.

At 0.5 J/cm^2 a sheet resistance value of 391 ± 164 Ω/sq showed relevant phosphorus activation. From the XTEM investigations it was possible to estimate a 110 nm original implant permanence which led to $4.3 \cdot 10^{-3} \pm 1.3 \cdot 10^{-3}$ Ω·cm resistivity value, close to common literature thermal annealings data [198,199,200]. Particularly Figure 76a reports sheet resistance and resistivity values emerged from T=1675 °C source implant annealing data with same implant doses and energies for t=15 min recently reported [201].

Despite the higher thermal budget at 0.6 and 0.7 J/cm^2, non coated samples showed higher sheet resistance values than graphite coated subjected to lower energies due to the etching of highest

concentration implant region. Nevertheless, from the XTEM analyses corresponding resistivity value between $2.15 \cdot 10^{-2}$ and $6.52 \cdot 10^{-2}$ Ω·cm were obtained. To estimate the P implanted activation following laser treatment, the electron carrier mobility values were extracted from semiempirical equation of Caughey-Thomas for electron concentrations comparable to P implanted dose in source region. By considering a mobility value as high as 22 cm^2/Vs activations for 0.4 J/cm^2 around $1.8 \cdot 10^{18}$ e/cm^3 were extracted, which corresponded to activation values below 2%. At 0.5 J/cm^2 the activation values obtained were equal to $6.59 \cdot 10^{19}$ ±1.95 e/cm^3 which corresponded to approximately 66% of P implanted activation (Figure 76b). This is slightly higher than the value coming from the thermally annealed sample (around 62%). Non coated reported tests suffer, instead, from considerable implant etching and consequently from higher P concentration plateau region remotion. The values thus obtained around $1.30 \cdot 10^{19}$ e/cm^3 and $1.16 \cdot 10^{19}$ e/cm^3 corresponded to implant tail areas total activation.

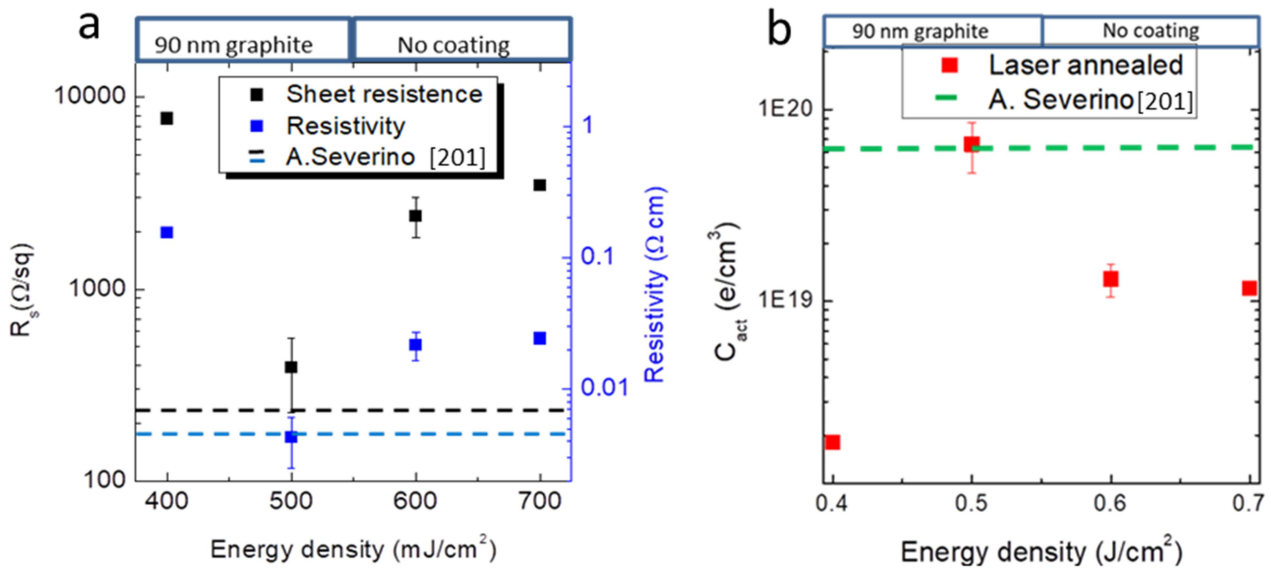

Figure 76.a) CTLM extracted Sheet resistance and resistivity b) Active P concentration values for 90 nm graphite coated laser annealed samples at 0.40 and 0.50 J/cm², uncoated laser annealed samples at 0.60 and 0.70 J/cm² and 1650 °C 30' thermally annealed sample,

To evaluate the temperatures profile reached inside the samples subjected to laser annealing, simulations of pulsed irradiation with a wavelength of 308 nm were carried out. A gaussian laser pulse with profile consistent with experimental profile data was used. Laser profile dimensions of

20x1mm and standard deviations along the two plane direcion σ_x=3.90 mm and σ_y=0.48 mm were adopted.

The Heat transfer equation solved was

$$\rho C_P \left(\frac{\partial T}{\partial t} + u_{trans}\right) + \nabla \cdot (q + q_r) = -\alpha T \frac{dS}{dT} + Q \quad (28)$$

The different quantities involved here are recalled below:

• ρ is the density (SI unit: kg/m^3)

• C_p is the specific heat capacity at constant stress (SI unit: J/(kg·K))

• T is the absolute temperature (SI unit: K)

• u_{trans} is the velocity vector of translational motion (SI unit: m/s)

• q is the heat flux by conduction (SI unit: W/m^2)

• q_r is the heat flux by radiation (SI unit: W/m^2)

• α is the coefficient of thermal expansion (SI unit: 1/K)

• S is the second Piola-Kirchhoff stress tensor (SI unit: Pa)

Q contains additional heat sources (SI unit: W/m^3) and is the body heat load within the sample involved in heat diffusion equation given by

$$Q(x, y, z,) = Q_0(1 - R_c)\frac{A_c}{\pi\sigma_x\sigma_y} e^{-[\frac{(x-x_0)^2}{\sigma_x{}^2} + \frac{(y-y_0)^2}{2\sigma_y{}^2}]} e^{-A_c z} \quad (29)$$

where Q_0 is the total power imput, R_c is the reflection coefficient and Ac is graphite reflection coefficient. The equation was solved with an extra elliptical boundary on the top surface to represent the zone of heat input.

The simulation involved 3 blocks: a first 90 nm thick block consisted of graphite, with an optical extinction coefficient k = 0.9 [202]. The thermal conductivity was set between 75 and 34 W/mK with temperature increase following the trend taken from [203] common to many polycrystalline graphites. The other two layers with a thickness of 550 nm and 350 µm respectively constituted the implanted layers and the epitaxial layer. The thermal conductivity of the implanted sample was described by a cubic function which, as the temperature increased, induced a reduction in thermal conductivity from 66 W/mK to 35 W/mK at SiC melting temperature. The thermal conductivity of

the non-implanted sample was considered 100 W/mK. The results are shown within the following two figures. Figure 77a portraits the temperature profile of graphite surface layers subjected to 0.50 J/cm^2 laser treatment and a laser power of $3.6 \cdot 10^6$ W. Following this irradiation, the simulation shows a temperature peak at 25 ns which corresponds to a temperature around 3500 °C. By observing the phase diagram of graphite [204], it can be observed that at the pressure of our experimental setup, graphite undergoes a phase transition in which the C desorbs from the surface graphite at 3800 °C. Reaching these temperatures could provide an explanation for the experimentally achieved erosion of graphite. Figure 77a-b provide the trend of temperatures in correspondence of the projected range at 180 nm of the source region deep 250 nm and at the center of the body region deep 550 nm from the SiC surface. The temperature reached in the body region is 1850 ° C with an annealing ramp as high as 9×10^{10} K/s, while in the center of the body region the temperature drops to 2000 ° C.

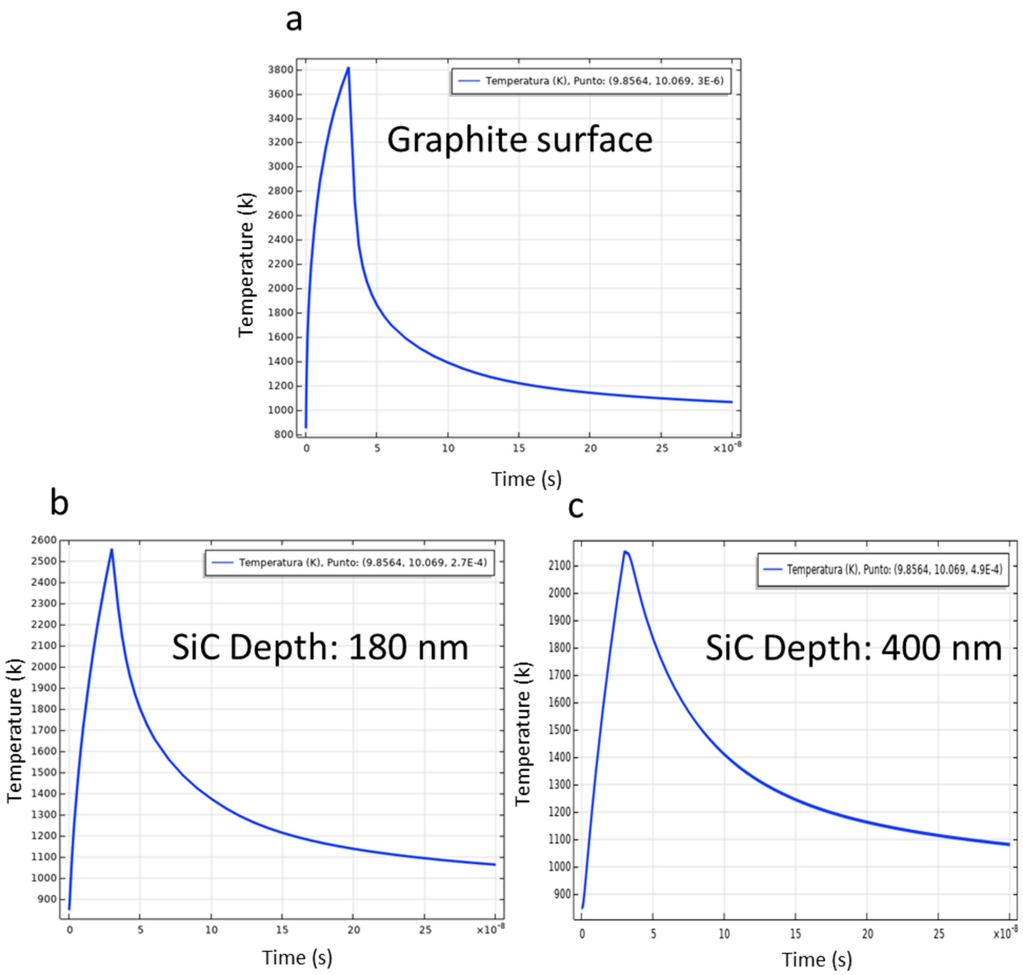

Figure 77. Laser annealing temperature profile for t=30 ns irradiations as function of time for 0.5 J/cm^2 90 nm graphite coated sample on a) graphite top layer, b) source central region c) body central region .

The source implant remains approximately 19 ns above 1600 °C and then thermalizes completely at the stage temperature after $3.4 \cdot 10^{-6}$ s. Considering that the annealing tests were carried out at a maximum frequency of 40 Hz, it is possible to state that the shots are thermally independent from each other.

The simulation of an irradiation at 0.4 J/cm^2 and a power equal to $2.9 \cdot 10^6$ W induces lower temperatures in the three examined layers. As further attested by the simulation in Figure 78a, the surface of the graphitic coating is almost preserved, however the maximum temperatures reached in the source implant are approximately 1900 °C with an annealing ramp of $8.8 \cdot 10^{-8}$ s and permanence times above 1600 °C as long as 10 ns (Figure 78b) which is shorter than the case shown above. The temperature reached in the center of the body region is approximately 1600 °C (Figure 78c). It is evident that in these simulations significantly higher temperatures than those achievable within the usual heat treatments have been reached, but the difference recorded in terms of dopant activation could be due to the introduction of a threshold effect in the activation both in terms of temperature and times.

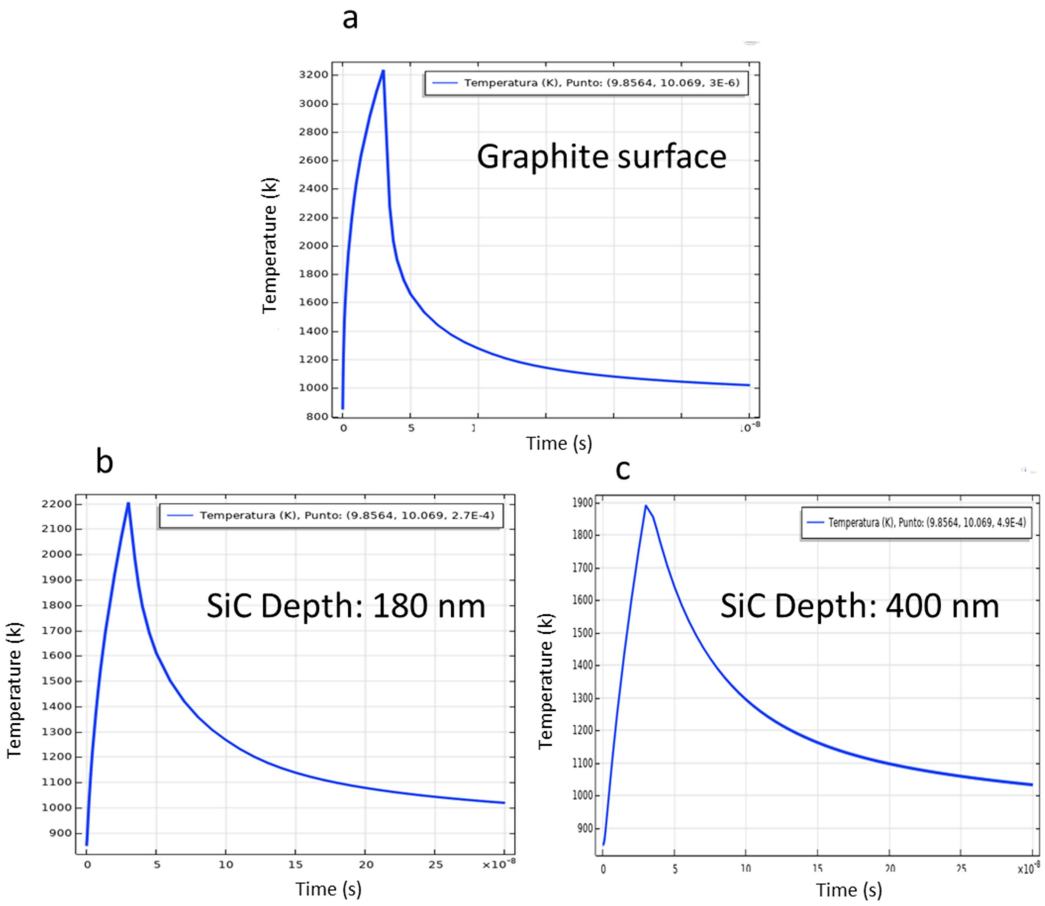

Figure 78. Laser annealing temperature profile for t=30 ns irradiations as function of time for 0.4 J/cm^2 90 nm graphite coated sample on a) graphite top layer, b) source central region c) body central region.

The transient model activation elaborated in [40] can be assumed as reliable for annealings performed in a thermal equilibrium regime, however it loses in accuracy for thermal non-

equilibrium regimes, such as the one described up to now and returns dopant activation values several orders of magnitude lower than those extracted from CTLM measurements. In absence of a model, it is possible to provide an empirical interpretation by arguing that in the regime of 30 ns irradiation, reaching the temperature of 1900 ° C with exposure times of the order of ns, is not still sufficient to achieve satisfactory activations in P highly doped implanted region. In order to obtain high activations, a further increase in temperature is still required.

Although a further investigation of the electrical activation must be conducted as well as the mobility of the carriers must be quantified through Hall measurements, it is possible to point out that from the first emerging data, the activated dopant concentration at low laser energies is competitive to that of common thermal annealings. In further activity progress a comprehensive model for transient model activation prediction can be developed. Laser annealing has strongly contributed to stimulate the fundamental research in the broader field of the nonequilibrium phenomena. As many material science branches, the driving force for the knowledge advancement is represented by the technological applications and in this sense the research in the field of laser annealing would bring advantageous properties, which enable significant improvements of power devices.

Conclusions

This work reports the synthesis of the research activity carried out during my Ph.D. An extensive introduction was given on the properties that make SiC attractive in the field of renewable energy, sensors and power electronics. Emphasis was placed on issues related to epitaxial growth defects in 3C-SiC as well as post implant thermal annealing defects which are a current issue for the reliability of SiC-based technology.

In the first chapter a description of the main defects affecting SiC crystal was provided. Elimination of dislocation defects (1D) remains an open point. Meanwhile, a central problem for 3C-SiC growth is the formation of 2D defects: stacking faults (SFs) and anti-phase or inverted domains boundaries (APB or IDB) defects. A synthesis of the carried out is provided below.

Stacking Faults

The stacking faults (SFs) after being generated are able to propagate into the SiC epilayer approaching the surface and affecting the mechanical and electrical properties of the material.

- *By means of an investigation in HRSTEM, SFs have been classified as intrinsic extrinsic and conservative, depending on the number of layers involved*

- *Plan-view TEM images showed that Partial Dislocations (PDs) limiting the SFs can lye in non-conventional line directions. Trough molecular dynamic simulation it was pointed out that [110] and [112] directions are stable while the [123] and [134] directions are unstable: they collapse to zig-zag lines thought [112] and [110] line directions*

Inverted Domain Boundaries

- *IDB displayed a rotation of 90° around [001] with an additional shift of a/2 [001] and is equivalent to flip the crystal upside down i.e. rotation of 180° around [110]. STEM investigations showed the formation of an inverted domain boundary (IDB) aligned with the*

{110} planes. To the best of our knowledge, this is the first atomic resolution image of an IDB in the (-110) plane. The alignment of the Si-C doublet across the two domains not only revealed the coherent nature of the boundary but also the peculiar structure

- *It was further shown atomic resolution images in the (111). Simple models were evaluated to understand how the IDB interacts with SF and stress relaxation mechanism leading to IDB direction variation.*

IDB and SFs interactions

- *It was observed that IDBs have an important role in the propagation of extended defects in the epilayer through the generation and termination of SFs.The mechanism for generating SFs from IDBs was explained in detail. Lattice partial dislocations (with an associated SF) can be emitted from GBs under applied stress leaving a disconnection on the grain boundary. According to the "Burger's vector" conservation law, an emission of PDs (and the associated SF) from the IDB creates a disconnection on the IDB with the "burger vector" as opposed to the emitted partial that has to be of the type a/6[112]. The formation of disconnections changes the IDB profile*

- *A Monte Carlo simulation was performed in order to shield light on the interaction (generation and termination) of SFs with IDBs. In particular, it was able to reproduce the main experimental results and was able to evidence that SF generation is driven by statistical surface instability during the growth of the crystal.*

Stacking Fault and doping interaction

New innovative tecqunique approach was presented and consisting of horizontal hot-wall chemical vapour deposition using (100)-oriented Si substrates. Heteroepitaxial growth of 3C-SiC on Si with subsequent melting of the Si wafer and the homo-epitaxial growth of 3C-SiC. Both the quality of 3C-SiC hetero-epitaxial layers and homo-epitaxial grown 3C-SiC wafer was widely investigated.

- *The 3C-SiC LO peak revealed that doping incorporation was strongly dependent from temperature. By increasing CVD growth temperature from 1600 to 1700 °C N dopant incorporation moved from 2.1 × 10^{18} N/cm^3 to 6.2 × 10^{18} N/cm^3.*

- *All the analysis related to the crystal structure revealed that SFs density rised, increasing the growth temperature from 1600 °C to 1700 °C. On the other hand, the density of point defects decreases by increasing the growth temperature from 1370 °C (heteroepitaxial process with Si substrate) to the homo-epitaxial growth at 1700 °C.*

- *By μ-Raman spectroscopy and room-temperature μ-photoluminescence, it was possible to detect the distribution of staking faults in the 3C-SiC cross-section. In particular, two kinds of SFs, 4H-like and 6H-like, were identified.*

- *Each kind of SF shows a characteristic PL emission of the 4H-SiC and 6H-SiC located at 393 and 425 nm, respectively. Even though 6H-like SFs show a lower formation energy than 4H-like, and are considered the most common inclusion of other polytypes in 3C-SiC, we observe the presence of 6H-like SFs only near the original interface with silicon, in particular in the first 15 μm. Meanwhile, it was possible to detect the 4H-like SFs along a thickness of 20–25 μm.*

- *Nitrogen suppresses the SF formation only when very close to the SF. Experimental estimation confirmed to be more certain about the range of the influence of the dopant. It was evident that if for the intrinsic sample the average SFs density was 2.2·10^4 cm^{-1} while by increasing doping to 2.9·10^{19} N^+/cm^3 and 5.8·10^{19} N^+/cm^3 such value was notably reduced.*

Compliant substrates

Several different approaches have been proposed to alleviate defectiveness in 3C-SiC. One of the most interesting techniques is the use of compliant substrates. The compliant substrate should be able to better adapt the SiC interface with the Si one and thus reduce the defectivity in the SiC layer grown on Si. Among these approaches, it was investigated the use of a SiGe buffer

layer between the epitaxial layer and the substrate in order to reduce the defectiveness and improve the overall quality of the SiC epi-film as well as the growth on a patterned substrate as inverted silicon pyramids (ISP).

SiGe Buffer Layer

- *Germanium contained in the first carbonized layer was "pushed down" into the $Si_{1-x}Ge_x$ layer giving rise to the segregation observed with TEM and Raman. Segregation was more efficient as the Ge amount is increased. As segregation reached a critical value poly-crystals come out. This phenomenon appeared on the entire surface for the sample grown with 1000 °C carbonization temperature, 15% Ge concentration sample while it is confined to polycrystalline dots in the 1150 °C, 15% sample.*

- *High carbonization temperatures allowed the diffusion of Ge inside the $Si_{1-x}Ge_x$ layer, thus decreasing the segregation at the interface and enhance the diffusion of C in the carbonized layer, realizing a thicker carbonized layer and "pushing down" more Ge in the $Si_{1-x}Ge_x$ layer and thus increasing segregation*

- *In 10% Ge concentration segregation occurs at higher carbonization temperature (1150 °C, 10%) while at low carbonization temperature (1000 °C, 10%) it is negligible. Higher temperatures enhanced the diffusion of C in the carbonized layer making the carbonized layer thicker. This effect increased the Ge concentration "pushed down" (segregated) at the interface. Sample carbonized at high temperature (1150 °C, 10%) manifested small black dots, rough surface, higher TO intensity and low mobility (< 100 $cm^2/V/s$) than the lower temperature counterpart (1000 °C, 10%).*

ISP substrate

- *SFs lying in the (111) plane cross the SF coming from the opposite sides of the pyramid and self-annihilate creating a Lomer dislocation or a "λ shaped defect, reducing the defectivity of the material.*

- *Through HRSTEM and geometrical configuration it was deduced that Si/SiC interface, in both adjacent sides of the pyramid, exposed a carbon face at Si/SiC interface, and thus, Si–C bond perpendicular to the (111) plane was revealed.*

- *Rapid exponential decay in APBs concentration was achieved after a few microns of growth. In particular, it was noted that in a 12 µm epitaxy, the APBs coverage was reduced by a factor 20 with respect to the initial layers. This suggested that increasing the layer thickness is an efficient way to lower the APBs concentration*

- *Formation of voids buried within pyramid was detected due to different growth rate between the plans (111) and the plan (001). Control of the void height and width is needed to reduce the SFs. Void height was triggered by acting on growth rate and pyramid pitch. A conformal growth could be observed if the ratio between (111) and (001) growth rates is about 0.81 and led to void free grown 3C-SiC.*

Convectional Annealing Processes

In the third chapter an analysis on P implanted 4H-SiC samples undergone double step annealing was presented. First annealing, in the temperature range 1650-1750 °C commonly used for dopant activation, is responsible for a wide intra bandgap PL signal. The samples evidenced a compressive stress that widens and shifts the TO peak in the Raman spectra with respect to the as grown sample. A second annealing process (1500 °C) gave rise to a partial reduction of intra-bandgap signal. Furthermore many laser annealing results related to implanted epitaxial layers with single P implantation and double P and Al implantations were delivered and compared with the single thermal annealing treatment.

- *High implant doses (~$10^{20}/cm^3$) require annealing temperatures well beyond conventional currently achievable furnace temperatures to be fully activated.*

- *Temperature increase from 1650 °C to 1750 °C has the collateral effect of increasing the concentration of the V_C intrinsic defect in the 4H-SiC ion implanted and epitaxial layer, which is a well-known minority carrier lifetime killer.*
- *Prismatic interstitial-type dislocation loops have been found as the dominant extended defect. Its average size are typically 1–20 nm in diameter and reside on the {0001} and {11-20} plane, consistent with Frank type behavior with Burger vector orthogonal to lying plane.*
- *Conventional annealing do not allow lattice relaxation towards low energy configurations. Anisotropic-next-nearest-neighbor Ising model demonstrated that evolution towards prismatic dislocation loops is highly energetic. Indeed, Raman E_2(TO) mode displayed large in plane stress values up to 172 Mpa.*
- *Double step annealing process contributed to defectiveness-related PL signal reduction saturating at values ranging between 12% and 20% and was not successful in extended defects remotion.*

Uncoated Laser Annealing Process

Pulsed-laser-based methods have been applied for post-implant annealing of single phosphorus (P) as well as double phosphorus and aluminum (Al) implanted 4H-SiC epitaxial layers in order to restore the crystal. Laser treatments were carried out through a LPX 300 XeCl pulsed excimer laser with 40 Hz repetition rate. Substrate holder inside the chamber was heated at a temperature of 580 °C and a mobile stage allowed to implement an irradiation process with a variable number of shots/points.

- *By observing the intensity variation of Raman phonon modes it was possible to plot crystal recovery trend as a function of energy density, from sub melting regime to phase separation where crystalline Si layers are stratified.*

- *Samples subjected to laser annealing show limited stress values. Especially in high recovery ranges between 0.50 and 0.60 J/cm^2, Raman vibrational frequencies modes close to epitaxy mode were detected and calculated Raman shift revealed almost stress-free samples resulted from laser annealing process.*

- *Room temperature photoluminescence showed at 550 nm a reduced defect-related PL band close with the emission signal of the as grown 4H-SiC epitaxial layer.*

- *Spherical SiO_2 compounds were detected on surface though STEM-EELS analysis and revealed active oxidation phenomena during laser treatment. It was possible to estimate that within the 0.40 J/cm^2 irradiated sample an implanted area of almost 130 nm was preserved, while with the increase of laser energy density this fraction is thinned to 90 nm. It can therefore be inferred that O presence in chamber may have played a role in superficial roughness while etching contributions of the sample are due to the local temperature rising at the surface layers and to the presence of photochemical effects inherent to the interaction with the environment inside the chamber during irradiation.*

- *The increase in the irradiation time from 1000 shots/point to 10000 shots/point did not entail a change in the stress recorded on the sample.*

Coated Laser Annealing Process

In order to acquire a substantial control over irradiated surface quality a pioneering technique was developed to implement implanted 4H-SiC crystalline and electrical properties. The technique exploits irradiations over an absorber layer obtained from the 950 °C bake of a spinned resist on SiC wafer surface. Thanks to its 3800 °C melting temperature and high absorption coefficient, graphite is, in fact, the best candidate to fully absorb laser radiation, allowing a heat diffusive regime along the underlying layers. The outcome of this work was:

- *Approaching towards the laser annealed area, the results show an evolution of the average graphite cristallite size which increases from <2 nm far from the irradiated area to ~8 nm*

- *At 0.50 J/cm^2 the 90 nm graphite coated sample are eroded and SiC surface remains uncovered inducing a slight surface damage.*
- *At 0.60 J/cm^2 the 180 nm graphite coated sample remains intact despite, as attested by optical microscopy investigations, graphite has been removed during laser irradiation. It is evident that the greater initial graphite thickness deposited on the implanted region was effective in damage prevention, as it allowed SiC absorption coefficient shift towards values closer to crystalline one.*

- *the increase in the irradiation time does not entail a change in the stress recorded on the sample*

- *Raman investigation focused on the E_2(TO) peak points out a linear trend with the increase in laser annealing energy. There is therefore a recovery of crystalline damage proportional to the irradiation strength*

- *The increase in the resist pyrolization temperature from 950 °C to 1100 °C resulted in scattering cross section enhancement as well as an increase in the PL signal. Twice the bandgap signal strength compared to the pyrolyzed sample at lower temperature was detected. The defect band in the latter case underwent blue-shift toward 495 nm.*

- *TEM investigation revealed limited source region defectiveness and body region remarkably free from dislocation loops. It can be deduced that, if on the one hand the shorter diffusion times result in smaller dislocation loops size distribution, on the other it is known that thermal non-equilibrium regime does not allow C interstitials diffusion times suitable for prismatic dislocation loops nucleation*
- *The 90 nm graphite coated sample revealed at 0.5 J/cm^2 activation values equal to 6.59·10^{19} ±1.95 e/cm^3 which corresponded to approximately 66% of P implanted activation. This is slightly higher than the value coming from the thermally annealed sample (around 62%).*

This work constitutes a pioneering activity, never carried out before, on the exploration of the energy thresholds accessible to laser annealing in order to guarantee the maintenance of 4H-SiC crystalline quality. In this sense, the new strategies adopted bear towards its adoption in the field of the semiconductor industry. The background analysis on the prospects concerns the use of laser annealing in further application not only in 4H-SiC-based technology, but in general practicable in all compound semiconductors. The annealing processes could therefore be aimed both at the acquisition of new scenarios in the field of activation of 3C-SiC eteroepitaxial wafers and in the field of ohmic contacts obtainable through specific variations to the usual laser annealing methodologies and proposed in this work. Laser annealing would so entail new manufacturing

approach, including the replacement of conventional annealings and the realization of new front side-compatible method for back-side ohmic contact formation. This technological strategy would allow to further reduce power devices R_{on}, postponing the back-grinding step at the end of the process flow-chart. Among the alternative approaches to RTA already featured for Si-based technologies, laser annealing could represent a viable technological solution for the formation of Ni-based ohmic contact on SiC together with higher dopant activation.

Acknowledgments

First of all, I wish to express my gratitude to my Ph.D. Tutor Prof. Lorenzo Torrisi for the consistent support within the PhD program and for providing guidance and feedback throughout these three years of intense work. I'm thankfull also to the Ph.D. coordinator Prof. Vincenza Crupi for the great support and to the entire teaching staff of the doctorate for the training activities during the doctoral lessons.

My deep gratitude goes to Dr. Francesco La Via of CNR-IMM Catania, who expertly guided me through my Ph.D. activity and who shared the excitement of three years of discovery. His unwavering enthusiasm and competence in SiC kept me constantly engaged with research, and his personal generosity involved myself in exciting activities in WInSiC4AP and Challenge projects, allowing me to range over the pioneering results of Laser Annealing on 4H-SiC to the remarkable acquisitions in 3C-SiC growth processes. The activity within SiCilab group in the CNR-IMM was fundamental for the scientific results achieved. Special thanks go to Dr. Simona Boninelli, for having introduced me to the study of SiC ion implantation defects and for mentoring me with extreme competence in TEM microscopy activity alongside Dr. Marta Agati and Dr. Corrado Bongiorno. My appreciation also extends to my laboratory colleagues, Dr. Massimo Zimbone for the numerous shared research activities on defects in 3C-SiC and to Dr. Viviana Scuderi for the experience collected and shared on Raman analysis and optical characterizations on 3C-SiC. Special thanks also to Dr. Annamaria Muoio for her immense and indispensable competence in the different simulation environments allowing me to develop the activity on Comsol. Great thanks to Dr. Salvo Di Franco for the availability of the CNR-IMM clean room, and to Dr. Stefania Privitera for her assistance in the electrical characterization.

I also wish to sincerly thank the research group of the CNR-IMM of Torvergata and in particular Dr. Alessandro Pecora and Dr. Guglielmo Fortunato for the availability of the laboratories and for the strong research contribution essential for the Laser annealing activity on SiC. Special thanks to Dr. Andrea Severino, Dr. Ruggero Anzalone and Dr. Nicolò Piluso of STMicroelectronics Catania for the work of constant scientific collaboration carried out and to Dr. Claudio Chibbaro for his assistance in wafer supply at the beginning of my Ph.D.

I also acknowledge Prof. Lucia Calcagno of University of Catania for her lively interest in the research topic and for her mentoring role that accompanied me in this Ph.D. And finally, I acknowledge my family. I thank them for their constant support, motivation and love. This thesis is dedicated to them.

References

[1]T. Kimoto, and J. Cooper, Fundamental of Silicon Carbide, IEEE Wiley, (2014)

[2] R. F. Davis, G. Kelner, M. Shur, J. W. Palmour, and J. A. Edmond,Proc.IEEE79, 677 (1991)

[3] H. Matsunami, Jpn. J. Appl. Phys. 43, 6835 (2004).

[4]B. J. Baliga, Silicon Carbide Power Devices, World Scientific, Singapore, (2006).

[5]T. Kimoto, Material science and device physics in SiC technology for high-voltage power devices (2018).

[6] J. A. Cooper, Jr. and A. Agarwal, Proc. IEEE 90, 956 (2002).

[7] J. A. Cooper, Jr., M. R. Melloch, R. Singh, A. Agarwal, and J. W. Palmour, IEEE Trans. Electron Devices 49, 658 (2002).

[8]J. W. Palmour, “Silicon carbide power device development for industrial markets,” Tech. Digest of 2014 Int. Electron Devices and Materials (San Francisco, 2014), 1.1.

[9] E. O. Johnson, "Physical Limitations on Frequency and Power Parameters of Transistors," RCA Review, vol. 26, pp. 163-177, (1965)

[10] R. W. Keyes, "Figure of Merit for Semiconductors for High Speed Switches," Proc.IEEE, vol. 60, pp. 225-232, (1972).

[11] B. J. Baliga, "Semiconductors for High-Voltage, Vertical Channel Field-Effect Transistors," J.Appl.Phys., vol. 53, no. 3, pp. 1759-1764, (1982).

[12] K Tone, JH Zhao, L Fursin, P Alexandrov, M Weiner. IEEE Electron Device Letters 24 (7), 463-465, 2003. 71, (2003). Nickel ohmic contacts to p and n-type 4H-SiC.

[13] ROHM Co., Ltd. [http://www.rohm.com/web/global/groups/-/group/groupname/SiC%20 Power%20Devices].

[14] T. Nakamura, Y. Nakano, M. Aketa, R. Nakamura, S. Mitani, H. Sakairi, and Y. Yokotsuji, IEDM Tech. Dig., 26.5.1, (2011),.

[15] D. Chaussende, F. Mercier, A. Boulle, F. Conchon, M. Soueidan, G. Ferro, A. Mantzari, A. Andreadou, E.K. Polychroniadis, C. Balloud, S. Juillaguet, J. Camassel, M. Pons, J. Cryst. Growth 310 (5), 976, (2008).

[16] M. Soueidan, G. Ferro, Adv. Funct. Mater. 16 (2006) 975.

[17] F. La Via, M. Camarda, A. La Magna, Appl. Phys. Rev. 1 (2014) 031301.

[18] N. Piluso, A. Severino, M. Camarda, A. Canino, A. La Magna, F. La Via, Appl. Phys.Lett. 97 (14), 142103, (2010).

[19] K. Sasaki, E. Sakuma, S. Misawa, S. Yoshida, S. Gonda, Appl. Phys. Lett. 45(1), 72, (1984).

[20] T. Tachibana, H.S. Kong, Y.C. Wang, R.F. Davis, J. Appl. Phys. 67, 6375, (1990).

[21] Y. Kondo, T. Takahashi, K. Ishii, Y. Hayashi, E. Sakuma, S. Misawa, H. Dai Mon, M. Yamanaka, S. Yoshida, IEEE Electron Device Lett. 7 (7), 404, (1986).

[22] MI Chaudhry, J. Appl. Phys. 69 (10) (1991) 7319.

[21] V.V. Afanasev, M. Bassler, G. Pensl, M. Schulz, Phys. Solid Status (a) 162, 321, (1997).

[23] A. Schoner, M. Krieger, G. Pensl, M. Abe, H. Nagasawa, Chem. Vap. Depos. 12, 523, (2006).

[24] M. Takahashi, S.-S. Im, M. Madani, H. Kobayashi, J. Electrochem. Soc. 155 (1), H47, (2008).

[25] A. Constant, N. Camara, M. Placidi, J.-M. Decams, J. Camassel, P. Godignon, J. Electrochem. Soc. 158 (1), G13, (2011).

[26] D. Okamoto, H. Yano, K. Hirata, T. Hatayama, T. Fuyuki, IEEE Electron Device Lett. 31 (7), 710, (2010).

[27] J. Senzaki, K. Kojima, S. Harada, R. Kosugi, S. Suzuki, T. Suzuki, K. Fukuda, IEEE Electron Device Lett. 23 (1), 13, (2002).

[28] H. Uchida, A. Minami, T. Sakata, H. Nagasawa, M. Kobayashi, Mater. Sci. Forum 717–720, 1109–1112, (2012).

[29] F. La Via, A. Severino et al. From thin film to bulk 3C-SiC growth: Understanding the mechanism of defects reduction, Materials Science in Semiconductor Processing, 78, 57, (2018).

[30] M. Ruff, H. Mitlehner, R. Helbig, IEEE Trans. Electron Devices 41 (6), 1040, (1994).

[31] G.A. Slack, S.F. Bartram, J. Appl. Phys. 46 (1), 89, (1975).

[32] V. Papaioannou, Ph Komninou, G.P. Dimitrakopulos, K. Zekentes, B. Pecz, Th Karakostas, J. Stoemenos, Diam. Relat. Mater. 6 (10), 1362, (1997).

[33] E. Polychroniadis, M. Syvajarvi, R. Yakimova, J. Stoemenos, J. Cryst. Growth 263, 68, (2004).

[34] F. La Via, M.Camarda et al. Mechanisms of growth and defect properties of epitaxial SiC, Jour. Of Appl. Physics,1,031301, (2014).

[35] F. La Via, Silicon Carbide Epitaxy, Research Signpost, (2014).

[36] TG.Feng, J. Suda, T. Kimoto, Characterization of stacking faults in 4 H - Si C epilayers by room-temperature microphotoluminescence mapping, Applied Physics Letters, 92, 221906, (2008).

[37] K.Kawara, G. Alfieri, and T. Kimoto, Detection and depth analyses of deep levels generated by ion implantation in n- and p-type 4H-SiC, Journal of Applied Physics, 106, 013719, (2009).

[38] H. M. Ayedh, A. Hallén, and B. G. Svensson, Elimination of carbon vacancies in 4H-SiC epi-layers by near-surface ion implantation: Influence of the ion species, Jour of Appl. Phys. 118, 175701, (2015).

[39] Silicon carbide: materials, processing, and devices" edited by Zhe Chuan Feng and Jian H. Zhao (Optoelectronic properties of semiconductors and superlattices / edited by M.O. Manasreh, v. 20) Taylor & Francis, (2004).

[40] V. Simonka, A. Toifl et al. Transient model for electrical activation of aluminium and phosphorus-implanted silicon carbide. Jour. Of Appl. Phys. 123, 235701 (2018).

[41] Sze, S.M. Semiconductor Devices, Physics and Technology, 2nd edn, John Wiley & Sons, Inc. (2002).

[42] Vodakov, Y.A. and Mokhov, E.N. Diffusion and solubility of impurities in Silicon Carbide (eds R.C. Marshall, J.W. Faust Jr., and C.E. Ryan), University of South Carolina Press, p. 508, (1974).

[43] E.M.Handy, M.V.Rao, O.W.Holland, K.A.Jones, M.A.Derenge, and N.Papanicolaou, J. Appl. Phys., 88, 5630, (2000).

[44] Sasaki, S., Suda, J. and Kimoto, T. Lattice mismatch and crystallographic tilt induced by high-dose ion-implantation into 4H-SiC. J. Appl. Phys., 111, 103715, (2012).

[45] P. Persson, L. Hulman et al. Dislocation loop evolution in ion implanted 4H–SiC, Journal of Applied Physics 93, 9395 (2003).

[46]H.M. Ayedh, M.E. Bathen et al. Controlling the Carbon Vacancy in 4H-SiC by Thermal Processing ECS Transactions, 86 (12), 91-97, (2018).

[47] R. Nipoti, H. M. Ayedh, et al Materials Science in Semiconductor Processing vol. 78, pp.13-21, (2018).

[48] A. Parisini, A. Parisini, Roberta Nipoti, J. Phys.: Condens. Matter 29, 035703, (2017).

[49] Bhatnagar, M.; Baliga, B.J. Comparison of 6H-SiC, 3C-SiC, and Si for Power Devices. IEEE Trans. Dev., 40, 645–655, (1993).

[50] Harris, G.L. Properties of Silicon Carbide; Institution of Electrical Engineers: London, UK, (1995).

[51] Ciobanu, F.; Pensl, G.; Nagasawa, H.; Schöner, A.; Dimitrijev, S.; Cheong, K.Y.; Afanas'ev, V.V.;Wagner, G.Traps at the interface of 3C-SiC/SiO2-MOS-structures. Mater Sci. Forum, 433–436, 551–554, (2003).

[52] Saddow, S.E.; Agarwal, A. Advances in Silicon Carbide Processing and Applications; Artech House Publisher:Boston, MA, USA, (2004).

[53] Litrico, G.; Anzalone, R.; Alberti, A.; Bongiorno, C.; Nicotra, G.; Zimbone, M.; Mauceri, M.; Coffa, S.; La Via, F. Stacking faults defects on 3C-SiC homo-epitaxial films. Mater. Sci. Foru, 924, 124–127, (2018).

[54] F. La Via, F. Roccaforte, A. La Magna, R. Nipoti, F. Mancarella, P. Wellman, D. Crippa, M. Mauceri, P. Ward, L. Miglio, M. Zielinski, A. Schöner, A. Nejim, L. Vivani, R. Yakimova, M. Syväjärvi, G. Grosset, F. Torregrossa, M. Jennings, P. Mawby, R. Anzalone, S. Coffa, H. Nagasawa, 3C-SiC Hetero-Epitaxially Grown on Silicon Compliance Substrates and New 3C-SiC Substrates for Sustainable Wide-Band-Gap Power Devices (CHALLENGE), Materials Science Forum, 924, 913-918 (2018).

[55] F. La Via, A. Severino, R. Anzalone, C. Bongiorno, G. Litrico, M. Mauceri, M. Schoeler, P. Schuh, P. Wellmann From thin film to bulk 3C-SiC growth: Understanding the mechanism of defects reduction, Materials Science in Semiconductor Processing 78, 57-68 (2018).

[56] Hristu, R., Stanciu, S.G., Tranca, D.E. et al. Identification of stacking faults in silicon carbide by polarization-resolved second harmonic generation microscopy. Sci Rep 7, 4870 (2017).

[57] J. D. Rittner and D. N. Seidman K. L. Merkle Grain-boundary dissociation by the emission of stacking faults Lomer dislocation; Physical Review B Volume 53, Number 8 (1996);

[58] Zou, L., Yang, C., Lei, Y. et al. Dislocation nucleation facilitated by atomic segregation. Nature Mater 17, 56–63 (2018).

[59] V. Borovikov , M. I. Mendelev,A H. King. Effects of solutes on dislocation nucleation from grain boundaries. International journal of plasticity 90, 146-155, (2017).

[60] Jian Han, Spencer L.Thomas, David J.Srolovitz. Grain-boundary kinetics: A unified approach Progress in Materials Science Volume 98, October, Pages 386-476, (2018).

[61] M. Zimbone, E. G. Barbagiovanni, C. Bongiorno, C. Calabretta, L. Calcagno, G. Fisicaro, A. La Magna, F. La Via; Generation and Termination of Stacking Faults by Inverted Domain Boundaries in 3C-SiC; Cryst. Growth Des., 20, 3104−3111, (2020).

[62] F. Giannazzo, G. Greco, S. Di Franco, P. Fiorenza, I. Deretzis, A. La Magna, C. Bongiorno, M. Zimbone, F. La Via, M. Zielinski, and F. Roccaforte; Impact of stacking faults and domain boundaries on the electronic transport in cubic silicon carbide probed by conductive atomic force microscopy Adv. Electron. Mater., 6, 1901171, 2020.

[63] Song, X.; Michaud, J.F.; Cayrel, F.; Zielinski, M.; Portail, M.; Chassagne, T.; Collard, E.; Alquier, D. Evidence of electrical activity of extended defects in 3C-SiC grown on Si. Appl. Phys. Lett., 96, 142104, (2010).

[64] Lebedev, A.A.; Abramov, P.L.; Lebedev, S.P.; Oganesyan, G.A.; Tregubova, A.S.; Shamshur, D.V. Influence of the defect density (twins boundaries) on electrical parameters of 3C-SiC epitaxial films. Physica B, 404,4758–4760, (2009).

[65] Stacking faults in 3C−,4H−, and 6H−SiC polytypes investigated by an ab initio supercell method Ulf Lindefelt, Hisaomi Iwata, Sven Öberg, and Patrick R. Briddon Phys. Rev. B 67, 155204 – Published 9 April (2003).

[66] Maya Marinova, Frederic Mercier, Alkioni Mantzari, Irina Galben, Didier Chaussende, Efstathios K.Polychroniadis. A TEM study of in-grown stacking faults in 3C-SiC layers grown by

CF-PVT on 4H-SiC substrates Physica B: Condensed Matter Volume 404, Issues 23–24, 15 December, Pages 4749-4751, (2009).

[67] A. Iijima,I. Kamata,H. Tsuchida,J. Suda and T. Kimoto. Correlation between shapes of Shockley stacking faults and structures of basal plane dislocations in 4H-SiC epilayers. Journal Philosophical Magazine Volume 97, 2017 - Issue 30 Pages 2736-2752, (2017).

[68] Steven Ceron ; Hiroyuki Nagasawa ; Maki Suemitsu Interactions between gliding dislocations in 3C-SiC(001), IEEE MIT Undergraduate Research Technology Conference (URTC), (2015).

[69] G. Ferro, 3C-SiC Heteroepitaxial Growth on Silicon: The Quest for Holy Grail, Critical Reviews in Solid State and Materials Sciences, 40:1, 56-76, (2015).

[70] T. Kimoto A.Itoh and H.Matsunami. Step-Controlled Epitaxial Growth of High-Quality SiC Layers Phys. Stat. Sol. (b) 202, 247, (1997).

[71] R. Anzalone, N. Frazzetto, A. Raciti; M.A. Salanitri, G. D'Arrigo, G. Abbondanza. Apparatus for manufacturing a silicon carbide wafer. U.S. Patent 15/715,940, 29 March (2018).

[72] Zimbone, M.; Mauceri, M.; Litrico, G.; Barbagiovanni, E.G.; Bongiorno, C.; La Via, F. Protrusions reduction in 3C-SiC thin film on Si. J. Cryst. Growth, 498, 248, (2018).

[73] La Via, F.; Severino, A.; Anzalone, R.; Bongiorno, C.; Litrico, G.; Mauceri, M.; Schoeler, M.; Schuh, P.; Wellmann, P. From thin film to bulk 3C-SiC growth: Understanding the mechanism of defects reduction. Mater. Sci. Semicond. Process. 78, 57–68, (2018).

[74] E. Polychroniadis, M. Syväjärvi, R. Yakimova, J. Stoemenos, Microstructural characterization of very thick freestanding 3C-SiC wafers, J. Cryst. Growth 263, 68, (2004).

[75] H. Nagasawa, K. Yagi, T. Kawahara, 3C-SiC hetero-epitaxial growth on undulant Si(001) substrate, J. Cryst. Growth 237, 1244, (2002).

[76] W. R. L. Lambrecht, B. Segall, Electronic-structure study of the (110) inversion grain boundary in SiC, Phys. Rev. B. 41, 2948, (1990).

[77] Introduction to dislocations D.Hull D.J.Bacon. Fifth edition Elsevier (2011).

[78] David B. Williams, C. Barry Carter - Transmission electron microscopy_ a textbook for materials science (2009, Springer).

[79] A. Sarikov, A. Marzegalli, L. Barbisan, F. Montalenti, and L. Miglio. Structure and Stability of Partial Dislocation Complexes in 3C-SiC by Molecular Dynamics Simulations; Materials (Basel). Sep; 12(18): 3027, (2019).

[80] E. Polychroniadis, M. Syväjärvi, R. Yakimova, J. Stoemenos, Microstructural characterization of very thick freestanding 3C-SiC wafers, J. Cryst. Growth 263, 68, (2004).

[81] H. Nagasawa, R. Gurunathan, M. Suemitsu, Controlling planar defects in 3C-SiC: Ways to wake it up as a practical semiconductor, Mater. Sci. Forum 821, 108, (2015).

[82] K. Momma, F. Izumi, VESTA 3 for three-dimensional visualization of crystal, J. Appl. Crystallogr. 44, 1272, (2011).

[83] G. Fisicaro, C. Bongiorno, I. Deretzis, F.Giannazzo, F. La Via, F. Roccaforte, M. Zielinski, M. Zimbone, A. La Magna Appl. Phys. Rev. (accepted)

[84] A. Hunter, I. J. Beyerlein, Unprecedented grain size effect on stacking fault width, APL Mater. 1, 032109, (2013).

[85] J. Rittner, D. Seidman, K. Merkle, Grain-boundary dissociation by the emission of stacking faults, Phys. Rev. B. 53, 465 R4241, (1996).

[86] Tsuru T, Shibutani Y, Kaji Y. Fundamental interaction process between pure edge dislocation and energetically stable grain boundary. Phys Rev B;79:012104, (2009).

[87] Minor AM, Lilleodden ET, Stach EA, Morris JW. Direct observations of incipient plasticity during nanoindentation of Al. J. Mater.Res.;19:176–82, (2004).

[88] Kondo S, Mitsuma T, Shibata N, Ikuhara Y. Direct observation of individual dislocation interaction processes with grain boundaries Science Advances, 2(11), e1501926, (2016).

[89] Wang L, Zhang Z, Ma E, Han XD. Transmission electron microscopy observations of dislocation annihilation and storage in nanograins. Appl. Phys. Lett.; 98:051905, (2011).

[90] Tschopp MA, McDowell DL. Grain boundary dislocation sources in nanocrystalline copper. Scr Mater;58,299, (2008).

[91] Spearot DE, Tschopp MA, Jacob KI, McDowell DL. Tensile strength of <100> and <110> tilt bicrystal copper interfaces. Acta Mater;55,705, (2007).

[92] Tucker GJ, Tschopp MA, McDowell DL. Evolution of structure and free volume in symmetric tilt grain boundaries during dislocation nucleation. Acta Mater,58, 6464, (2010);

[93] Tucker GJ, McDowell DL. Non-equilibrium grain boundary structure and inelastic deformation using atomistic simulations. Int J Plast; 27(6):841-857, (2011).

[94] Zhang L, Lu C, Tieu K. Atomistic simulation of tensile deformation behavior of Σ5 tilt grain boundaries in copper bicrystal. Sci. Re.p 4, Article number: 5919, (2015).

[95] Wyman RD, Fullwood DT, Wagoner RH, Homer ER. Variability of non-Schmid effects in grain boundary dislocation nucleation criteria. Acta Mater;124:588, (2017).

[96] Spearot DE, Tschopp MA, Jacob KI, McDowell DL. Tensile strength of <100> and <110> tilt bicrystal copper interfaces. Acta Mater; 55:705, (2007).

[97] A. Mantzari, C. B. Lioutas, E. K. Polychoniadis, A tem study of inversion domain boundaries annihilation mechanism in 3C-SiC during growth, Mater. Sci. Forum 615, 331, (2009).

[98] Elkajbaji M, Thibault-Desseaux J. Interactions of deformation-induced dislocations with Σ = 9 (122) grain boundaries in Si studied by HREM. Philos Mag A,58:325, (1988).

[99] H. Long, Y. Liu, D. Kong, H. Wei, Y. Chen, S. Mao, Shearing mechanisms of stacking fault and anti-phase-boundary forming dislocation pairs in the γ' phase in Ni-based single crystal superalloy,J. Alloys Compd. 724, 287, (2017).

[100] J. T. M. D. Hosson, Superlattice dislocations in L12 ordered alloys and in alloys containing L12 ordered precipitates, Mater. Sci. Eng. 81, 515, (1986).

[101] J. Yamasaki, S. Inamoto, Y. Nomura, H. Tamaki, N. Tanaka, Atomic structure analysis of stacking faults and misfit dislocations at 3C-SiC/Si(001) interfaces by aberration-corrected transmission electron microscopy, J. Phys. D 45, 494002, (2012).

[102] Y. Sun, S. Izumi, S. Sakai, K. Yagi, H. Nagasawa, Core element effects on dislocation nucleation in 3C-SiC: Reaction pathway analysis, Comput. Mater. Sci. 79, 216, (2013).

[103] N.Piluso, M. Camarda, and F. La Via; A novel micro-Raman technique to detect and characterize 4H-SiC stacking faults; Journal of Applied Physics 116, 163506, (2014).

[104] E. G. Barbagiovanni, A. Alberti , C. Bongiorno, E. Smecca, M. Zimbone, R. Anzalone, G. Litrico, M. Mauceri, A. La Magna, F. La Via "High Resolution Investigation of Stacking Fault Density by HRXRD and STEM", Materials Science Forum, 963:346-349, (2019).

[105] G. Hug, A. Loiseau, P. Veyssiere, Dislocation in TiAl, Revue de Physique Appliquee 23, 673, (1988).

[106] P. Pirouz, P. M. Hazzledine, Cross-slip and twinning in semiconductors, Scr. Metall. Mater. 25, 1167, (1991).

[107] R. S. Gates, The role of grain boundaries dislocations in grain boundary sliding, Acta Metall. 21, 855, (1973).

[108] F.Giannazzo, G.Greco, S.Di Franco, P.Fiorenza, I.Deretzis, A.La Magna, C.Bongiorno, M.Zimbone, F.La Via, M.Zielinski, F.Roccaforte. Adv. Electron.Mater., 6, 1901171, (2020).

[109] Song, X.; Michaud, J.F.; Cayrel, F.; Zielinski, M.; Portail, M.; Chassagne, T.; Collard, E.; Alquier, D. Evidence of electrical activity of extended defects in 3C–SiC grown on Si. Appl. Phys. Lett., 96, 142104, (2010).

[110] La Via, F.; Severino, A.; Anzalone, R.; Bongiorno, C.; Litrico, G.; Mauceri, M.; Schoeler, M.; Schuh, P.Wellman, P. From thin film to bulk 3C-SiC growth: Understanding the mechanism of defects reduction, Mater. Sci. Semicond. Proc. 78, 57–68, 2018.

[111] Feng, G.; Suda, J.; Kimoto, T. Characterization of stacking faults in 4H-SiC epilayers by room-temperature microphotoluminescence mapping. Appl. Phys. Lett., 92, 221906, (2008).

[112] Feng, G.; Suda, J.; Kimoto, T. Characterization of stacking faults in 4H-SiC epilayers by room-temperature microphotoluminescence mapping. Appl. Phys. Lett., 92, 221906, (2008).

[113] Litrico, G.; Piluso, N.; La Via, F. Detection of Crystallographic Defects in 3C-SiC by Micro-Raman and Micro-PL Analysis. Mater Sci. Forum, 897, 303–306, (2017).

[114] Wang, K.; Fang, X.Y.; Li, Y.Q.; Yin, A.C.; Jin, H.B.; Yuan, J.; Cao, M.S. Radiative recombination model of degenerate semiconductor and photoluminescence properties of 3C-SiC by P and N doping. J. Appl. Phys., 112, 033508, (2012).

[115] Feng, G.; Suda, J.; Kimoto, T. Characterization of stacking faults in 4H-SiC epilayers by room-temperature microphotoluminescence mapping. Appl. Phys. Lett. 92, 221906, (2008).

[116] Deretzis, I.; Camarda, M.; La Via, F.; la Magna, A. Electron backscattering from stacking faults in SiC by means of ab initio quantum transport calculations. Phys. Rev. B, 85, 235310, (2012).

[117] Scalise, E.; Marzegalli, A.; Montalenti, F.; Miglio, L. Temperature-Dependent Stability of Polytypes and Stacking Faults in SiC: Reconciling Theory and Experiments. Phys. Rev. Appl. 12, 021002, (2019).

[118] Mahadik, N.A.; Stahlbush, R.E.; Qadri, S.B.; Glembocki, O.J.; Alexson, D.A.; Hobart, K.D.; Caldwell, J.D.; Myers Ward, R.L.; Tedesco, J.L.; Eddy, J.R.; et al. Structure and Morphology of Inclusions in 4_ O_cut 4H-SiC Epitaxial Layers. J. Electron. Mater., 40, 413–418, (2011).

[119] Perova, T.S.; Wasyluk, J.; Kukushkin, S.A.; Osipov, A.V.; Feoktistov, N.A.; Grudinkin, S.A. Micro-Raman Mapping of 3C-SiC Thin Films Grown by Solid–Gas Phase Epitaxy on Si (111). Nanoscale Res. Lett., 5, 1507–1511, (2010).

[121] Shalish, I.; Altfeder, I.B.; Narayanamurti, V. Observations of conduction-band structure of 4H- and 6H-SiC. Phys. Rev. B, 65, 073104, (2002).

[122] Severino, A.; Locke, C.; Anzalone, R.; Camarda, M.; Piluso, N.; La Magna, A.; Saddow, S.E.; Abbondanza, G.; D'Arrigo, G.; La Via, F. 3C-SiC film growth on Si substrates. ECS Trans., 35, 99–116, (2001).

[123] Mitani, T.; Nakashima, S.; Okumura, H.; Nagasawa, H. Raman Scattering Analyses of Stacking Faults in 3C-SiC Crystals. Mater. Sci. Forum, 527–529, 343–346, (2006).

[124] Boulle, A.; Dompoint, D.; Galben-Sandulache, I.; Chaussende, D. Polytypic transformations in SiC: Di_use x-ray scattering and Monte Carlo simulations. Phys. Rev. B, 88, 024103, (2013).

[125] Bernstein, N.; Gotsis, H.J.; Papaconstantopoulos, D.A.; Mehl, M.J. Tight-binding calculations of the band structure and total energies of the various polytypes of silicon carbide. Phys. Rev. B, 71, 075203, (2005).

[126] Kawanishi, S.; Mizoguchi, T. E_ect of van derWaals interactions on the stability of SiC polytypes. J. Appl. Phys., 119, 175101, (2016).

[127] Marinova, M.; Mercier, F.; Mantzari, A.; Galben, I.; Chaussende, D.; Polychroniadis, E.K. A TEM study of in-grown stacking faults in 3C-SiC layers grown by CF-PVT on 4H-SiC substrates. Phys. B, 404, 4749–4751, (2009).

[128] F. La Via et al. From thin film to bulk 3C-SiC growth: Understanding the mechanism of defects reduction, Mat. Sci. Semic. Proc. 78, 57–68, (2018).

[129] Y. Umeno et al. Ab initio density functional theory calculation of stacking fault energy and stress in 3C-SiC. Phys. Status Solidi B, 1–6, (2012).

[130] Silicon Carbide Epitaxy; La Via, F., Ed.; Research Signpost: Thiruvananthapuram, Kerala, India, ISBN 978-81-308-0500-9, (2012).

[131] Schuh, P.; Schöler, M.; Wilhelm, M.; Syväjärvi, M.; Litrico, G.; La Via, F.; Mauceri, M.; Wellmann, P.J. Sublimation growth of bulk 3C-SiC using 3C-SiC-on-Si (1 0 0) seeding layers. J. Cryst. Growth, 478, 159–162, (2017).

[132] Nakashima, S.; Nakatake, Y.; Ishida, Y.; Talkahashi, T.; Okumura, H. Detection of defects in SiC crystalline films by Raman scattering. Physica B, 308–310, 684–686, (2001).

[133] Camarda, M.; la Magna, A.; Canino, A.; La Via, F. Stacking faults evolution during epitaxial growths: Role of surface the kinetics. Surf. Sci., 604, 939, (2010).

[134] Al Atem, A.S.; Ferrier, L.; Canut, B.; Chauvin, N.; Guillot, G.; Bluet, J.M. Luminescent point defect formation in 3C-SiC by ion implantation. Phys. Status Solidi C, 13, 860–863, (2016).

[135] La Via, F.; Camarda, M.; la Magna, A. Mechanisms of growth and defect properties of epitaxial SiC. Appl. Phys. Rev., 1, 031301, (2014).

[136] Nakashima, S.; Harima, H. Raman investigation of SiC polytypes. Phys. Status Solidi, 162, 39, (1997).

[137] Calabretta, C.; Zimbone, M.; Barbagiovanni, E.G.; Boninelli, S.; Piluso, N.; Severino, A.; Di Stefano, M.A.; Lorenti, S.; Calcagno, L.; La Via, F. Thermal Annealing of High Dose P Implantation in 4H-SiC. Mater. Sci. Forum, 963, 399–402, (2019).

[138] Nishino, S.; Powell, J.A.; Will, H.A. Production of large-area single-crystal wafers of cubic SiC for semiconductor devices. Appl. Phys. Lett., 42, 460–462, (1983).

[139] Reyes, M.; Shishkin, Y.; Harvey, S.; Saddow, S.E. Development of a high-growth rate 3C-SiC on Si CVD process. MRS Online Proc. Lib. Arch.,911, (2006).

[140] Zimbone, M.; Zielinski, M.; Barbagiovanni, E.G.; Calabretta, C.; La Via, F. 3C-SiC grown on Si by using a $Si_{1-x}Ge_x$ buffer layer. J. Cryst. Growth, 519, 1–6, 2019.

[141] La Via, F.; D'Arrigo, G.; Severino, A.; Piluso, N.; Mauceri, M.; Locke, C.; Saddow, S.E. Patterned substrate with inverted silicon pyramids for 3C–SiC epitaxial growth: A comparison with conventional (001) Si substrate. J. Mater. Res. 28, 94–103, (2013).

[142] Albani, M.; Marzegalli, A.; Bergamaschini, R.; Mauceri, M.; Crippa, D.; La Via, F.; Von Känel, H.; Miglio, L. Solving the critical thermal bowing in 3C-SiC/Si (111) by a tilting Si pillar architecture. J. Appl. Phys. 123, 185703, (2018).

[143] Namavar, F.; Colter, P.C.; Planes, N.; Fraisse, B.; Pernot, J.; Juillaguet, S.; Camassel, J. Investigation of porous silicon as a new compliant substrate for 3C-SiC deposition. Mater. Sci. Eng. 61, 571–57, (1999).

[144] Nagasawa, H.; Yagi, K.; Kawahara, T. 3C-SiC hetero-epitaxial growth on undulant Si (001) substrate. J. Cryst. Growth, 1244, 237–239, (2002).

[145] Nagasawa, H.; Yagi, K.; Kawahara, T. 3C-SiC hetero-epitaxial growth on undulant Si (001) substrate. J. Cryst. Growth, 1244, 237–239, (2002).

[146] Schöner, A.; Krieger, M.; Pensl, G.; Abe, M.; Nagasawa, H. Fabrication and characterization of 3C-SiC-based MOSFETs. Chem. Vap. Deposition, 12, 523–530, (2006).

[147] Nagasawa, H.; Abe, M.; Yagi, K.; Kawahara, T.; Hatta, N. Fabrication of high performance 3C-SiC vertical MOSFETs by reducing planar defects. Phys. Status Solidi B, 245, 1272–1280, (2008).

[148] Nagasawa, H.; Kawahara, T.; Yagi, K.; Hatta, N.; Uccida, H.; Kobayashi, M.; Reshanov, S.; Esteve, R.; Schoner, A. High quality 3C-SiC substrate for MOSFET fabrication. Mater. Sci. Forum, 711, 91–98, (2012).

[149] Nagasawa, H.; Yagi, K.; Kawahara, T.; Hatta, N. Reducing planar defects in 3C-SiC. Chem. Vap. Deposition, 12, 502–508, (2006).

[150] Anzalone, R.; Litrico, G.; Piluso, N.; Reitano, R.; Alberti, A.; Fiorenza, P.; Co_a, S.; La Via, F. Carbonization and transition layer e_ects on 3C-SiC film residual stress. J. Cryst. Growth, 473, 11–19, (2017).

[151] Polychroniadis, E.; Syväjärvi, M.; Yakimova, R.; Stoemenos, J. Microstructural characterization of very thick freestanding 3C-SiC wafers. J. Cryst. Growth, 263, 68–75, (2004).

[152] Litrico, G.; Anzalone, R.; Alberti, A.; Bongiorno, C.; Nicotra, G.; Zimbone, M.; Mauceri, M.; Coffa, S.; La Via, F. Stacking Faults Defects on 3C-SiC Homo-Epitaxial Films. Mater. Sci. Forum, 924, 124–127, (2018).

[153] Namavar, F.; Colter, P.C.; Planes, N.; Fraisse, B.; Pernot, J.; Juillaguet, S.; Camassel, J. Investigation of porous silicon as a new compliant substrate for 3C-SiC deposition. Mater. Sci. Eng., 61, 571–575, (1999).

[154] P. Masri, M.R. Laridjani, T. Wohner, J. Pezoldt, M. Averous, Optimization of 3CSiC/Si heterointerfaces in epitaxial growth, Comput. Mater. Sci. 17, 544–550, (2000).

[155] J. Pezoldta, Ch. Forster, P. Weih, P. Masri, Electrical characterization of SiC/Si heterostructures with Ge-modified interfaces, Appl. Surf. Sci. 184, 79–83, (2001).

[156] P. Masri, N. Moreaud, M.R. Laridjani, J. Calas, M. Averous, G. Chaix, A. Dollet, R. Berjoan, C. Dupuy, The physics of heteroepitaxy of 3C–SiC on Si: role of Ge in the optimization of the 3C–SiC: Si heterointerface, Mater. Sci. Eng., B 61–62, 535–538¸ (1999).

[157] T. Fuyuki, T. Hatayama, H. Matsunami, Heterointerface control and epitaxial growth of 3C-SiC on Si by gas source molecular beam epitaxy, Phys. Stat. Sol. (b) 202, 359, (1997)

[158] W.L. Sarney, L. Salamanca-Riba, R.D. Vispute, P. Zhou, C. Taylor, M.G. Spencer, K.A. Jones, SiC/Si(111) film quality as a function of GeH4 flow in an MOCVD reactor, J. Electron. Mater. 29 (3) (2000).

[159] W.L. Sarney, M.C. Wood, L. Salamanca-Riba, P. Zhou, M. Spencer, Role of Ge on film quality of SiC grown on Si, J. Appl. Phys. 91 (2) (2002).

[160] D. De Salvador, M. Petrovich, M. Berti, F. Romanato, E. Napolitani, A. Drigo, Lattice parameter of $Si_{1-x-y}Ge_xC_y$ alloys, Phys. Rev. B 61 (19) (2000).

[161] N. Piluso, M. Camarda, R. Anzalone, A. Severino, S. Scalese, F. La Via, Analysis on 3C-SiC layer grown on pseudomorphic-Si/Si 1–x Ge x/Si (001) heterostructures, Mater. Sci. Forum 806 (2015).

[162] S. Nakashima, H. Harima, Raman investigation of SiC polytypes, Phys. Stat. Sol. (a) 162 (1997) 39.

[163] H. Chen, Y.K. Li, C.S. Peng, H.F. Liu, Y.L. Liu, Q. Huang, J.M. Zhou, Qi-Kun Xue, Crosshatching on a SiGe film grown on a Si(001) substrate studied by Raman mapping and atomic force microscopy, Phys. Rev. B 65, 233303, (2002).

[164] V. Simonka, A. Hossinger, S. Selberherr, and J. Weinbub. 123, 235701, (2018).

[165] J. Senzaki, K. Fukuda, and K. Arai, J. Appl, Phys. 94, 2942, (2003);

[166] Y. Hishida, M. Watanabe, K. Nakashima, and O. Eryu, Excimer laser annealing of ion-implanted 6H-silicon carbide Mater. Sci. Forum, 873, 338–342, (2000).

[167] S. Ahmed, C. J. Barbero, and T. W. Sigmon, Activation of ion implanted dopants in αSiC Appl. Phys. Lett., 712-714,66, (1995).

[168]Y. Tanaka, H. Tanoue, and K. Arai, Electrical activation of the ion-implanted phosphorus in 4H-SiC by excimer laser annealing, J. Appl. Phys, 93, 5934, (2003).

[169]C. Boutopoulos, P.Terzis, et al., Laser annealing of Al implanted silicon carbide: Structural and optical characterization Appl. Surf. Sci., 7912-7916, 253, (2007).

[170] F. Mazzamuto, S. Halty, Y. Mori, Silicon Carbide recrystallization mechanism by non-equilibrium melting laser anneal, Mat. Sci Forum, 858, 540-543, (2016).

[171] E. Fontana, N. Piluso, A. Russo, S, Lorenti, C.M. Marcellino, S. Coffa, F. La Via. Material Science Forum. 858, 418-421, (2016).

[172] H. M. Ayedh, R. Nipoti, A. Hallén, and B. G. Svensson, J. Appl. Phys. 122, 025701, (2017).

[173] S. Nakashima, T. Mitani, J. Senzaki, H. Okumura et al. J. Appl. Phys. 97, 123507, (2005).

[174] P. O. Å. Persson and L. Hultman, Jour. App. Phys. 100, 053521, (2006).

[175]P.O.A. Persson, and Hultman, Dislocation loop in ion implanted 4H-SiC, Jour. of Apll. Phys.,03, 9395, (2003).

[176] L.H. Karlsson, A.Hallén, J.Birch, L.Hultman, P.O.Å.Persson Mater. Letters 181, 325–327, (2016).

[177] P.O.A. Persson et al, Otswald ripening of interstitial-type dislocation loops in 4H-Silicon Carbide, Jour of Appl. Phys, 100, 053521 (2006);

[178] Song, Y., Dhar, S., Feldman, L.C. et al. Modified Deal-Grove model for the thermal oxidation of silicon carbide. J. Appl. Phys., 95, 4953, (2004).

[179] M. H. Hong, A. V. Samant, and P. Pirouz, Philos. Mag. A 80, 919, (2000).

[180] H. Iwata, U. Lindefelt, S. Öberg, and P. R. Briddon, Mater. Sci. Forum 389-393, 439, (2002).

[181] H. Iwata, U. Lindefelt, S. Öberg, and P. R. Briddon, J. Phys.: Condens. Matter 14, 12 733 (2002).

[182] S. Nakashima and H. Harima, Raman Investigation of SiC Polytypes, Phys. Stat. Solidi ,32, p. 162, (1997).

[183] C. Dutto, E. Fogarassy, D. Mathiot, et al, Numerical and experimental analysis of pulsed excimer laser processing of silicon carbide Appl. Surf. Sci., 292, pp. 362-366, (2003).

[184]R. Sugie and T. Uchida, Determination of stress components in 4H-SiC power devices via Raman spectroscopy, J. Appl. Phys, 122, p. 195703, (2017).

[185] H. M. Ayeddh, V. Bobal, R. Nipoti, et al., Elimination of carbon vacancies in 4H-SiC employing thermodynamic equilibrium conditions at moderate temperatures, J. Appl. Phys, 115, p. 012005-1, (2014).

[186] C. Calabretta, M. Zimbone, et al., Thermal Annealing of high dose P implantation in 4H-SiC, Mat. Sci. Forum ,963, pp. 399-402, (2019).

[187] R. Nipoti, H. M. Ayeddh, and G. Svensson, Defects related to electrical doping of 4H-SiC by ion implantation, Mat. Sci. Semicon. Proc., 78, p. 13-21, (2017).

[188] Choi, I.; Jeong, H.Y.; Shin, H.; Kang, G.; Byun, M.; Kim, H.; Chitu, A.M.; Im, J.S.; Ruoff, R.S.; Choi, S.Y.; et al. Laser-induced phase separation of silicon carbide. Nat. Commun., 7, 13562, (2016).

[189] F. Mazzamuto, S. Halty, Y. Mori, Silicon Carbide recrystallization mechanism by non-equilibrium melting laser anneal, Mat. Sci Forum, 858, 540-543, (2016).

[190] T. Kimoto, J.A.Cooper, Fundamentals of Silicon Carbide, JohnWiley & Sons Singapore Pte. Ltd. , 202, (2014).

[191]Y. Song, anf F.W. Smith, Phase diagram for the interaction of oxygen with SiC, Appl. Phys Let., 81, 3061, (2002).

[192] A.C. Ferrari Raman Spectroscopy of graphene and graphite: Disorder, electron-phonon coupling, doping and nonadiabatic effects, Solid State communications 143, 47-57, (2007).

[193] S. Piscanec, M. Lazzeri,F. Mauri et al. Phys. Rev. Lett, 93, 185503, (2004).

[194] M.A. Pimenta et al. Studyng disorder in graphite-based system by Raman spectroscopy,Physical Chemistry Chemical Physics 1276, 9, (2007).

[195]M. Quian, Formation of graphene sheets through laser exfoliation of highly ordered pyrolytic graphite, Applied Physics Letters, 98,17, (2011).

[196] A. Galeckas et al., Temperature Dependence of the Absorption Coefficient in 4H- and 6H-Silicon Carbide at 355 nm Laser Pumping Wavelength, Phys. Stat. Sol(a) 191 2, 613, (2002)

[197] Wagner, B. Magnusson, W. M. Chen, and E. Janze , Electronic structure of the neutral silicon vacancy in 4Hand 6HSiC, Mt. of Physics and Measurement Technology, Linköping University, S-581 83 Linköping, Sweden Phys. Rev. B 62, 16555, (2000).

.

[198] J. Senzaki, K. Fukuda, and K. Arai, "Influences of postimplantation annealing conditions on resistance lowering in high-phosphorus-implanted 4H-SiC," J. Appl. Phys. 94, 2942–2947, (2003).

[199] M. Laube, F. Schmid, G. Pensl, G. Wagner, M. Linnarsson, and M. Maier, "Electrical activation of high concentrations of N^+ and P^+ ions implanted into 4H-SiC," J. Appl. Phys. 92, 549–554, (2002).

[200] V. Simonka, A. Hossinger, J. Weinbub, and S. Selberherr, "Modeling of electrical activation ratios of phosphorus and nitrogen doped silicon carbide," in Proceedings of the International Conference on Simulation of Semiconductor Processes and Devices (SISPAD), 125–128, (2017).

[201] A. Severino, D. Mello et al. Effects of thermal annealing processes in Phosphorous implanted 4H-SiC layers, Mat. Sci. Forum., 963,407-411, (2019).

[202] D. Applin et al. Icarus 307, 40–82, (2018).

[203] T.Pavlov, L.Vlahivic et al. Thermochimica Acta, 652, 39-52, (2017)

[204] A. Oganov et al. Structure, Bonding, and Mineralogy of Carbon at Extreme Conditions, Rev. in mineralogy and geochemistry, 75(1) 47-77, (2013)